

INFORMATION TO USERS

This manuscript has been reproduced from the microfilm master. UMI films the text directly from the original or copy submitted. Thus, some thesis and dissertation copies are in typewriter face, while others may be from any type of computer printer.

The quality of this reproduction is dependent upon the quality of the copy submitted. Broken or indistinct print, colored or poor quality illustrations and photographs, print bleedthrough, substandard margins, and improper alignment can adversely affect reproduction.

In the unlikely event that the author did not send UMI a complete manuscript and there are missing pages, these will be noted. Also, if unauthorized copyright material had to be removed, a note will indicate the deletion.

Oversize materials (e.g., maps, drawings, charts) are reproduced by sectioning the original, beginning at the upper left-hand corner and continuing from left to right in equal sections with small overlaps. Each original is also photographed in one exposure and is included in reduced form at the back of the book.

Photographs included in the original manuscript have been reproduced xerographically in this copy. Higher quality 6" x 9" black and white photographic prints are available for any photographs or illustrations appearing in this copy for an additional charge. Contact UMI directly to order.

UMI

A Bell & Howell Information Company
300 North Zeeb Road, Ann Arbor MI 48106-1346 USA
313/761-4700 800/521-0600

University of Alberta

**Influence of the impeller and tank geometry on low frequency
phenomena and flow stability**

by



Biljana Grgic

A thesis submitted to the faculty of graduate study and research in partial fulfillment
of the requirements for the degree of

Master of Science

in

Chemical Engineering

Department of Chemical and Material Engineering

Edmonton, Alberta

Fall 1998



National Library
of Canada

Acquisitions and
Bibliographic Services

395 Wellington Street
Ottawa ON K1A 0N4
Canada

Bibliothèque nationale
du Canada

Acquisitions et
services bibliographiques

395, rue Wellington
Ottawa ON K1A 0N4
Canada

Your file Votre référence

Our file Notre référence

The author has granted a non-exclusive licence allowing the National Library of Canada to reproduce, loan, distribute or sell copies of this thesis in microform, paper or electronic formats.

The author retains ownership of the copyright in this thesis. Neither the thesis nor substantial extracts from it may be printed or otherwise reproduced without the author's permission.

L'auteur a accordé une licence non exclusive permettant à la Bibliothèque nationale du Canada de reproduire, prêter, distribuer ou vendre des copies de cette thèse sous la forme de microfiche/film, de reproduction sur papier ou sur format électronique.

L'auteur conserve la propriété du droit d'auteur qui protège cette thèse. Ni la thèse ni des extraits substantiels de celle-ci ne doivent être imprimés ou autrement reproduits sans son autorisation.

0-612-34369-3

Canada

University of Alberta

Library Release Form

Name of Author: Biljana Grgic

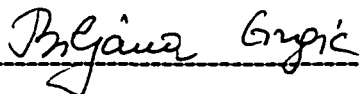
Title of Thesis: Influence of the impeller and tank geometry on low frequency phenomena and flow stability

Degree: Master of Science

Year this Degree Granted: 1998

Permission is hereby granted to the University of Alberta Library to reproduce single copies of this thesis and to lend or sell such copies for private, scholarly, or scientific research purposes only.

The author reserves all other publication rights in association with the copyright in the thesis, and except as herein before provided, neither the thesis nor any substantial portion thereof may be printed or otherwise reproduced without the author's prior written permission.



Biljana Grgic

202, 10230-114 Street

Edmonton, Alberta, Canada


T5K 1R9

Date: Sept. 23, 1998


University of Alberta

Faculty of Graduate Studies and Research

The undersigned certify that they have read, and recommend to the Faculty of Graduate Studies and Research, a thesis entitled **Influence of the impeller and tank geometry on low frequency phenomena and flow stability** submitted by Biljana Grgic in partial fulfillment of the requirements for the degree of Master of Science in Chemical Engineering.



Dr. S.M Kresta (Supervisor)



Dr. L.W. Sigurdson



Dr. P.A.J. Mees

Date: August 28/98

Abstract

The main objective of this thesis is to investigate the existence of low frequency phenomena, or nonstationary aspects of the flow in a stirred tank using different impeller and tank geometries. Two data analysis techniques were used to analyze the velocity field: frequency analysis and data smoothing. Frequency analysis required investigation of the binned autocorrelation technique used on the unevenly spaced data records. In all, three techniques were used to calculate the frequency spectrum from the LDV velocity record, finally showing that the existing signal processing unit cannot resolve high frequency (turbulent) fluctuations. The second technique (data smoothing) was then applied to analyze flow stability for four impellers: the Rushton turbine (RT), the pitched blade turbine (PBT), the hydrofoil (A310) and the high efficiency turbine (HE3). The effect of tank geometry: number of baffles (N_f), impeller (D) to tank (T) diameter ratio (D/T), and off bottom clearance (C) to the impeller diameter ratio C/D for PBT, HE3, and A310, and off bottom clearance C for RT (due to the inherently different nature of this impeller), on flow stability was investigated for each impeller. Flow stability was characterized in terms of the intensity and magnitude of the RMS deviation of the smoothed velocity profile from the long time mean velocity. The dominant variable was shown to be the impeller diameter. The number of baffles is the second important variable for flow stability. The least stable flow patterns, in terms of intensity, are generated by the PBT impeller, followed by the A310, the HE3, and the RT. In terms of the magnitude of

the low frequency fluctuations, or the forces the flow exerts on the internals, the least stable is the RT, followed by the PBT, the A310, and the HE3.

To my family

Acknowledgments

I would like sincerely to thank Dr. Suzanne Kresta for her encouragement and guidance in the completion of this thesis.

I would like to thank to DACS center and machine shop personnel for their help during this work.

I have enjoyed the time I spent with my colleagues at Dr. Kresta's group.

The National Science and Engineering Council of Canada (NSERC) provided financial support for this project.

Table of Contents		page
Chapter 1 Introduction		1
1.1	Turbulent flow field in agitated tanks	2
1.2	Low frequency phenomenon	3
1.3	Definition of a stirred tank	4
1.4	Previous investigations	7
1.5	Approach used in this work	14
Table		16
Figures		19
References		21
Chapter 2 LDV Theory, Apparatus and Signal Processing		25
2.1	The principle of laser Doppler velocimetry (LDV)	25
2.2	The Aerometrics LDV - an overview	30
2.2.1	Optics	33
2.2.2	Sample size and signal validation	34
2.2.3	Signal processing using the DSA and RSA	36
2.2.3.1	Doppler signal analyzer (DSA)	36
2.2.3.2	Mixer frequency	39
2.2.3.3	Low pass filter	40
2.2.3.4	Sampling rate	41
2.2.4	RSA vs. DSA single burst processing	43
Table		45
Figures		46
References		52

Chapter 3 Frequency Analysis	54
3.1 Fourier domain spectral analysis	55
3.1.1 Turbulent power spectrum	56
3.1.2 Velocity autocorrelation	58
3.1.3 Transformation to frequency domain using FFT	59
3.1.4 Methods used for computing power spectrum from unevenly spaced data	62
3.2 Studies on simulated data	67
3.2.1 Different slot width	68
3.2.2 Noise addition	69
3.2.3 Notch filtering	69
3.3 Spectral estimates from the LDV data	71
3.3.1 PSD from three different techniques	72
3.3.2 Poisson sampling	73
3.3.3 Assumption - aliasing	74
3.3.4 Ambiguity noise and velocity biasing	75
3.3.5 Measurement noise	78
3.3.6 Spectral estimate from the RSA processor	80
3.4 Summary	80
Tables	82
Figures	83
References	102
Chapter 4 Macroinstabilities of flow in stirred tank	106
4.1 Introduction	106
4.2 Experimental	107
4.3 Resampling and smoothing of time series	110

4.3.1.	Velocity decomposition	112
4.4	Statistical significance of the effects: factorial design and 95% confidence interval (C.I.)	114
4.5	Results and discussion	116
4.5.1	PBT results	117
4.5.2	HE3 results	120
4.5.3	A310 results	122
4.5.4	RT results	123
4.5.5	Comparison of different type of impellers	125
Tables		128
Figures		142
References		153
Chapter 5	Conclusions and recommendations	157
Appendix A		159
Appendix B		178
Appendix C		274

List of Tables

page

Table

1.1	Experimental techniques, design and system geometries used by different investigators	16
2.1	LDV optical properties	45
3.1	Program and subroutine summary (binned-autocorrelation code)	82
3.2	Filter coefficients used for numerical filtering	82
4.1a	Experimental design and results (impeller stream) - PBT	128
4.1b	Experimental design and results (bottom corner) - PBT	129
4.1c	Experimental design and results (top corner) - PBT	130
4.2a	Experimental design and results (impeller stream) - HE3	131
4.2b	Experimental design and results (bottom corner) - HE3	132
4.2c	Experimental design and results (top corner) - HE3	133
4.3a	Experimental design and results (impeller stream) - A310	134
4.3b	Experimental design and results (bottom corner) - A310	135
4.3c	Experimental design and results (top corner) - A310	136
4.4a	Experimental design and results (impeller stream) - RT	137
4.4b	Experimental design and results (bottom corner) - RT	138
4.4c	Experimental design and results (top corner) - RT	139
4.5a	Comparison of different impellers (average from 8 geometries) impeller stream	140

4.5a	Comparison of different impellers (average from 8 geometries)	
	bottom corner	140
4.5a	Comparison of different impellers (average from 8 geometries)	
	top corner	141

List of Figures	page
Figure	
1.1 Turbulent mixing impellers: (a) general flow pattern for a radial flow impeller; (b) general flow pattern for an axial flow impeller (from Tatterson, 1991)	19
1.2 Geometry of the four impellers: PBT, HE3, A310 and RT	20
2.1 LDA measuring volume as envisioned by the fringe interpretation (from George, 1988)	46
2.2 Appearance and size of the measuring volume (Petersson, 1996)	46
2.3 Schematic of the Aerometrics LDV/PDPA optical configuration	47
2.4 LDV experimental arrangement	48
2.5 Sampling over one Doppler burst	49
2.6 Block diagram for the Doppler Signal Analyzer	50
2.7 Flowsheet for the DSA	50
2.8 Frequency spectrum from one single burst	51
3.1 Form of the one-dimensional energy spectrum in the various wavenumber ranges (from Harnby, Edwards and Nienow, 1985)	83
3.2 Typical autocorrelation coefficient at the impeller tip (from Kresta, 1991)	84
3.3 Test data: three sine waves (combination of the three sine waves at 0.01, 0.1 and 0.25 Hz)	85
3.4 Autocorrelation coefficient calculated from the binned technique	86
3.5 Spectral estimates for different slot size τ	87
a) $\tau=0.5s$	87
b) $\tau=0.125s$	87
c) $\tau=0.05s$	88
3.6 Spectral estimates with superimposed noise over initial data set	89
a) 1% noise	89
b) 5% noise	89

	c) 10% noise	90
3.7	PSD with notch filter applied at 0.05Hz (at width 1)	90
3.8	Time series data of the instantaneous axial velocity signal (pitched blade turbine-PBT, $sf=498$, $rpm=300$)	91
3.9	A typical frequency spectrum along the lower edge of the impeller (PBT)	91
3.10	Frequency spectrum, from axial velocity component; sampling frequency of 1612Hz, 300rpm, PBT	92
	a) autocorrelation technique	92
	b) discrete Fourier transform	93
	c) fast Fourier transform	94
3.11	Probability density function for the particle interarrival time, and the average sampling frequency of 779Hz	95
3.12	PSD for two different sampling frequencies	96
	a) low sf (0.2kHz, $f_{Nyq}=0.1kHz$)	96
	b) high sf (6.4kHz, $f_{Nyq}=3.2kHz$)	96
3.13	The RMS axial velocity profile across the lower edge of the PBT for various sampling frequencies	97
3.14	Effect of sampling frequency on measured RMS velocity	98
3.15	Effect of sampling frequency on measured mean velocity	98
3.16	Filtered PSD at the frequency band between 2 and 50Hz	99
3.17	Low-pass filter (cut-off at 100Hz)	99
3.18	RMS vs. cut-off frequency of low-pass filter (for LDV data)	100
3.19	Power spectrum, averaged over 10 blocks, autocorrelation technique; axial velocity component; sampling frequency 4305Hz, 300rpm, PBT	101
4.1	Geometry of the stirred tank used in this work	142
4.2	Time series of the axial velocity component (PBT impeller) after various stages of data processing	143

4.3	PBT, impeller stream, effects of geometric variables on v_{LF}/v_{tot}	144
4.4a	PBT general flow pattern, $D=T/2$, $C/D=0.5$, $N_f=4$ (baffle plane)	145
4.4b	PBT general flow pattern, $D=T/2$, $C/D=1$, $N_f=4$ (baffle plane)	146
4.5	HE3 general flow pattern, $D=T/2$, $C/D=1$, $N_f=4$ (baffle plane)	147
4.6	HE3, impeller stream, effects of geometric variables on v_{LF}/V_{tip}	148
4.7	A310 general flow pattern, $D=T/2$, $C/D=1$, $N_f=4$ (baffle plane)	149
4.8	A310, impeller stream, effects of geometric variables on v_{LF}/V_{tip}	150
4.9	RT general flow pattern, $D=T/2$, $C/D=1$, $N_f=4$ (baffle plane)	151
4.10	A310, impeller stream, effects of geometric variables on v_{LF}/V_{tip}	152

Appendix B

1	PBT time series: $D=2$, $C/D=1$, $N_f=4$, smoothed over 6(2+4) blade passages	178
	1a) impeller stream	178
	1b) bottom corner	179
	1c) top corner	180
2	PBT time series: $D=2$, $C/D=1$, $N_f=2$, smoothed over 6(2+4) blade passages	181
	2a) impeller stream	181
	2b) bottom corner	182
	2c) top corner	183
3	PBT time series: $D=2$, $C/D=0.5$, $N_f=4$, smoothed over 6(2+4) blade passages	184
	3a) impeller stream	184
	3b) bottom corner	185
	3c) top corner	186
4	PBT time series: $D=4$, $C/D=1$, $N_f=4$, smoothed over 8(4+4) blade passages	187
	3a) impeller stream	187

	4b) bottom corner	188
	4c) top corner	189
5	PBT time series: $D=T/4$, $C/D=0.5$, $N_f=2$, smoothed over 8(4+4) blade passages	190
	5a) impeller stream	190
	5b) bottom corner	191
	5c) top corner	192
6	PBT time series: $D=T/4$, $C/D=0.5$, $N_f=4$, smoothed over 8(4+4) blade passages	193
	6a) impeller stream	193
	6b) bottom corner	194
	6c) top corner	195
7	PBT time series: $D=T/2$, $C/D=0.5$, $N_f=2$, smoothed over 6(2+4) blade passages	196
	7a) impeller stream	196
	7b) bottom corner	197
	7c) top corner	198
8	PBT time series: $D=T/4$, $C/D=1$, $N_f=2$, smoothed over 8(4+4) blade passages	199
	8a) impeller stream	199
	8b) bottom corner	200
	8c) top corner	201
9	HE3 time series: $D=T/2$, $C/D=1$, $N_f=4$, smoothed over 10(4+6) blade passages	202
	9a) impeller stream	202
	9b) bottom corner	203
	9c) top corner	204
10	HE3 time series: $D=T/2$, $C/D=1$, $N_f=2$, smoothed over 10(4+6) blade passages	205

	10a) impeller stream	205
	10b) bottom corner	206
	10c) top corner	207
11	HE3 time series: $D=T/2$, $C/D=0.5$, $N_f=4$, smoothed over 12(4+8) blade passages	208
	11a) impeller stream	208
	11b) bottom corner	209
	11c) top corner	210
12	HE3 time series: $D=T/2$, $C/D=0.5$, $N_f=2$, smoothed over 10(4+6) blade passages	211
	12a) impeller stream	211
	12b) bottom corner	212
	12c) top corner	213
13	HE3 time series: $D=T/4$, $C/D=1$, $N_f=4$, smoothed over 10(4+6) blade passages	214
	13a) impeller stream	214
	13b) bottom corner	215
	13c) top corner	216
14	HE3 time series: $D=T/4$, $C/D=1$, $N_f=2$, smoothed over 10(4+6) blade passages	217
	14a) impeller stream	217
	14b) bottom corner	218
	14c) top corner	219
15	HE3 time series: $D=T/4$, $C/D=0.5$, $N_f=4$, smoothed over 10(4+6) blade passages	220
	15a) impeller stream	220
	15b) bottom corner	221
	15c) top corner	222
16	HE3 time series: $D=T/2$, $C/D=0.5$, $N_f=2$, smoothed over 10(4+6) blade	

	passages	223
	16a) impeller stream	223
	16b) bottom corner	224
	16c) top corner	225
17	A310 time series: $D=T/2$, $C/D=1$, $N_f=4$, smoothed over 4(2+2) blade	
	passages	226
	17a) impeller stream	226
	17b) bottom corner	227
	17c) top corner	228
18	A310 time series: $D=T/2$, $C/D=1$, $N_f=2$, smoothed over 4(2+2) blade	
	passages	229
	18a) impeller stream	229
	18b) bottom corner	230
	18c) top corner	231
19	A310 time series: $D=T/2$, $C/D=0.5$, $N_f=4$, smoothed over 4(2+2) blade	
	passages	232
	19a) impeller stream	232
	19b) bottom corner	233
	19c) top corner	234
20	A310 time series: $D=T/2$, $C/D=0.5$, $N_f=2$, smoothed over 4(2+2) blade	
	passages	235
	20a) impeller stream	235
	20b) bottom corner	236
	20c) top corner	237
21	A310 time series: $D=T/4$, $C/D=1$, $N_f=2$, smoothed over 4(2+2) blade	
	passages	238
	21a) impeller stream	238
	21b) bottom corner	239
	21c) top corner	240

22	A310 time series: $D=T/2$, $C/D=1$, $N_f=4$, smoothed over 10(4+6) blade passages	241
	22a) impeller stream	241
	22b) bottom corner	242
	22c) top corner	243
23	A310 time series: $D=T/4$, $C/D=0.5$, $N_f=4$, smoothed over 10(4+6) blade passages	244
	23a) impeller stream	244
	23b) bottom corner	245
	23c) top corner	246
24	HE3 time series: $D=T/4$, $C/D=0.5$, $N_f=2$, smoothed over 10(4+6) blade passages	247
	24a) impeller stream	247
	24b) bottom corner	248
	24c) top corner	249
25	RT time series: $D=T/2$, $C=T/2$, $N_f=4$, smoothed over 8(4+4) blade passages	250
	25a) impeller stream	250
	25b) bottom corner	251
	25c) top corner	252
26	RT time series: $D=T/2$, $C=T/2$, $N_f=2$, smoothed over 8(4+4) blade passages	253
	26a) impeller stream	253
	26b) bottom corner	254
	26c) top corner	255
27	RT time series: $D=T/2$, $C=T/3$, $N_f=4$, smoothed over 8(4+4) blade passages	256
	27a) impeller stream	256
	27b) bottom corner	257

	27c) top corner	258
28	RT time series: $D=T/2$, $C=T/3$, $N_f=2$, smoothed over 8(4+4) blade passages	259
	28a) impeller stream	259
	28b) bottom corner	260
	28c) top corner	261
29	RT time series: $D=T/3$, $C=T/2$, $N_f=4$, smoothed over 9(6+3) blade passages	262
	29a) impeller stream	262
	29b) bottom corner	263
	29c) top corner	264
30	RT time series: $D=T/3$, $C=T/2$, $N_f=2$, smoothed over 9(6+3) blade passages	265
	30a) impeller stream	265
	30b) bottom corner	266
	30c) top corner	267
31	A310 time series: $D=T/2$, $C=T/3$, $N_f=4$, smoothed over 9(6+3) blade passages	268
	31a) impeller stream	268
	31b) bottom corner	269
	31c) top corner	270
32	RT time series: $D=T/3$, $C=T/3$, $N_f=2$, smoothed over 9(6+3) blade passages	271
	32a) impeller stream	271
	32b) bottom corner	272
	32c) top corner	273

Appendix C

1	PBT, effects of geometric variables on v_{LF}/v_{tot}	274
	1a) bottom corner	274
	1b) top corner	275
2	PBT, effects of geometric variables on v_{LF}/V_{tip}	276
	2a) impeller stream	276
	2b) bottom corner	277
	2c) top corner	278
3	HE3, effects of geometric variables on v_{LF}/v_{tot}	279
	3a) impeller stream	279
	3b) bottom corner	280
	3c) top corner	281
4	HE3, effects of geometric variables on v_{LF}/V_{tip}	282
	4a) bottom corner	282
	4b) top corner	283
5	A310, effects of geometric variables on v_{LF}/v_{tot}	284
	5a) impeller stream	284
	5b) bottom corner	285
	5c) top corner	286
6	A310, effects of geometric variables on v_{LF}/V_{tip}	287
	6a) bottom corner	287
	6b) top corner	288
7	RT, effects of geometric variables on v_{LF}/v_{tot}	289
	7a) impeller stream	289
	7b) bottom corner	290
	7c) top corner	291
8	RT, effects of geometric variables on v_{LF}/V_{tip}	292
	8a) bottom corner	292
	8b) top corner	293

Nomenclature

A_1	constant	(-)
c, d	filter constants	(-)
C	off bottom clearance	(m)
d_b	diameter of laser beam	(mm)
d_w	diameter of measuring volume	(mm)
D	impeller diameter	(m)
E_1	one-dimensional power spectrum	(m ² /s)
f	frequency, used in general expressions	(Hz)
f	transmitter focal length in Chapter 2	(mm)
f_d	Doppler frequency	(MHz)
f_{mix}	mixer frequency	(MHz)
f_n	discrete frequency	(Hz)
$f_{sampling}$	signal sampling frequency, in Chapter 2	(MHz)
h_k	discrete time series data	(m/s)
$h(t)$	continuous time series of data	(m/s)
H	liquid height	(m)
H_k	discrete Fourier transform	(m/s)
H^*	complex conjugate of H_k	(m/s)
$H(f)$	continuous Fourier transform	(m/s)
k_l	one-dimensional wave number	(m)
l_w	length of measuring volume	(mm)
L	characteristic length	(m)
n	number of points in velocity record, in Chapter 4	(-)
n_{data}	number of recorded data points in time series	(-)
nn	working array size (in FFT analysis)	(-)
N	FFT working array size, in Chapter 3	(-)
N	rotational speed of the impeller	(min ⁻¹)

N_B	number of points in single block in FFT analysis	(-)
N_f	number of baffles	(-)
p	probability density function	(-)
$P_n(f)$	power spectral density, as defined by Press et al.(1989)	(m ² /s)
r	radial coordinate	(m)
Re	Reynolds number	(-)
R_E	autocorrelation coefficient function	(-)
R_{Ep}	autocorrelation coefficient function, periodic component	(-)
R_{Er}	autocorrelation coefficient function, random component	(-)
RMS	root-mean-square of fluctuating velocity	(m/s)
s	beam separation	(mm)
sf	sampling frequency	(Hz)
t	time	(s)
t_i	discrete time	(s)
t_{min}	transit time limitation	(s)
t_r	random number between 0 and 1	(-)
T	tank diameter	(m)
T	total measured time, in Chapter 3	(s)
T_B	length of single block in FFT analysis	(s)
u	fluctuating velocity, used in Chapter 3	(m/s)
U	instantaneous velocity, in Chapter 3 , used in general expression	(m/s)
\bar{U}_i	mean velocity, in Chapter 3	(m/s)
v	RMS of fluctuating velocity	(m/s)
v_{LF}	RMS of smoothed velocity profile	(m/s)
v_{raw}	RMS of initial fluctuating velocity	(m/s)
v_{tot}	RMS of resampled fluctuating velocity	(m/s)
v'	fluctuating velocity, used in Chapter 4	(m/s)
v'_{BP}	initial (resampled) fluctuating velocity due to the blade passage	(m/s)
v'_{LF}	initial (resampled) fluctuating velocity due to the low frequencies	(m/s)

v'_{rand}	initial (resampled) fluctuating velocity due to turbulence	(m/s)
v'_{raw}	initial (measured) fluctuating velocity	(m/s)
v'_{tot}	initial (resampled) fluctuating velocity	(m/s)
V	instantaneous velocity	(m/s)
\bar{V}_{raw}	mean initial velocity	(m/s)
V_{max}	maximum velocity	(m/s)
\bar{V}_{tot}	mean resampled velocity	(m/s)
V_{tip}	impeller tip velocity	(m/s)
W	width of the impeller blades	(m)
W_b	width of baffles	(m)
$x(t)$	generated time domain signal	(m/s)
z	axial coordinate	(m)

Greek

δ_f	fringe spacing	(μm)
Δ	time interval between samples	(s)
ε	width of frequency notch, in Chapter 3	(-)
ε	turbulence energy dissipation rate	(m^2/s^3)
η	Kolmogoroff length	(m)
λ	wavelength of laser light, in Chapter 2	(nm)
λ	wavelength of velocity fluctuations, in Chapter 3	(m)
θ	beam intersection angle	($^\circ$)
τ	gate time, in Chapter 2	(s)
τ	time lag	(s)
ν	kinematic viscosity	(m^2/s^2)

ω	angular frequency	(Hz)
$\mathcal{H}(f)$	filter function	(-)

Abbreviations

A310	three bladed aerofoil impeller by Lightnin'
ADC	analog to digital converter
DFT	Discrete Fourier transform
DSA	Doppler signal analyzer
FFT	Fast Fourier transform
HE3	three bladed high efficiency turbine by Chemineer
LPF	low pass filter
MV	measuring volume
PBT	4 bladed, 45° pitched blade turbine
RSA	real time signal analyzer
RT	6 bladed Rushton turbine
SNR	signal to noise ratio

Chapter 1. Introduction

Mechanically agitated vessels are in widespread use in industry for a variety of mixing processes. Their diverse range of applications includes storage tanks, blending operations, crystallization, fermentation, and chemical reaction. The main function of agitation is to accelerate the rate of transport occurring in the vessel. This is achieved by introducing mechanical energy into the vessel using a rotating impeller, and converting this energy into kinetic energy.

The physical and chemical processes taking place in the stirred tank are complex and closely coupled to the underlying transport processes, in particular - the flow field. Therefore, a detailed understanding of the hydrodynamics of this vessel (velocity field, turbulence, stress field etc.) is useful for optimum design. The vessel geometry is also key to understanding mixing. In fact, the geometry is so important that processes can be considered "geometry specific". Solid suspension is very much dependent upon the shape of the tank bottom; gas-liquid and liquid-liquid dispersion depend upon the impeller geometry; blending upon the relative size of the tank to the impeller diameter; and power draw upon the impeller geometry.

There are three different perspectives used for analyzing the flow field in a fully turbulent stirred tank: overall studies, statistical turbulence studies, and

structural turbulence studies. Overall studies are concerned with the flow pattern in the stirred vessel and the agitator pumping capacity. In order to be scalable, studies in the turbulent regime must be performed at $Re > 2 \times 10^4$ ($Re = ND^2/\nu$). The statistical turbulence studies involve measurement of average velocity profiles, fluctuating velocities, turbulence intensities and pumping capacities. This analysis is based on pointwise measurements using pitot tubes, hot wire anemometry or laser Doppler velocimetry (LDV). The structural study of turbulence involves the identification of different flow structures and their interactions. The mean flow at various scales and the time dependent flow patterns are of interest in this approach. Two approaches: statistical and structural turbulence, are used in this study.

1.1 Turbulent flow field in agitated tanks

Traditionally, the circulation pattern in stirred tank was considered steady and two-dimensional as shown in Figure 1.1. In fact, the flow is much more complex: three-dimensional and highly turbulent. The mechanical energy of the rotating impeller is transmitted both directly to the recirculation of the fluid and to the large trailing vortices at the tip of the blades. Impeller passages impose periodicity in the flow and are considered as pseudo-turbulent, since they are nonrandom. As each blade passes, a stationary observer can observe a strong oscillation in the mean velocity due to trailing vortices at the tip of the impeller blade. These vortices maintain their identity in a region around impeller. Further

away they decay into random turbulence, as they meet either the relatively stationary flow in the bulk of the tank or the baffles and the vessel wall. However, some vortex remnants do reach the tank wall and are carried by the recirculation flow upward along the wall to the center of the tank. As a result, the flow pattern in a stirred tank is not uniform in all zones of the vessel and can be classified into: the impeller discharge stream or well mixed region, the bulk of the tank where the circulation is weaker and the top third of the tank which can be considered poorly mixed.

It is important, at this point, to distinguish micromixing from macromixing. Ultimately, mixing is achieved by molecular diffusion. However, convective transport and bulk motion or macromixing greatly influences the speed at which micromixing is achieved. Macromixing is the time controlling factor in achieving a uniform mixture. Macromixing creates high concentration gradients between the materials being mixed. In this study, the time varying characteristics of macromixing will be discussed.

1.2 Low frequency phenomenon

The existence of low frequencies in the stirred tank has regularly been reported in the literature in the past several years (Winardi 1988, 1991, Bruha et al. 1993-1996, Kresta and Wood 1993a, 1993b, Chapple and Kresta, 1994, Myers et al., 1995, 1997, Montes et al., 1997) . The macroinstabilities (or low frequencies) in

the stirred vessel are due to the time varying flow field. This phenomenon indicates the existence of eddy fields whose time and length scale considerably exceeds those associated with blade passages and small scale turbulence. Despite numerous recent observations and studies, their origin is still not well defined.

The low frequencies can be considered the basic characteristic of large-scale motions in agitated liquid. These motions can have considerable dynamic effects on the solid surfaces inside the vessel. The dynamic effects arise when large eddies, sometimes as large as the vessel diameter, interact with components of the system (baffles, shaft, impeller or vessel wall). In severe cases, this has caused mechanical damage to the vessel and internals. On the other hand, these macroinstabilities promote macromixing, since they allow a larger part of the vessel to be active.

1.3 Definition of a stirred tank

Mixing tanks and impellers come in variety of shapes and sizes. The standard tank geometry for single phase flow in the turbulent flow regime is shown in Figure 1.1 for two different impellers. The main geometric variables are: the tank diameter T , the impeller diameter D , the blade width W , the off-bottom clearance C of the impeller, the liquid height H , and the baffle width B . Although the standard geometric configuration is number of baffles $N_f=4$, impeller diameter D ($D=1/4$ to $1/2T$), liquid height H ($H/T=1$), and impeller off bottom clearance C ($C=1/6$ to

1/2T), the optimum tank and impeller geometry is a function of the application.

Various impellers produce different flow patterns, but no single impeller is sufficiently versatile and energy efficient to perform all the functions of mechanical agitation. For each application, the impeller should generate a flow pattern which enhances the rate of that application. To agitate solid suspension, an impeller with a strong axial velocity component is needed in order to sweep solid off the bottom of the tank, while for the gas-liquid systems, an impeller with a dominant radial velocity component disperses gas into liquid better and resists flooding.

In the turbulent flow regime, impellers are classified into two general types on the basis of the flow pattern generated: axial flow impellers and radial-flow impellers. Radial flow impellers (Figure 1.1a) discharge fluid towards the vessel wall in the horizontal (radial) direction. Axial flow impellers (Figure 1.1b) produce flow parallel to the vessel shaft, along the impeller axis. Axial flow impellers can be further classified according to the design of their blades: the pitched blade turbine with flat blades, and modern hydrofoils with profiled and angled blades (McFarlane and Nienow, 1995). Pitched blade impellers do not produce truly axial flow. Instead, the fluid discharge angle is around 45° with a relatively strong radial component (Ibrahim and Nienow, 1995, Ranade and Joshi, 1989). Hydrofoil impellers produce strong axial flow. They are designed for efficient pumping and can generate pressure distribution on the suction and pressure surfaces of the blades to produce a positive

lift. The same principle is employed in aircraft wings. The profiled blades reduce the drag forces associated with the motion of the blades and thus the energy requirements for the mixing process.

Four standard impellers were used for this study: a radial flow 6-blade Rushton disc turbine (RT), an axial flow pitched blade turbine (PBT), an axial flow hydrofoil Lightnin' A310, and an axial flow hydrofoil Chemineer HE3 impeller. A schematic drawing of these impellers is given in Figure 1.2. The radial Rushton turbine has a disc diameter of $2/3D$, a blade length of $D/4$, and a blade width W ($W=D/5$). The 4-blade pitched blade turbine has 45° blade angle, with the blade width $W=D/5$. The A310 and HE3 are three blade impellers with the blades mounted at shallow angle to reduce drag of the leading edges. Progressing from the hub to the tip, the blade angle of the A310 becomes smaller (reaching 21° at the tip) and the blade narrower. Therefore the A310 has nearly constant pitch across the blade. The HE3 has a uniform blade width and straight edges. The blade angle is 30° at the hub, but it is bent a further 20° toward the horizontal plane along the line connecting the middle points of the length and the width (Ibrahim and Nienow, 1995).

The axial-flow impellers in particular do not create a truly steady flow pattern, but are subject to long time scale instabilities, which is the subject of several previous and present investigations.

1.4 Previous investigations

In this section, previous investigations on the phenomenon of macroinstabilities will be reviewed in terms of the different techniques used and the different final results. For reference, the studies are summarized in Table 1.1. It is important to summarize the different impeller and tank geometries used in previous investigations, since the system geometry affects the macroinstabilities.

Research into the long time scale flow instabilities in the stirred tanks has only begun over the past decade. The dynamic effects of low frequency phenomena have been observed as sudden changes in shaft torque or mechanical damage to vessel internals (e.g. broken baffles). Most of the investigations have been done on the PBT impeller due to its widespread use and highly unstable flow pattern, although recently, investigations on the flow stability of other types of axial impellers (A310, A315, MIXEL TT, HE3) have been undertaken.

Various measurement techniques have been used to analyze the low frequency phenomenon: flow visualization, particle image velocimetry (PIV), laser Doppler velocimetry (LDV), spectral analysis and mechanical devices such as the "tornadometer" (Bruha et al. 1994, 1995, 1996). Some authors have attempted to investigate the problem using CFD (Bakker and Van den Akker, 1994b, Myers et

al., 1995). Flow visualization methods can give an overall picture of the complex time varying aspects of the flow, which is difficult to reproduce from a pointwise experiment such as LDV. Advances in flow visualization techniques rely on the development of more powerful cameras with higher speeds to capture nearly instantaneous flow field. Most of the investigations on macroinstabilities in the stirred tank include this technique as will be shown in this section.

Winardi et al. (1988) were among the first to observe that the visualized flow field, for a paddle impeller, is different from the mean velocity field measured using LDV. Quite different flow patterns and various combinations of patterns appear over time, causing large-scale flow fluctuations. These macroinstabilities are manifested in abrupt changes in the torque on the shaft. In a second paper, Winardi et al. (1991), used several flow visualization techniques (human eye, high speed VTR, and video recording), and LDV to examine the time varying flow pattern of a marine propeller. They found that the semi-instantaneous flow pattern was asymmetric with respect to the impeller shaft. The circulation flow pattern is classified as quick return, full circulation, and intermediate circulation. They measured the lifetime distribution of these patterns using 2D flow visualization and found that flow pattern changes were random in their order and that the lifetime of a given flow could range from half a second to several minutes.

Kresta and Wood (1993a, 1993b) observed variations in the bulk circulation

pattern when they analyzed the flow field of a PBT impeller using flow visualization, LDV, and spectral analysis. They were the first to report a change in the mean circulation pattern with off bottom clearance and impeller to tank diameter (D/T) ratio. This phenomenon is more prevalent for certain geometries (bigger D/T ratio and higher off bottom impeller clearance C). A later paper by Chapple and Kresta (1994) considers the influence of geometric parameters such as off bottom clearance, impeller diameter and number of baffles on flow stability for two axial impellers: the Lightnin' A310 impeller and the pitched blade turbine (PBT). Chapple and Kresta (1994) also found that the flow and stability pattern is different for different geometries. Significant geometric variables governing the flow stability were found to be: the type of impeller, the impeller diameter, the number of baffles and the off bottom clearance.

Bakker and Van den Akker (1994b) analyzed the flow pattern for the Rushton turbine (RT) and two axial impellers: Lightnin A315 and PBT. They used LDV data and simulation (CFD). They found that PBT flow pattern in the upper part of the tank has bimodal and trimodal velocity distributions. This suggests that the flow is bistable (or tristable) and oscillates periodically between a number of quasi-stable flows. Steady state CFD simulations cannot predict this phenomenon.

Bruha et al. (1993), in their early work on this phenomenon, investigated the impact of the impeller rotational speed for the PBT impeller, and for different

geometries under which macroinstabilities occur. They observed a vortex which appears on the fluid surface with a larger time and length scale than those of the turbulent eddies. To capture the shape and dimensions of the large vortex they used a video camera. A round probe above the fluid surface was used to measure the frequency of this "surface swelling". They concluded that this frequency is linearly dependent on the impeller rotational speed. Different impellers and tank geometries were used. However, the effect of geometry wasn't considered systematically.

Further work by Bruha et al. (1994, 1995, and 1996) studies flow macroinstabilities for the PBT impeller. In this work, flow visualization and a special mechanical device called a tornadometer are used. The tornadometer is placed below the surface in the vicinity of the agitator and deflects whenever macroinstabilities occur, changing the direction of the mean flow. Bruha et al. confirmed their earlier report that frequency of this phenomenon is linearly related to the impeller rotational speed. They also observed that changes in the angle of the impeller discharge flow and the appearance of an unstable secondary circulation loop accompany the low frequency macroinstabilities.

Myers et al. (1995) analyzed the PBT velocity flow field using digital particle image velocimetry (DPIV). They compared the DPIV velocity flow field with that obtained by the LDV method. The time averaged velocity fields show good agreement between both techniques. However, the DPIV semi-instantaneous

velocity flow field is different from the time averaged flow pattern (LDV) and it clearly indicates long time scale fluctuations in the flow. Then, they used DPIV images to analyze the vorticity field and calculated power spectral density (PSD) from spatially averaged vorticities. Low frequency oscillations were present on the frequency spectrum as a dominant spike. In later work, Myers et al. (1997) compared two axial impellers (PBT and HE3) by employing the same techniques - DPIV, LDV and spectral analysis. They confirmed their previous findings that the LDV flow field is different from the instantaneous flow field, and that the low frequency peak on frequency spectrum is more dominant for larger off bottom clearance, for the PBT (see Table 1.1). The HE3 and the PBT (with lower C) show similar level of instabilities.

Bakker et al. (1996) extended this analysis to evaluate the performance of different computational mixing models (CFM) for the PBT impeller in both turbulent and laminar flow regimes. For the laminar flow regime, the computational tool gave an accurate results. For the turbulent flow regime significant discrepancies between the experimental results and simulations were observed. These were attributed to the time varying flow field, which is not included in a steady state computational model.

Montes et al. (1997) used LDV measurements, flow visualization, spectral analysis, and wavelet transforms to analyze flow macroinstabilities in a stirred tank equipped with a PBT impeller. They found that the occurrence of macroinstabilities

is accompanied by the presence of a big vortex in the upper part of the vessel, and it is linearly coupled with the frequency of the impeller revolution. The RMS velocity vs. Reynolds number plot shows a sudden rise in fluctuating intensity at a Reynolds number around 600. They concluded that this change corresponds to the first appearance of the low frequency occurrence at that Re. The frequency spectrum also shows a distinct peak for low frequency oscillations (for $Re > 600$). This implies that both the transitional and fully turbulent flow regimes are subject to this type of instability. This result is reported by several other authors (Bruha et al., 1996, Myers et al. 1997).

Mavros et al. (1996) investigated the velocity field for three impellers (the axial MIXEL TT, and Lightnin A310, and the radial RT impeller), using LDV and flow visualization. The flow visualization reveals that the flow pattern in a stirred vessel is not stable and that it changes with time from an organized to a completely random state. They hypothesized that this arises due to low frequencies, which originate at the wall of the vessel and propagate into the bulk of the tank.

Jaworski et al. (1996) also found long-term fluctuations for the HE3 axial impeller near the vessel wall, by examining the mean and the RMS velocity profile in the bulk of the vessel. A repeatability test for the mean velocity profile was performed and it was poorer than that of the RMS. These variations between two consecutive measurements are caused by the long-term fluctuations of the mean

flow or low frequencies and will appear only if the velocity is not measured for a time significantly longer than the period of the low frequency fluctuations.

There are a few process-oriented papers published in recent years which describe the impact of the unstable nature of flow patterns produced by axial-flow impellers. McFarlane and Nienow (1995), in their review paper on gas-liquid mixing, pointed out mechanical instabilities (vessel vibrations and large fluctuations in shaft torque and power draw) which occur in stirred vessel when axial impellers are used for gas dispersion. Haam et al. (1992) found that the heat transfer coefficient at the vessel wall varies with time. They attributed these oscillations to the slow (relative to the impeller speed) precession of an axial vortex structure between the fluid surface and the impeller. Bakker and Van den Akker (1994a) observed an unstable and slow precessing asymmetrical flow pattern in the gas holdup for systems agitated with axial flow impellers (PBT, Lightnin A315, and Leuwrik). This phenomenon was observed for higher gassing flow rates or lower rotational speeds. These authors hypothesized that vertical vortices behind the baffles, formed due to the tangential flow, interact with horizontal vortices, formed due to the axial flow, leading to instabilities and asymmetrical flow conditions.

1.5 Approach used in this work

The main objective of this work is to investigate systematically the time varying nature of the flow in stirred tanks, particularly low frequency variations, using different tank and impeller geometries. Four impellers are studied in some detail. The first two - the Rushton turbine (RT) and the pitched blade turbine (PBT), are in widespread use, and their flow field (particularly the mean flow) is well established. The other two impeller designs are the high efficiency turbine by Chemineer (HE3) and the aerofoil impeller by Lightnin' (A310). Studies of their flow fields in the open literature are still scarce. Eight tank geometries were used for each type of the impeller, in a factorial experimental design.

A Laser Doppler velocimeter (LDV) was used to measure the axial velocity component for the PBT, HE3 and A310 and radial velocity component for the RT. The experimental setup, and signal processing issues are discussed in Chapter 2.

The first approach to analyzing the low frequency instabilities, discussed in Chapter 3, is based on frequency analysis. The LDV time series has been analyzed using the autocorrelation function and spectral analysis. Since traditional FFT analysis cannot be employed for the unevenly sampled data collected by our instrument, a binned autocorrelation was applied. Two other techniques: the discrete

Fourier transform (DFT) and the fast Fourier transform (FFT) were tested.

The second approach, used in Chapter 4, is decomposition of the velocity signal. This was done by resampling (windowing) and smoothing the LDV time series. The smoothed velocity profile represents the contribution of low frequency fluctuations to the overall signal. Using this, the impact the low frequency on the measured turbulent RMS velocity can be assessed. This, together with the factorial design and 95 % confidence interval, gives a comprehensive picture of the impact of tank and impeller geometry on the flow stability and the dominance of low frequencies in a stirred tank.

Table 1.1: Experimental technique, design and system geometries used by different investigators

Investigators	Impeller Geometry	Operating parameters	Measurement technique
Bakker and Van den Akker (1994a)	PBT, Leeuwrik impeller Lightnin' A315	$T=0.444\text{ m}$, $N_f=4$, $D=0.4\text{ T}$, $C/D=0.75$; 1	Flow visualization, photograph
Bakker and Van Den Akker (1994b)	PBT, Lightnin' A315	$T=0.444\text{ m}$, $N_f=4$, $D=0.4\text{ T}$ $C=0.3\text{ T}$, $C/D=0.75$	LDV
Bakker et al. (1996)	PBT	$T=0.145\text{ m}$, $N_f=4$, $D=0.35\text{ T}$, $C=0.46\text{ T}$	LDV, DPIV
Bruha et al. (1993)	PBT	$T=0.294\text{ m}$, $H/T=1$, $N_f=3,4,6$ $C=0.33\text{ T}$; 0.4 T ; 0.5 T , $D=0.1$; 0.075 m	Flow visualization, "round probe" on the fluid surface
Bruha et al. (1994, 1995, 1996)	PBT	$T=0.3\text{ m}$, $N_f=4$, $D=0.1\text{ m}$, $C=0.1$; 0.35 T ; 0.5 T	Mechanical device –tornadometer, flow visualization

Table 1.1: cont.

Investigators	Impeller Geometry	Operating parameters	Measurement technique
Chapple and Kresta (1994)	PBT, Lightnin A310	T=0.24m, $N_r=4$; 2, D=T/2; T/3, C/D=0.6; 1.0	Tuft visualization
Haam and Brodkey (1992)	HE3, PBT	T=0.387 m, $N_r=4$, D=0.5T; 0.33T, C=0.33T; 0.25T	Heat transfer coefficient measurement
Kresta and Wood (1993a and 1993b)	PBT	T=0.152 m, $N_r=4$, D=T/2; T/3, C=T/2; T/3; T/4	LDV, flow visualization, spectral analysis
Mavros et al. (1996)	RT, MIXEL TT, A310	$N_r=4$, D/T=0.5, C/T=0.33	flow visualization
Montes et al. (1997)	PBT	T=0.3 m, $N_r=4$, D=0.33T, C=0.35T	LDV, flow visualization, spectral analysis, wavelet transform

Table 1.1 cont.

Investigators	Impeller Geometry	Operating parameters	Measurement technique
Myers and Ward (1994)	PBT	T=0.292 m, $N_f=4$, D=0.35T, C=0.46T, C/D=1.41	DPIV (digital particle image velocimetry)
Myers et al. (1997)	PBT, HE3	T=0.292, $N_f=4$, D=0.35T(PBT); 0.39T(HE3), C=0.46T(PBT); 0.33T(HE3)	DPIV, spectral analysis
Winardi et al. (1988)	Paddle impeller	T=0.46 m, C=0.2 m, D=0.16 m, $N_f=4$	Flow visualization (VTR)
Winardi and Nagase (1991)	Marine propeller	T=0.46 m, C=0.135 m, D=0.16 m, $N_f=4$	Flow visualization, LDV

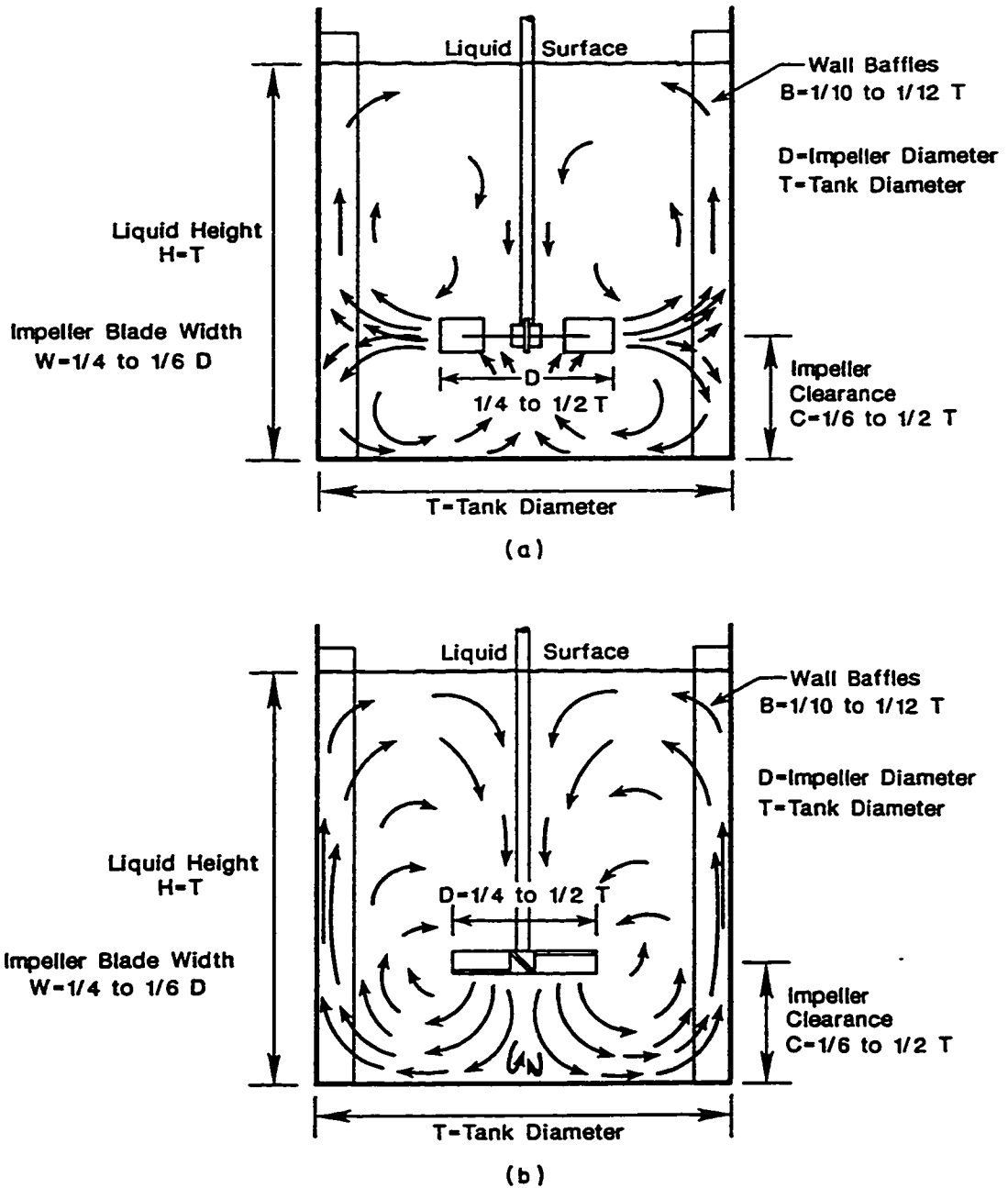
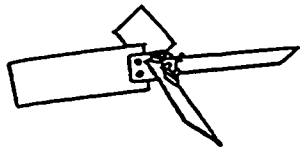
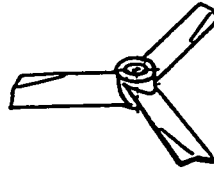


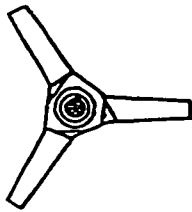
Figure 1.1: Turbulent mixing impellers: (a) general flow pattern for a radial flow impeller; (b) general flow pattern for an axial flow impeller; (from Tatterson, 1991).



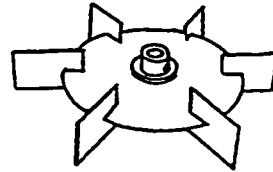
PBT



HE3



A310



RT

Figure 1.2: Geometry of the four impellers: PBT, HE3, A310 and RT.

References

Bakker, A., and H.E.A. Van den Akker, 1994a, Gas-Liquid Contacting with Axial Flow Impellers, 1994a, *Trans I. Chem. E.*, 72, Part A, 573-582.

Bakker, A., and H.E.A. Van den Akker, 1994b, Single-Phase Flow in Stirred Reactors, *Trans. I.Chem. Eng.* 72, 583-593.

Bakker, A., K. J. Myers, R.W. Ward, and C.K. Lee, 1996, The Laminar and Turbulent Flow Pattern of a Pitched Blade Turbine, *Trans. I. Chem. E.* 74, Part A, 485-491.

Bruha, O., I. Fort, and P. Smolka, 1993, Large Scale Unsteady Phenomenon in a Mixing Vessel, *Acta Polytechnica*, Czech Tech. Univ. Prague 27, 33.

Bruha, O., I. Fort, and P. Smolka, 1994, Flow Transition Phenomenon in an Axially Agitated System, *Proceedings of the Eighth European Conference on Mixing (ICHEME Symposium series No. 136)*, 121-128, Cambridge, United Kingdom.

Bruha, O., I. Fort, and P. Smolka, 1995, Phenomenon of turbulent macroinstabilities in agitated systems, *Collect. Czech. Chem. Commun.* 60, 85-94.

Bruha, O., I. Fort, P. Smolka, and M. Jahoda, 1996, Experimental Study of Turbulent Macroinstabilities in an Agitated System with Axial High-Speed Impeller and with Radial Baffles, *Collect. Czech. Chem. Commun.* 61, 856-867.

Chapple, D., and S.M. Kresta, 1994, The Effect of Geometry on the Stability

of Flow Patterns in Stirred Tank, *Chem. Eng. Sci.* **49**(21), 3651-3660.

Haam, S., R.S. Brodkey, and J. Fasano, 1992, Local Heat Transfer in a Mixing Vessel Using Heat Flux Sensors, *Industrial and Engineering Chemistry Research*, **31**, 1384-1391.

Hockey, R.M., and J.M. Nouri, 1996, Turbulent Flow in a Baffled Vessel Stirred by a 60° Pitched Blade Impeller, *Chem. Eng. Sci.* **51**, No. 19, 4405-4421.

Ibrahim, S.B., and A.W. Nienow, 1995, Power Curves and Flow Patterns for a Range of Impellers in Newtonian Fluids: $40 < Re < 5 \times 10^5$, *Trans. Inst. Chem. Eng.* **73**, Part A, 485-491.

Jaworski, Z., A.W. Nienow, E. Koustasakos, K. Dyster, and W. Bujalski, 1991, An LDA Study of Turbulent Flow in a Baffled Vessel Agitated by a Pitched Blade Turbine, *Trans. I.Chem.E.* **69**, Part A, 313-320.

Jaworski, Z., A.W. Nienow, and K.N. Dyster, 1996, An LDA Study of the Turbulent Flow Field in a Baffled Vessel Agitated by an Axial, Down-Pumping Hydrofoil Impeller, *Can. J. Chem. Eng.* **74**, 3-15.

Kresta, S.M., 1991, *Characterization, Measurement, and Prediction of the Turbulent Flow in Stirred Tanks*, Ph.D. thesis, McMaster University, Hamilton, Ontario.

Kresta, S.M. and P.E. Wood, 1993a, The Flow Field Produced by a Pitched Blade Turbine: Characterization of the Turbulence and Estimation of the Dissipation Rate, *Chem. Eng. Sci.* **48**, 1761-1774.

Kresta, S.M. and P.E. Wood, 1993b, The Mean Flow Field Produced by a

45° Pitched Blade Turbine: Changes in the Circulation Pattern due to Off-bottom Clearance, *Can. J. Chem. Eng.* **71**, 42-53.

Kresta, S.M., *Mixing notes*, 1998.

Mavros, P., C. Xuereb, and J. Bertrand, 1996, Determination of 3D-Flow Fields in Agitated Vessels by Laser Doppler Velocimetry: Effect of the Impeller Type and Liquid Viscosity on Liquid Flow Patterns, *Trans. I. Chem. E.* **74**, Part A, 658-668.

McFarlane, K., and A.W. Nienow, 1995, Studies of High Solidity Ratio Hydrofoil Impellers for Aerated Bioreactors, *Biotechnol. Prog.* **11**, 601-607.

Mishra, V.V., and J.B. Joshi, 1993, Flow Generated by a Disc Turbine: Part II: Effect of Impeller Diameter, Impeller Location and Comparison with Other Radial Flow Turbines, *Chem. Eng. Res. Des.* **71**, Part A, 563-573.

Montes, J.L., H.C. Boisson, I. Fort, and M. Jahoda, 1997, Velocity field macro-instabilities in an axial agitated mixing vessel, *Chem. Eng. J.* **67**, 139-145.

Myers, K.J., R.W. Ward, A. Bakker, and L.B. Fasano, 1995, A DPIV investigation of flow pattern instabilities of axial-flow impellers, *15th Biennial North American Mixing Conference, Experimental Method Session*, June 18-23, Banff, Alberta, Canada.

Myers, K.J., R.W. Ward, and A. Bakker, 1997, A digital particle image velocimetry investigation of flow field instabilities of axial flow impellers, *J. Fluids Eng.*, **119**, 623-632.

Ranade, V.V., and J.B. Joshi, 1989, Flow Generated by Pitched Blade

Turbines I: Measurement Using Laser Doppler Anemometer, *Chem. Eng. Comm.* **81**, 197-224.

Schafer, M., M. Hofken, and F. Durst, 1997, Detailed LDV Measurement for Visualization of the Flow Field within a Stirred Tank Reactor Equipped with a Rushton Turbine, *Trans. I. Chem. Eng.* **75**, Part A, 729-736.

Tatterson, G.B., and H.H.S. Yuan, 1980, Stereoscopic Visualization of the Flows for Pitched Blade Turbines, *Chem. Eng. Sci.* **35**, 1369-1375.

Tatterson, G.B., 1991, Fluid Mixing and Gas Dispersion in Agitated Tanks, McGraw-Hill, Inc.

Winardi, S., S. Nakao, and Y. Nagase, 1988, Pattern Recognition in Flow Visualization around a Paddle Impeller, *J. Chem. Eng. Japan* **21**, 503-508.

Winardi, S., and Y. Nagase, 1991, Unstable Phenomenon of Flow in Mixing Vessel with a Marine Propeller, *J. Chem. Eng. Japan*, **24** (2), 243-249.

Yianneskis, M., Z. Popiolek, and J.H. Whitelaw, 1987, An Experimental Study of the Steady and Unsteady Flow Characteristics of Stirred Reactors, *J. Fluid Mech.* **175**, 537-555.

Zhou, G. and S.M. Kresta, 1996, Impact of the Tank Geometry on the Maximum Turbulence Energy Dissipation Rate for Impellers, *A.I.Ch.E. Journal* **42**, 2476-2490.

Zhou, G., 1996, *Characteristics of Turbulence Energy Dissipation and Liquid-Liquid Dispersions in an Agitated Tanks*, Ph.D. thesis, University of Alberta, Edmonton, Alberta.

Chapter 2. LDV Theory, Apparatus, and Signal Processing

In this chapter, the theoretical basis of laser Doppler velocimetry (LDV), the specific application of this theory in our equipment, and Fourier domain burst detection signal processing are described. The initial experimental validation was carried out by Zhou (1996). In this work, two similar signal processors were used: a Doppler Signal Analyzer (DSA) and a Real Time Signal Analyzer (RSA). The signal processing parameters were validated and optimized for both processors. These parameters are critical for accurate measurement of a wide range of turbulent frequencies in the velocity record.

2.1 The principle of Laser Doppler Velocimetry (LDV)

Laser Doppler anemometry (LDA) or laser Doppler velocimetry (LDV) is a non-intrusive optical measurement technique which allows local, time-resolved, measurement of velocity. It was discovered by Yeh and Cummins in 1964, who observed the shift of light scattered from particles carried in a water flow. It gives a virtually instantaneous response to flow fluctuations, and there is a linear relationship between the measurement and the fluid velocity. LDV is now used in a wide variety of environments including supersonic and hypersonic flows, but its application to the study of turbulence and non-stationary flow is the most important

for our research.

When a beam of light with a coherent frequency reaches a moving object, the light will change its frequency. In any form of wave propagation, frequency changes occur due to movement of the source, receiver, propagation medium or an intervening reflector or scatter. This phenomenon is called the “Doppler shift” after the Austrian physicist who first considered the phenomenon in 1842. Since the velocities commonly encountered are very small compared with the velocity of light, the corresponding Doppler shifts are too low for direct measurement and are beyond the resolution of optical spectrometers. Most laser Doppler measurements therefore make use of optical interference in one form or another.

The differential Doppler technique is the most commonly used technique for measuring the Doppler shift. Two beams of linearly polarized laser light and equal intensity are crossed at the beam waist, which is located at the point under investigation, as shown in Figure 2.1. The intersection gives rise to an interference pattern as the two beams cancel each other in some regions (represented by dark lines) and reinforce each other in other regions (represented by bright lines) due to the coherent properties of the laser light. A pattern of alternatively dark and bright planes - or virtual fringes-with a known spacing, can be seen if the point of intersection is enlarged. The orientation of these fringes is exactly parallel to the bisector of the angle between the two incoming laser beams. From these fringes,

which are stationary in the fluid, the fluid velocity is to be determined.

Velocity directional discrimination is crucial for measurement of turbulent flows. In some applications, the direction of the flow is known and is always the same, but in many flow situations reversals of velocities are important. These include recirculating and pulsating flow, and for this work, highly turbulent flows, in stirred tank where velocities fluctuate rapidly. Since the Doppler frequency is independent of the direction of flow for stationary fringes, some means of directional discrimination must be employed. This is accomplished by shifting the frequency of one of the two beams, leaving the wavelength unaffected. This causes the fringes to move with a velocity proportional to the frequency shift. Hence, a particle moving in the measuring volume scatters light at the modulated (Doppler) frequency, f_d . Motion in the same direction as the fringe movement will reduce f_d , while motion in the opposite direction will increase f_d . The difference between this modulated frequency and the imposed shift frequency is proportional to the particle velocity. The frequency shift must exceed the maximum expected velocity in order to discriminate all signals. In the Aerometrics LDV systems a 40 MHz shift is imposed using a Bragg cell.

To scatter the light needed to generate Doppler signals, seeding particles are needed. When the seeding particles cross the measuring volume, they scatter light with a modulated intensity corresponding to their passage through the fringes. The

modulated light flux is detected as a frequency f_d in the receiving optics. The detected frequency is independent of the direction of the scattered light and is proportional to the component of particle velocity which is perpendicular to the fringes (see Figure 2.1). Since the velocity that is measured is the velocity of the particles, the accuracy of measurement depends on how closely the particles follow the flow. No additional seeding was used for this work, since the working fluid was tap water containing naturally occurring impurities with a mean diameter of approximately $1\mu\text{m}$. When the particle settling velocity is negligible compared to the fluid velocity and the particle inertia (mass) is small, the particles present in the fluid follow the fluid fluctuations exactly. Since tap water particulate has specific gravity of 2.5, the terminal (settling) particle velocity can be calculated from Stokes' law, giving $1\times 10^{-6}\text{m/s}$, which is negligible compared to the fluid velocity.

The boundaries of the measuring volume, or fringes, are defined using the Gaussian distribution of light intensity within a laser beam. The edge of the measuring volume is defined to be the point where the combined beams have decayed to $1/e^2$ of their maximum intensity. This definition results in a measuring volume which is ellipsoidal in shape as shown in Figure 2.2. With the diameter of the laser beam, d_b , and known intersection angle, the size of the effective measuring volume can be calculated using:

$$l_w = 0.8 \frac{d_b}{\sin(\frac{\theta}{2})} = \frac{8\lambda f^2}{\pi d_b s} \quad (2-1)$$

$$d_w = 0.8 \frac{d_b}{\cos(\frac{\theta}{2})} = \frac{4\lambda f}{\pi d_b} \quad (2-2)$$

where l_w and d_w are the length and diameter of the measuring volume; s is the beam separation, λ the wavelength of the laser light, and f the focal length of transmitter lens (see Table 2.1).

The fringe spacing, δ_f , is dependent on the wavelength of the laser light λ , and the beam intersection angle, θ , and is given by:

$$\delta_f = \frac{\lambda}{2\sin(\frac{\theta}{2})} \approx \frac{\lambda f}{s} \quad (2-3)$$

For measurement in media with refractive indices different from air (1.0), the intersection angle and the wavelength of the laser beam are affected in the same way, so the fringe spacing is not changed: only the size of the measuring volume changes. In this work, the wavelength of laser light $\lambda=514.5$ nm, the transmitter focal length $f=500$ mm and three different beam separations - s (given in Table 2.1),

corresponding to three different beam intersection angles, were used. The resulting fringe spacing and measured velocity ranges are given in Table 2.1.

The velocity, V , is obtained by multiplying the fringe spacing, δ_f by the output frequency, f_d , which is the number of fringes traversed per unit time: $V = \delta_f f_d$. The number of fringes that a particle passes depends on the flow direction, the orientation of the fringes, and frequency shift. The number of fringes, or measuring cycles, required depends on the signal processor and the evaluation algorithm being used. The seeding particle has to pass a minimum number of fringes to be measured. Frequency ranges and thus velocity ranges to be measured also depend on the signal processor parameters.

2.2 The Aerometrics LDV - an overview

An Aerometrics laser Doppler velocimeter/phase Doppler particle analyzer (LDV/PDPA) was used for this study. It can measure the diameter and one velocity component of spherical particles or drops simultaneously (PDPA mode), or the velocity only (LDV mode). The LDV is one-dimensional and forward scattering. Forward scattering means that the scattered light, which is dispersed in all directions, is detected in the forward scattering direction where the signal is strongest. The photodetector is located opposite the laser light source.

The laser Doppler velocity measurement system consists of the laser, a beam splitter, Bragg cell, focusing lenses, photodetectors, amplifiers and a signal processor, as shown in Figure 2.3. The angle between the line bisecting the angle between two beams and receiver, ψ , was for the most measurements approximately 20° and is not critical for velocity measurements. The instrument is designed for off-axis light collection which is necessary for the PDPA mode.

Figure 2.4 shows the experimental layout. A laser beam from the source (1) passes through the transmitting and focusing optics (2) including the Bragg cell. The intersection of the two beams forms a measuring volume within a cylindrical tank (3), which can be moved horizontally using computer controlled traverses (6), and vertically using a manual traverse (7). The impeller and motor were mounted on a vertical traverse (7a), to allow exact variation of the off bottom clearance of the impeller. The speed of the motor was measured using an optical tachometer (4). The receiving optics (5) are operating in a forward scattering mode. An Aerometrics Doppler signal analyzer (DSA) and/or a real time signal analyzer (RSA) were used (8) to convert the analog signal from the receiving optics into the velocity and particle arrival time. The signal processor (DSA or RSA) and traverse controller (9) are connected to a computer (10).

A 300 mW argon-ion laser was used, which generates laser radiation in the 457 nm to 514.5 nm regime. The laser beam experiences several reflections and

passages, thus losing some of its intensity. It has an intensity of approximately 100 mW as it exits from the transmitting optics.

The accuracy of the LDV measurement is determined partly by the quality of the components of the system but mostly by the following parameters:

- 1) Alignment - the laser beams must be aligned correctly, otherwise the beams will not cross exactly at the beam waists and the fringes will not be parallel.
- 2) Polarization - the plane of polarization of the light is adjusted to be perpendicular to the plane of the beams. This sets up the interference of the fringes.
- 3) Coherence - the two laser beams maintain constant phase relation as the time passes; otherwise no fringe pattern could be formed.
- 4) Beam intensity - the two beams should have the same intensity. The Bragg cell is adjusted to obtain equal intensities.

The beam intensity is the only quantity adjusted by laser user. Tuning of alignment and polarization requires the assistance of the instrument manufacturer.

2.2.1 Optics

The beam splitter (a prism), located within the transmitter, separates the laser beam into two beams with the same intensity, then the focusing lens focuses the beams at the probe volume. One of the beams is frequency shifted using a 40 MHz Bragg cell. The beams then pass through the modular focusing optics. The final focusing lens has a focal length of 500 mm. The transmitting optics can be adjusted by changing the optical orientation to measure any of the three velocity components in a cylindrical coordinate system. The beams then pass through the model, crossing at the measurement position.

There are three different tracks, to be chosen by user, corresponding to different beam separations and different fringe spacings, as shown in Table 2.1. It is expected that the measurements of mean and fluctuating velocity using different tracks are equal. This was verified by Zhou (1996). However, the data obtained using track 1 (minimum beam separation) gives the best reproducibility. Track 1 was used for this work.

The receiver, equipped with a lens of focal length 500 mm, converts the scattered light into electronic signals. There are three photomultiplier tubes (PMT) in our receiver. All three PMTs are used for particle size measurements, while only one is needed for velocity measurements, and thus is used for this work. The PMT's

produce light signals as a current, which is multiplied at a gain determined by the high voltage to the PMT set via the user and which can be varied from 200 to 800 V. Experimental validation, for mean and fluctuating velocities, done by Zhou (1996) shows that voltages between 400 and 680 V give repeatable measurements. Very high voltage may damage photomultiplier tubes, while lower voltages limit detection to signals with high magnitudes and have a lower repeatability. For this work, a range between 400 and 500 V was used.

2.2.2 Sample size and signal validation

The Aerometrics LDV configuration allows the user to set either the sample size (number of determinations) or the sample time (length of record in seconds). Experimental results showed that both the sample size and the sampling time are critical to velocity measurements. It was reported by Zhou (1996) that the sample time must be long enough to cover at least 80 passages of the impeller blade, i.e. for an impeller with 4 blades rotating at 400 rpm, the sampling time should be no less than 3 seconds (i.e. $3 \times 4 \times 400 / 60 = 80$ blade passages). If the sample time is too short, the reproducibility of measurement is poor even with a sample size larger than 10,000 data points. This is due to the long term instabilities in the flow whose time scale considerably exceeds that of a single blade passage or turbulent eddy, so that a longer time record is needed to get repeatable results.

The LDV/PDPA system employs "validation" of the results of measurements on a Doppler burst, rejecting them if their accuracy is suspect. Errors can arise if signals are obtained from particles that do not pass through the center of detection - the fringe system, if there are insufficient cycles left in a burst after passing the threshold, if a second particle enters the volume during the timing interval, or if a timing period starts in one burst and finishes in another. Excessive electronic or optical noise may also affect the measurements. Hence, the preset sample size is not equal to the actual sample size, i.e. the validated samples are not equal to the attempted samples and in most cases the validation of samples is less than 100%. The relationship between the sample size or validated samples and the attempted samples is:

$$\text{validation percent} = \frac{\text{sample size}}{\text{attempted samples}} \times 100$$

Validation of the velocity measurement by Zhou (1996) used four criteria: reproducibility of mean and RMS velocity profiles, symmetry of the flow field, comparison of experimental data with previous investigations, and mass conservation. From Zhou's results was concluded that the LDV/PDPA used in this work gives accurate and reproducible mean and RMS velocity measurements.

2.2.3 Signal processing using the DSA and RSA

The signal to be measured takes the form of short sinusoidal bursts produced by individual particles moving across the measuring volume (MV) as shown in Figure 2.5. With more than one particle present in the MV, scattered light from several particles can reach the receiving optics at the same time.

The frequency of the signal contained within single burst or within the time required for the particle to pass through the MV is proportional to the instantaneous fluid velocity in the MV. The frequencies varies rapidly from one burst to another and depends on the turbulence intensities. This together with measurement noise (optical, electronic) makes the evaluation of the correct Doppler frequency difficult, so that sophisticated signal processing techniques may be needed.

2.2.3.1 Doppler Signal Analyzer (DSA)

The Doppler signal analyzer (DSA) is a frequency domain signal processor. It is capable of accurately measuring signals with a low signal to noise ratio. It consists of a front end high pass or bandpass filter, a burst detection system, frequency down mixers, fast analog to digital converters (ADC), and either software (DSA) or hardware (RSA) array processors which compute a discrete Fourier transform (DFT) using the fast Fourier transform (FFT) algorithm. The processor is

used in conjunction with optical systems that incorporate frequency shifting to: a) avoid directional ambiguity and b) introduce a large separation between the pedestal and Doppler components of the signal. For this work, the detailed working of the signal processor was examined in some detail. A description of the process follows.

The signal from the preamplifier, located within receiver, (see Figures 2.6 and 2.7) is split (DSA unit) into two paths on entry to the DSA, with one leading to the peak detector. This is used together with the burst detector to locate and center the burst signal. On the other path the high pass filter (20 MHz -frequency above pass) is used to remove low frequencies known as the Doppler pedestal. The low frequency variations are due to the Gaussian light intensity distribution within the measuring volume (MV). Higher frequencies correspond to the velocity of the particle within the MV. Once the pedestal is removed, the signal is log amplified and sent to the burst detector. The log amplification forces the signal toward a square wave which is important for the phase measurement used in particle sizing. In this form, the points of zero crossings are much better defined, and the magnitude of the signal relative to the noise is increased.

The burst detector is the first essential part of the DSA. With this detector, the burst threshold level, which is based on the signal to noise ratio (SNR), is applied. This determines the time interval over which the Doppler burst is evaluated. The signal voltage must exceed a selected threshold level to be

considered for processing. The DSA has circuitry which can detect the center of the burst around which the signal to noise ratio will be the greatest. By using the burst centering, only the central part of the signal is included in the results. The detected burst is called “gated” during the transit time of seeding particle. The gate is open when the signal is detected (exceeds threshold) and goes down when signal drops below the threshold level. In reality, the burst detector is not capable of detecting every signal and may produce a false signal. When the SNR ratio is very low the signal is even more difficult to detect within the background noise. This is overcome by applying an FFT analysis and examining the results in the frequency domain. The basis for frequency validation is comparison of frequency packets (16 samples times 16 packets) in a single burst.

The second central component of the processor is the controller, which controls the settings of the instrument functions via the computer interface. A 160 MHz Master Oscillator is used to supply the Bragg cell driver with a precise frequency that is synchronized with the other signal processor functions (Figure 2.5). Programmable mixers are used to reduce the signal frequency before it is presented to the ADC (analog to digital converters). Quadrature down mixing is used where the signal is multiplied by sine and cosine signal from the local oscillator in order to get rid of shift frequency. This allows the sampling of a frequency bandwidth which is twice as wide as is possible with sampling only of real values. Quadrature sampling allows the central frequency of the signal to be down mixed to

zero.

Up to this stage of the signal processing, all settings are done by the manufacturer. The following stages are determined by the user and are constrained by the system configuration. To ensure accurate measurement, a proper choice of mixer frequency, sampling rate, and low pass filter must be made. The first step in optimizing signal processing is an estimate of the highest Doppler frequency, f_d expected in the flow. For the LDV configuration and stirred tank used in this work and smallest beam separation (track 1), with the maximum velocity estimated to be 3 m/s, $f_d = V_{\max} / \delta_f \approx 0.2$ MHz. This value determines the choice of mixer, signal sampling frequency and low pass filter frequency that further determine velocity and velocity ranges to be measured. Discussion from this point on will focus on track 1 (beam separation of 16.9mm). Similar calculations can be done for tracks 2 and 3.

2.2.3.2 Mixer frequency

Although most flows use the 40 MHz mixer, the following steps indicate which mixer is the best suited to the flow:

$$f_d > \text{LPF}_{\max} \text{ then } f_{\text{mix}} = 80 \text{ MHz} \quad (2-4)$$

where LPF_{\max} is the maximum value for low pass filter, and f_{mix} is the mixer

frequency;

otherwise $f_{\text{mix}}=40$ MHz

Since the maximum value of the low pass frequency for the DSA/RSA processor is 80 MHz, an f_{mix} of 40 MHz was chosen for this work.

2.2.3.3 Low pass filter

The signal is low pass filtered before being sampled. The low pass filter (LPF) attenuates frequencies above its value. It serves to prevent undersampling (aliasing) and eliminate background noise from the signal, improving the SNR. The minimum value of the LPF must be above the signal frequency. If this value is set below the output from the mixer, higher frequency signals (and higher velocity particles) will be attenuated and not measured. The maximum value of the low pass filter (LPF) is one half the sampling frequency. Setting this value above one half of sampling frequency will allow an aliased signal to be processed. Since the mixer output frequency is 0.2 MHz, the low pass filter has to be set above this value and it was set 1.25, 2.5 and 5 MHz depending on the choice of signal sampling.

2.2.3.4 Sampling rate

The signal is sampled using analog to digital converters (ADC's). A pair of ADC's, capable of sampling at frequencies up to 160 MHz, are used to digitize the output frequency from the mixers. The signal to be sampled is a sine wave function. The ADC has one bit resolution, converting the signal into plus ones and minus ones to form a square wave at the input signal frequency.

The choice of the sampling frequency is made upon two limitations:

1) the signal has to be sampled at a frequency least twice that of its highest frequency (estimated Doppler frequency). However, sampling at more than twice the highest frequency in the flow does not improve resolution and accuracy (for LDV only).

2) transit time limitation (t_{\min}).

The DSA needs 256 samples for each LDV measurement. Therefore, there is a minimum transit time t_{\min} (the time the particle takes to move through the probe volume) that will give 256 samples at a certain sampling rate. If the transit time is less than the time necessary to measure the 256 samples at the selected signal sampling frequency, the particle will not be measured. The transit time determines both the signal sampling frequency and the value of the low pass filter in this work.

$$t_{\min} = \frac{d_w}{V_{\max}} > \frac{256}{f_{\text{sampling}}} \quad (2-5)$$

d_w is the beam waist diameter and V_{\max} the estimated maximum fluid velocity. Since the Doppler frequency is 0.2 MHz, and $t_{\min}=93.3 \cdot 10^{-6}$ s, the sampling frequency has to be higher than 2.5 MHz. The next higher value available in the DSA was 5 MHz. The low pass filter was set at 2.5 MHz.

The record length (or gate time) or period over the signal is sampled, τ , is given as:

$$\tau = \frac{N}{f_{\text{sampling}}} \quad (2-6)$$

where $N=16 \times 16$ (16 sample packets) samples per single burst and f_{sampling} is the sampling frequency. The record length should be shorter than the Doppler burst signal period, otherwise noise may be included in the sampled signal (Figure 2.5). The DSA only processes signals with a SNR greater than the threshold value. The SNR is calculated for each burst in order to discriminate a single tone signal. The accuracy of the Doppler frequency depends on the length of the FFT. The more points considered the better the chance of enhancing the signal. Doppler Signal Processing is performed in the frequency domain using the FFT for each burst signal. The new time domain array is transformed in the frequency domain and then

the power spectrum is calculated. For a single burst, a single tone frequency band, corresponding to the burst Doppler frequency, predominates over the power spectrum (Figure 2.8). After determination of the Doppler frequency, the DSA passes the results to the system software for statistical analysis and presentation of the size and velocity information in histogram form.

2.2.4 RSA vs. DSA single burst processing

For this study, two different signal processing units were used: the Doppler signal analyzer (DSA) and the Real-time signal analyzer (RSA). They both employ the same principle of single burst processing, performing a DFT on each burst and pulling out the dominant frequency. The DSA is an older version based on software. It has a predetermined "transit time" (or length of the burst) given as a number samples over the signal sampling rate, and operates with a fixed number of samples (256) per burst. The RSA is hardwired. It can vary the number of samples for each burst depending on the burst length. Thus, when the DSA is used and the length of the signal is shorter than that expected, some noise is included in sampled signal. A transit time which is longer than the expected transit time does not get the best possible resolution. In Chapter 3, the frequency analysis of time series taken using both processors will be extensively discussed. It will be shown that the DSA processor has a frequency resolution limited to one 20th the data rate and the RSA to one 10th the data rate. For other processing methods, the frequency resolution

extends up to one half the data rate. This is a serious limitations of the DSA approach for analysis of turbulent frequency spectra.

Table 2.1: LDV optical properties

Track	1		2		3	
	transmitter focal length, f , (mm)	300	500	300	500	300
beam expander ratio	1.0	1.0	2.0	2.0	3.8	3.8
waist diameter, d_w , (μm)	168	280	84	140	45	75
beam separation s , mm	16.9	16.9	33.8	33.8	63.4	63.4
fringe spacing, δ_r , μm	9.1	15.2	4.6	7.6	2.4	4.1
nominal fringe count	18	18	18	18	18	18
velocity range, m/s	-31+1004	-532+1673	-160+502	-266+837	-85+268	-142+446

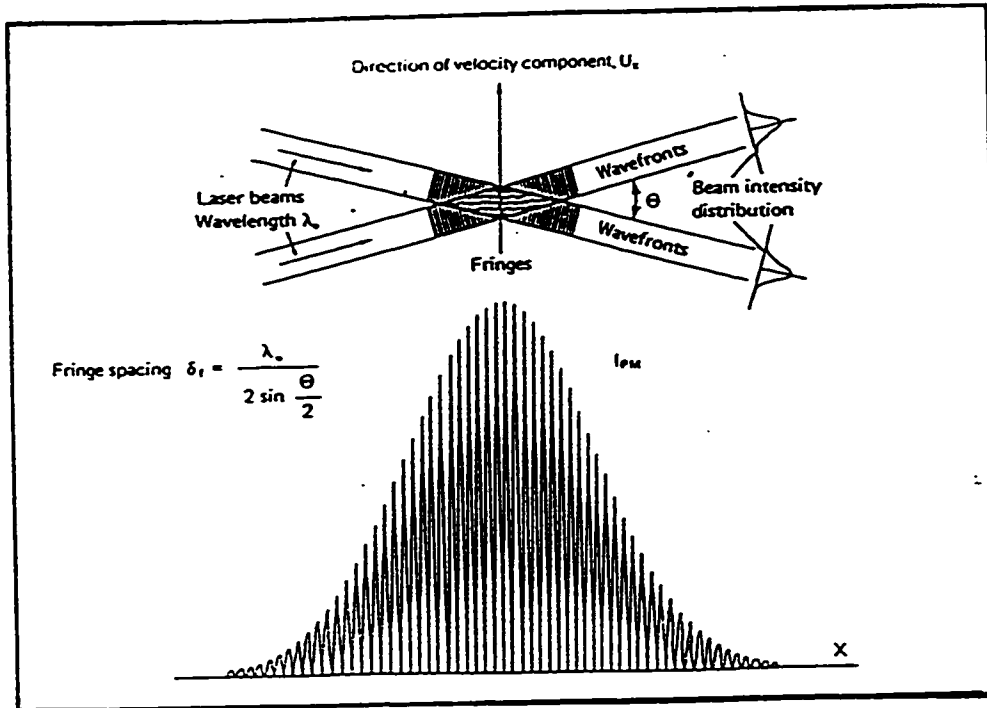


Figure 2.1: LDA measuring volume as envisioned by the fringe interpretation (from George, 1988.).

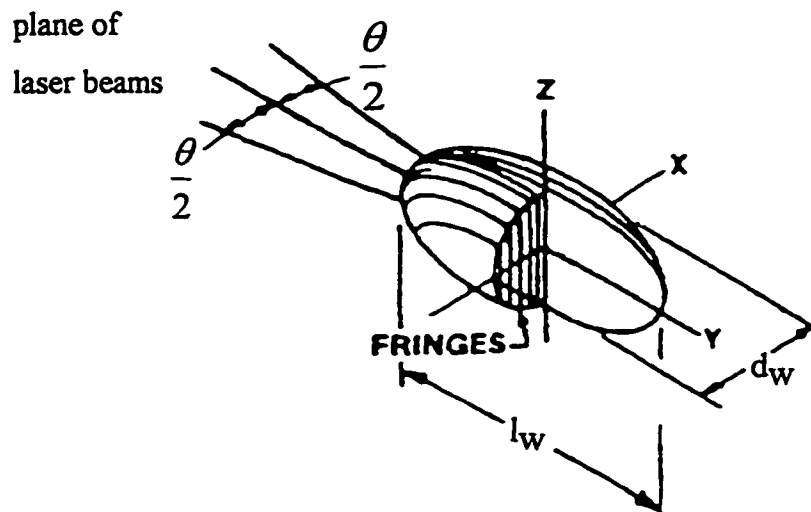


Figure 2.2: Appearance and size of the measuring volume (Pettersson, 1996.).

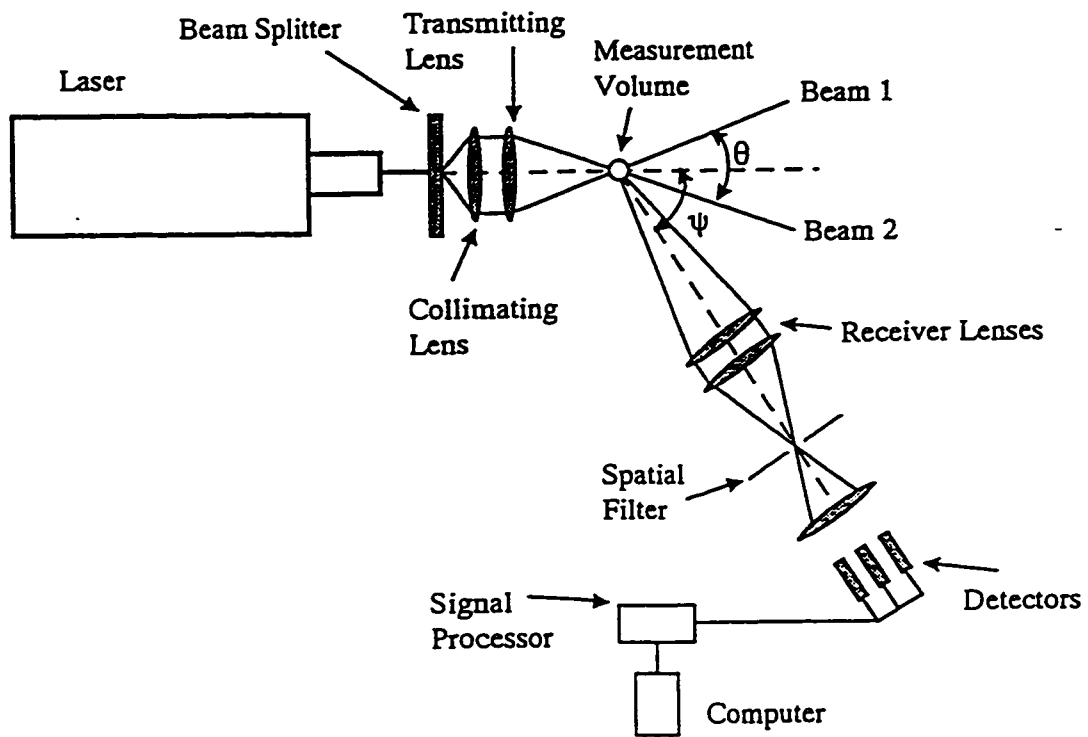


Figure 2.3: Schematic of the Aerometrics LDV/PDPA optical configuration.

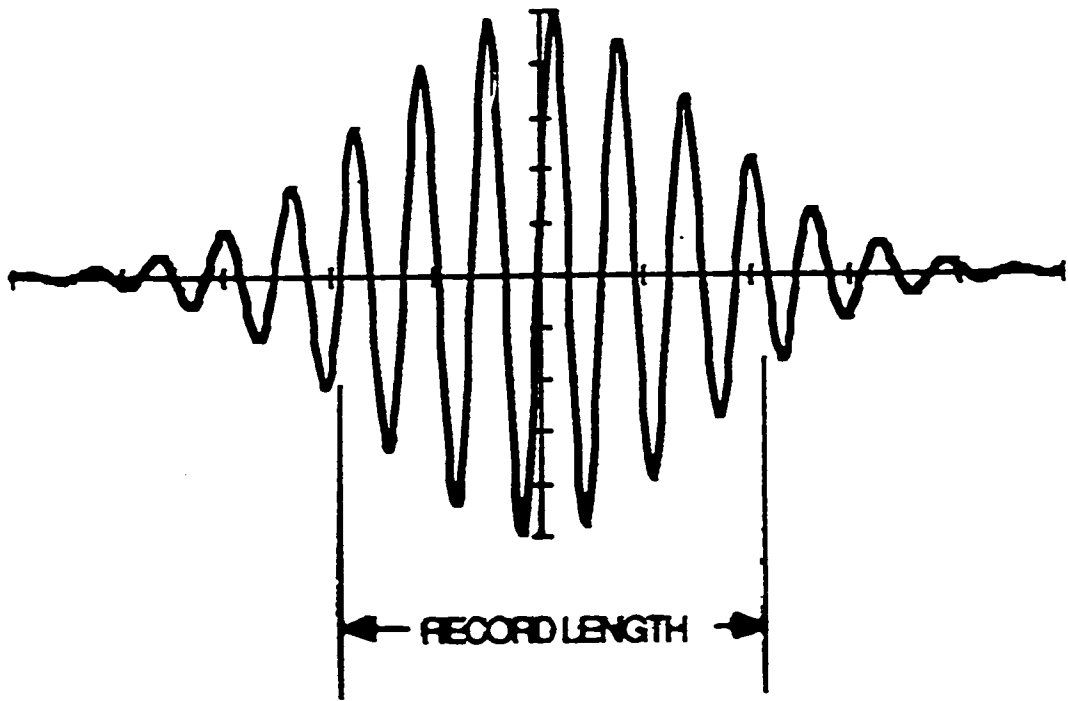


Figure 2.5: Sampling over one Doppler burst (Bachalo, 1994.).

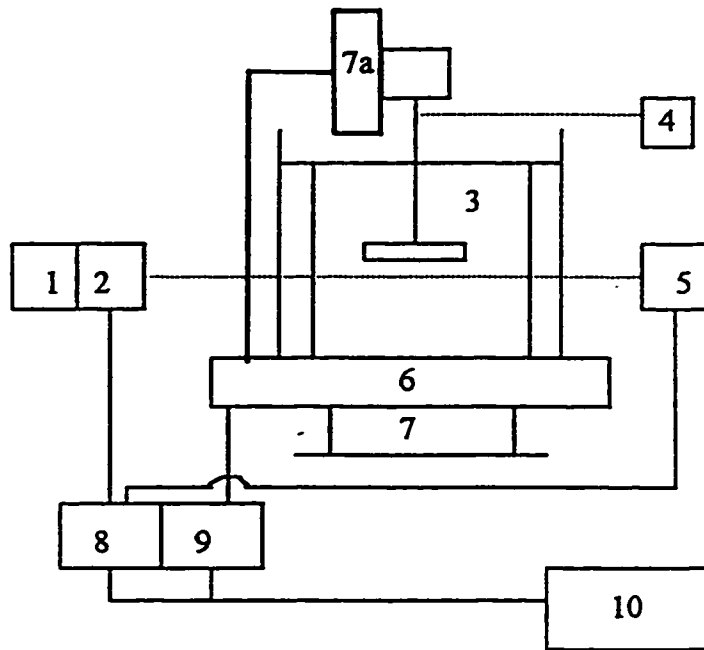


Figure 2.4: LDV experimental arrangement: (1) laser; (2) transmitting optics; (3) agitated tank; (4) tachometer; (5) receiving optics; (6) X-Y traverses; (7) and (7a) manual traverses; (8) Doppler signal analyzer; (9) traverse controller; (10) computer.

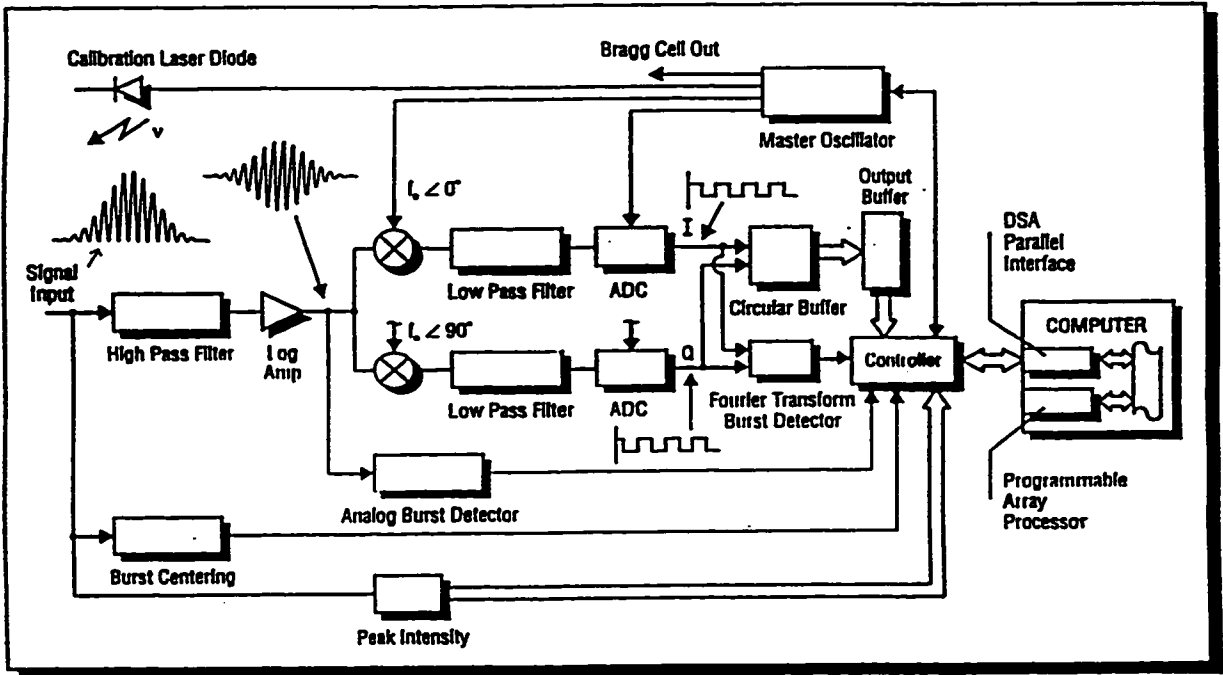


Figure 2.6: Block diagram for the Doppler Signal Analyzer (Bachalo, 1994.).

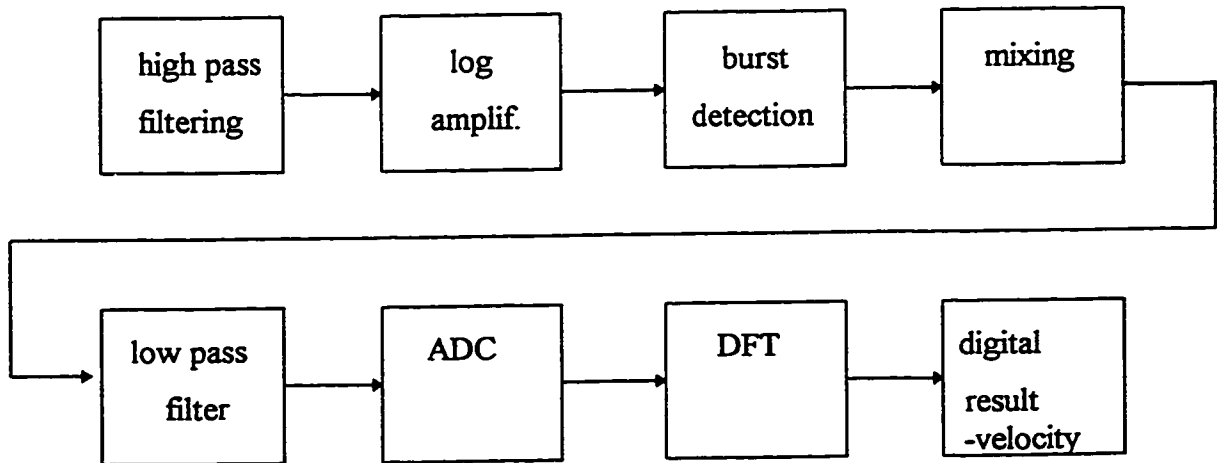


Figure 2.7: Flowsheet for the DSA.

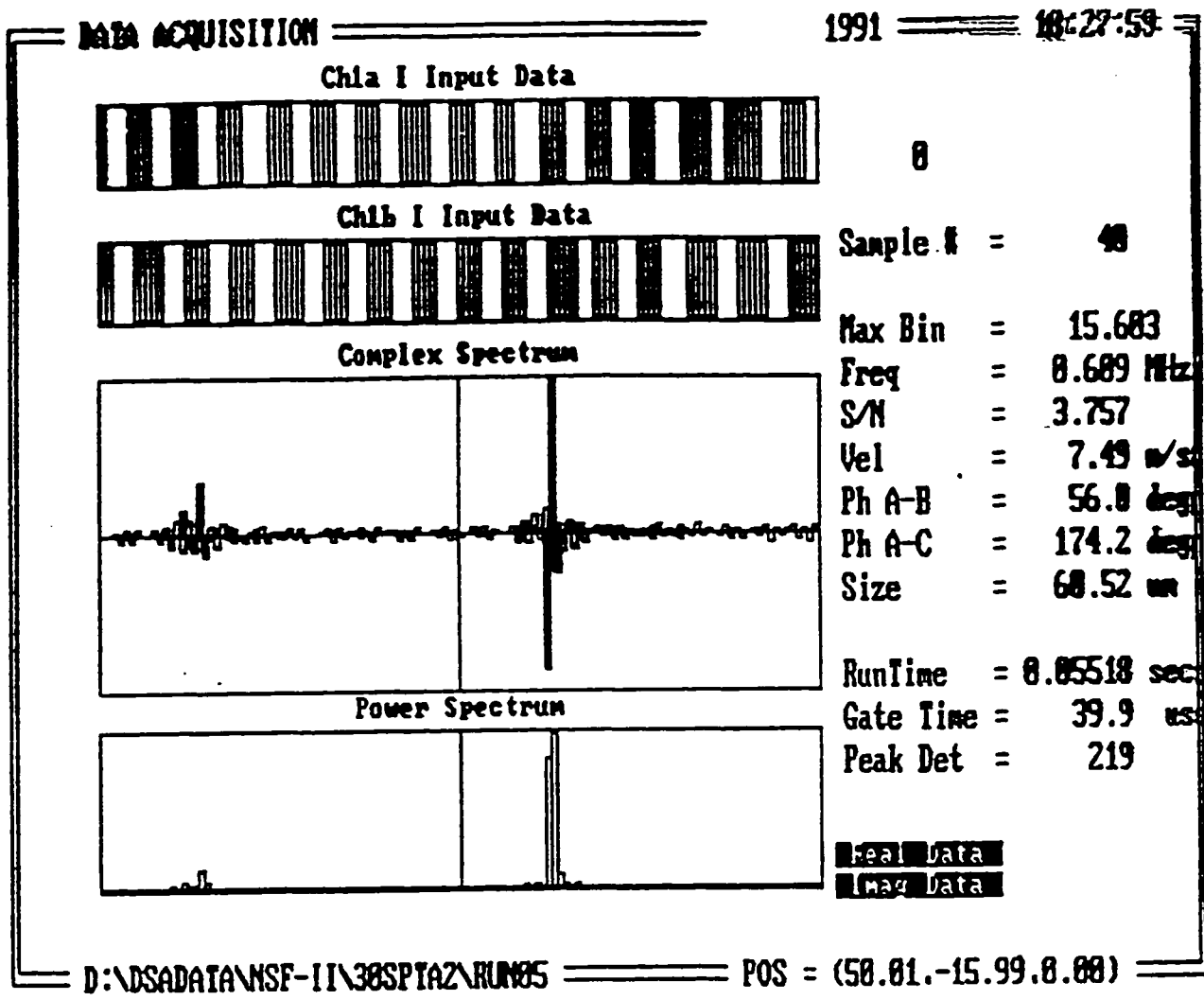


Figure 2.8: Frequency spectrum from one single burst.

References

Aerometrics: Phase Doppler Particle Analyzer/Doppler Signal Analyzer-1-Component User's Manual, 1993.

Aerometrics: Real Time Signal Analyzer, User's Manual, April, 1997.

Bachalo, W.D., Lecture on DSA Signal Processor, March, 1994.

Bachalo, W.D., D. Werthimer, R Raffanti., and R.J Hermes., A high speed Doppler signal processor for frequency and phase measurements. *Third Int. Conf. on Laser Anemometry, Advances and Applications*, Sept. 1989.

Drain, L.E., *The Laser Doppler Technique*, 1980, John Wiley and Sons, Toronto.

Durrani, S.T., and A.C Greated, *Laser Systems in Flow Measurement*, 1977, Plenum Press, New York and London.

Durst, F., A. Melling, and H.J. Whitelaw, 1981, *Principles and Practice of Laser Doppler Anemometry*, Second Edition, Academic Press Inc., New York.

Hong Tan, and Loh Julie, 1992, Real-Time Laser Doppler Signal Processors, *Optics and Lasers in Engineeing*, vol. 17, 229-240.

George, W.K., 1988, Quantitative measurement with the burst-mode Laser Doppler anemometer, *Exptl. Thermal and Fluid Sci.*, 1, 29-40.

Ibrahim, K. M., G. D. Werthimer, and W.D. Bachalo, 1990, Signal Processing Considerations for Laser Doppler and Phase Doppler Applications, *Fifth*

Int. Symp. on the Application of Laser Technique of Fluid Mechanics Lisbon, Portugal, July 9-12.

Kresta, S.M., 1991, *Characterization and Prediction of the Turbulent Flow in Stirred Tanks*, Ph.D, Thesis, Mc Master University, Hamilton, Canada.

Petersson, P., 1996, *Laser Doppler Velocity Measurement in an Impeller-Generated Turbulent Jet*, Report 3195, Lund, Sweden.

Zhou G., 1996, *Characteristics of Turbulence Energy Dissipation and Liquid-Liquid Dispersions in an Agitated Tank*, Ph.D Thesis, University of Alberta, Canada.

Chapter 3. Frequency Analysis

In this chapter, spectral analysis is used in an attempt to analyze low frequencies in the velocity record. Only data taken with the PBT impeller, measured at the impeller stream, will be discussed in this chapter. The objective of this analysis was to detect low frequencies and estimate their time and length scale. The integral time scale is obtained from the integral of the autocorrelation function which falls out directly from the frequency spectrum. The integral length scale, or more generally the size of the coherent structure, is equal to the integral time scale times the mean velocity. The magnitude of the integral time scale is very sensitive to the presence of low frequencies. By using spectral analysis and digital (notch) filtering of the autocorrelation function to remove the low frequency component, a quantitative measure of the integral time scale of turbulence can be obtained (Kresta and Wood, 1993). With the equipment used in this study, however, this proved impossible. This chapter will discuss the development and testing of numerical techniques for spectral analysis, and the testing of the experimental system, finally showing why the DSA cannot be used for frequency analysis with the current experimental results.

3.1 Fourier domain spectral analysis

The instantaneous velocity signal from a turbulent flow can be interpreted as the sum of a wide spectrum of signals, each of which has a single frequency. The relative contributions of the individual frequencies to the sum are represented by the frequency spectrum or spectral density. The power spectral density (PSD) and the autocorrelation function provide powerful information for a physical interpretation of the dominant frequencies and time scales in the flow field. The PSD gives the energy (or power) content of the signal in a specified frequency band. The autocorrelation gives a measure of the extent to which a signal correlates with a displaced version of itself in time.

The central quantity used for calculations in following sections is the fluctuating velocity component, $u=U-\bar{U}$, where U is the instantaneous velocity and \bar{U} is the time averaged (mean) velocity. The instantaneous velocity is divided into two components in order to isolate the study of the time-varying flow field from that of the mean flow field.

3.1.1 Turbulent power spectrum

The power spectrum or energy spectrum is a decomposition of the measured velocity into different waves of different frequencies or wavenumbers. The value of the spectrum at a given frequency (or wavelength) is the mean energy in that wave length.

The energy spectrum describes how energy is transferred in the turbulent flow field from the large eddies to the smaller eddies. The whole turbulence energy spectrum range can be divided into four ranges (Figure 3.1): large eddy range, energy containing eddy range and universal equilibrium range which is further divided into the inertial subrange and viscous subrange. The flow behavior which establishes the spectrum in a stirred tank is the turbulent kinetic energy contained in the trailing vortex system close to the impeller. These vortices decay to low wave number eddies which transfer their energy to smaller eddies further away from the blade. Since our turbulence measurements are for the Eulerian spectrum, which measures fluctuations caused by random group of eddy orientations as they sweep past a probe with velocity U , only a one-dimensional slice of the complete three-dimensional spectrum can be measured.

The one-dimensional spectral density $E_1(f)$ for the crossflow fluctuating velocity u is given by (Hinze, 1975):

$$u_1^2 = \int_0^{\infty} E_1(f) df \quad (3-1)$$

or expressed in wavenumber k_1 , $k_1 = 2\pi f / \bar{U}$:

$$u_1^2 = \int_0^{\infty} E_1(k_1) dk_1 \quad (3-2)$$

where 1 denotes the streamwise component of velocity. The energy spectrum, $E_1(f)$, is a continuous function in the frequency domain. However, the spectrum is made up of eddies of discrete sizes.

Hinze (1975), states, based on the Kolmogorov hypothesis, that at a sufficiently high Reynolds number, there is a range of high wavenumbers where the turbulence is at equilibrium and is determined only by the rate of transfer of energy through the scales, given by the dissipation rate, ϵ , and viscosity, ν . This state of equilibrium is universal and is unaffected by the large scale parameters. The turbulence spectrum in this range can be represented by a simple power function:

$$E(k_1) = A_1 \epsilon^{2/3} k_1^{-5/3} \quad (3-3)$$

where $A_1 \cong 0.56$ (Hinze, 1975), for isotropic turbulence.

3.1.2 Velocity autocorrelation

The autocorrelation coefficient is a key component in the analysis of low frequency phenomena in a stirred tank. The autocorrelation coefficient function R_E (or autocorrelation) is calculated from the following equation:

$$R_E(\tau) = \frac{\overline{u(t)u(t+\tau)}}{\overline{u(t)^2}} \quad (3-4)$$

where τ is the time lag.

In the stirred tank, where periodic blade passages and random turbulent components are present, the total autocorrelation of these two time functions is:

$$R_T(\tau) = R_{Ep}(\tau) + R_{Er}(\tau) \quad (3-5)$$

where $R_{Ep}(\tau)$ is the periodic and $R_{Er}(\tau)$ the random autocorrelation component. The random component $R_{Er}(\tau)$ reaches zero at small τ - 0.2 s (Kresta and Wood, 1993). Oscillations about zero at large τ (of the order of several seconds) are only due to blade passages and low frequency instabilities in the flow. Figure 3-2 shows a typical autocorrelation curve (Kresta and Wood, 1993) for a velocity vs. time record in the impeller vicinity, indicating low frequency oscillations (at 0.8s) and the higher blade

passage frequency of 0.04s. Oscillations on the autocorrelation curve can be explained by the fluid flow directional changes. For example, at the blade passage frequency (BPF), the impeller blade (or low frequency eddy) approaches the fixed probe, displaces the fluid ahead of it and the velocity of the displaced fluid is greater than the average. Then, at the time between two consecutive blade passages, fluid will go in the opposite direction into the wake of the blade that has just passed. The magnitude and period of positive and negative deviations are approximately equal and thus the time scale over which this correlation (oscillation) exists can be identified. Although the blade passage frequency can be observed using the autocorrelation function, it is best observed on the power spectral density plot. Conversely, the autocorrelation function gives the best identification of the low frequency.

3.1.3 Transformation to frequency domain using FFT

A physical process can be described either in the time domain, by the value of some quantity h as a function of time t , $h(t)$, or in the frequency domain, where the process is specified by giving its amplitude H (generally a complex number including the phase) as a function of frequency f . $h(t)$ and $H(f)$ are two different representations of the same function. One goes back and forth between these two representations by means of the Fourier transform equations (Press et al. 1989, pg. 381):

$$H(f) = \int_{-\infty}^{\infty} h(t) e^{2\pi i f t} dt \quad (3-6)$$

$$h(t) = \int_{-\infty}^{\infty} H(f) e^{-2\pi i f t} df \quad (3-7)$$

where time t is in seconds and frequency f is in Hertz. The frequency is expressed as an angular frequency ω ($\omega=2\pi f$), which is given in radians per second.

Computational work using a Fourier transform involves a discrete list of measurements - $h_k(t)$, rather than a continuous function $h(t)$. Thus, the integral (3-6) in its discrete form is (Press et al., 1989):

$$\begin{aligned} H(f_n) &= \int_{-\infty}^{\infty} h(t) e^{i2\pi f_n t} dt \approx \sum_{k=0}^{N-1} h_k(t) e^{i2\pi f_n t_k} \Delta t_k = \\ &= \sum_n \sum_k h_k(t) e^{i2\pi n t_k / T} \Delta t_k \end{aligned} \quad (3-8)$$

Equation (3-8) gives discrete Fourier transform of N points h_k where k denotes the point in the time domain and $k=0,1,2,\dots,N-1$; n denotes the point in the frequency domain $f_n \equiv n/T$ and $n=1,2,\dots,N$; and $\Delta t_k = t_{k+1} - t_k$ is the sampling interval.

From equation (3-8), it is obvious that the discrete Fourier transform (DFT) involves N^2 complex multiplications. In fact, this number can be reduced with an algorithm called the Fast Fourier transform (FFT), which involves data reordering by bit reversal order and the Danielson-Lanczos lemma. Data are subdivided into $N/2$ even-numbered and $N/2$ odd-numbered points and their discrete Fourier transform is calculated. This subdivision goes further down to 1. Thus, bit-reordering data takes N operations, and the discrete Fourier transform of length 2,4,8... N takes $\log_2 N$, so that whole algorithm takes $N \log_2 N$ operations.

Table 3.1 shows the structure of the FFT algorithm. Three subroutines: FOUR1, REALFT, and COSFT are taken directly from Press et al. (1987). COSFT employs cosine transform of the initial data array, so that data can be repacked as real and imaginary part of complex number (in subroutine REALFT). The actual FFT transform is in subroutine FOUR1. For more detail on the FFT calculations Press et al. (1987) should be consulted.

After computing the Fourier transform of the initial time series, the autocorrelation can be obtained by multiplying the FFT transform by its complex conjugate:

$$R_E(\tau) \equiv H_k H_k^* = |H_k|^2 \quad (3-9)$$

where H_k is discrete Fourier transform and H_k^* is the complex conjugate of H_k .

3.1.4 Methods used for computing power spectrum from unevenly spaced data

The laser Doppler velocimeter (LDV), when operating in the burst-signal processing mode, measures velocity only when a seeding particle is detected in the measuring volume. The time interval between two consecutive measurements is determined by the seeding density, which is random. Thus, LDV “individual realization” measurements lead to data sets which are randomly sampled time series of velocity. The nonuniform data distribution precludes use of the standard spectral estimates based on a fixed sampling frequency, such as the FFT. Algorithms used for computing the power spectrum from randomly sampled data tend to be much slower.

Methods for computing power spectra from unevenly sampled data can be classified into two categories: those that use interpolation between points and those that work with the original data. Interpolation provides a new sequence of values which is evenly sampled from existing randomly sampled sequence. The resulting sequence can be analyzed using the FFT. The principal disadvantage of the interpolation is that new velocity data are generated which are not present in the

original record, and it may distort the high frequency turbulent fluctuations which are essential for turbulence analysis, so that it hasn't been used for this study.

Two direct techniques are generally used to obtain the power spectrum: the first, the binned autocorrelation (Bell, 1986), is based on taking the Fast Fourier transform of the autocorrelation function. The second method, the discrete Fourier transform (DFT) involves calculating the discrete Fourier transform of the original signal. For this study, both of these methods were used. In addition, the FFT was applied to the data to test the sensitivity of the spectrum to the signal spacing.

With the binned autocorrelation method, an estimate of the auto- or cross-correlation function is first determined. This estimate is formed by dividing the lagged time axis of the correlation function into equidistant intervals or slots. The LDV data consist of discrete points $U(t_i)$ in time t_i . The mean velocity is first computed and subtracted from the measured values (mean centering), based on the assumption of the stationarity of the measured process. The new time sequence is expressed in terms of the slot size and used, together with the fluctuating velocities, to compute the autocorrelation. This is done by forming the product between each and every pair of data points, determining the time difference (lag) between them, and finding the time slot that best approximates the time difference. The sum of products at each slot are then formed and their average determined. The average value of the lagged product within each slot is taken as an estimate of the correlation

function at the center of the lagged time slot. Finally, the values in each and every slot are divided by the value of the autocorrelation slot corresponding to $\tau=0$ to yield the normalized autocorrelation function R_E . Since the time slots are now equidistant, the FFT is applied. The structure of the binned code is given in Table 3.1.

In the discrete Fourier transform (DFT), power spectra are calculated in a frequency interval f to $f+df$. This calculation must include positive and negative f . The total power in a signal is the same whether we compute it in the time domain or in the frequency domain. This result is known as Parseval's theorem:

$$\text{Total Power} \equiv \int_{-\infty}^{\infty} |h(t)|^2 dt = \int_{-\infty}^{\infty} |H(f)|^2 df \quad (3-10)$$

Then the one sided power spectrum may be calculated as:

$$P_n(f) = |H(f)|^2 + |H(-f)|^2 \quad (3-11)$$

When the function $h(t)$ is real, then $H(f)=H(-f)$, so that a factor of 2 is expected in above equation. Since the sum of interest is not power, but RMS velocity squared, the factor of 2 drops out.

The discrete form of equation (3-2) gives (Hinze, 1975) the one-dimensional energy spectrum E_1 as:

$$\int_0^{\infty} E_1(f) df = \frac{\sum_{k=0}^{n_{\text{data}}} u_{1,k}^2}{n_{\text{data}} + 1} \quad (3-12)$$

where $E_1(f)$ is a continuous function in the frequency domain. The relation between the discrete Fourier transform H_k of a set of numbers and their continuous function $H(f_k)$ sampled at the sampling frequency, sf can be written as:

$$H(f_k) \approx \frac{H_k}{sf} \quad (3-13)$$

where H_k is the discrete Fourier transform (m/s). The discrete form of Parseval's theorem (Press, 1987) states that:

$$\sum_{k=0}^{nn-1} |h_k|^2 = \frac{1}{nn} \sum_{k=0}^{nn-1} |H_k|^2 \quad (3-14)$$

where h_k is time domain data and H_n is the discrete Fourier transform of the N points h_k . Combining (3-12) and (3-14) gives:

$$\frac{1}{(\text{ndata} + 1)} \sum_{k=0}^{\text{ndata}} |u_k|^2 = \frac{1}{\text{nn}(\text{ndata} + 1)} \sum_{k=0}^{n-1} |H_n|^2 \quad (3-15)$$

where (ndata+1) is the number of data points in time series and nn is the number of points used in the FFT algorithm. nn must be an integer power of two because of the nature of the FFT algorithm.

From (3-8) the frequency spectrum is obtained as:

$$E(f)_{\text{DFT}} = \frac{|H(f_n)|^2}{sf \times N} \quad (3-16)$$

where sf is the mean sampling rate. The direct transform method can be applied to either one single block of length T , or to the entire record can be divided into N_B blocks, each of length $T_B=T/N_B$. The method can be individually applied to each short block, finally averaging the results over N_B blocks. Averaging over short blocks has the effect of smoothing the power spectrum and improving its accuracy. The lowest frequency at which a spectral estimate can be made is inversely proportional to the block length; short blocks cannot provide accurate estimates at low frequencies (due to the lower frequency resolution). Note that the block concept can also be applied to the autocorrelation method.

3.2 Studies on simulated data

In order to test the two spectral analysis algorithms for unevenly spaced data, signals whose spectral characteristics are known were tested. Because the binned autocorrelation (AAC) is much faster, while the DFT is the exact transform, the DFT was used as a reference benchmark for the binned autocorrelation method. The code was written in Fortran 77, then tested and optimized using well defined signals. Table 3.1 shows the structure of the code (included in Appendix A). As a check on the power spectrum density (PSD) calculations, two functions were tested. The first test function was a sine signals with three frequency components: 0.01, 0.1, and 0.025 Hz, with corresponding amplitudes of 13.7, 15.3, and 20.3:

$$x(t)=13.7\sin(2\pi 0.01t) + 15.3\sin(2\pi 0.1t) + 20.3\sin(2\pi 0.25t) \quad (3-17)$$

The signal is evenly sampled at the sampling rate of 1 Hz. The second signal is the same sine waves, but sampled unevenly at an average sampling rate of 1 Hz. A random time sequence was obtained as $t=t+\tau$, where t is the average sampling rate and τ is a random number between 0 and 1, generated using the random number generator by Etter (1987). The results are given in Figures 3.3 (PSD) and 3.4 (autocorrelation), and show fairly good agreement. All frequencies can be detected, however, the PSD plots with distinct spikes at the 0.01, 0.1 and 0.25 Hz, give a better identification of the frequencies present in the input signal than the

autocorrelation plots. Different sampling rates had no effect on the final results (not shown).

3.2.1 Different slot size

Before applying the autocorrelation technique, the optimum size of the time slot should be determined in order to reduce the variance of the autocorrelation function. The variance of the autocorrelation function estimate is inversely proportional to the number of points per lagged time slot and the total sampling time (Bell, 1983). The number of points per lag time slot can be increased by increasing the sampling rate, total time or the lag time width, τ , in order to achieve maximum accuracy. However, increasing τ may increase the bias and aliasing of the autocorrelation estimate if the Nyquist criterion is not satisfied. If the slot width is decreased then the frequency range of the spectral estimate is increased, but the variance or scatter in the tail of the spectrum is also increased. In this study, three different slot widths were used for the previously discussed unevenly sampled signal while keeping sample size and sampling frequency constant: 0.5, 0.125 and 0.05 seconds. It is evident (Figure 3.5) that a smaller slot width introduces additional variability in the spectral estimate, but a smaller slot size also provides more points in the spectral estimate. It is not possible to detect the main contribution to the variability.

Mean centering of the initial data set also gives significant reduction in the variance on computing the power spectrum. This was reported by Gaster and Roberts (1980) as “filtering out” the zero frequency component. Thus, the power spectrum is not estimated at $f = 0$. Hz.

3.2.2 Noise addition

In order to simulate the actual conditions that exist in the LDV data sets and test the sensitivity of the binned technique to the presence of noise, white noise was added to the unevenly sampled test data set. The data required for the white noise (random numbers) were generated independently and then combined with the initial time sequence ($t = t \pm 0.1\%$ error (Δt)) to get a new time sequence. The resulting PSD estimates are shown on Figure 3.6 (a, b, and c). The frequency peaks are still well defined, while the rise in the ambiguity level due to the presence of noise is negligible.

3.2.3 Notch filtering

Digital filtering is used to modify certain frequencies relative to others, passing certain frequency components and totally rejecting others. High-pass or low-pass filtering is used to eliminate noise at low and high frequencies. When an interesting part of the signal lies in a certain frequency band, a band-pass filter is

used. If measurements are contaminated by a specific frequency, a notch filter is applied to remove only a narrow band around that frequency.

In this work, notch filtering was used to remove a narrow band from the generated signal and examine its effect on the spectrum. This was done in order to optimize the filter subroutine used to examine the effects of the low frequency and the blade passage frequency removal on the spectrum. Digital filtering is quite straightforward in the Fourier domain.

The general filter equation is given by Press et al.(1989) as:

$$\mathcal{H}(f) = \frac{\sum_{k=0}^M c_k e^{-2\pi i k (f\Delta)}}{1 - \sum_{j=1}^N d_j e^{-2\pi i j (f\Delta)}} \quad (3-18)$$

where $\Delta=1/sf$. For a notch filter, the c 's and d 's to be used are given as:

$$c_0 = \frac{1 + \omega_0^2}{(1 + \varepsilon\omega_0)^2 + \omega_0^2} \quad (3-19)$$

$$c_1 = -2 \frac{1 - \omega_0^2}{(1 + \varepsilon\omega_0)^2 + \omega_0^2} \quad (3-20)$$

$$c_2 = c_0 \quad (3-21)$$

$$d_1 = 2 \frac{1 - \varepsilon^2 \omega_0^2 - \omega_0^2}{(1 + \varepsilon \omega_0)^2 + \omega_0^2} \quad (3-22)$$

$$d_2 = - \frac{(1 - \varepsilon \omega_0)^2 + \omega_0^2}{(1 + \varepsilon \omega_0)^2 + \omega_0^2} \quad (3-23)$$

where

$$\omega = \tan(\pi f \Delta)$$

ω_0 - center of frequency notch

ε - width of frequency notch as a fraction of ω_0

Figure 3.7 shows the result of applying a notch filter, centered at 0.05 Hz with an ε of 0.5 to the PSD in Figure 3.3b.

3.3 Spectral estimates from the LDV data

The real data is substantially more difficult to analyze. A sample time series of the instantaneous velocity is shown in Figure 3.8. Figure 3.9 shows a typical frequency spectrum along the lower edge of the impeller blades obtained from the autocorrelation technique. The blade passage frequency (BPF) is evident at 76 Hz. The high frequency end of the spectrum, however is contaminated by noise. This

opposes the physics of the system, where the flow is highly turbulent and locally isotropic so that a $-5/3$ slope (on log-log scale) on the high frequency end was expected. A number of investigators over the past three decades (Kim and Manning, 1964, Mujumdar et al., 1970, Gunkel and Weber, 1975, Rao and Brodkey, 1972, Kresta and Wood, 1991, Zhou and Kresta, 1996, Wernersson, 1997) have confirmed this characteristic slope. There are several possible reasons for the spectrum to appear in its current form. These range from numerical to experimental errors (aliasing, ambiguity noise, velocity bias, measurement noise etc.). Each of these possibilities will be addressed in turn.

3.3.1 PSD from three different techniques

Three different codes were used to calculate the frequency spectrum: binned autocorrelation, discrete Fourier transform (DFT) and Fast Fourier Transform (FFT). The power spectrum was calculated using equation (3-15) for the FFT and binned techniques and equation (3-16) for the DFT. For each technique, initial data sets were divided into six blocks of length 2048 points, the spectral estimate was obtained for each block and the final estimate was obtained as an average out of six. Frequency spectra on Figures 3.10 (a,b,c) show white noise (flat frequency spectrum) contamination on the higher frequency ends for all three methods. None of the plots clearly indicates the dominance of the blade passage frequency. The FFT and binned autocorrelation techniques show a similar indication of a $-5/3$ drop

off up to 100 Hz. The DFT gives an inferior spectral estimate, where white noise dominates over the whole frequency range (Figure 3.10b). This shows essentially the same problems for different numerical methods, which leads to the conclusion that data processing doesn't significantly affect the final result. Another cause for contamination of the spectrum at high frequency must be present.

3.3.2 Poisson sampling

Randomly sampled data with a Poisson distribution of arrival times has an advantage over regularly sampled data, since it is not aliased. With periodic sampling, aliasing arises when the sampling rate falls below the Nyquist frequency (2 times highest frequency component in the signal). Accurate spectral estimates up to frequencies higher than the half of the sampling frequency can be obtained if the particle arrival rate has a Poisson distribution. This has been reported over the past three decades by several authors (Shapiro and Silverman, 1960, Gaster and Roberts, 1980, Sree, 1994). Gaster and Roberts (1980) found that this assumption doesn't hold for turbulent flows of high intensity where deviations with time are expected. This was restated by Sree (1994) who observed that this type of distribution is exhibited only in well controlled LDV experiments. He also found that, even for a non-Poisson sampling distribution, good spectral estimates can be made only up to two-thirds of the Nyquist frequency.

The probability density function for Poisson sampling, p in a time interval Δt between successive samples is (Roberts et al., 1980, Sree, 1994):

$$p(\Delta t) = sf \exp(-sf\Delta t) \quad (3-24)$$

where sf is the mean occurrence rate or the mean sampling rate.

The theoretical Poisson distribution is linearly dependent on the Δt . The actual probability density function shown in Figure 3.11, using the LDV data, indicates well defined Poisson sampling distribution.

3.3.3 Assumption - aliasing

Although Poisson sampling is expected to be alias free, an additional check for aliasing was done. The procedure consists of computing the spectral estimate from the data taken at low and high mean sampling rates (or sampling frequency sf). If aliasing is present, a significant change in the power spectral density (at the higher frequency end) will be evident.

In order to get as high a sampling rate as possible a series of experimental measurements were performed. The highest sampling frequency achieved was $\cong 7$ kHz. The PSD was unchanged over a wide range of sampling frequencies. Figure 3.12 shows PSD's for two different sampling frequencies - sf . For the low $sf=100$

Hz (Figure 3.12a), the estimated PSD is a flat white noise spectrum, while the higher sf decays to white noise above 100 Hz or approximately one twentieth of the sf (Figure 3.12b). This implies that by changing the sampling frequency, some of the noise contamination is removed, but the frequency limits is still far below the expected Nyquist frequency.

The second attempt to correct for aliasing was made with measurements using additional seeding particles - TiO_2 (particle size $< 5 \mu\text{m}$). Seeding did increase the sampling rate (from about 2.5 kHz to 5.4 kHz) but the PSD plots remained the same.

3.3.4 Ambiguity noise and velocity biasing

Complete characterization of the frequency spectrum of the velocity fluctuations must be balanced by the size of measuring volume and the need to eliminate velocity bias error. The size of the measuring volume sets the limit of phase ambiguity, or Doppler ambiguity noise. Up to this point, it has been assumed that only one particle is present in the measuring volume. In fact, many particles are present and the signal collected by the photomultiplier is the sum of the light scattered by all particles in the measuring volume. The dominant frequency or instantaneous particle arrival time is determined by spatial averaging. In order to resolve high frequency fluctuations in the turbulence spectrum, it is necessary to use

a small measuring volume, so that small scale fluctuations are not attenuated by the spatial averaging. The LDV configuration used for this work has three different sizes of measuring volumes available (see Table 2.1, Chapter 2).

To estimate the frequency at which phase ambiguity becomes significant, consider the dimension of the measuring volume perpendicular to the fringes, and the wave number k_1 as defined by Hinze's (1975):

$$k_1 = \frac{2\pi f}{\bar{U}} = \frac{2\pi}{\lambda} \quad (3-25)$$

where \bar{U} is the measured mean velocity, f is the frequency and λ is the wavelength of the velocity fluctuation i.e. the dimension of measuring volume (all wavelengths smaller than this will be completely contained in the measuring volume). For this work, two different fringe spacings were used (track 1 and 3). For channel 1, λ is 280 μm and for channel 3, λ is 75 μm (see Table 2.1). Substituting the mean velocity \bar{U} equal to 0.3 m/s, limiting frequencies are 1.07 and 4 kHz. This implies that no useful information on the frequency spectrum is available about the turbulence beyond these points. According to the Nyquist criterion, this suggests sampling frequencies of 2.14 and 8 kHz. Measurements were performed using both channels, but no change was observed in the spectra - white noise dominates beyond

one twentieth of the sampling frequency, so that it was impossible to separate contamination due to the ambiguity noise from other sources of noise.

The presence of ambiguity noise and reproducibility of the experiments was checked with a comparison of the RMS velocity profiles at various average sampling frequencies. Figure 3.13 demonstrates the repeatability of the RMS velocity profile along the lower edge of the impeller blade (PBT impeller). Sampling frequencies tested range from 0.27 kHz to 5.2 kHz. Different sampling rates were achieved by changing the angle of the receiver. All other parameters (high voltage, rpm) were kept constant in order to exclude any other effect on measurements. This set of measurements also gives a check on the stability of measurements. From these experiments it can be concluded that Doppler ambiguity noise is not present.

The second limitation is velocity biasing. Assuming that seeding particles in the fluid are uniformly distributed, more high velocity particles will cross the measuring volume than low velocity particles so averaging will include a systematic bias towards the higher velocities in the flow. The easiest way to correct this systematic error is to sample at a rate much lower than the validated data rate.

A series of measurements were taken to determine the effect of possible velocity biasing. If velocity bias affects the flow, the measured mean and the RMS velocities will be reduced by reducing the sampling frequency, up to a certain point.

Beyond that point, further reduction in the sampling frequency will not change the measured velocity. The results are shown in figures 3.14 and 3.15. There is no observable effect of sampling frequency on measurement of either the mean or the RMS velocity.

3.3.5 Measurement noise

The LDV time series can also be contaminated by measurement noise, which may come from two different sources: system optics or electronic component such as signal processing unit. However, all signal processing units include analog filtering (band limited) in order to eliminate noise contamination. In fact, a very large number of factors influence the frequency estimation process and measurement noise could cover either broad band or band-limited frequencies in the resulting signal.

Our frequency spectrum shows substantial noise contamination on its higher frequency end, and several numerical techniques have been used in an attempt to extract the real signal: numerical filtering to filter contaminated frequency band; resampling initial data set to get new sequence (Biron et al 1995, Srikantaiah, 1987); and extrapolating the spectrum plot from the region where the signal dominates through the noise spectrum (Press et al., 1987). For this study, numerical filtering was used, while other two techniques were found to be inapplicable: resampling affects the high frequency fluctuations and no reliable spectral estimate can be made;

extrapolation cannot be used since the signal dominates over only a very short frequency range.

To check for measurement noise in the LDV data set, band-pass and low pass filters were used. Equation (3.18) was used, with the c's and d's given in Table 3.2. A band-pass filter for the frequency band 2 to 50 Hz was set since in that frequency band on spectral estimates, the signal dominates (lowest noise level and dominant frequency in the flow - BPF). The resulting power spectrum is shown in Figure 3.16.

A variable low-pass filter was used to find the real RMS velocity, and then the RMS vs. cutoff frequency was plotted on Figure 3.17. A linear relation which should be obtained at higher frequencies may be extrapolated back to zero frequency to give the real root mean square (RMS) velocity and cut-off frequency for noise. A corresponding cut-off frequency was found to be 100 Hz. Figure 3.18 shows the result of a 100 Hz cut-off filter. Since the spectrum in Figures 3.18 doesn't exhibit the expected higher frequency slope, it can be concluded that the spectral estimate is contaminated with white noise, which has a flat (constant) power spectrum over the entire frequency range (theoretically from $-\infty$ to $+\infty$ Hz), rather than band width limited noise.

3.3.6 Spectral estimate from the RSA processor

All previously reported sources of error in LDV measurements have been examined, and shown to have little or no effect on the final results, so a different signal processing unit - the RSA was optimized and used for a set of measurements.

The RSA signal processor provides on line data analysis of the autocorrelation and spectral estimate. It implements the binned autocorrelation technique. The resulting spectrum is shown on Figure 3.19. The new processor, the RSA, gives the expected spectral estimate up to no more than one-tenth of the mean sampling frequency. This points to the signal processing unit as a source of experimental error so that further modifications toward extracting Doppler frequencies from the turbulent signal should be directed towards the signal processor, not the experimental methods or data analysis technique.

3.4 Summary

From frequency analysis it can be concluded that the modification of time centering of the Doppler burst results (applied in the RSA) is more accurate measurements; while the old signal processing unit (the DSA) has a predetermined number of samples per each burst so that the "gate time" is fixed and cannot be adjusted to the different lengths of the Doppler burst. The preset (discussed in

Chapter 2) mixer (oscillator) frequency of 40 MHz is mixed with a Doppler burst frequency of 0.2 MHz. Less than 0.1% random deviation in mixer frequency may result in an erroneous velocity record of up to $\pm 20\%$. This is not a problem for measuring the mean and the RMS velocities, since through averaging random errors are canceled out. When the velocity vs. time record is used, however, this results in errors in the frequency spectrum results.

Table 3.1: Program and subroutine summary (binned-autocorrelation code)

Subroutine	Function
Main	- read data as time series - mean center - calculate autocorrelation (A\C) in time domain - direct calculation (A\C,PSD)
FOUR1	- FFT transform and inverse transform - apply Danielson - Lanczos lemma
REALFT	- calculate FFT for the real set of data
COSFT	- calculate cosine transform for the real set of data
FILTER	-calculate band-pass or low-pass filter

Table 3.2: Filter coefficients used for numerical filtering

filter coefficients	band-pass filter	low-pass filter
c_0	$-\frac{b}{(1+a)(1+b)}$	$-\frac{a}{(1+a)}$
c_1	0	$\frac{a}{(1+a)}$
c_2	$\frac{b}{(1+a)(1+b)}$	0
d_1	$\frac{(1+a)(1-b)+(1-a)(1+b)}{(1+a)(1+b)}$	$\frac{(1-a)}{(1+a)}$
d_2	$-\frac{(1-a)(1-b)}{(1+a)(1+b)}$	0

a - lower cutoff frequency end, Hz

b - upper cutoff frequency end, Hz

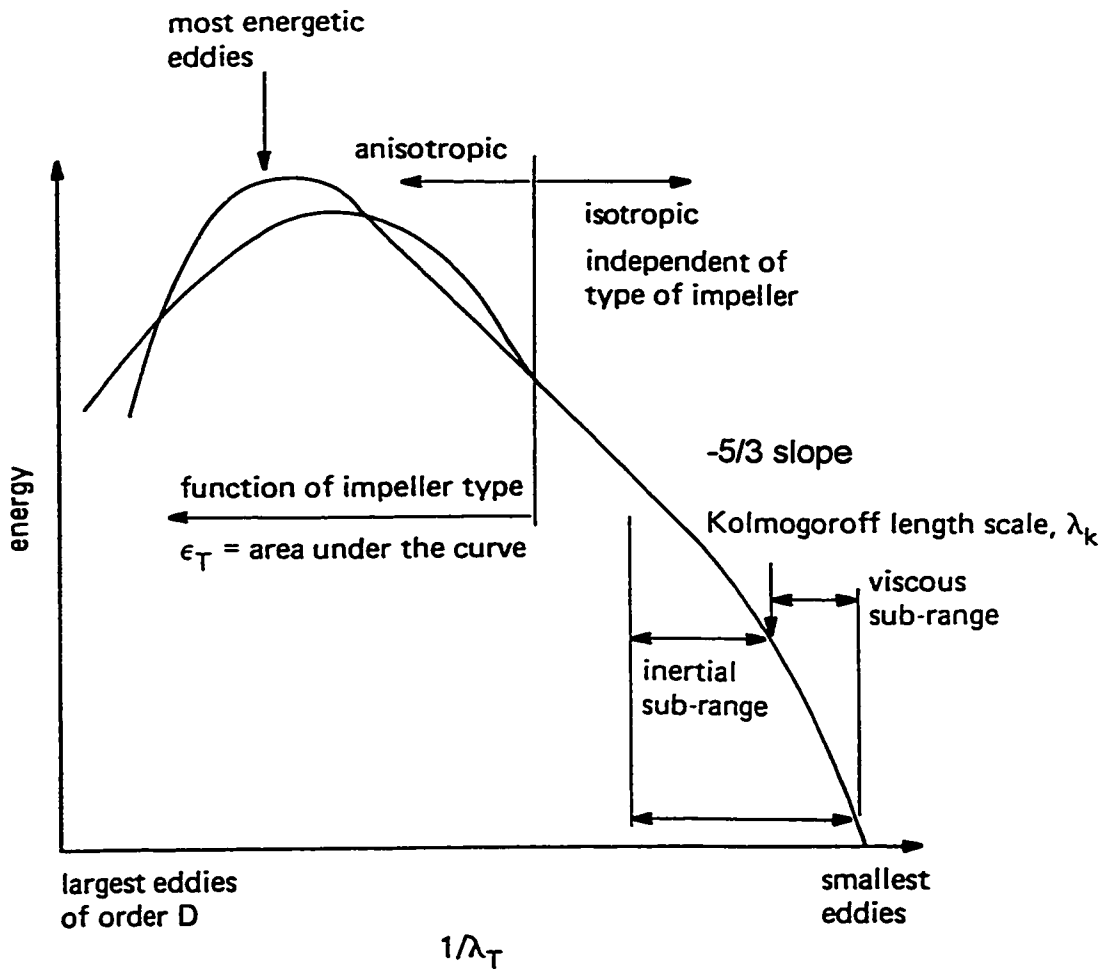


Figure 3.1: Form of the one-dimensional energy spectrum in the various wavenumber ranges (from Harnby, Edwards and Nienow, 1985, pg. 9).

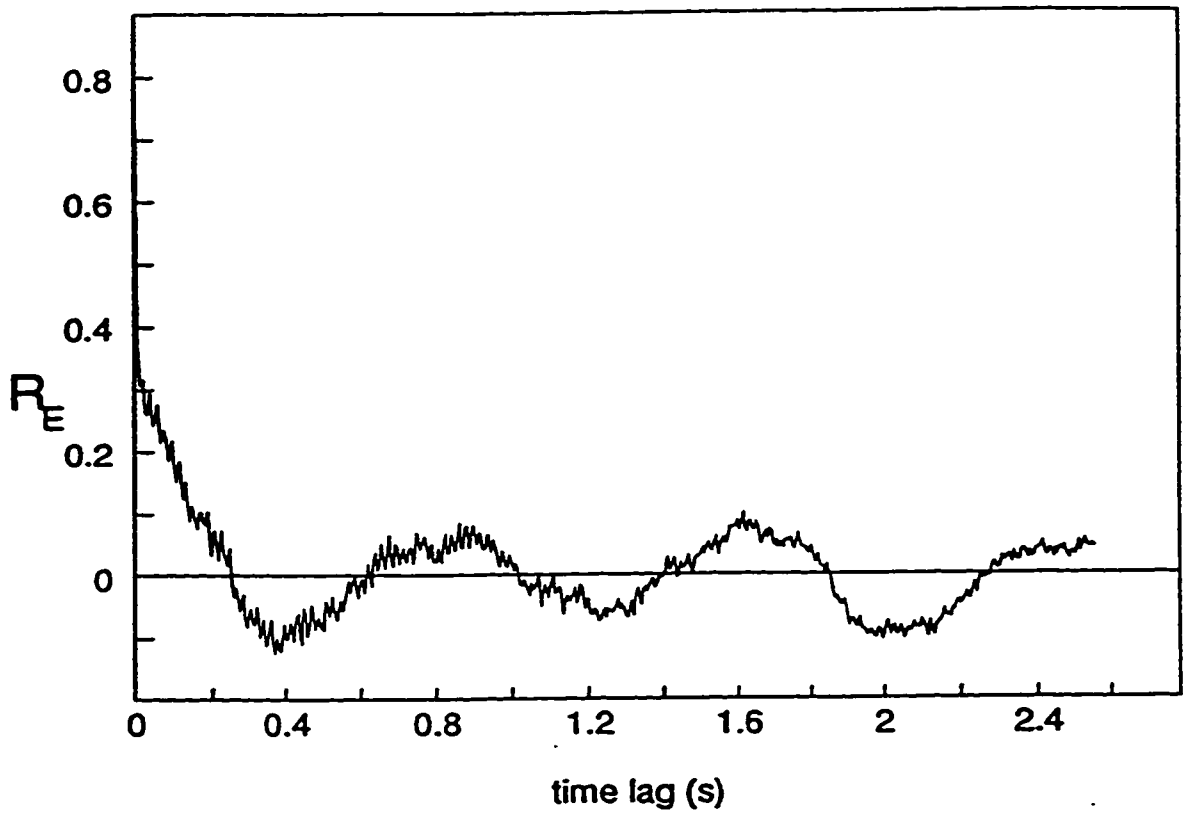
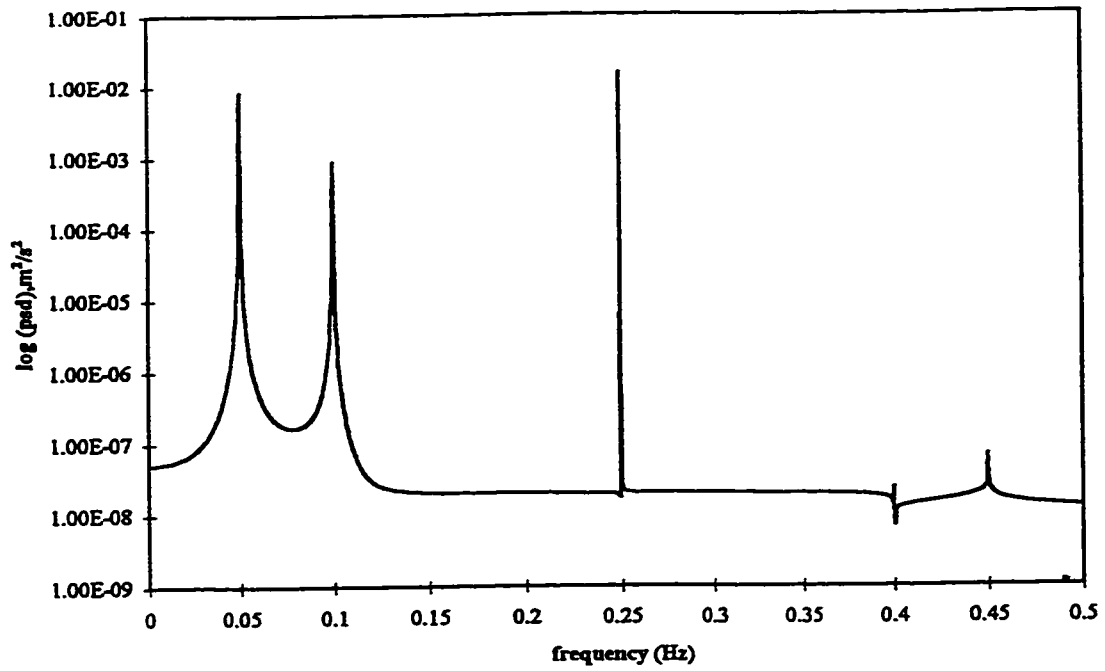
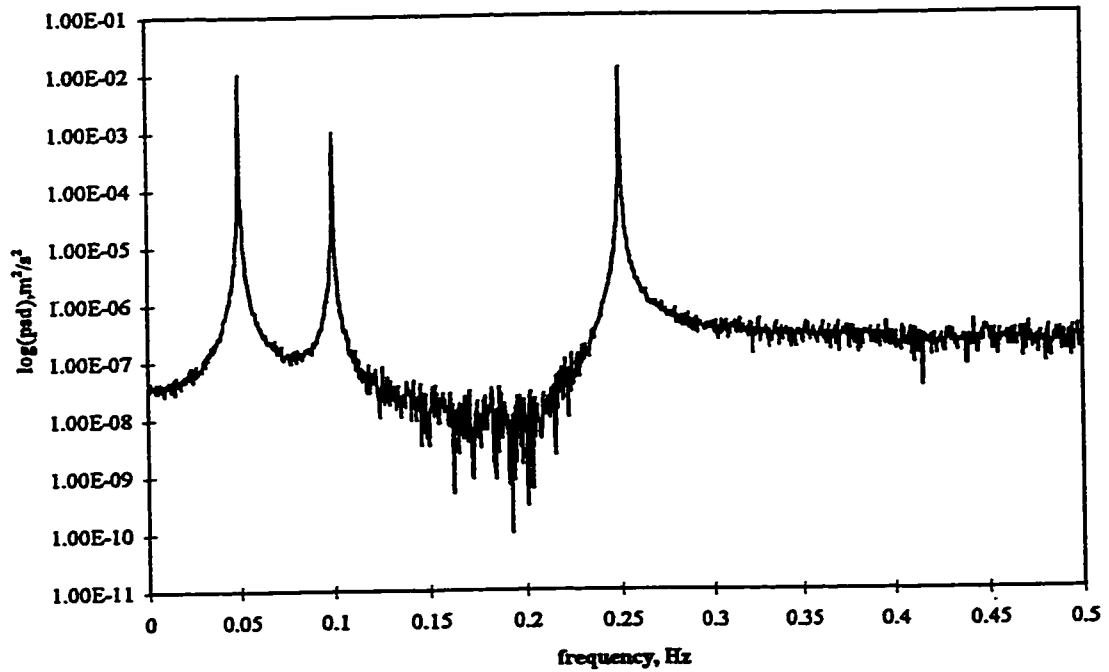


Figure 3.2: Typical autocorrelation coefficient at the impeller tip (from Kresta, 1991.).

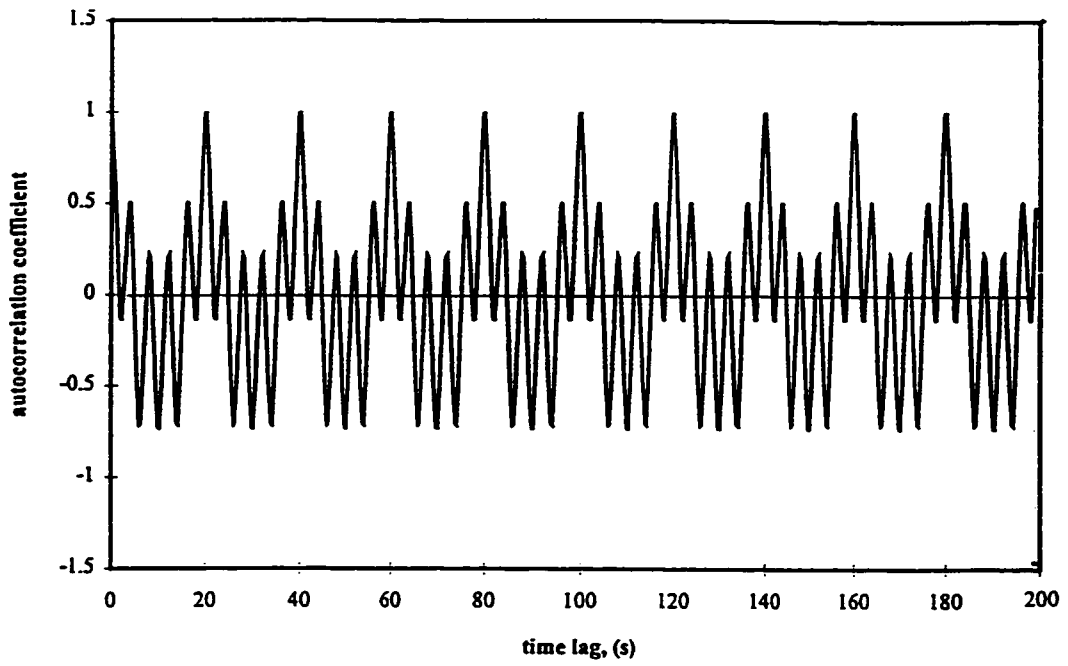


a) evenly spaced

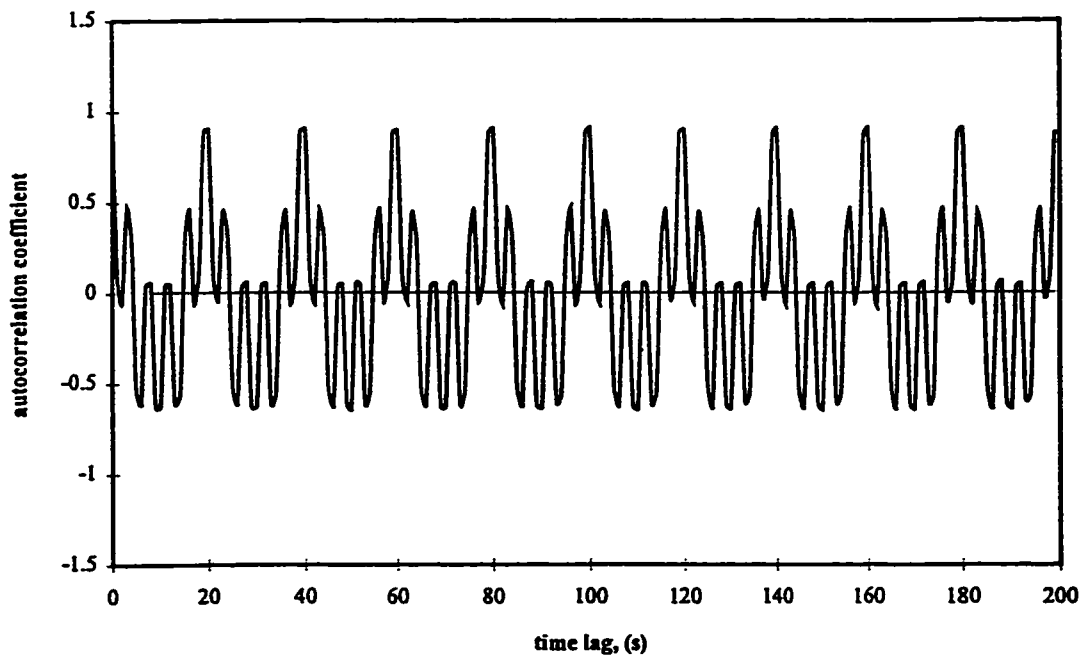


b) randomly spaced

Figure 3.3: Test data: three sine waves (combination of three sine waves at 0.01, 0.1, and 0.25 Hz).

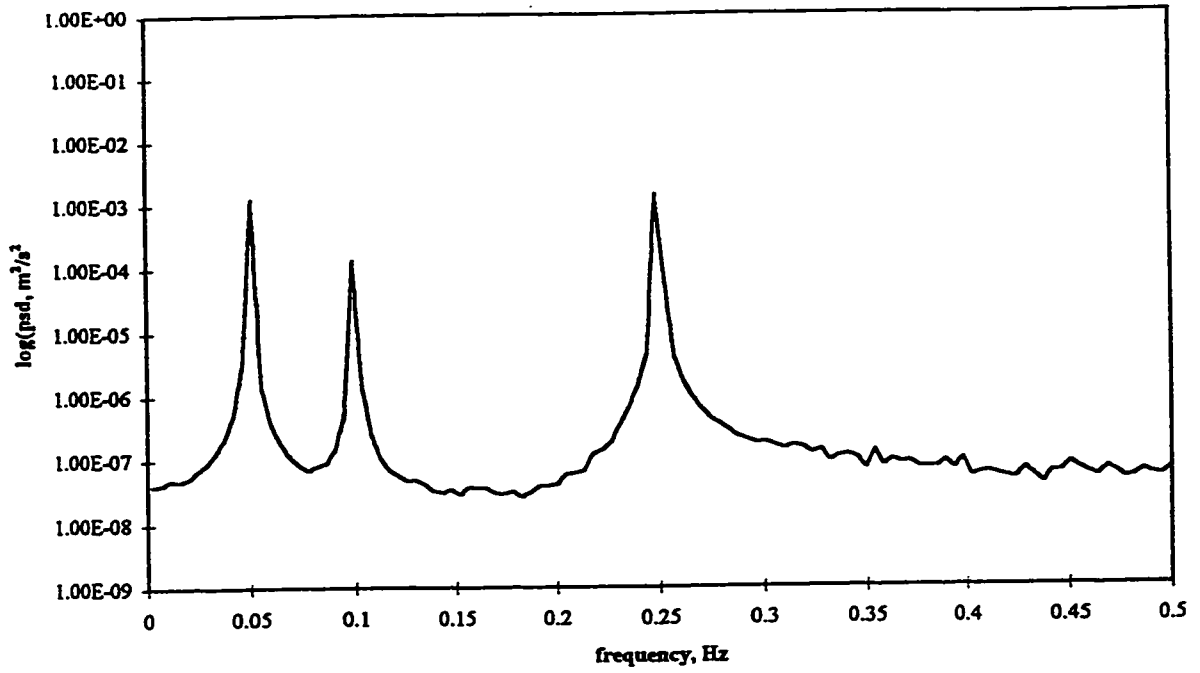


a) evenly spaced



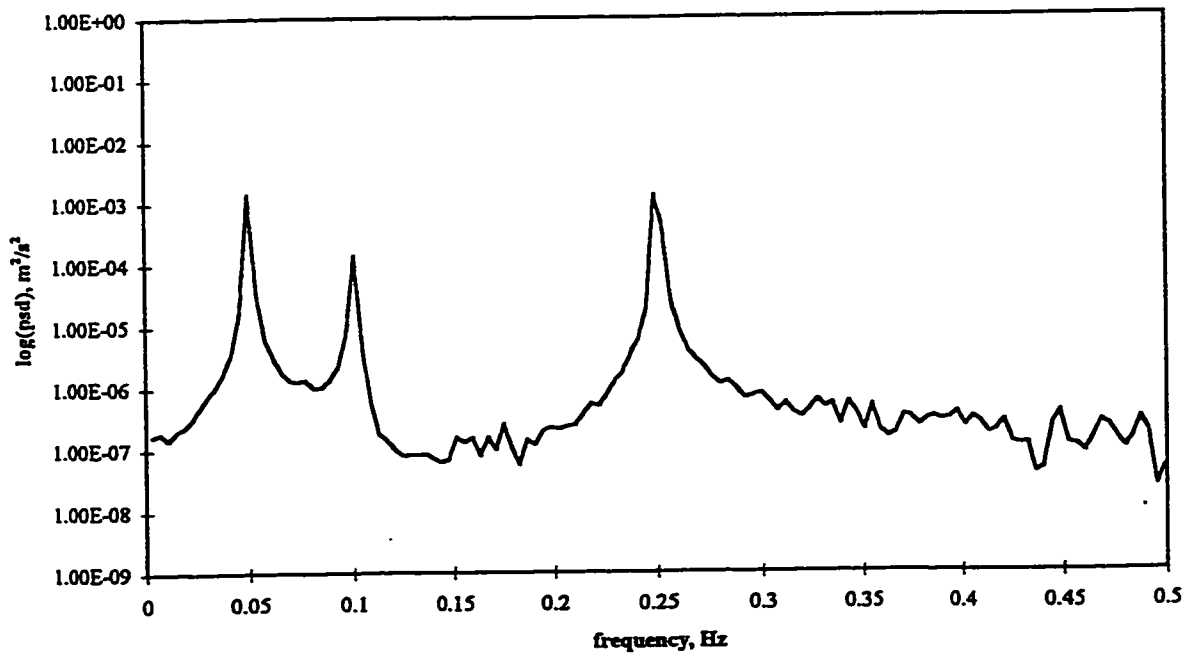
b) randomly spaced

Figure 3.4: Autocorrelation coefficient calculated from the binned technique.

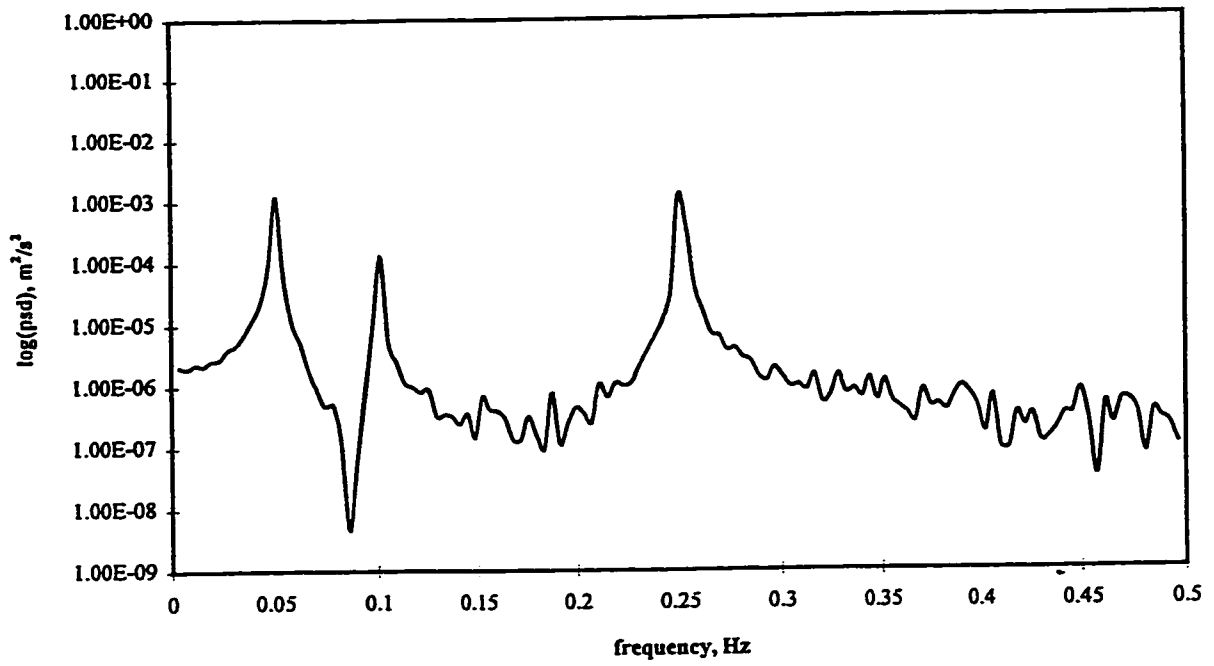


a) $\tau = 0.5$ s

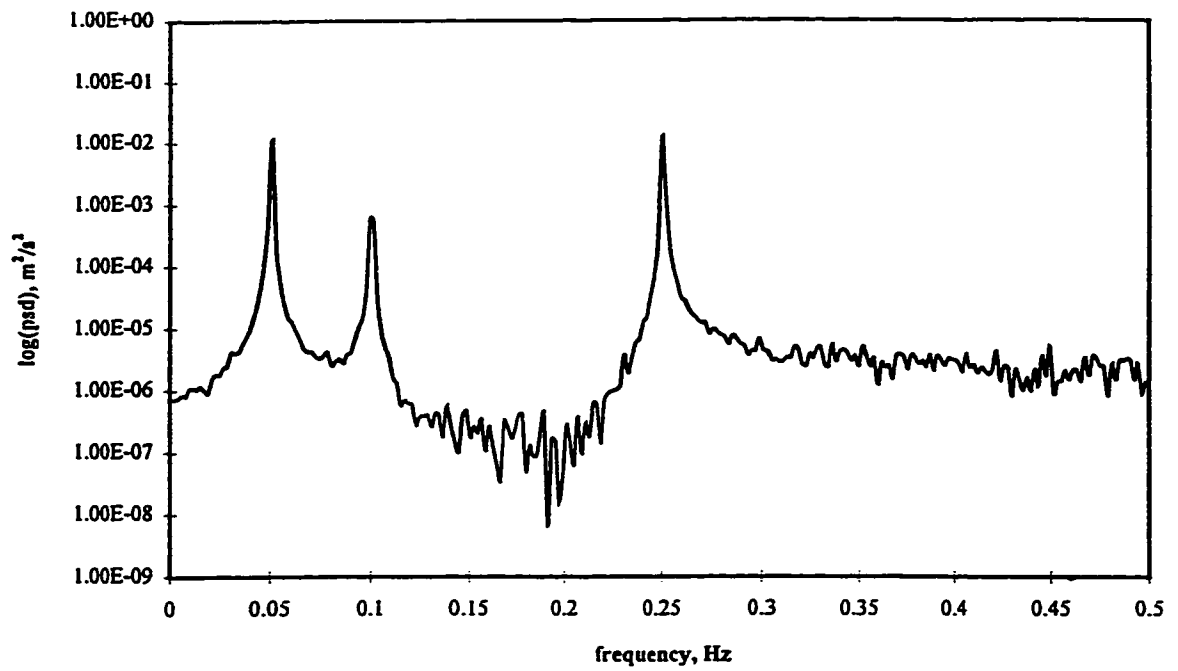
Figure 3.5: Spectral estimates for different slot size τ .



b) $\tau = 0.125$ s

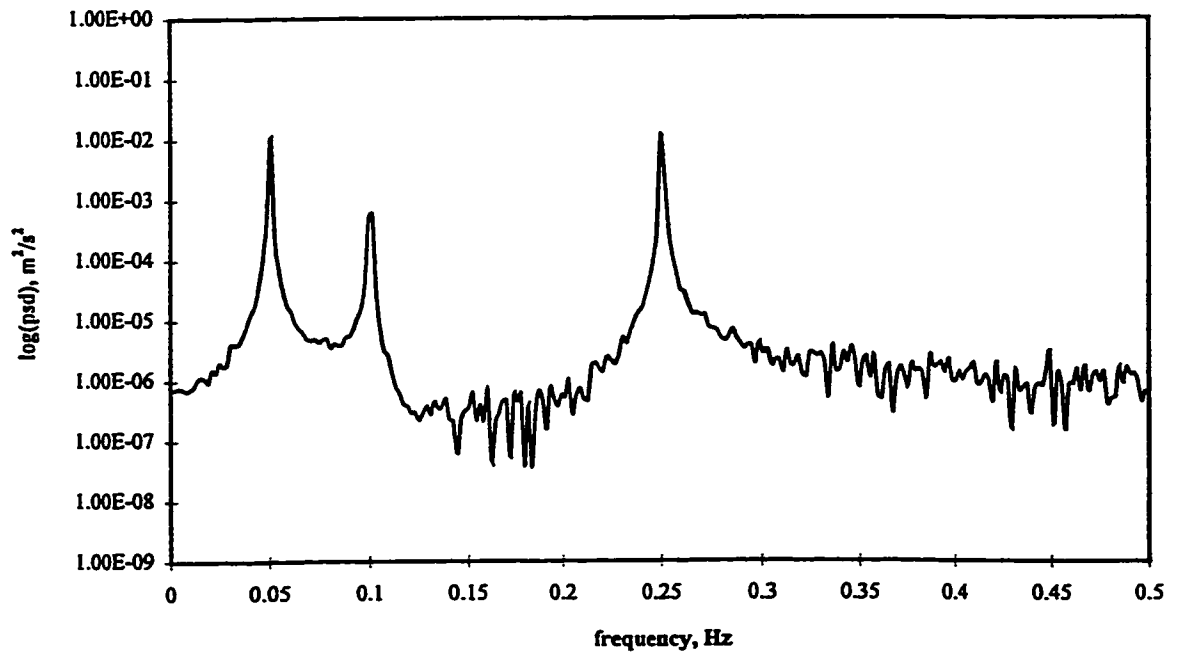


c) $\tau=0.05$ s

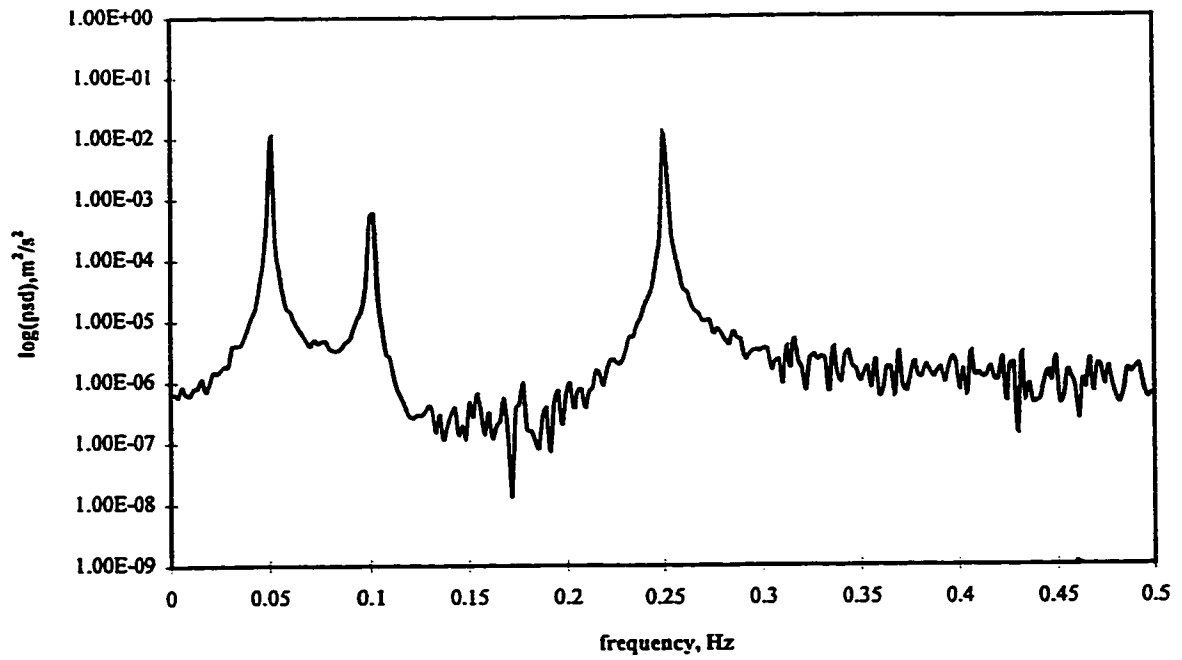


a) 1% noise

Figure 3.6: Spectral estimates with superimposed noise over initial data set.



b) 5% noise



c) 10% noise

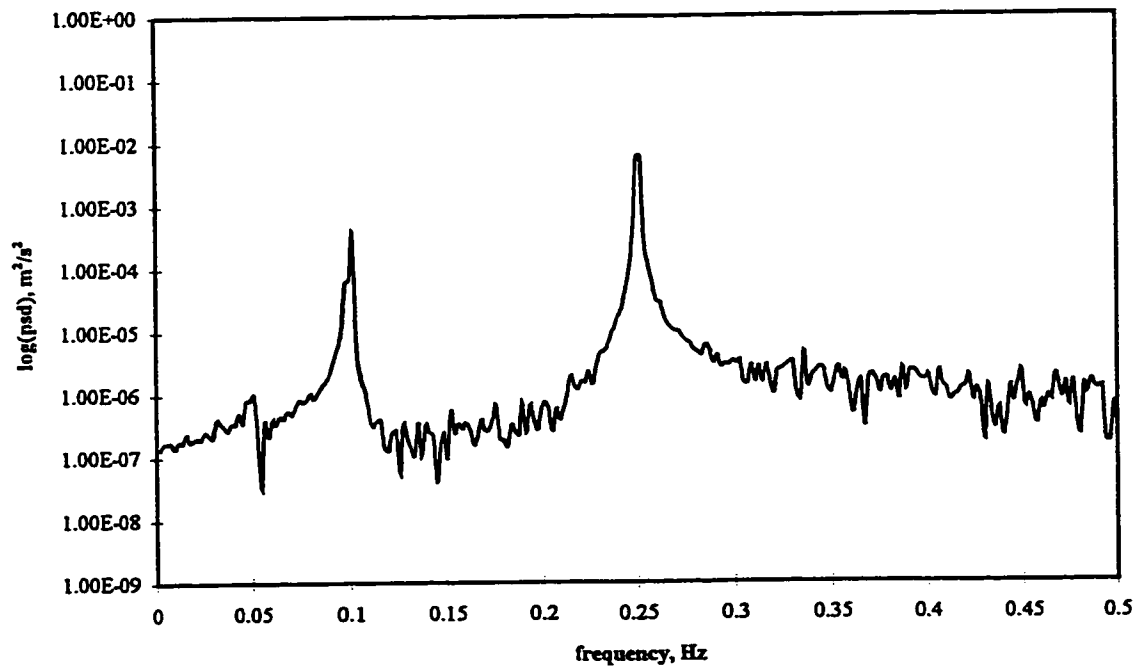


Figure 3.7: PSD with notch filter applied at 0.05 Hz.

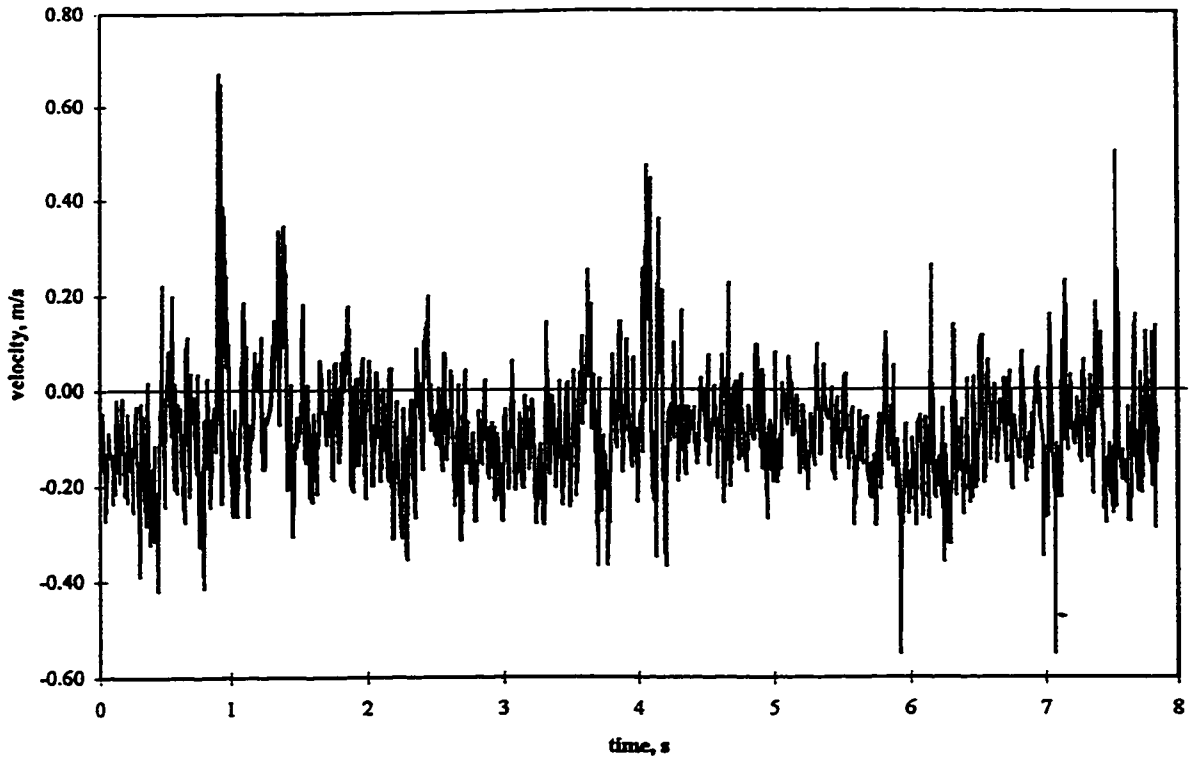


Figure 3.8: Time series data of the instantaneous axial velocity signal (pitched blade turbine-PBT, $sf=498$ Hz, $rpm=300$).

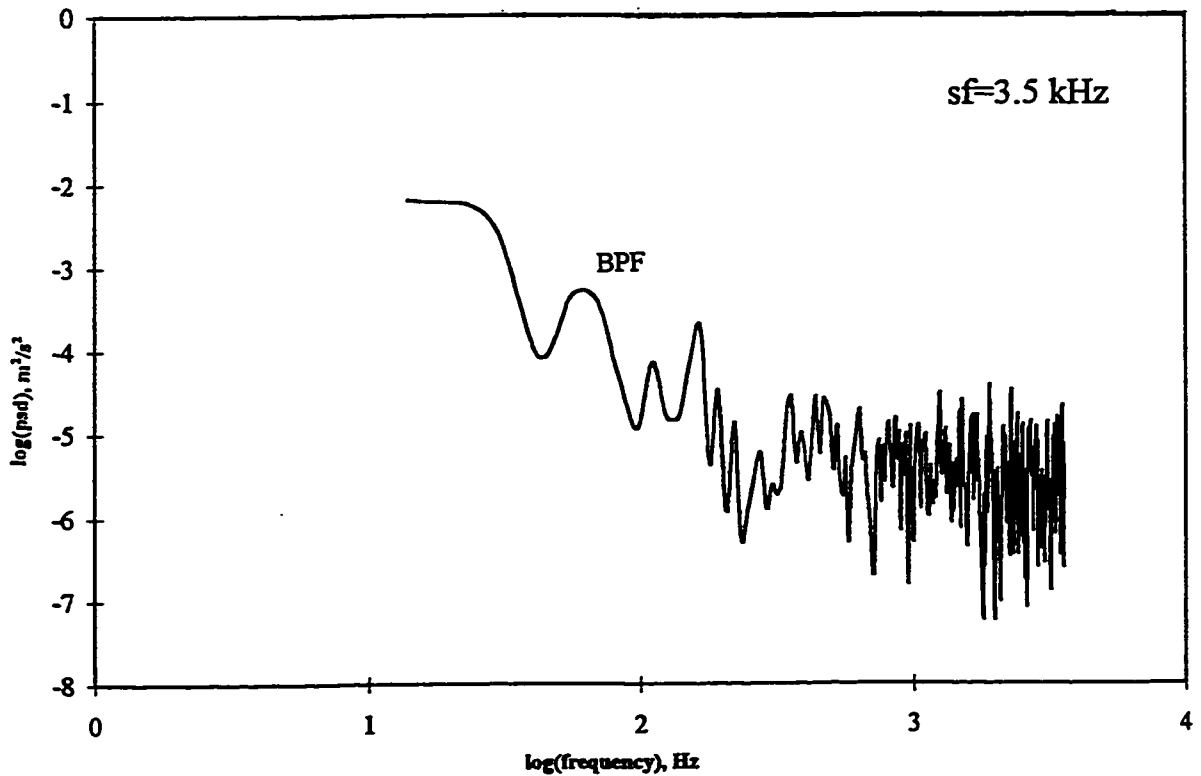
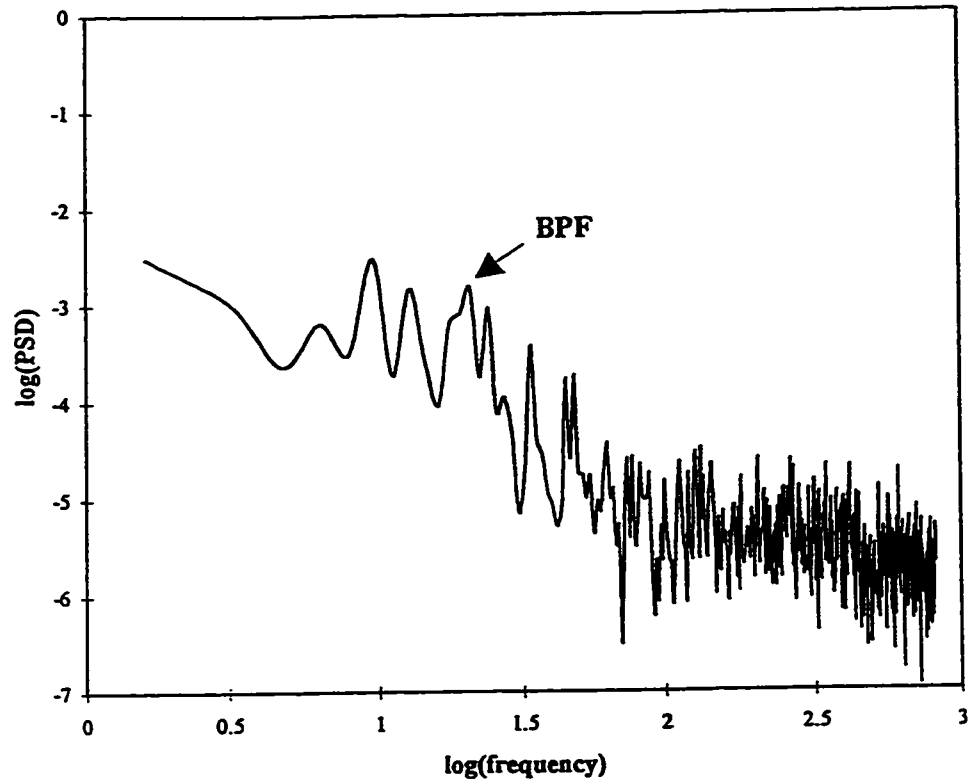
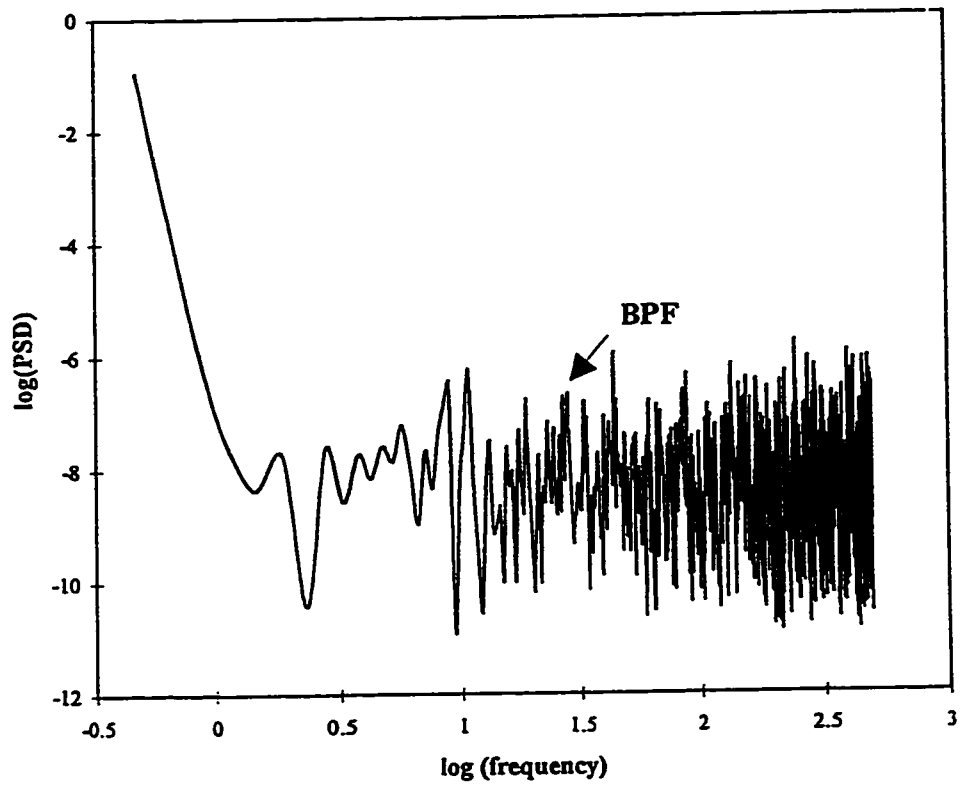


Figure 3.9: A typical frequency spectrum along the lower edge of the impeller (PBT).

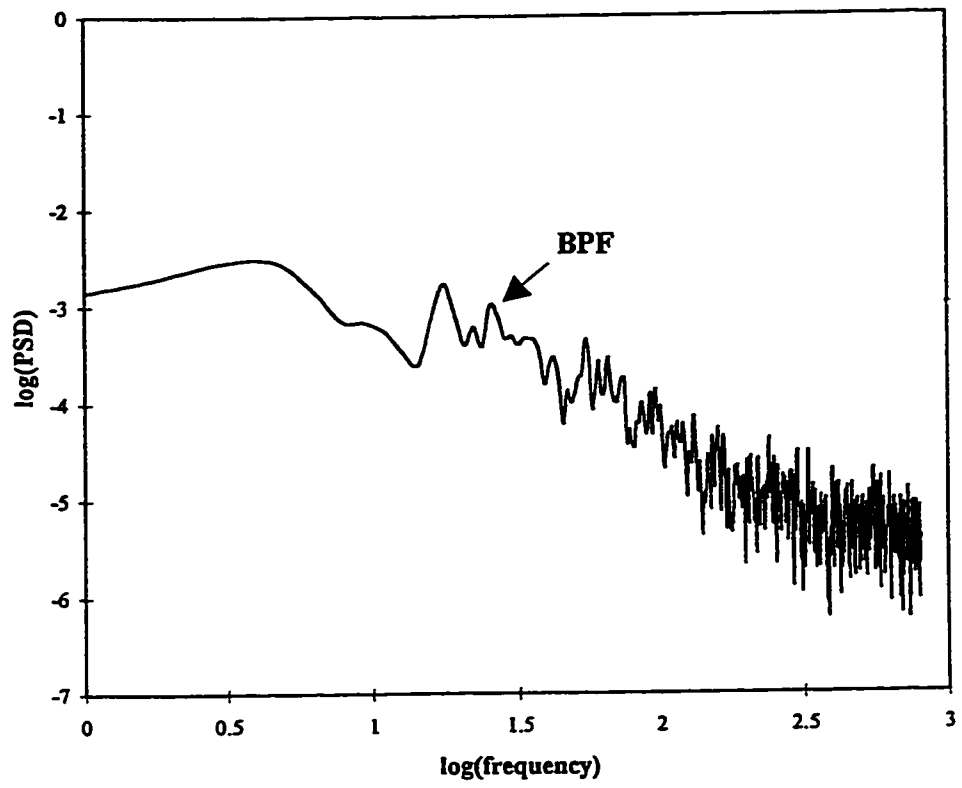


a) autocorrelation technique

Figure 3.10: Frequency spectrum, from axial velocity component; sampling frequency of 1612 Hz, 300 rpm, PBT.



b) Discrete Fourier Transform



c) Fast Fourier Transform

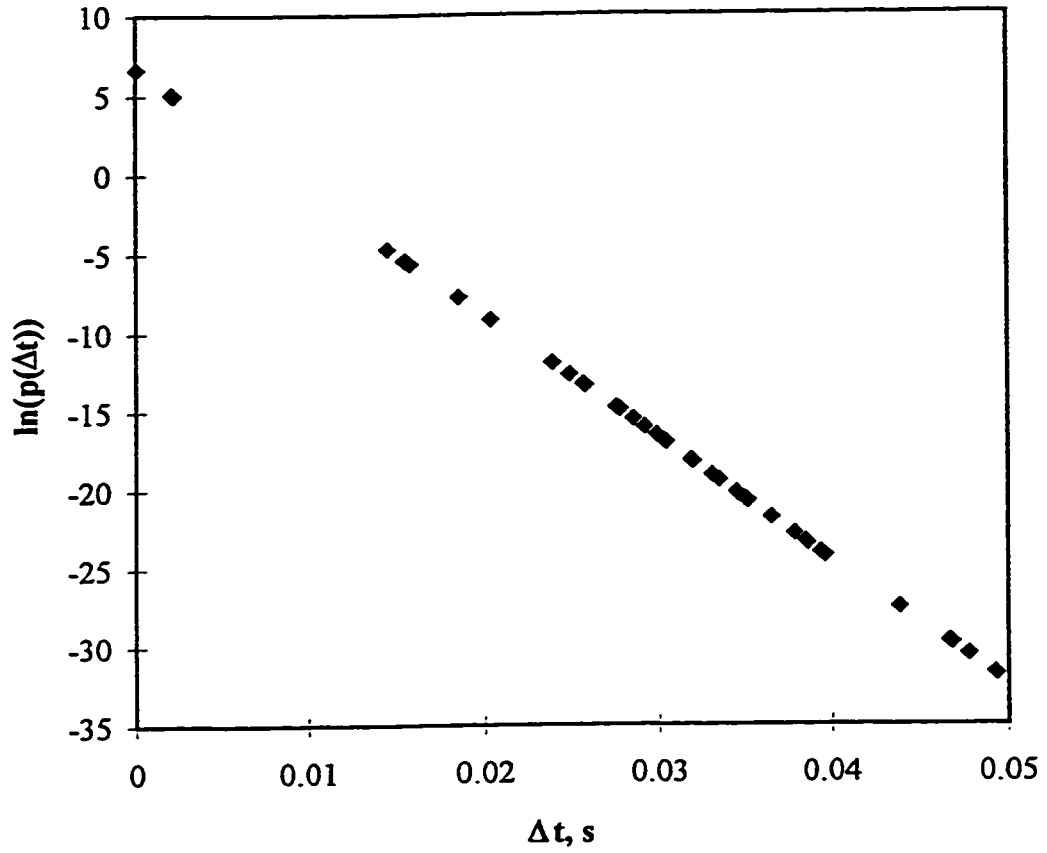


Figure 3.11: Probability density function for the particle interarrival time, and the average sampling frequency of 778.68 Hz.

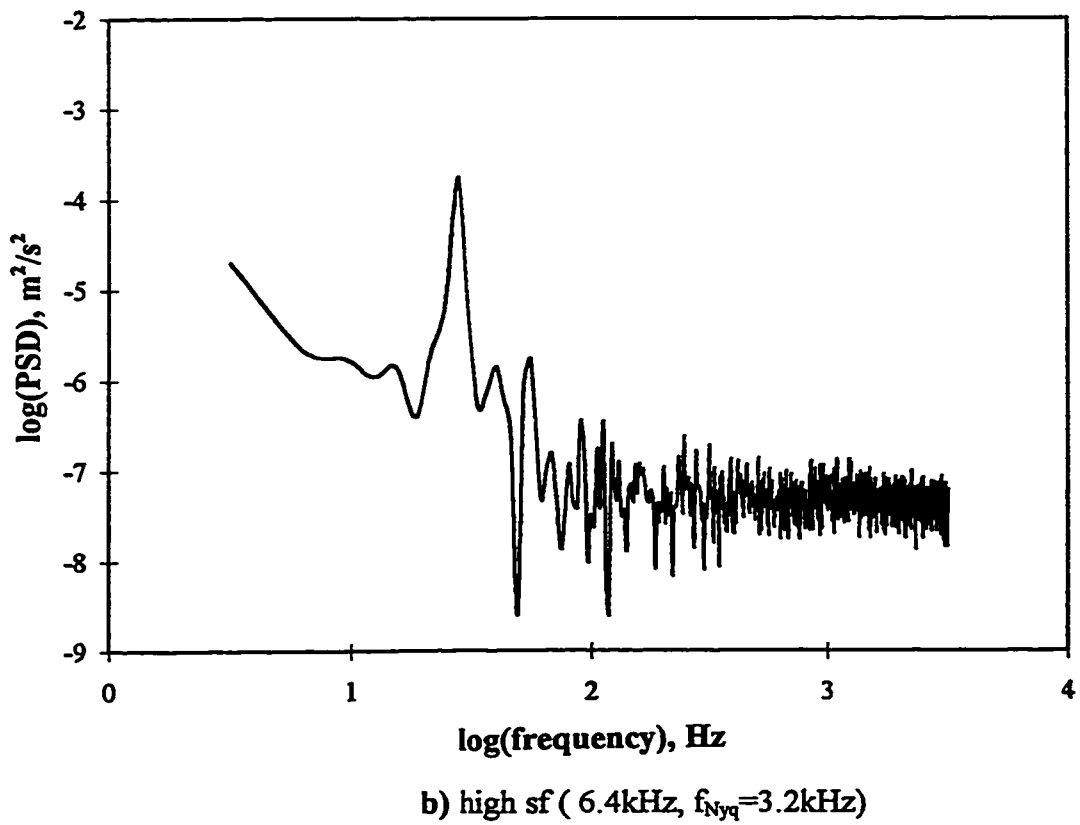
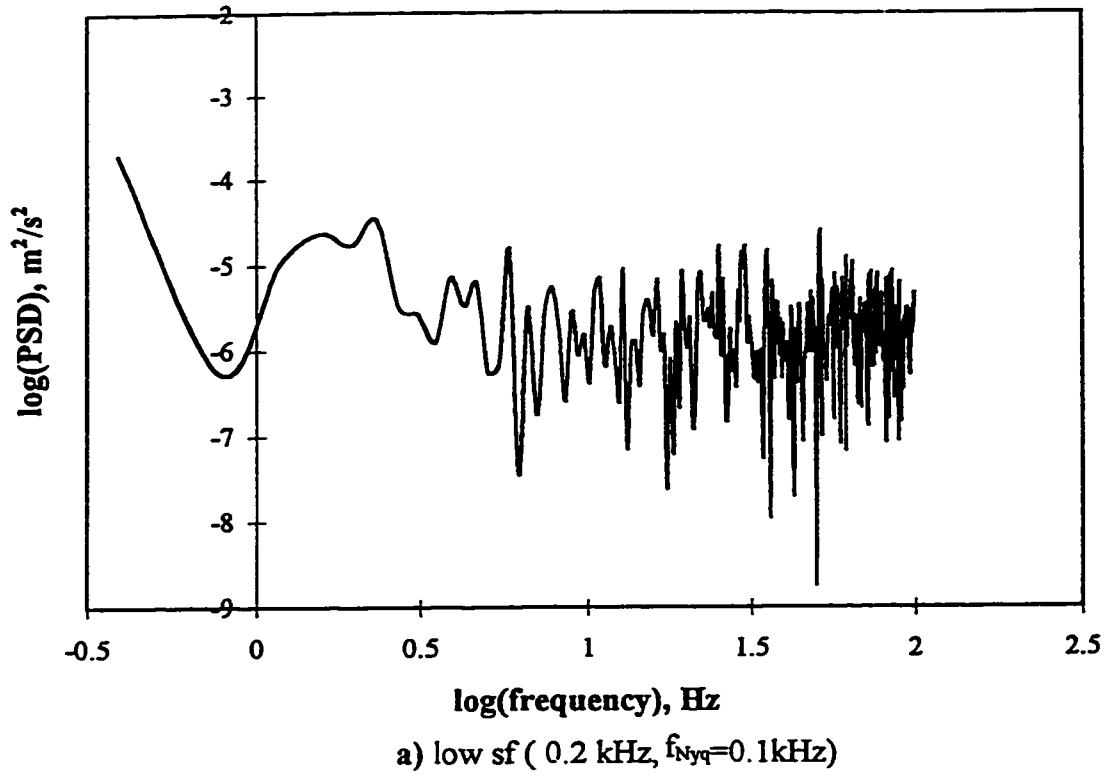


Figure 3.12: PSD for two different sampling frequencies.

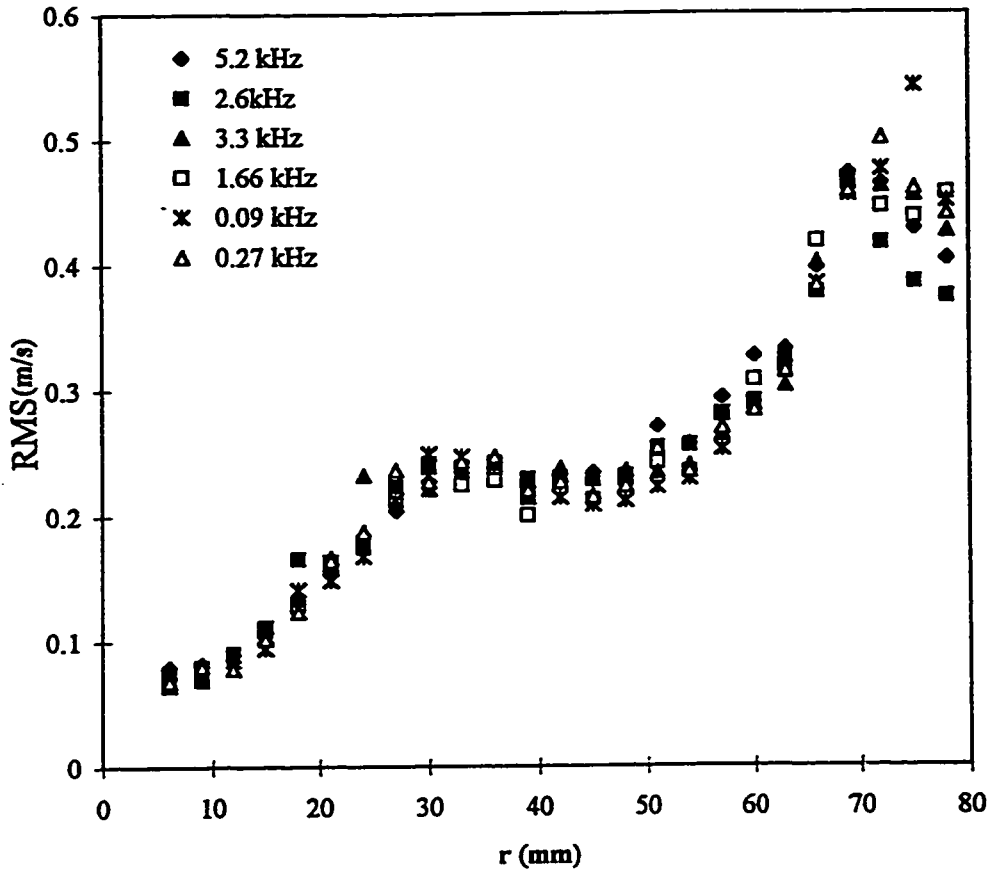


Figure 3.13: The RMS axial velocity profile across the lower edge of the PBT for various sampling frequencies.

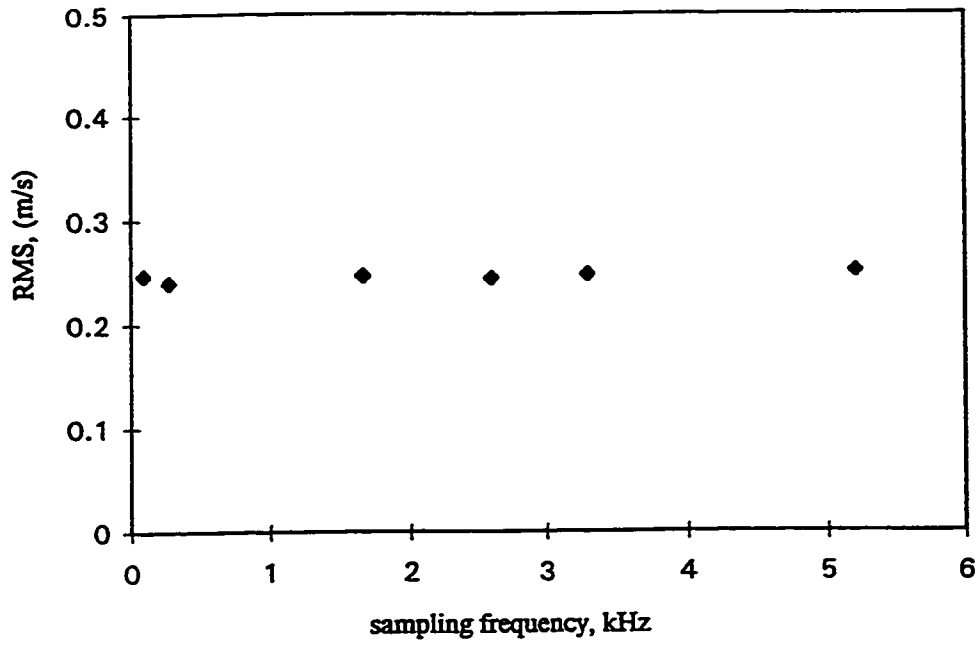


Figure 3.14: Effect of sampling frequency on measured RMS velocity.

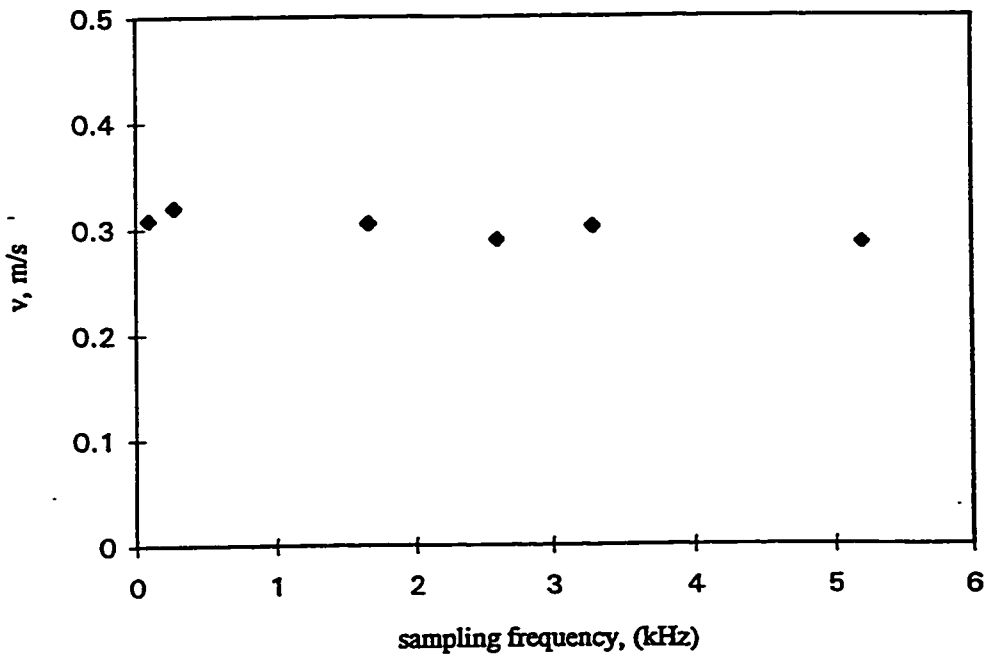


Figure 3.15: Effect of sampling frequency on measured mean velocity.

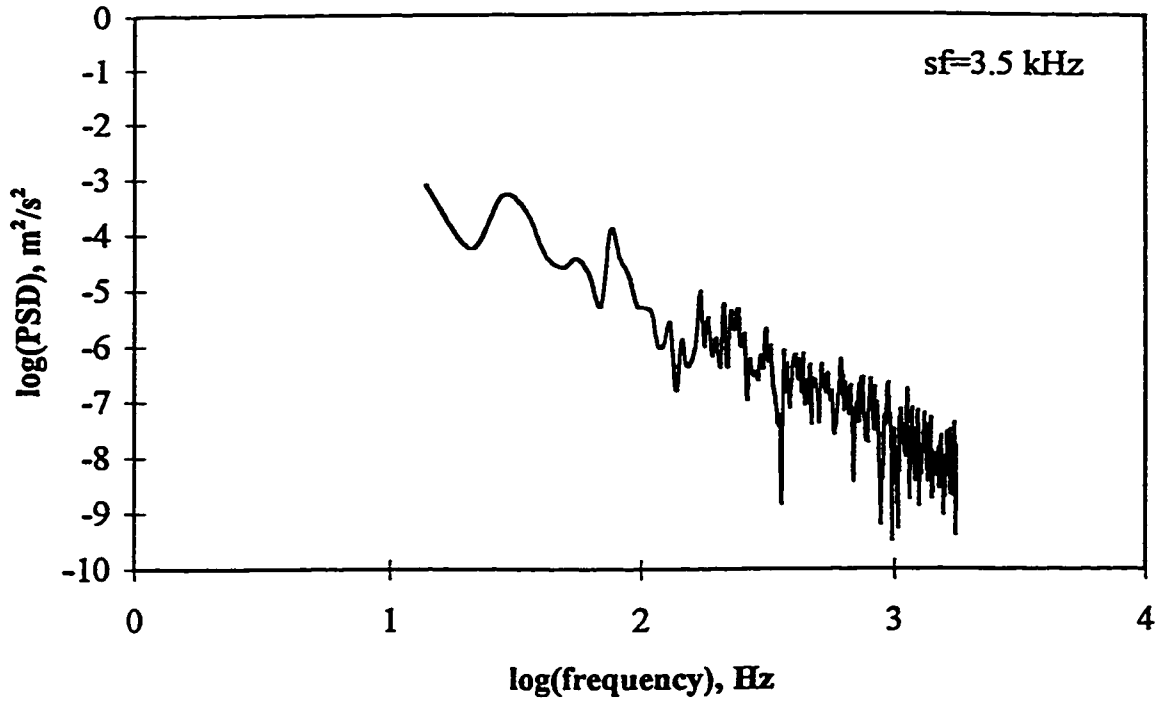


Figure 3.16: Filtered PSD at the frequency band between 2 and 50 Hz.

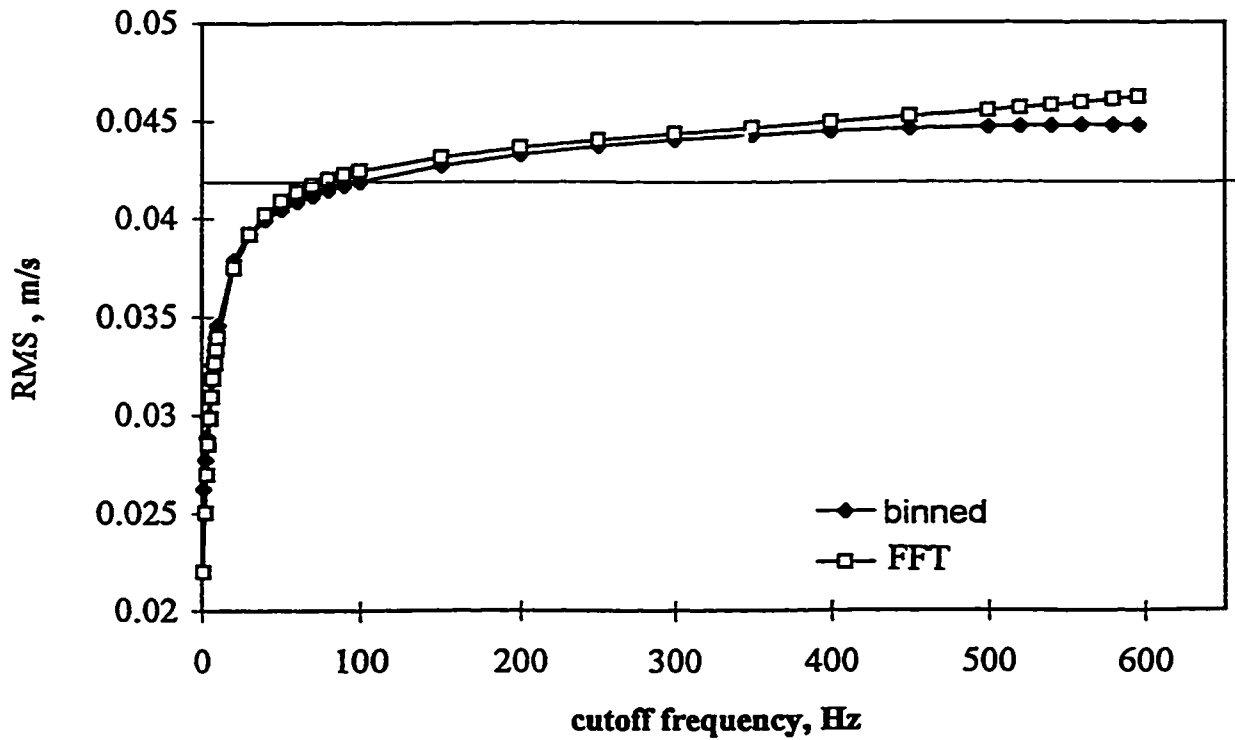


Figure 3.17: RMS vs. Cut-off frequency of low-pass filter (for LDV data).

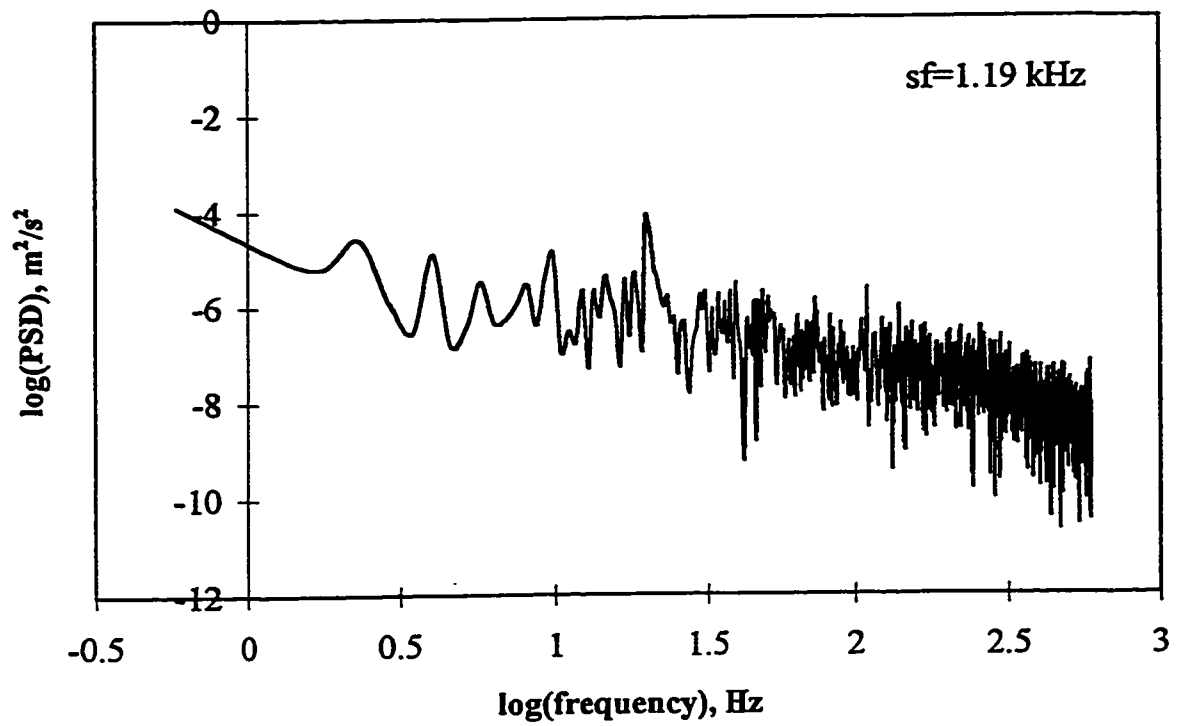


Figure 3.18: Low-pass filter (cut-off at 100 Hz).

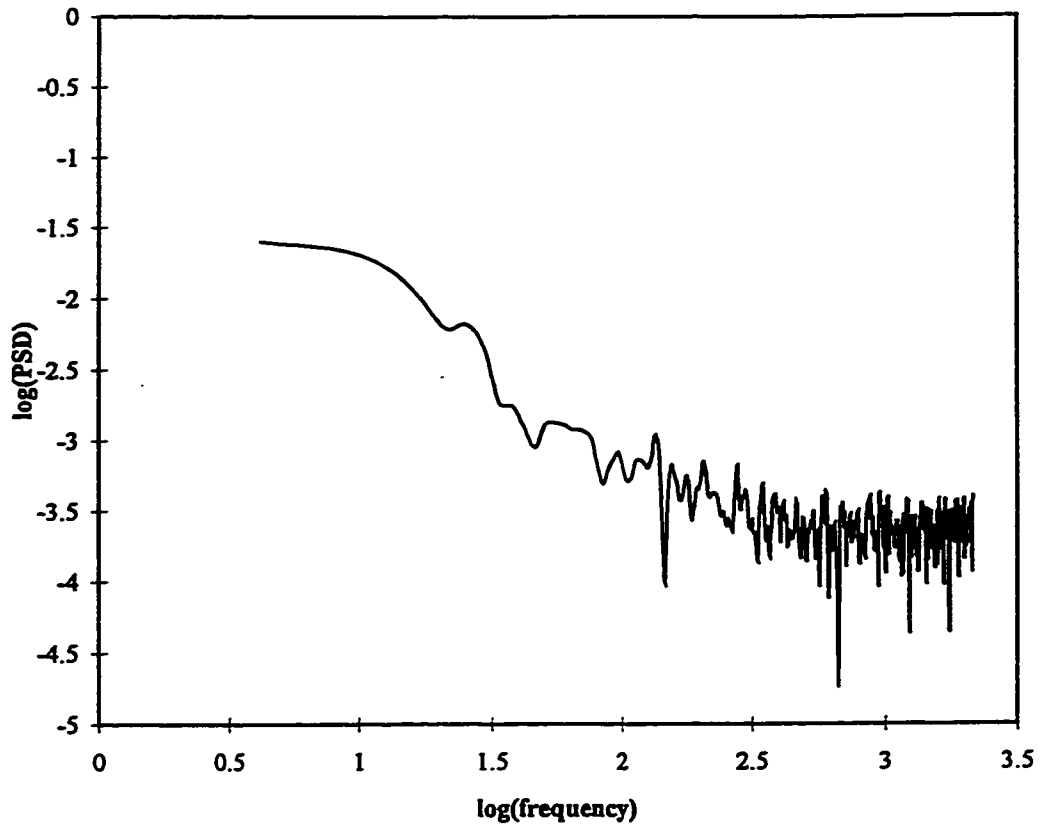


Figure 3.19: Power spectrum, averaged over 10 blocks, autocorrelation technique; axial velocity component; sampling frequency 4305 Hz, 300 rpm, PBT.

References

Bell, W.A., 1981, Spectral Analysis Algorithms for the Laser Velocimeter: A Comparative Study, AIAA, *14th Fluid and Plasma Dynamics Conference*, Paolo Alto, Calif., June 23-25.

Bell, W.A., 1986, Spectral Analysis of Laser Velocimeter Data with the slotted Correlation Method, May 12-14, AIAA/ASME *4th Fluid Mechanics, Plasma Dynamics and Laser Conference*, Atlanta, GA.

Biron, P., G.A. Roy, and L.J. Best, 1995, A Scheme for Resampling, Filtering, and Subsampling Unevenly Spaced Laser Doppler Anemometer Data, *Math. Geology*, **27**, No. 6, 731-748.

Bradshaw, P., 1978, *Turbulence*, Second Edition, Springer-Verlag, New York.

Etter, D.M., 1987, *Structured FORTRAN 77 for Engineers and Scientists*, The Benjamin/Cummings Publishing Company Inc., Menlo Park, California.

Gaster, M., and J. B. Roberts, 1975, Spectral Analysis of Randomly Sampled Signals, *J. Inst. Maths. Applics.*, **15**, 195-216.

George, W.K., 1974, The measurement of turbulence intensities using real-time laser Doppler velocimetry, *J.Fluid Mech.*, vol.**66**, part1, 11-16.

Gunkel, A.A. and M.E. Weber, 1975, Flow Phenomena in Stirred tanks: Part I. The impeller Stream. *AIChEJ.*, **21**, 931-949.

Harnby, N., M.F. Edwards, and A.W. Nienow, *Mixing in the process industries*, First ed., Butterworth, 1985.

Hinze, J. O., 1975, *Turbulence*, 2nd edition, Mc Graw Hill, Toronto.

Kim, W.L. and F.S. Manning, 1964, Turbulence Energy and Intensity Spectra in a Baffled Stirred Vessel. *AIChEJ.*, **10**, 747-752.

Konig, M., 1986, Experimental investigation of the angular dependence of laser light scattered in laser-Doppler anemometry, *Experiments in Fluids*, vol.4, 302-308.

Kresta, S.M., 1991, *Characterization and Prediction of the Turbulent Flow in Stirred Tanks*, PhD Thesis, McMaster University, Hamilton, Canada.

Kresta, S.M. and P.E. Wood, 1993a, The Flow Field Produced by a Pitched Blade Turbine: Characterization of the Turbulence and Estimation of the Dissipation Rate, *Chem. Eng. Sci.*, **48**, 1761-1774.

Mujumdar, A. S., B. Huang, D. Wolf, E. M. Weber, and M. J. Douglas, 1970, *Can. J. Chem. Eng.*, **48**, 475-483.

Press, W.H., B.P. Flannery, S.A. Teukolsky, and W.T. Vetterling, 1989, *Numerical Recipes, The Art of Scientific Computing*, Cambridge University Press, New York.

Rao, M.A. and R.S. Brodkey, 1972, Continuous flow stirred tank turbulence parameters in the impeller stream, *Chem. Eng. Sci.*, **27**, 137-156.

Roberts, B.J., and D. B. S. Ajmani, 1986, Spectral Analysis of randomly Sampled Signals Using a Correlation-Based Slotting technique, *IEEE Preceedings*, 133, Pt. F., No 2.

Shapiro, H.S., and R.A. Silverman, 1960, Alias Free Sampling of Random Noise, *J. SIAM*, 21, 714-719.

Sommerfield M., 1992, Method for Determing The Measurement Volume Size Particle Mass Flux Using Phase-Doppler Anemometry, *Experiments in Fluids*, 13, 393-404.

Sree Dave, 1994, Effect of Non-Poisson Samples on Turbulence Spectra from Laser Velocimetry, *AIAA Journal*, 32, No. 12: Technical Notes.

Srikantaiah, D.V., 1982, *An Anytical and Experimental Study of Spectral Analysis Techniques for Turbulence Data Obtained Using Laser Velocimetry*, Ph.D. Thesis, Mechanical and Nuclear Engineering Department, Mississippi State University.

Srikantaiah, D.V., and H.W. Coleman, 1985, Turbulence Spectra from Individual Realization Velocimetry Data, *Experiments in Fluids*, 3, 35-44.

Tropea, C., 1987, Turbulence Induced Spectral Bias in Laser Anemometry, 1987, *AIAA*, 25, 306-309.

Tatterson, B.G., 1991, *Fluid Mixing and Gas Dispersion in Agitated Tanks*, McGraw-Hill Inc., New York.

Tennekes, H., and J. L. Lumley, 1972, *A First Course in Turbulence*, MIT Press, Cambridge, Mass.

Wernersson, E.S., 1997, *Some Fluid Characteristics in the Scale-up of Rushton Turbine-agitated Tanks*, Ph.D. Thesis, Lund University, Sweden.

Zhou, G., 1996, *Characteristics of Turbulence Energy Dissipation and Liquid-Liquid Dispersions in An Agitated Tank*, Ph.D. Thesis, University of Alberta, Canada.

Chapter 4. Macroinstabilities of flow in stirred tank

4.1 Introduction

In this chapter, the stability of the flow pattern for four commonly used impellers (PBT, RT, HE3 and A310) is investigated. The experiments were performed using the LDV. Measurements were undertaken at three positions within the tank: impeller stream, top and bottom corner, based on previous work on flow stability in a stirred vessel by Chapple and Kresta (1994). For each impeller eight geometric configurations were used in order to investigate a) the impact of the tank and impeller geometry on flow stability; and b) the contribution of low frequencies to the measured RMS velocity component - v_{raw} . Large instabilities in the flow can lead to large cyclic forces on tank internals, which may cause mechanical failure. It is desirable to avoid those configurations which lead to the largest instabilities. The portion of v_{raw} which is due to turbulence (or random fluctuations) is also determined from this data. This allows estimation of errors in the calculation of the turbulence energy dissipation ϵ ($\epsilon=v^3/L$), where only the measured or total RMS - v_{raw} velocity is currently being used.

Data analysis was performed to find the statistical significance of the geometric effects - a factorial design followed by data windowing to isolate the low

frequency component of the signal. Data resampling was applied in order to eliminate the high frequency fluctuations and to achieve approximately equally spaced data. Then data windowing, or averaging over an appropriate time window, was used to determine the contribution of the low frequency fluctuations to the total RMS velocity (v_{raw}). This was quantified in three ways: as the low frequency intensity or ratio of v_{LF}/v_{tot} ; as the magnitude of v_{LF} or ratio of v_{LF} to V_{tip} ($V_{tip}=\pi ND$); and as the percentage of the time the smoothed velocity exceeds 5% of the impeller tip speed. All of these measures were used to assess the statistical significance of the geometric effects. Normal probability plots give an indication of which geometric variables have a significant effect on the flow stability for each impeller.

4.2 Experimental

The LDV experimental setup was discussed in Chapter 2. The main parameters are: beam separation - 0.01691m (track 1), high voltage - 400V, signal sampling frequency - 2.5 MHz, average data rate - 1.2 kHz, data validation $\geq 99\%$. The sampling time was chosen to be 10s, or a time equivalent to at least 120 blade passages, whichever is longer. All measurements were done in the fully turbulent flow regime ($Re \geq 2 \times 10^4$).

The stirred vessel used for this work is shown on Figure 4.1. The tank diameter $T=0.24$ m is equal to the liquid height $T=H$. To prevent air entrainment

and surface vortexing, a lid was placed on the top of the tank and covered with 5 cm of water to seal the tank. There are four (or two) vertical rectangular baffles of width W ($W=T/10$) spaced at an equal distance around periphery of the tank at a small distance from the wall. A tank with four baffles is considered to be fully baffled; the two baffle configuration is used to test the sensitivity of instabilities to the number of baffles.

The axial impellers (A310, HE3, PBT) of diameters $D=T/2$ and $T/4$ at dimensionless off bottom clearances of $C/D=0.5$ and 1 were used. The dimensionless impeller diameter (D/T) and the off bottom clearance (C/D) are used in practice as a part of scale-up procedure. The factorial design of experiments also has the capacity to obtain information about the interaction between variables. For the radial impeller - Rushton turbine, diameters: $D=T/2$ and $T/3$ and dimensional off bottom clearances $C=T/2$ and $T/3$ were used, due to the inherently different flow pattern produced by this impeller. For the radial impeller, the off bottom clearance determines the symmetry or asymmetry of the two circulation loops. For the axial impeller, the dimensionless off-bottom clearance allows for the effect of C and D on changes in the flow pattern (Kresta and Wood, 1993b).

A large shaft diameter (9 mm) was used in order to eliminate shaft run-out (or wobbling) at the end of the shaft. For this work, it is critical to eliminate any possibility of additional vibration of any of the components in the system, which may

be introduced as an erroneous frequency in the measured velocity record. The impeller geometries used in this work were discussed in detail in Chapter 1. All four impellers were used in their standard configurations. The A310 was used as supplied by Lightnin' Inc; the HE3 as supplied by Chemineer. For most of the measurements (PBT, RT, and HE3) the impeller rotational speed was chosen so that the impeller tip velocity (V_{tip}) was constant. For the A310 measurement, V_{tip} was slightly different. In order to compare the different impellers, all reported velocities are normalized with V_{tip} . All experimental runs and experimental results are summarized in Tables 4-1 to 4-4.

For the axial impellers, the axial velocity was measured, since it gives the clearest indication of the flow pattern and it is the primary velocity component for these impellers. Similarly, for the radial impeller (RT), the radial velocity component was chosen (in the impeller stream). In the vessel corners (bottom and top), only the axial velocity was measured in all cases. For each geometry and each measurement location five repeat measurements were done. The average mean and RMS velocities are reported.

The three locations in the stirred tank which were chosen for detailed investigation: the impeller stream, bottom corner and top corner of the tank, are based on tuft visualization work reported by Chapple and Kresta (1994). The impeller stream velocity, although not highly unstable, can capture all frequencies

present in the flow. It contains the blade passages, the high frequency turbulent components, and the low frequencies of interest for this work. The bottom corner of the tank is less stable than the impeller stream, since it is located at the boundary of the primary circulation loop. Any instability of the primary circulation loop due to the low frequencies can easily be captured here. The top corner of the tank is the third region. It is also considered unstable, since the velocities are low and the flow changes direction frequently (from radially inward to radially outward).

The exact location of the impeller stream measurement point was 3mm below the impeller blade at a radial distance $2r/D=0.8$ (for PBT and HE3) and $2r/D=0.5$ (for the A310). For the bottom corner, measurements were taken at a 25mm off bottom clearance and 3mm in front of the baffle. For the top corner, measurements were taken 5mm away from the lid and 3mm in front of the baffle. For the RT, impeller stream measurements were taken 3mm away from the blade tip ($r=D/2+3\text{mm}$) and at the centerline of the impeller.

4.3 Resampling and Smoothing of Time Series

In Chapter 3 LDV data processing was discussed extensively. The main objective of this work is investigation of low frequencies i.e. slow variations in the mean velocity or the nonstationary aspect of the flow. A typical time series of the axial velocity signal, measured at the impeller stream, is shown on Figure 4.2a. The

velocity record shows the turbulent fluctuations, the fluctuations due to the individual blade passages, and the fluctuations due to the low frequencies. However, high intensity turbulent fluctuations obscure the longer time scale fluctuations.

To eliminate the high frequency fluctuations, a data resampling and smoothing sequence was used. Data resampling entails selecting velocity values in the recorded signal with arrival times closest to regularly spaced time lags. Resampling gives rise to a small time error which is equal to the difference between new assigned time and the initial arrival (t_{lag}) time with a maximum error in time of $\sim t_{lag}/2$. This technique laterally stretches and compresses initial signal along the time axis. A resampling window equal to the mean sampling interval (mean sampling frequency) was applied for this study. Since the mean sampling frequencies were higher than 1kHz and the low frequencies being investigated are of the order of 1Hz, the resampling error is negligible, as shown in Figure 4.2. The mean sampling frequencies vary from several hundred (600Hz) to several (up to 5) kHz at the three measurement locations within the tank. In the impeller stream, the turbulence intensities are the highest, and the data rate (sampling rate) is the highest, while in the vessel corners weak (unstable) flow causes low data density.

Once the raw signal is resampled it can be low-pass filtered according to the desired frequency range. Data smoothing as a special case of numerical low -pass filtering was used in order to eliminate higher frequency fluctuations, and to

quantify the low frequency contribution to the total measured fluctuating velocity. A smoothing window based on a number of blade passages, was used for this investigation; however, the first round of smoothing proved not to be sufficient i.e. higher frequency fluctuations were still apparent in the signal. Thus, second round of smoothing was applied. For different impellers and different rotational speeds, the smoothing window was optimized. At each stage, visual observation was used to compare the smoothed velocity profile with the raw signal. The procedure was considered to be complete when smoothed signal overlapped the slow variation in the initial mean velocity signal, and no observable higher fluctuations were present (in the resulting signal). The effects of each step of data processing on the raw signal are presented in Figure 4.2(a, b, c, d). The shape of the smoothed signal (4.2d) is virtually identical to that of raw signal in terms of the slow variation in the mean. A complete set of raw and smoothed signals is given in Appendix 2. In all cases, some slow variations on the mean were observed.

4.3.1 Velocity Decomposition

The concept of velocity decomposition is useful for determining how much turbulence a given impeller can generate, and the relative contribution of the regular periodic components blade passages and low frequency fluctuations to the total fluctuations. Velocity decomposition has previously been done using the autocorrelation function and filtering (Rao and Brodkey, 1972, Wu and Patterson,

1989, Hockey and Nouri, 1996) to characterize the pure turbulent component in the measured velocity. Their main concern was to eliminate the non-random blade passage frequency from the turbulent analysis. The combined effect of blade passages and low frequency fluctuations on the RMS velocity was first reported by Kresta (1991). This work focuses on analyzing the low frequency contributions.

The instantaneous mean centered velocity, v'_{tot} can be defined as:

$$v'_{tot} = v'_{BP} + v'_{LF} + v'_{rand} \quad (4-1)$$

where BP and LF denote the blade passage and low frequency, and rand denotes the random or turbulent component. With selection of a long window relative to the blade passage frequency, data smoothing filters out the random (turbulent) and periodic (due to the blade passages) velocity components. Then the low frequency RMS velocity - v_{LF} , can be calculated from the smoothed velocity profile as:

$$v_{LF} = \sqrt{\frac{1}{n} \sum_{i=1}^n v'_{LF}{}^2} \quad (4-2)$$

The other two velocity components, v_{BP} and v_{rand} can not be separated; firstly because a shaft encoder was not included in the experimental configuration; and the secondly because motor speed varied by ± 2 rpm. Finally, in order to determine v_{BP} , at

least 500 blade passages must be measured and then an average cycle and its RMS velocity determined. The data storage and handling requirements for this amount of data are limited on the existing computer so that no more than 200 blade passages were measured. Discussion in the following sections will be limited to the RMS velocity component (v_{LF}) due to the low frequency fluctuations, and the percentage contribution of the low frequency component to v_{tot} .

4.4 Statistical Significance of the Effects: Factorial Design and 95% confidence interval (C.I.)

To minimize the number of required experiments and examine the effects of many variables and their interactions at the same time, a factorial design is used. First, the number of variables is selected, then a number of levels for each variable is selected. Experiments are performed with all possible combinations of selected variables and their levels. This is of particular importance in a stirred tank, where the effects of geometric variables often interact.

Three geometric variables at 2 levels were used for each of the four impellers in this study. They are: the baffling arrangement (N_f), the impeller diameter (D), and the dimensionless off bottom clearance i.e. the ratio of off bottom clearance to impeller diameter (C/D). For the RT, as explained earlier, the dimensional off bottom clearance was used. Three variables with two levels requires eight

experimental runs. For a detailed explanation of factorial designs the reader is referred to Box et al.(1978). Each set of experiments results in three main effects due to: N_f , D , and C/D and four effects due to interactions between variables: N_f - D , N_f - C/D , D - C/D , and N_f - D - C/D ; therefore there are seven possible geometric effects.

The effects of geometry on v_{LF} are estimated using the method given by Box et al. (1978). By denoting two levels of each variable with +1 and -1, the effect of each variable on v_{LF} can be calculated using the following expression:

$$e_i = \frac{\sum_{i=1}^8 l_i v_{LF}}{4} \quad (4-3)$$

where \sum means to take the sum of all eight runs, and l_i is the product of the levels for the interaction i . This can be clarified by the following example: for the N_f - D interaction (first run in Table 4-1 to 4-4) the impeller diameter has a level +1 and a number of baffles also +1, thus their product is +1 i.e. $l_{12}=+1$; in the second run D has a level +1 and N_f -1, thus $l_{12}=-1$, where subscript 12 denotes the interaction between N_f and D variables 1 and 2. The main effects and other interactions are calculated similarly. The effects which fall on straight line on a normal probability plot can be considered a result of random variation about a fixed mean indicating that changes in the level of variables have no real effect. Effects which do not fall on a straight line are considered significant.

As an additional criterion for assessment of the significance of effects, the 95% confidence interval was used. For each experiment, the 95% C.I., assuming a t -distribution and four degrees of freedom, was calculated. From these, an average 95% C.I. was calculated for each impeller. Average values for 95% C.I. were plotted on corresponding probability plots. Effects which fall the inside 95% C.I. may be explained as experimental error, while those falling outside may be considered statistically significant. However, due to the limits of experimental system (insufficient length of measurement), no reliable conclusions could be drawn using this criterion. Initial results showed that the A310 impeller, which was previously reported (Zhou, 1996) as the most stable impeller with the smallest 95% C.I., gives the largest 95% C.I. (0.182) in this work. Unlike the A310, the PBT, as the least stable impeller considered in this study, shows a smaller 95% C.I. (0.147). This means that the PBT has faster variations in smoothed velocity profile than the A310 and thus the current measurement covers more cycles of this variation, giving more repeatable results. The length of measurement has to be extended and optimized for each impeller in order to get a more repeatable v_{LF} .

4.5 Results and Discussion

The significant effects were determined from two different perspectives: probability plots and direct data evaluation. The former gives an indication of

significance and the latter gives the magnitude and intensity of the low frequency effects. Data evaluation is based on the RMS smoothed velocity profile (v_{LF}), the ratio v_{LF}/v_{tot} , where v_{tot} is the RMS velocity before smoothing, and the percentage of the time the smoothed velocity magnitude exceeds 5% of the tip velocity (V_{tip}). Experimental results are summarized in Tables (1-4). Time series of initial and smoothed velocity profiles for all geometries and impellers are given in Appendix B. Probability plots are given in Appendix C.

4.5.1 PBT Results

The probability plots indicate that the most dominant effect on flow stability for the PBT is the impeller diameter D . Time series (Figures 1-8, Appendix B), probability plots Figure 4.3 and Figures C-1 and C-2 (Appendix C), and Table 4.1 indicate that the bigger the diameter, the less stable flow pattern is, for all three measured locations (stream-bottom-top). This also implies that the bigger impeller ($D=T/2$) distributes more energy throughout the tank.

The interaction $D-C/D$ is also factor affecting flow stability. This is evident on the probability plots at the impeller stream (Figure 4.3). However, the top corner and bottom corner data show that this effect does not persist throughout the tank. For a bigger impeller diameter ($D=T/2$) and higher C/D ratio ($C/D=1$), the highest level of instabilities is observed. This can be explained by the change in the impeller

discharge conditions (Figure 4.4a). The angle of the impeller discharge stream is 45° . When smaller C/D ratio is used, the discharge flow impinges on the bottom of the vessel, and travels the side walls in a well defined wall jet which extends up two-thirds of the vessel height as observed by Bittorf and Kresta (1997) before it returns to the impeller stream through the core of the tank. This is how the primary circulation loop is formed. Weak reverse flow exists below the hub of the impeller. For a higher C/D ratio and large D , the fluid impinges on the vessel wall (Figure 4.4b), which causes a relatively strong reverse (radially inward) flow at the bottom of the vessel. This counter-rotating secondary loop causes deflection of the discharge angle of the primary circulation loop previously reported by Kresta and Wood (1993b) and Bruha et al. (1996). Thus, flow is redirected in radial direction and the axial velocity component is decreased. However, the small impeller (T/4) interacts with changing C/D ratio in opposite fashion. For a bigger C/D (1.0), the flow pattern is more stable, although an outlier exists. This implies that a region of recirculating flow below the impeller hub is constrained by the vessel base (Ranade and Joshi, 1989) for a smaller C/D (0.5), causing a decrease in stability.

The number of baffles (N_f) appears as a significant effect at the impeller stream (Figure 4.3) and from data evaluation throughout the tank (with some outliers). For $N_f=2$, the flow pattern becomes less stable, which indicates that quiescent zones where constant flow is not maintained develop between the baffles. Again, the top and bottom probability plots show no signs of this effect. Data for the

bottom corner (Table 4.1b) are scattered with respect to the N_f effect.

From the perspective of three regions (stream-bottom-corner) in the tank, the most stable is impeller stream in terms of average v_{LF}/v_{tot} (0.444), then top corner (0.515), and bottom corner (0.543). The smoothed RMS velocity v can be seen to be the largest in the impeller stream, but the fluctuating and the mean velocity are also highest in this region. Hence, the relative ratio v_{LF}/v_{tot} is the lowest. The magnitude of low frequencies or v_{LF}/V_{tip} ratio and deviation from the 5% of the V_{tip} give the highest values for impeller stream – 0.057 (33.21 %) indicating that the impeller stream is the least stable, followed by the bottom: 0.049 (22.95 %), and the top corner: 0.03 (12.24%). This implies that the forces which large flow structures exert on the vessel internals die out further away from the impeller.

This finding opposes the previous investigation on flow stability reported by Chapple and Kresta (1994), where the bottom corner of the tank was found to be somewhat more stable than the top of the tank. Their measurements were taken further away from the lid, where the flow may be less stable than at the location used in this work. They also calculated the flow stability coefficient as an average from several neighboring points, while this time only one point was measured.

The flow pattern in the vessel corners (top and bottom) is very unstable. The mean velocity changes direction frequently, from radially inward to radially outward.

Flow direction changes imply flow asymmetry, and thus the existence of large flow structures. This is reported for the PBT and HE3 impellers by Myers et al., 1997. Mean (resampled) velocities on the top of the tank are very low, below 5% of the tip speed: $0.022V_{tip}$ ($D=T/2$) and $0.005 V_{tip}$ ($D=T/4$) with a corresponding standard deviation of 0.076 and 0.038. This means that the wall jet almost has no effect at the top of the tank.

The velocity flow field at the bottom of the tank is also characterized to be weak relative to V_{tip} : 0.023 ($D=T/2$) and 0.022 ($D=T/4$) with corresponding standard deviations of 0.109 and 0.074, with frequent changes in direction. This is due to fluid redirection by the baffles from radial to axial (upward) and interactions to the internals: impeller-baffles-vessel wall.

4.5.2 HE3 results

The general flow pattern for this impeller is given in Figure 4.5. The HE3 flow field exhibits a strong axial velocity component with a discharge angle close to 90° . Fluid impinges on the vessel base, where it turns radially due to the base constraint. At the vessel corner, it turns axially upward, due to presence of the baffles, in the form of wall jet and then is drawn back to the impeller stream. A small, weak zone of recirculation is present below the impeller hub.

Although the HE3 flow field is similar to that of the PBT, the only significant effect on flow stability is due to impeller diameter D (Figures 4.6 and 3 and 4 - Appendix C). The top corner probability plots do not indicate this effect. The time series for all geometries are shown in Figures 9-16 (Appendix B). It is evident that the big impeller ($D=T/2$) produces a less stable flow pattern, although some outliers exist (see Appendix 2). The decrease in stability for $D=T/2$ can be attributed to the increase of the turbulence intensity and low frequency fluctuations. This is evident from the data given in Tables (4-2 a, b, c) by comparing v_{LF}/v_{tot} , v_{LF}/V_{tip} , and 5% V_{tip} deviation. No other effects or interactions are important for flow stability for the HE3 impeller.

From the perspective of different zones, the most stable is the impeller stream, with the average ratio $v_{LF}/v_{tot}=0.341$, then top corner (0.444), and bottom corner (0.545). Mechanical forces due to momentum quantified by v_{LF}/V_{tip} and 5% V_{tip} deviation are also the highest at the bottom of the tank (0.032 and 13.74%), then at the impeller stream (0.018 and 1.34%), and the top corner (0.016 and 0.49%). The flow field at the opposite corners of the vessel is very weak, but highly unstable with frequent directional changes. Mean velocities at the top of the tank are $0.007V_{tip}$ ($D=T/2$) and $0.011V_{tip}$ ($D=T/4$). The higher value of mean velocity for small impeller ($T/4$) is due to the presence of outliers. The mean velocities at the bottom corner are somewhat higher, but are still below 5% of V_{tip} , $0.048V_{tip}$ ($T/2$ impeller) and $0.002V_{tip}$ ($T/4$ impeller). Unlike the mean velocities, standard

deviations (v_N) are very high (Table 4-2b, c) indicating unstable flow. This was also reported for the HE3 impeller by Jaworski et al. (1996), where the least stable flow pattern is found in the vicinity of the vessel wall. Since this type of impeller is relatively new, only a few investigations in open literature are available.

4.5.3 A310 results

The A310 impeller generates an axial flow pattern, with an outflow angle close to 90° . A well-established primary circulation loop around the agitator is evident as well as a small weak circulation below the hub (Figure 4.7). The A310 time series are shown in Figures 17-24 (Appendix B). Corresponding probability plots are given on Figures 4.8 and 5 and 6 (Appendix C).

The stability of the flow pattern is difficult to evaluate from the probability plots due to the relatively wide scattering of plotted points or variability. However, the data analysis results are less scattered, and as the most relevant indication of stability the ratios v_{LF}/v_{tot} and v_{LF}/V_{tip} , and 5% V_{tip} deviation were used (Table 4.3a, b, c).

The impeller diameter is the most important factor on flow stability, although on the probability plots at the top of the tank, the results are inconclusive. The big impeller (T/2) produces less stable flow, not only due to the increase of turbulent

energy but also because the low frequency contribution (v_{LF}/v_{tot} and v_{LF}/V_{tip}) is higher.

From the perspective of different zones within the tank: the most stable flow is in the impeller stream where $v_{LF}/v_{tot}=0.389$, then the top corner (0.521), and the bottom corner (0.523). Unlike the two previous axial impellers (PBT and HE3) the A310 shows almost the same level of instabilities for the top and bottom corner. This may be due to the higher pumping efficiency of the A310. In terms of the magnitude of low frequencies the most stable is the top corner $v_{LF}/V_{tip}= 0.023$ and 5.15% V_{tip} deviation, then impeller stream (0.034 and 14.44%) and bottom corner (0.038 and 19.2%). The flow field in the vessel corners (bottom and top) is characterized by low mean velocities, high turbulent fluctuations, and frequent directional changes from radially inward to radially outward. Mean velocities are below 5% of the V_{tip} : $0.014V_{tip}$ at the bottom and $0.017V_{tip}$ at the top for $D=T/2$, and corresponding values of 0.042 and $0.019 V_{tip}$ for $D=T/4$.

4.5.4 RT results

The RT impeller generates radially outward flow emerging from the impeller tip. This high speed radial jet entrains the surrounding fluid and slows down as it approaches the tank wall. Near the tank wall this stream divides and circulates through the rest of the tank, forming two ring vortices above and below the impeller

blade (Figure 4.9). Since the RT impeller has an inherently different flow pattern from the axial impellers the experimental design was also different (discussed in section 4.2). Time series plots are given in Appendix B (Figures 25-32).

The flow pattern of the RT impeller is affected the most strongly by the number of baffles, N_f and the diameter of the impeller, D . This is consistent on most probability plots (Figure 4.10 and 7 and 8 in Appendix C) and from data analysis (Table 4-4a, b, c) in terms of v_{Lr}/v_{tot} , v_{Lr}/V_{tip} and 5% V_{tip} deviation. However, top corner probability plot doesn't indicate significance of any of the considered effects. Two baffles configurations give less stable flow, based on v_{Lr}/v_{tot} and v_{Lr}/V_{tip} ratios (Table 4-4a, b, c). Four baffle configurations are more stable because the breakup of the impeller stream (large scale motion) is more intensive due to the additional imposed drag. Unlike axial impellers, the RT shows greater instabilities when a small ($D=T/3$) impeller is used. When the big impeller is used, impeller radial jet is stronger and it is confined with the vessel wall. Hence, it gives stable flow without large fluctuations. When a small impeller is used, the impingement distance is bigger so that the radially discharged jet may pulsate into the bulk of the tank, giving rise to long-term instabilities. This was also observed and reported for liquid and liquid-air systems by McFarlane and Nienow (1995).

As previously shown for all axial type of impellers, the impeller stream gives the most stable flow pattern with an average v_{Lr}/v_{tot} ratio of 0.282; then, unlike axial

impellers, the bottom corner 0.437 and the top of the tank 0.479. In terms of magnitude v_{Lr}/V_{tip} the least stable is the impeller stream (0.107 and 55.5 % deviation from $5\%V_{tip}$), then the top corner (0.05 and 31.52%) and bottom corner (0.047 and 28.46%). The top seems to be less stable than the bottom corner. This can be attributed not only to the inherent instabilities for the RT impeller but also to the different experimental design (higher off bottom clearance) from the axial impellers. Mean flow at the vessel corners is higher than that of the axial type of impellers and it is up to 25% of the V_{tip} : at the bottom $0.245 V_{tip}(T/2)$ and $0.103 V_{tip}(T/3)$; at the top $0.147 V_{tip}(T/2)$ and $0.038 V_{tip}(T/3)$; No flow directional changes can be observed and turbulent intensities are lower than those for the axial impellers.

4.5.5 Comparison of different type of impellers

A general comparison of the four impellers used for this study is given in Tables 4.5 (a, b, c). The most important variable for flow stability can be considered impeller diameter D , for the axial type of the impellers, and the number of baffles N_f for the radial impeller - RT. The effect of impeller diameter is different for the axial and radial type impeller: a bigger impeller gives a less stable flow pattern for the axial impellers; while for the RT, a small impeller ($T/3$) generates more instabilities. Larger impeller diameter related instabilities (for the axial impellers) are attributed to the occurrence of low frequencies and more intensive interactions with the components of the stirred tank: impeller-vessel wall-baffles. The effect of the

number of baffles is the same for all impellers used: configurations with $N_f=2$ give a less stable flow pattern.

The RT impeller generates the most stable flow pattern regarding low frequency intensities. The PBT impeller gives, on the average, the highest level of instabilities. The two hydrofoil impellers (HE3 and A310) have similar level of instabilities for all different configurations and different regions in the tank. However, the HE3 is more stable at the impeller stream and the top of the tank than the A310. The A310 gives the most uniform level of instabilities in the vessel corners, making this type of the impeller suitable for agitating solid suspensions. All three axial impellers exhibit a similar level of instabilities at the bottom of the tank. The PBT produces the highest level of instabilities and they are spread throughout the vessel, while the hydrofoils' (HE3, A310) instabilities vary over a wider range. This makes the PBT suitable for solid suspensions.

In terms of the magnitude of low frequencies - v_{LF}/V_{tip} and 5% V_{tip} deviation, the RT is the least stable (Table 4.5a, b, and c) at all three measured locations. Since the RT gives the highest mean flow and turbulent intensities, this will manifest as the highest force (torque) on the shaft and internals and the highest (in an absolute sense) power draw fluctuations. Long-term torque fluctuations and power draw for the RT (and PBT) impeller have been reported by Chapman et al. (1983) for gas-liquid systems. Work done by Wernersson (1997) also shows long term instabilities

in the velocity record for this impeller.

The magnitude of the low frequencies is the highest for the RT only at the impeller stream, but at the vessel corners is the same as for three other axial impellers (see Table 4.5a, b, and c). Since axial impellers have a very low mean velocity at the vessel corners – several percents of the V_{tip} , most of the fluctuations come from the low frequencies that dominate the flow in those regions. The RT has much higher mean velocities – between 10 and 20% of the tip speed, thus most of the fluctuations come from the turbulent motion.

Table 4.1a: Experimental design and results (impeller stream)- PBT

Run	D	C/D	N _r	N (rpm)	Re	$\frac{\bar{V}_{\text{me}}}{V_{\text{tip}}}$	$\frac{V_{\text{me}}}{V_{\text{tip}}}$	$\frac{\bar{V}_{\text{ax}}}{V_{\text{tip}}}$	$\frac{V_{\text{ax}}}{V_{\text{tip}}}$	$\frac{V_{\text{E}}}{V_{\text{tip}}}$	$\frac{V_{\text{E}}}{V_{\text{ax}}}$	V _E > 0.05V _{tip} , %
1	+	+	+	200	48000	0.357	0.155	0.360	0.135	0.072	0.538	51.13
2	+	+	-	200	48000	0.395	0.167	0.392	0.158	0.090	0.568	56.82
3	-	+	+	400	24000	0.393	0.103	0.40	0.086	0.026	0.306	5.60
4	-	+	-	400	24000	0.338	0.107	0.348	0.084	0.031	0.368	11.85
5	+	-	+	200	48000	0.451	0.131	0.456	0.122	0.054	0.444	33.07
6	+	-	-	200	48000	0.412	0.146	0.412	0.139	0.071	0.509	46.74
7	-	-	+	400	24000	0.324	0.094	0.332	0.084	0.032	0.381	11.62
8	-	-	-	400	24000	0.327	0.188	0.337	0.178	0.079	0.442	48.85

Table 4.1b: Experimental design and results (bottom corner)- PBT

Run	D	C/D	Nr	N	Re	$\frac{V_{rms}}{V_{tip}}$	$\frac{V_{max}}{V_{tip}}$	$\frac{V_{min}}{V_{tip}}$	$\frac{V_{ca}}{V_{tip}}$	$\frac{V_{LF}}{V_{tip}}$	$\frac{V_{LF}}{V_{ca}}$	$V_{LF} > 0.05V_{tip}, \%$
	+T/2	+1	+4	200	48000	0.088	0.094	0.082	0.088	0.082	0.928	29.75
1	+	+	+	200	48000	0.068	0.088	0.066	0.083	0.045	0.538	27.82
2	+	+	-	200	48000	-0.072	0.107	-0.071	0.10	0.045	0.452	10.95
3	-	+	+	400	24000	-0.050	0.088	-0.045	0.079	0.036	0.454	15.35
4	-	+	-	400	24000	-0.045	0.145	-0.033	0.133	0.054	0.407	36.80
5	+	-	+	200	48000	-0.031	0.141	-0.024	0.135	0.072	0.539	43.17
6	+	-	-	200	48000	0.006	0.073	0.014	0.064	0.034	0.531	13.27
7	-	-	+	400	24000	0.007	0.062	0.014	0.053	0.026	0.492	6.50
8	-	-	-	400	24000							

Table 4.1c: Experimental design and results (top corner)- PBT

Run	D	C/D	N _r	N (rpm)	Re	$\frac{\bar{V}_{ms}}{V_{tp}}$	$\frac{V_{ms}}{V_{tp}}$	$\frac{\bar{V}_{lat}}{V_{tp}}$	$\frac{V_{lat}}{V_{tp}}$	$\frac{V_{LF}}{V_{tp}}$	$\frac{V_{LF}}{V_{lat}}$	$V_{LF} > 0.05V_{tp}, \%$
1	+	+1	+4	200	48000	-0.003	0.095	0.002	0.085	0.042	0.495	25.68
2	+	+1	-4	200	48000	-0.029	0.096	-0.021	0.083	0.053	0.635	34.9
3	-	+1	+4	400	24000	0.006	0.037	0.007	0.033	0.018	0.548	0.56
4	-	+1	-4	400	24000	-0.011	0.062	-0.011	0.054	0.025	0.456	4.71
5	+	-0.5	+4	200	48000	-0.016	0.090	-0.012	0.070	0.033	0.477	14.74
6	+	-0.5	-4	200	48000	-0.069	0.072	-0.057	0.065	0.033	0.50	16.03
7	-	-0.5	+4	400	24000	0.007	0.039	0.010	0.034	0.021	0.488	0.52
8	-	-0.5	-4	400	24000	-0.029	0.036	-0.025	0.033	0.018	0.524	0.76

Table 4.2a: Experimental design and results (impeller stream)- HE3

Run	D	C/D	N _r	N (rpm)	Re	$\frac{\bar{V}_{imp}}{V_{tp}}$	$\frac{V_{max}}{V_{tp}}$	$\frac{\bar{V}_{ax}}{V_{tp}}$	$\frac{V_{ax}}{V_{tp}}$	$\frac{V_{LF}}{V_{tp}}$	$\frac{V_{LF}}{V_{ax}}$	$V_{LF} > 0.05V_{tip}, \%$
1	+	+	+	200	48000	0.223	0.072	0.226	0.060	0.021	0.350	2.69
2	+	+	-	200	48000	0.232	0.072	0.236	0.062	0.026	0.419	2.41
3	-	+	+	400	24000	0.221	0.059	0.224	0.048	0.019	0.396	0.45
4	-	+	-	400	24000	0.252	0.062	0.255	0.049	0.010	0.204	0.0
5	+	-	+	200	48000	0.205	0.064	0.206	0.054	0.016	0.296	0.0
6	+	-	-	200	48000	0.232	0.067	0.236	0.058	0.025	0.431	5.15
7	-	-	+	400	24000	0.190	0.057	0.194	0.047	0.016	0.340	0.0
8	-	-	-	400	24000	0.192	0.058	0.194	0.045	0.013	0.289	0.0

Table 4.2b: Experimental design and results (bottom corner)- HE3

Run	D	C/D	N _r	N	Re	$\frac{V_{rpm}}{V_{ip}}$	$\frac{V_{ax}}{V_{ip}}$	$\frac{V_{ax}}{V_{op}}$	$\frac{V_{ax}}{V_{ip}}$	$\frac{V_{LF}}{V_{op}}$	$\frac{V_{LF}}{V_{ax}}$	$V_{LF} > 0.05V_{ip}, \%$
1	+T/2	+1	+4	200	48000	-0.043	0.068	-0.033	0.064	0.039	0.609	20.53
2	-T/4	-0.5	-2	200	48000	-0.045	0.075	-0.043	0.072	0.051	0.708	36.42
3	-	+	+	400	24000	-0.014	0.055	-0.013	0.049	0.026	0.531	6.52
4	-	+	-	400	24000	0.010	0.041	0.011	0.036	0.017	0.472	0.57
5	+	-	+	200	48000	-0.057	0.083	-0.055	0.076	0.041	0.539	20.4
6	+	-	-	200	48000	-0.066	0.062	-0.063	0.071	0.040	0.563	22.88
7	-	-	+	400	24000	0.002	0.051	0.005	0.045	0.021	0.467	2.45
8	-	-	-	400	24000	0.003	0.043	0.006	0.036	0.017	0.472	0.12

Table 4.2c: Experimental design and results (top corner) - HE3

Run	D	C/D	N _f	N	Re	$\frac{\bar{V}_{inr}}{V_{tp}}$	$\frac{V_{mr}}{V_{tp}}$	$\frac{\bar{V}_{lat}}{V_{tp}}$	$\frac{V_{lat}}{V_{tp}}$	$\frac{V_{LF}}{V_{tp}}$	$\frac{V_{LF}}{V_{lat}}$	$V_{LF} > 0.05V_{tip}, \%$
	+T/2	+1	+4									
	-T/4	-0.5	-2									
1	+	+	+	200	48000	0.006	0.041	0.006	0.036	0.017	0.472	0.6
2	+	+	-	200	48000	0.001	0.049	0.002	0.044	0.023	0.523	2.33
3	-	+	+	400	24000	0.010	0.041	0.013	0.033	0.014	0.424	0.0
4	-	+	-	400	24000	0.003	0.045	0.004	0.034	0.016	0.471	0.62
5	+	-	+	200	48000	0.007	0.046	0.008	0.040	0.020	0.500	0.0
6	+	-	-	200	48000	0.010	0.041	0.012	0.033	0.013	0.394	0.36
7	-	-	+	400	24000	0.018	0.041	0.018	0.029	0.010	0.345	0.03
8	-	-	-	400	24000	0.006	0.043	0.008	0.033	0.014	0.424	0.0

Table 4.3a: Experimental design and results (impeller stream) - A310

Run	D	C/D	N _f	N (rpm)	Re	$\frac{\bar{V}_{\text{imp}}}{V_{\text{ip}}}$	$\frac{V_{\text{imp}}}{V_{\text{ip}}}$	$\frac{\bar{V}_{\text{ax}}}{V_{\text{ip}}}$	$\frac{V_{\text{ax}}}{V_{\text{ip}}}$	$\frac{V_{\text{LF}}}{V_{\text{ip}}}$	$\frac{V_{\text{LF}}}{V_{\text{ax}}}$	V _{LF} > 0.05V _{tip} , %
	+0.55T	+1	+4									
	-0.35T	-0.5	-2									
1	+	+	+	150	43560	0.270	0.097	0.275	0.079	0.032	0.405	13.02
2	+	+	-	150	43560	0.199	0.101	0.199	0.088	0.051	0.579	33.54
3	-	+	+	400	47040	0.263	0.073	0.269	0.057	0.018	0.316	0.04
4	-	+	-	400	47040	0.276	0.070	0.281	0.060	0.018	0.243	0.0
5	+	-	+	150	43560	0.255	0.101	0.259	0.086	0.036	0.419	15.51
6	+	-	-	150	43560	0.219	0.153	0.227	0.138	0.060	0.435	37.49
7	-	-	+	400	47040	0.155	0.099	0.161	0.096	0.032	0.333	11.55
8	-	-	-	400	47040	0.216	0.072	0.221	0.065	0.025	0.385	4.38

Table 4.3b: Experimental design and results (bottom corner)- A310

Run	D	C/D	N _r	N (rpm)	Re	$\frac{\bar{V}_{\text{int}}}{V_{\text{tip}}}$	$\frac{V_{\text{int}}}{V_{\text{tip}}}$	$\frac{\bar{V}_{\text{ax}}}{V_{\text{tip}}}$	$\frac{V_{\text{ax}}}{V_{\text{tip}}}$	$\frac{V_{\text{LF}}}{V_{\text{tip}}}$	$\frac{V_{\text{LF}}}{V_{\text{ax}}}$	V _{LF} > 0.05V _{tip} , %
	+0.55T	+1	+4									
	-0.35T	-0.5	-2									
1	+	+	+	150	43560	0.010	0.080	0.013	0.072	0.045	0.625	23.03
2	+	+	-	150	43560	0.042	0.059	0.041	0.055	0.037	0.673	17.41
3	-	+	+	400	47040	-0.060	0.061	-0.052	0.058	0.027	0.466	7.19
4	-	+	-	400	47040	-0.036	0.075	-0.030	0.069	0.033	0.478	15.57
5	+	-	+	150	43560	-0.049	0.091	-0.038	0.084	0.044	0.524	23.26
6	+	-	-	150	43560	-0.073	0.098	-0.070	0.095	0.057	0.600	39.11
7	-	-	+	400	47040	-0.053	0.080	-0.044	0.076	0.030	0.395	11.39
8	-	-	-	400	47040	-0.051	0.075	-0.043	0.069	0.028	0.406	16.65

Table 4.3c: Experimental design and results (top corner)- A310

Run	D	C/D	N _f	N	Re	$\frac{\bar{V}_{int}}{V_{tp}}$	$\frac{V_{int}}{V_{tp}}$	$\frac{\bar{V}_{tot}}{V_{tp}}$	$\frac{V_{tot}}{V_{tp}}$	$\frac{V_{LF}}{V_{tp}}$	$\frac{V_{LF}}{V_{tot}}$	V _{LF} > 0.05V _{tip} , %
	+0.55T	+1	+4	150	43560	-0.037	0.057	-0.028	0.052	0.030	0.577	14.33
	-0.35T	-0.5	-2	150	43560	-0.017	0.059	-0.013	0.047	0.024	0.511	5.41
1	+	+	+	400	47040	-0.046	0.041	-0.041	0.039	0.018	0.462	4.23
2	+	+	-	400	47040	-0.013	0.042	-0.011	0.037	0.018	0.486	2.01
3	-	-	+	150	43560	-0.023	0.063	-0.030	0.056	0.033	0.589	9.23
4	+	-	-	150	43560	0.001	0.054	0.003	0.045	0.018	0.400	0.6
5	-	-	+	400	47040	-0.031	0.044	-0.044	0.041	0.023	0.561	4.27
6	-	-	-	400	47040	-0.004	0.035	-0.003	0.032	0.019	0.594	1.08

Table 4.4a: Experimental design and results (impeller stream)- RT

Run	D	C	Nr	N	Re	$\frac{\bar{V}_{\text{ca}}}{V_{\text{tp}}}$	$\frac{V_{\text{rms}}}{V_{\text{tp}}}$	$\frac{\bar{V}_{\text{ca}}}{V_{\text{tp}}}$	$\frac{V_{\text{ca}}}{V_{\text{tp}}}$	$\frac{V_{\text{LF}}}{V_{\text{tp}}}$	$\frac{V_{\text{LF}}}{V_{\text{ca}}}$	$V_{\text{LF}} > 0.05V_{\text{tip}}, \%$
1	+	+	+	200	48000	0.729	0.337	0.712	0.327	0.044	0.134	25.56
2	+	+	-	200	48000	0.456	0.357	0.455	0.346	0.107	0.308	65.38
3	-	+	+	300	32000	0.740	0.444	0.756	0.355	0.077	0.217	53.02
4	-	+	-	300	32000	0.571	0.391	0.596	0.390	0.152	0.390	73.92
5	+	-	+	200	48000	0.830	0.383	0.829	0.385	0.051	0.132	34.51
6	+	-	-	200	48000	0.693	0.269	0.568	0.395	0.139	0.351	68.48
7	-	-	+	300	32000	0.658	0.355	0.682	0.339	0.053	0.155	32.82
8	-	-	-	300	32000	0.278	0.410	0.293	0.415	0.235	0.566	90.32

Table 4.4b: Experimental design and results (bottom corner)- RT

Run	D	C	N _r	N	Re	$\frac{\bar{V}_{int}}{V_{ip}}$	$\frac{V_{int}}{V_{ip}}$	$\frac{\bar{V}_{int}}{V_{ip}}$	$\frac{V_c}{V_{ip}}$	$\frac{V_{ip}}{V_{int}}$	$\frac{V_{ip}}{V_{int}}$	$V_{ip} > 0.05V_{tip}, \%$
1	+T/2	+T/2	+4	200	48000	0.306	0.154	0.312	0.140	0.042	0.301	23.35
2	-T/3	-T/3	-2	200	48000	0.246	0.157	0.242	0.148	0.056	0.376	36.82
3	-	+	+	300	32000	0.141	0.095	0.139	0.088	0.041	0.459	22.42
4	-	+	-	300	32000	0.050	0.090	0.052	0.083	0.058	0.702	41.74
5	+	-	+	200	48000	0.248	0.136	0.253	0.132	0.033	0.253	13.14
6	+	-	-	200	48000	0.174	0.132	0.174	0.129	0.051	0.395	33.93
7	-	-	+	300	32000	0.053	0.091	0.051	0.083	0.042	0.510	21.89
8	-	-	-	300	32000	0.167	0.113	0.169	0.107	0.053	0.500	34.35

Table 4.4c: Experimental design and results (top corner)- RT

Run	D	C	N _r	N (rpm)	Re	$\frac{\bar{V}_{int}}{V_{tp}}$	$\frac{V_{int}}{V_{tp}}$	$\frac{\bar{V}_{int}}{V_{tp}}$	$\frac{V_{ca}}{V_{tp}}$	$\frac{V_{LF}}{V_{tp}}$	$\frac{V_{LF}}{V_{ca}}$	$V_{LF} > 0.05V_{tip}, \%$
	+T/2 -T/3	+T/2 -T/3	+4 -2									
1	+	+	+	200	48000	0.100	0.156	0.088	0.149	0.053	0.353	33.93
2	+	+	-	200	48000	0.174	0.154	0.172	0.153	0.065	0.427	45.02
3	-	+	+	300	32000	0.030	0.090	0.024	0.083	0.041	0.490	23.32
4	-	+	-	300	32000	0.081	0.100	0.071	0.096	0.064	0.667	51.50
5	+	-	+	200	48000	0.174	0.137	0.172	0.133	0.051	0.383	34.22
6	+	-	-	200	48000	0.158	0.151	0.154	0.146	0.073	0.500	46.60
7	-	-	+	300	32000	0.015	0.048	0.019	0.043	0.021	0.500	2.31
8	-	-	-	300	32000	0.048	0.072	0.038	0.066	0.033	0.510	15.24

**Table 4.5a: Comparison of different impellers (average from 8 geometries) -
impeller stream**

impeller	RT	PBT	HE3	A310
$\frac{\bar{V}_{tot}}{V_{tip}}$	0.611	0.379	0.221	0.236
$\frac{v_{tot}}{V_{tip}}$	0.369	0.123	0.053	0.084
$\frac{v_{LF}}{V_{tip}}$	0.107	0.057	0.018	0.034
deviation from 5% V_{tip} , %	55.5	33.21	1.34	14.44
$\frac{v_{LF}}{v_{tot}}$	0.282	0.444	0.341	0.389

**Table 4.5b: Comparison of different impellers (average from 8 geometries) -
bottom corner**

impeller	RT	PBT	HE3	A310
$\frac{\bar{V}_{tot}}{V_{tip}}$	0.174	0.0004	0.023	0.033
$\frac{v_{tot}}{V_{tip}}$	0.114	0.092	0.056	0.072
$\frac{v_{LF}}{V_{tip}}$	0.047	0.049	0.032	0.038
deviation from 5% V_{tip} , %	28.46	22.95	13.74	19.2
$\frac{v_{LF}}{v_{tot}}$	0.437	0.542	0.545	0.521

Table 4.5c: Comparison of different impellers (average from 8 geometries) - top corner

impeller	RT	PBT	HE3	A310
$\frac{\bar{V}_{tot}}{V_{tip}}$	0.092	0.013	0.009	0.021
$\frac{V_{tot}}{V_{tip}}$	0.109	0.057	0.035	0.044
$\frac{V_{LF}}{V_{tip}}$	0.050	0.03	0.016	0.023
deviation from 5% V_{tip} , %	31.52	12.24	0.49	5.15
$\frac{V_{LF}}{V_{tot}}$	0.479	0.520	0.444	0.523

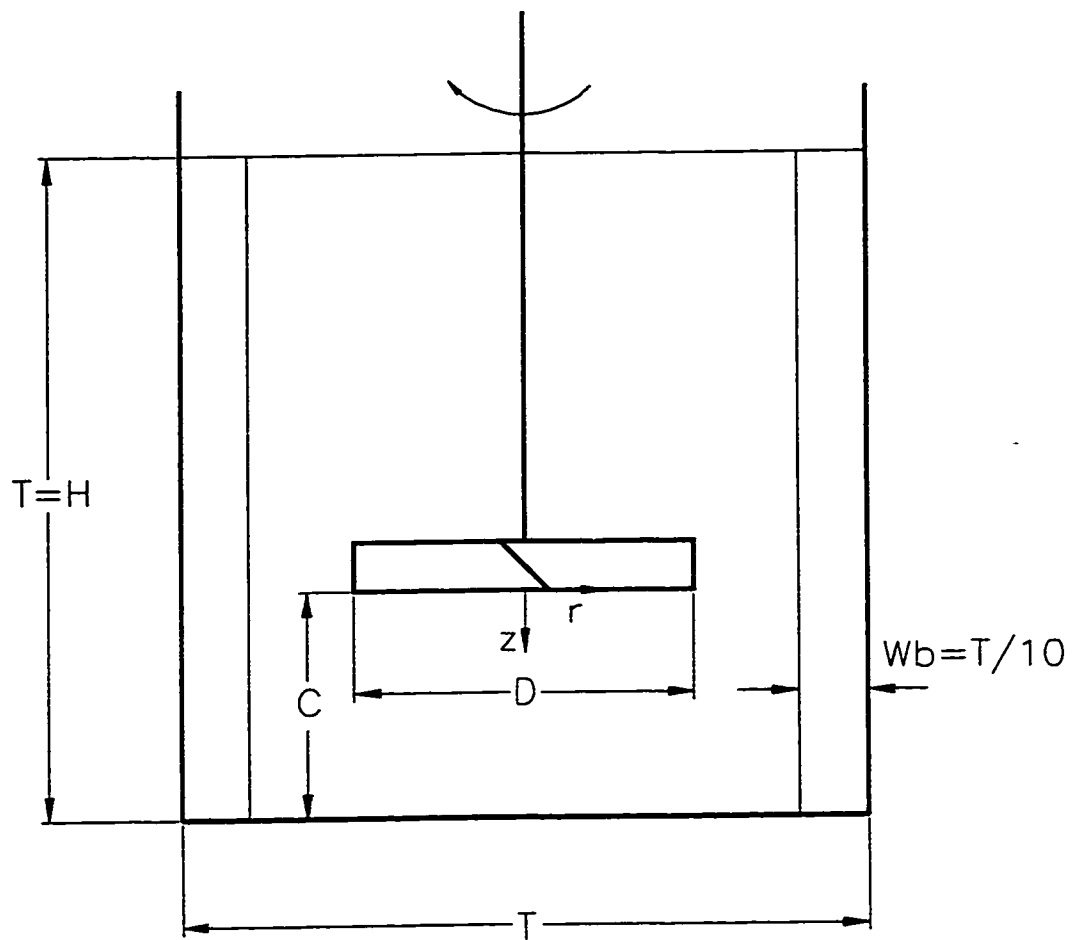


Figure 4.1: Geometry of the stirred tank used for this work.

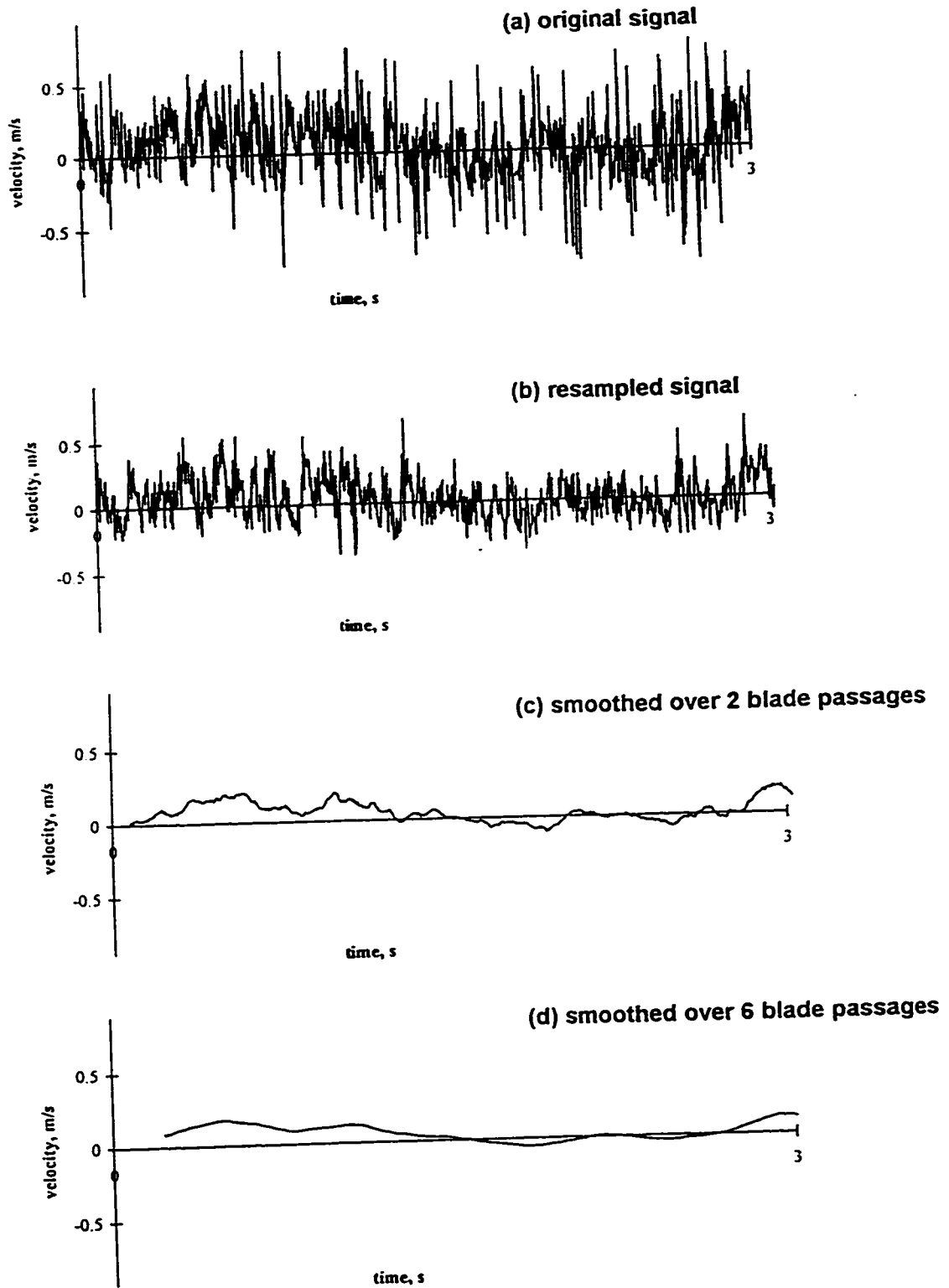


Figure 4.2: Time series of the axial velocity component (PBT impeller) after various stages of data processing.

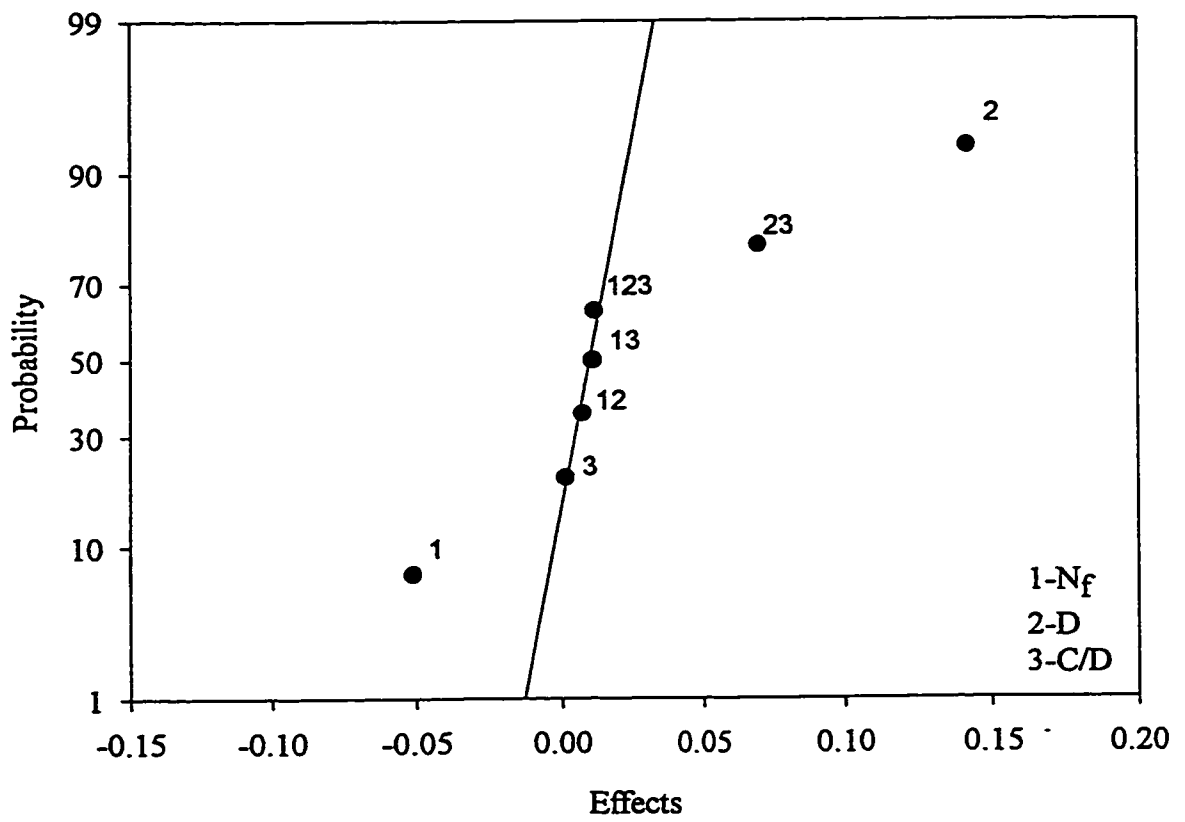


Figure 4.3: PBT, impeller stream, effects of geometric variables on v_{LF}/v_{tot}

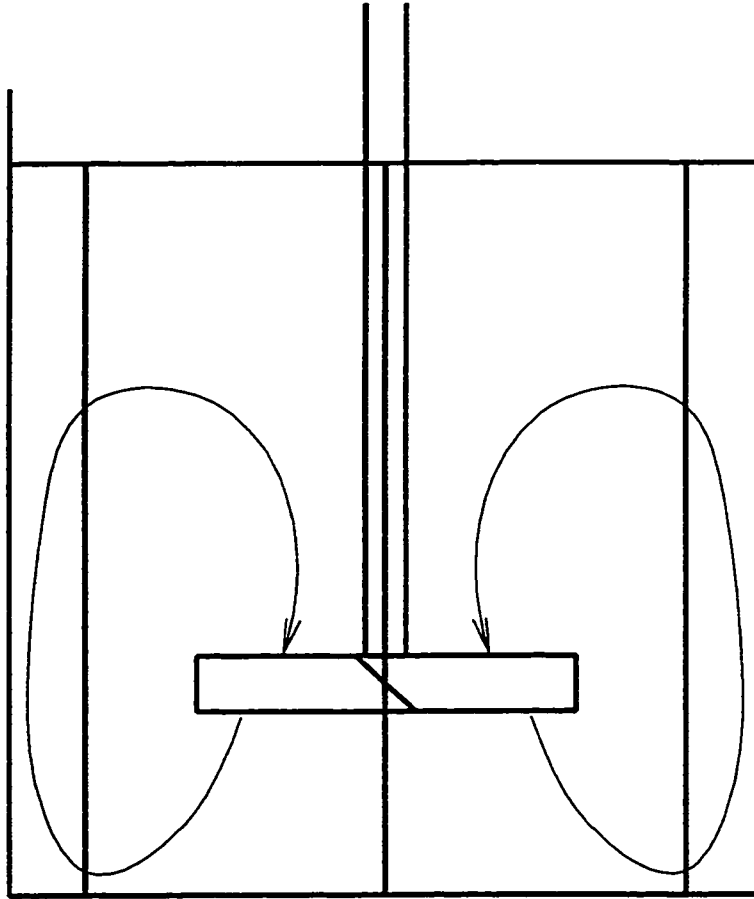


Figure 4.4a: PBT general flow pattern, $D=T/2$, $C/D=0.5$, $N_f=4$ (baffle plane).

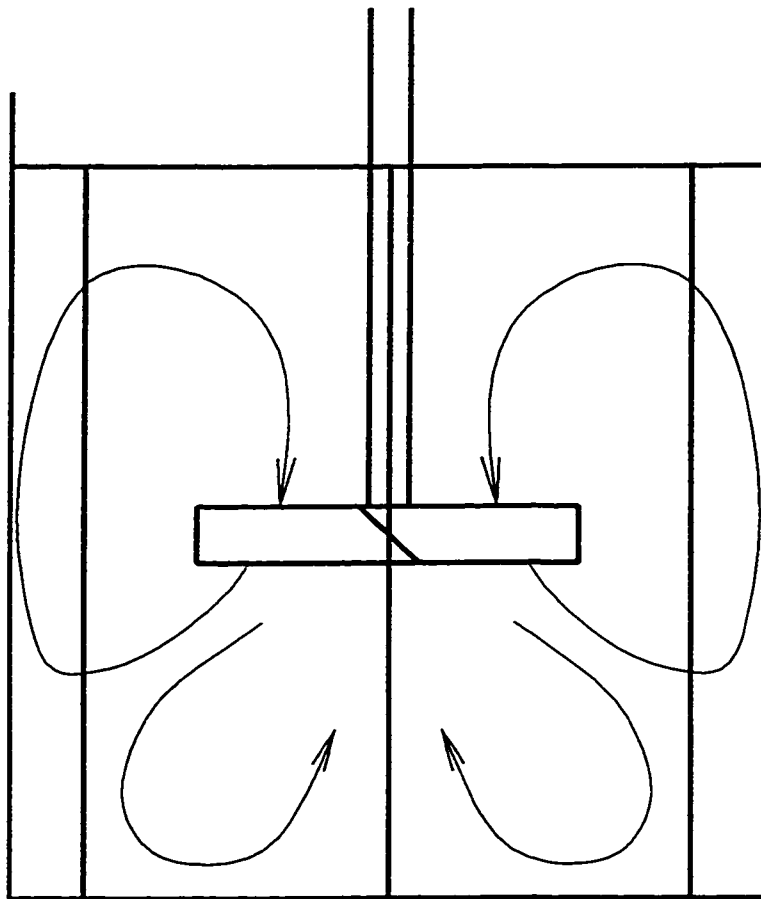


Figure 4.4b: PBT general flow pattern, $D=T/2$, $C/D=1$, $N_f=4$ (baffle plane).

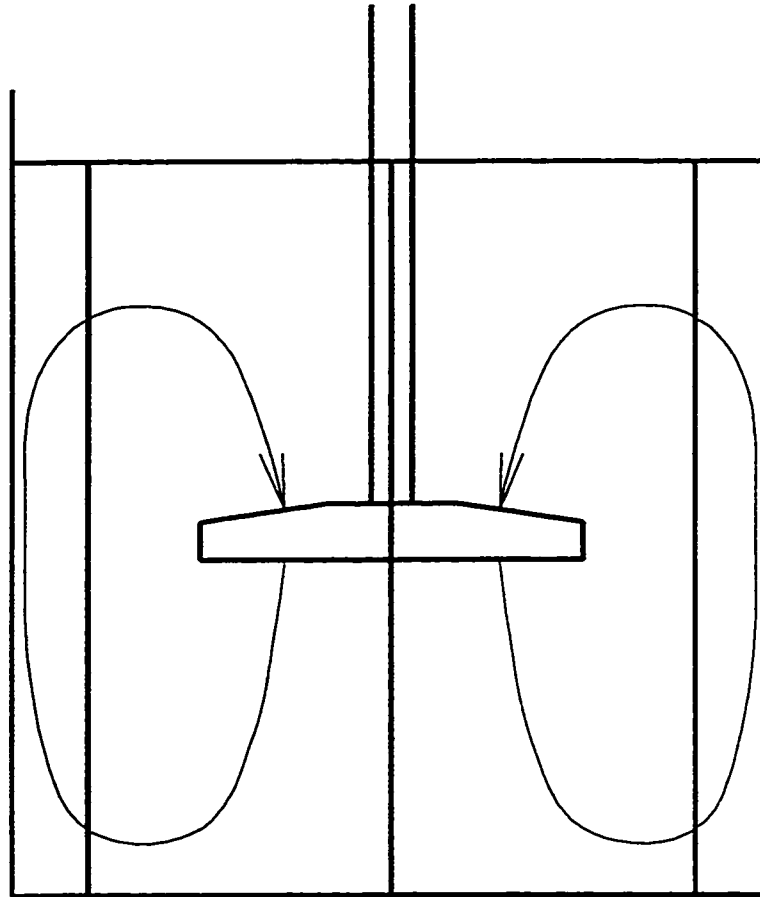


Figure 4.5: HE3 general flow pattern, $D=T/2$, $C/D=1$, $N_f=4$ (baffle plane).

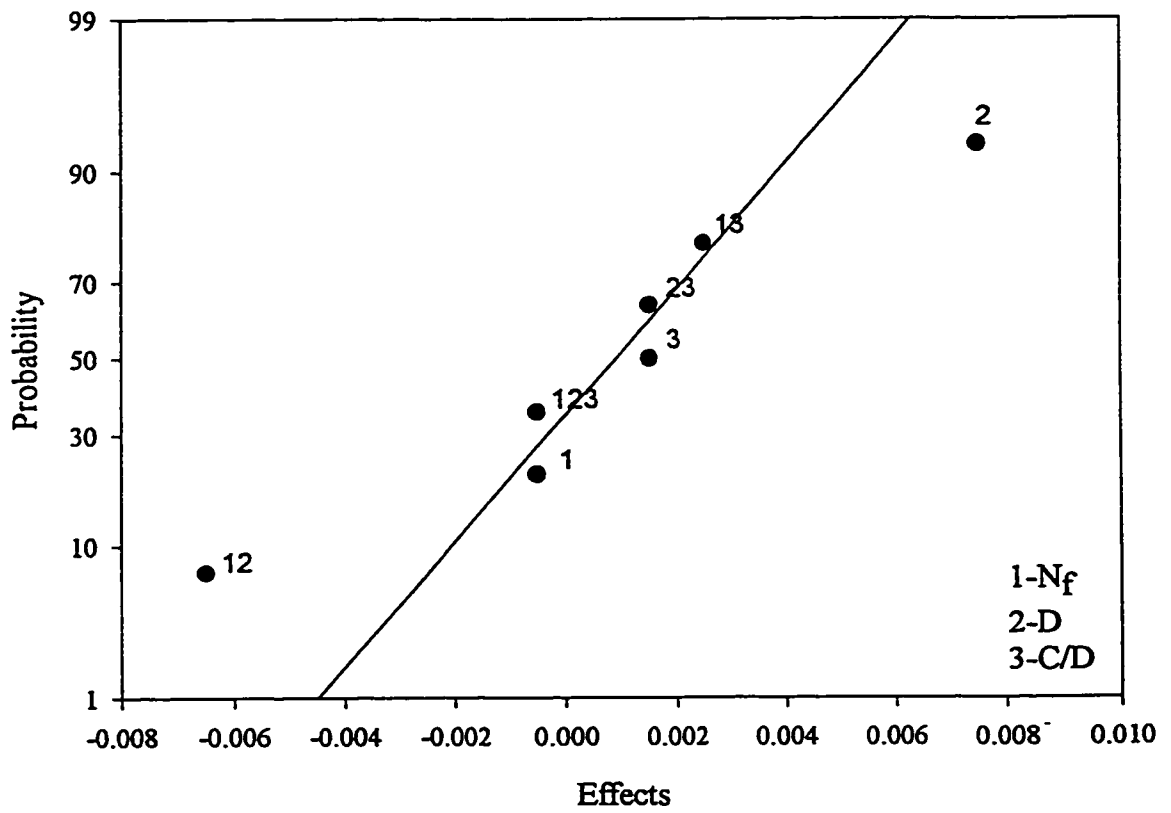


Figure 4.6: HE3, impeller stream, effects of geometric variables on v_{LF}/V_{tip} .

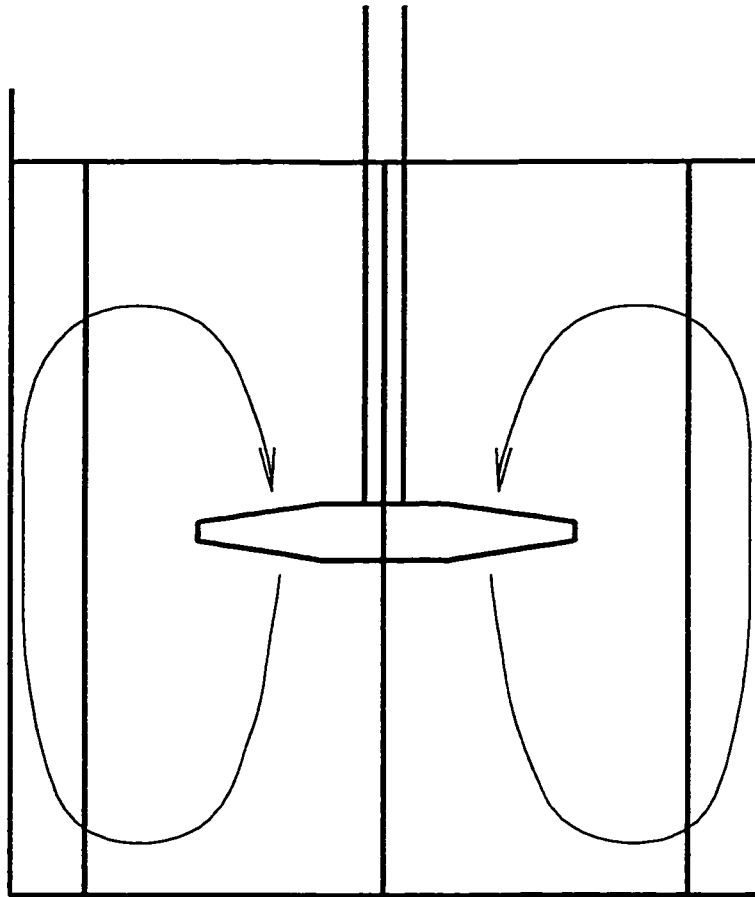


Figure 4.7: A310 general flow pattern, $D=T/2$, $C/D=1$, $N_f=4$ (baffle plane).

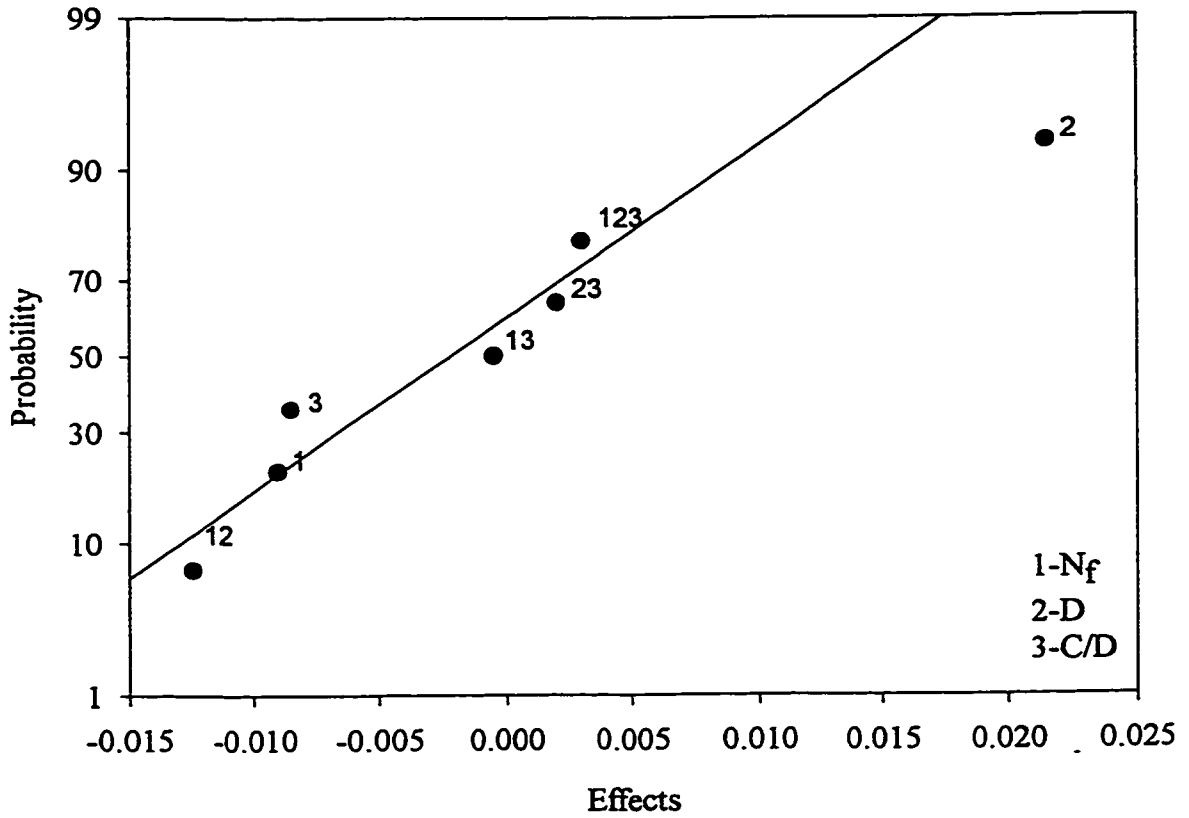


Figure 4.8: A310, impeller stream, effects of geometric variables on v_{LF}/V_{tip} .

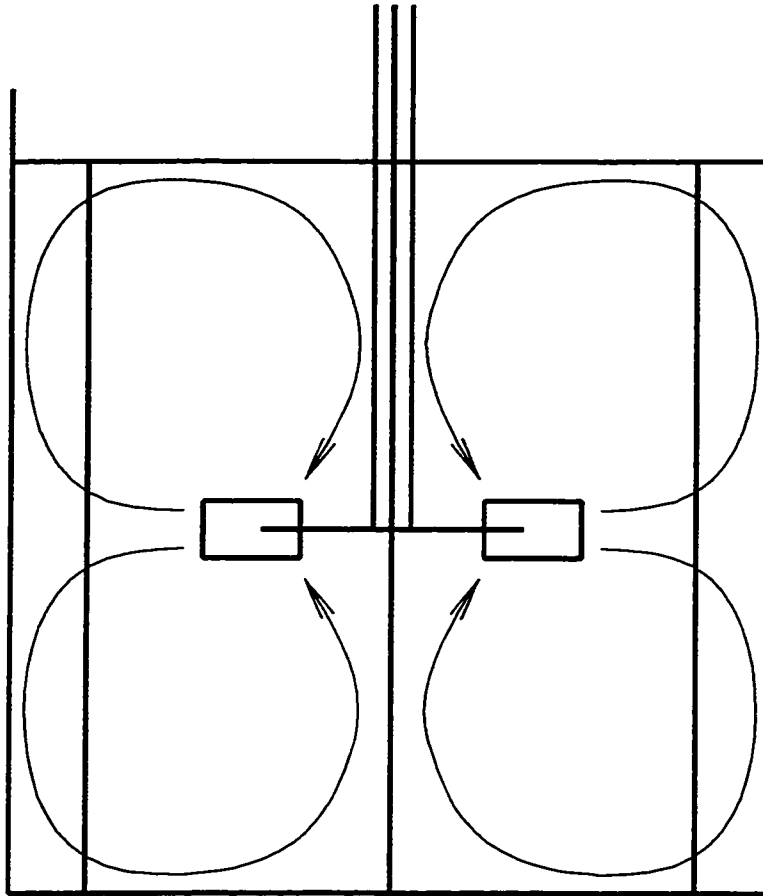


Figure 4.9: RT general flow pattern, $D=T/2$, $C/D=1$, $N_f=4$ (baffle plane).

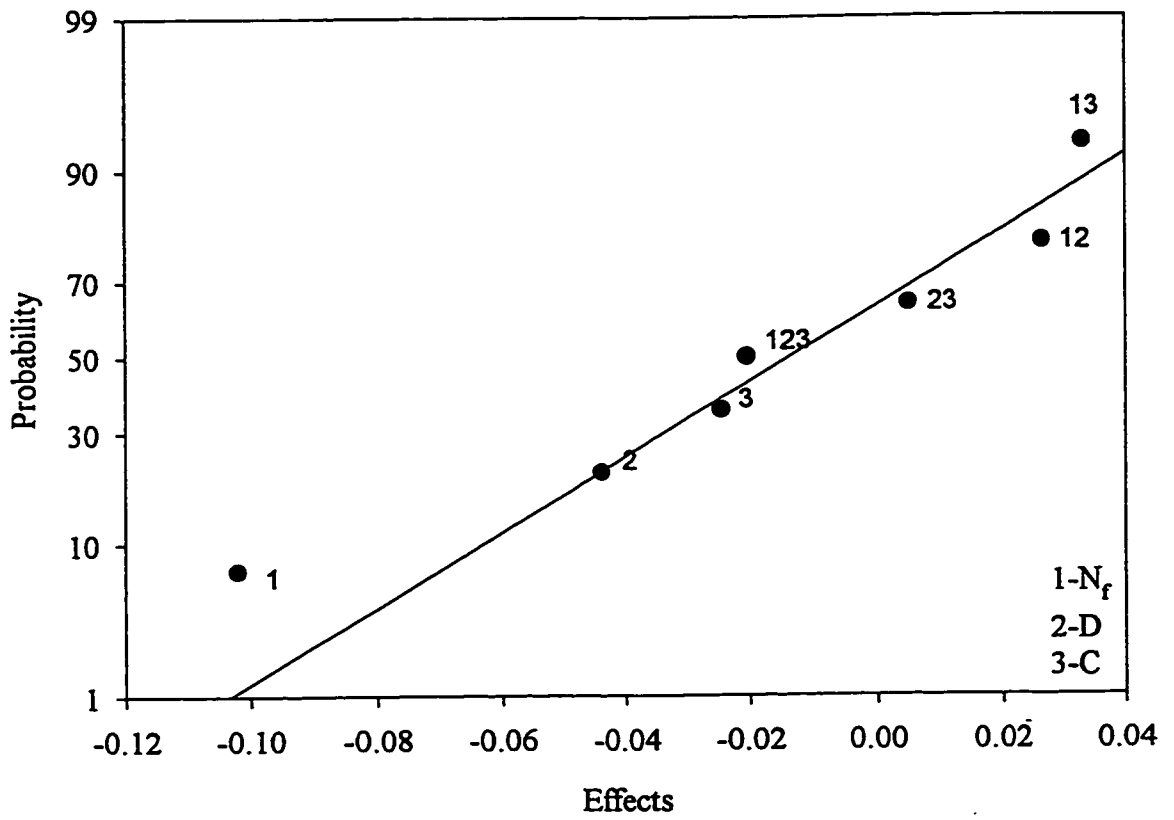


Figure 4.10: RT, impeller stream, effects of geometric variables on v_{LF}/V_{tip} .

References

Bakker, A., and H.E.A. Van den Akker, 1994, Single-Phase Flow in Stirred Reactors, *Trans. I.Chem. Eng.* **72**, 583-593.

Biron, P., Roy A.G., Best J.L., A Scheme for Resampling, Filtering and Subsampling Unevenly Spaced Laser Doppler Anemometer Data, 1995, *Mathematical Geology*, **27**, 6, 731-748.

Bittorf, K. and S.M. Kresta, 1997, *Flow Regimes in a Stirred Tank: Effective Volume of Fully Turbulent Flow*, AIChE Annual Meeting, Los Angeles, Nov 16-21.

Bruha, O., I. Fort, P. Smolka, and M. Jahoda, 1996, Experimental Study of Turbulent Macroinstabilities in an Agitated System with Axial High-Speed Impeller and with Radial Baffles, *Collect. Czech. Chem. Commun.* **61**, 856-867.

Holloway, J.L., Smoothing and filtering of time series and space fields, 1958, *Adv. Geophys.*, **4**, 351-388.

Chapman, C.M., A.W. Nienow, M. Cooke, and J.C. Middleton, 1983, Particle-Gas-Liquid Mixing in Stirred Vessel, *Chem. Eng. Res. Des.*, **61**, (parts I-IV), 71-81, 82-95, 167-181, 182-185.

Chapple, D., and S.M. Kresta, 1994, The Effect of Geometry on the Stability of Flow Patterns in Stirred Tank, *Chem. Eng. Sci.* **49**(21), 3651-3660.

Haam, S., R.S. Brodkey, and J. Fasano, 1992, Local Heat Transfer in a Mixing Vessel Using Heat Flux Sensors, *Industrial and Engineering Chemistry Research*, **31**, 1384-1391.

Hockey, R.M., and J.M. Nouri, 1996, Turbulent Flow in a Baffled Vessel Stirred by a 60° Pitched Blade Impeller, *Chem. Eng. Sci.* **51**, No. 19, 4405-4421.

Ibrahim, S.B., and A.W. Nienow, 1995, Power Curves and Flow Patterns for a Range of Impellers in Newtonian Fluids: $40 < \text{Re} < 5 \times 10^5$, *Trans. Inst. Chem. Eng.* **73**, Part A, 485-491.

Jaworski, Z., A.W. Nienow, and K.N. Dyster, 1996, An LDA Study of the Turbulent Flow Field in a Baffled Vessel Agitated by an Axial, Down-Pumping Hydrofoil Impeller, *Can. J. Chem. Eng.* **74**, 3-15.

Kresta, S.M., 1991, *Characterization, Measurement, and Prediction of the Turbulent Flow in Stirred Tanks*, Ph.D. thesis, McMaster University, Hamilton, Ontario.

Kresta, S.M. and P.E. Wood, 1993a, The Flow Field Produced by a Pitched Blade Turbine: Characterization of the Turbulence and Estimation of the Dissipation Rate, *Chem. Eng. Sci.* **48**, 1761-1774.

Kresta, S.M. and P.E. Wood, 1993b, The Mean Flow Field Produced by a 45° Pitched Blade Turbine: Changes in the Circulation Pattern due to Off-bottom Clearance, *Can. J. Chem. Eng.* **71**, 42-53.

Kresta, S.M., *Mixing notes*, 1998.

Kresta, S.M., 1998, Turbulence in Stirred Tanks: Anisotropic, Approximate, and Applied, *Can. J. Chem. Eng.* (submitted).

Mavros, P., C. Xuereb, and J. Bertrand, 1996, Determination of 3D-Flow Fields in Agitated Vessels by Laser Doppler Velocimetry: Effect of the Impeller Type and Liquid Viscosity on Liquid Flow Patterns, *Trans. I. Chem. E.* **74**, Part A, 658-668.

McFarlane, K., and A.W. Nienow, 1995, Studies of High Solidity Ratio Hydrofoil Impellers for Aerated Bioreactors, *Biotechnol. Prog.* **11**, 601-607.

Mishra, V.V., and J.B. Joshi, 1993, Flow Generated by a Disc Turbine: Part II: Effect of Impeller Diameter, Impeller Location and Comparison with Other Radial Flow Turbines, *Chem. Eng. Res. Des.* **71**, Part A, 563-573.

Myers, K.J., R.W. Ward, and A. Bakker, 1997, A digital particle image velocimetry investigation of flow field instabilities of axial flow impellers, *J. Fluids Eng.*, **119**, 623-632.

Nouri, J.M., and J.H. Whitelaw, 1990, Flow Characteristics of Stirred Reactors with Newtonian and Non-Newtonian Fluids, *AIChE Journal*, **36**, 627-629.

Ranade, V.V., and J.B. Joshi, 1989, Flow Generated by Pitched Blade Turbines I: Measurement Using Laser Doppler Anemometer, *Chem. Eng. Comm.* **81**, 197-224.

Rao, M.A and R.S. Brodkey, 1972, Continuous Flow Stirred Tank Turbulence Parameters in the Impeller Stream, *Chem. Eng. Sci.*, **27**, 137-156.

Wernersson, E.S., 1997, Some Fluid Dynamic Characteristics in the Scale-up of Rushton Turbine-agitated Tanks, Ph.D. Thesis, Lund University, Sweden.

Wu, H. and G.K. Patterson, 1989, Laser Doppler Measurement of Turbulent Flow Parameters in a Stirred Mixer, *Chem. Eng. Sci.*, **44**, 2207-2221.

Yianneskis, M., Z. Popiolek, and J.H. Whitelaw, 1987, An Experimental Study of the Steady and Unsteady Flow Characteristics of Stirred Reactors, *J. Fluid Mech.* **175**, 537-55.

Zhou, G. and S.M. Kresta, 1996, Impact of the Tank Geometry on the Maximum Turbulence Energy Dissipation Rate for Impellers, *A.I.Ch.E. Journal* **42**, 2476-2490.

Zhou, G., 1996, *Characteristics of Turbulence Energy Dissipation and Liquid-Liquid Dispersions in an Agitated Tanks*, Ph.D. thesis, University of Alberta, Edmonton, Alberta.

Chapter 5. Conclusions and recommendations

This study was undertaken to examine the time varying (nonstationary) characteristics of the flow field or low frequencies in the stirred tank. The four impellers used were: three axial impellers; the pitched blade turbine (PBT), the hydrofoil (A310), and the high efficiency (HE3); and one radial impeller, the Rushton turbine (RT).

Two data analysis techniques were used: frequency analysis and data smoothing. Frequency analysis shows that the current signal processing units (DSA and RSA) cannot resolve high frequency (turbulent) fluctuations. Further modifications for measuring small Doppler frequencies are necessary, such as better time resolution of the Doppler burst, and a lower shift and mixer frequencies.

The second approach (data smoothing) was applied to analyze the effect of different tank and impeller geometries on the flow stability. The effect of the tank geometry: number of baffles N_f , impeller diameter D , and off bottom clearance, C (for the RT) and C/D (for axial impellers), on flow stability was investigated. The flow stability was characterized in terms of the intensity of the low frequencies (ratio of the RMS smoothed velocity profile v_{LF} over the RMS of the initial velocity record) and magnitude of the low frequency component (ratio of the RMS

smoothed velocity profile over impeller tip velocity V_{tip}). The most important variable affecting flow stability is the impeller diameter D . The number of baffles, N_b , is the second most important variable in flow stability. The axial impellers: PBT ($0.502v_{tot}$), A310 ($0.478v_{tot}$) and HE3 ($0.443v_{tot}$) exhibit a higher intensity instabilities compared to the radial RT impeller ($0.399v_{tot}$). In terms of the magnitude of forces the flow instabilities exert on the internals, the RT ($0.068V_{tip}$) is the largest, followed by the PBT ($0.045V_{tip}$), then the A310 ($0.032V_{tip}$), and the HE3 ($0.022V_{tip}$).

From this study, the following opportunities for further research exist. These include:

- flow visualization using different tank and impeller geometries to analyze the general flow pattern and flow stability for different geometric configurations.
- optimization of the length of the measurements for each impeller in order to get: more repeatable results and to cover more cycles of the low frequency fluctuations and blade passage cycles. This will allow estimation of the RMS velocity due to the blade passages to the total (measured) RMS velocity and accurate calculations of the 95%CI.
- effect of the flow regime on flow stability in a stirred tank using different rpms and fluids of different (higher than water) viscosities. This will help in determining the origin of the low frequency phenomenon.

Appendix A I Algorithms used for spectral analysis

```
c          Slotted technique

c program main
c   This program computes a binned estimate of the autocorrelation
c   function, and employs the result to estimate the power spectrum
c   using a Fast Fourier Transform.

c   General:
c
c   ndata: number of data points
c   t(i): time of arrival of particle i
c   u(i): velocity of particle i
c   uavg: average velocity

c   Autocorrelation
c
c   del: slot size
c   avgdr: average data rate
c   asmp: desired average number of data samples per bin
c   it(i): integer time in units of slot size
c   itmax: max abscisa used in autocorrelation
c   num(i): number of points counted in slot i
c   prod(i): autocorrelation for integer time i
c   nn: number of points that will be used in fourier transform
c   iexp: nn = 2**(iexp -1)

parameter (idim=10000)

integer ndata, nn, iexp ,num(0:idim)
real t(0:idim),it(0:idim),u(0:idim),prod(0:idim),ans(0:idim)
c complex*8 c(idim/2+1)
c equivalence (c,prod)
c character*8 file

c*****
c   Initialization
c*****
```

```

asmp=1

c initialize accumulators
do i = 0, idim
  prod(i) = 0.0
  num(i)=0.0
end do

itmax = 0

c*****
c read in the data, and readjust time to begin at zero
c*****

open(1,file='dsaraw01')
read(1,*) u(0), t(0)
ndata=0
5 read(1,*,end=1001) u(ndata+1),t(ndata+1)
t(ndata+1) = t(ndata+1)-t(0)
ndata=ndata+1
go to 5
1001 continue
close(1)
t(0) = 0
if(ndata.eq.0)then
  write(*,*) 'Error, only one data point found'
  stop
endif
write(*,*) ndata+1, ' points read'
write(*,*) 'maximum time =', t(ndata)
close(1)

c*****
c calculate approximate mean and subtract it from the data
c also, compute variance
c simple average implemented.
c*****

sum = 0.
do i = 0,ndata
  sum = sum + u(i)
end do

```

```
uavg = sum/(ndata+1)
```

```
c Calculate RMS
```

```
do i=0,ndata
u(i)=u(i)-uavg
sm=sm+u(i)*u(i)
end do
rms=sqrt(sm/ndata)
```

```
write(*,*) 'root mean squared = ',rms
```

```
do i = 0,ndata
u(i) = u(i) - uavg
end do
```

```
write(*,*) 'average velocity =', uavg
```

```
c*****
c calculate the average data rate, avgdr, and the slot size, del
c convert the time into an integer time (at) in terms of slot size units
c*****
```

```
avgdr = (ndata+1)/t(ndata)
del = asmp/avgdr
do i = 0, ndata
it(i) = t(i)/del
end do
```

```
c*****
c Compute the autocorrelation
c limit u(i) to half the time, and the search for half the
c time.
c*****
```

```
i=0
25 if (it(i) .le. (it(ndata)/2)) then
num(0) = num(0) + 1
prod(0) = prod(0) + u(i)*u(i)

j=i+1
49 if ((it(j)-it(i).le.it(ndata)/2) .and. (j.le.ndata)) then
itdelta = it(j) - it(i)
if (itdelta.gt. itmax) itmax =itdelta
num(itdelta) = num(itdelta) + 1
```

```

        prod(itdelta) = prod(itdelta) + u(i)*u(j)
        j=j+1
        goto 49
    end if
    i=i+1
    goto 25
end if

c*****
c    normalize each bin by the number of points in the bin and the value
c    at bin 0
c*****

    if (prod(0).eq.0) then
        write(*,*) 'Error: zero variance?'
    end if

    prod(0)=prod(0)/num(0)
    do i=1,itmax
        if (num(i).ne.0) prod(i)=prod(i)/num(i)/prod(0)
    end do
    prod(0)=1.

    write(*,*) 'Autocorrelation completed'
    write(*,*) itmax, ' bins used'
    write(*,*) 'Writing autocorrelation in file AUTOCORR'
    open(1,file='AUTOCORR')
    do i=0,itmax
        write(1,*) del*i,prod(i)
    end do
c    write(1,*) 'join'
    close(1)
c*****
c    Determine the closest power of 2 to itmax
c*****

    iexp = int( (log(float(itmax))) / log(2.)) + 1
    if (2**(iexp-1) .eq. itmax) then
        iexp = iexp-1
    end if
    nn=2**(iexp-1)
    write(*,*) '2**',iexp-1, '=',nn, ' points will be used for fft'

```

```

c*****
c  call the cosft routine and output
c*****
    call cosft(prod,nn,1)
    write(*,*) 'FFT completed'
    write(*,*) 'Writing power spectrum in file SPECTRUM'

    open(1,file='SPECTRUM')
    do 23 i = 1,nn-2,2
        delta = ((i+1)/2)/del/(2**(iexp-1))
        sp=prod(i)*prod(i)+prod(i+1)*prod(i+1)
        sp=sp/float(nn*(ndata+1))
        write(1,107) delta,sp
107  format(2x,f17.10,3x,f17.10)
23  continue
    close(2)

c*****
c  call the filter routine
c*****

    call filter(prod,nn,del)
    write(*,*) 'Filtered first frequency'
    write(*,*) 'Writing filtered spectrum data in file FILTER1'
    open(3,file='FILTER1')
    do 24 i=1,nn-2,2
        delta= ((i+1)/2)/del/(2**(iexp-1))
        sp=prod(i)*prod(i)+prod(i+1)*prod(i+1)
        sp=sp/float(nn*(ndata+1))
        write(3,17) delta,sp
17  format(2x,f17.10,5x,f17.10)
24  continue
    close(3)

    call filter(prod,nn,del)
    write(*,*) 'Filtered second frequency'
    write(*,*) 'Writing filtered spectrum in file FILTER2'
    open(4,file='FILTER2')
    do 26 i=1,nn-2,2
        delta= ((i+1)/2)/del/(2**(iexp-1))
        fl=prod(i)*prod(i)+prod(i+1)*prod(i+1)
        fl=fl/float(nn*(ndata+1))
        freq=delta
        write(4,*)delta,fl

```

```

19  format(5x,f17.10,5x,f17.10)
26  continue
    close(4)
end

```

```

c*****
c Notch filtering
c*****

```

```

subroutine filter(y,n,del)
  real w0,c0,c1,c2,d1,d2,fa,fb,pi,bottom,del
  real fdelta,sin1,sin2,cos1,cos2,renum,reden,imnum,imden
  real hre,him,fftre,fftim,y(n),a,b

```

```

c Enter filtering parameters

```

```

  print*, 'center of frequency notch '
  read*, f0
  print*, 'width of frequency notch, as fraction of fa'
  read*, eps
  pi=acos(-1.0)
  w0=tan(pi*del*f0)
  bottom=(1+eps*w0)**2+w0**2
  c0=(1+w0*w0)/bottom
  c1=-2*(1-w0*w0)/bottom
  c2=(1+w0*w0)/bottom
  d1=2*(1-eps*eps*w0*w0-w0*w0)/bottom
  d2=-((1-eps*w0)**2+w0*w0)/bottom

```

```

c Loop to apply filter

```

```

  do 10 i=1,n-1,2

```

```

c Calculate real and imaginary parts of numerator and denominator

```

```

  fdelta=float(i)/4/float(n)
  sin1=sin(2*pi*fdelta)
  sin2=sin(4*pi*fdelta)
  cos1=cos(2*pi*fdelta)
  cos2=cos(4*pi*fdelta)
  renum=c0+c1*cos1+c2*cos2
  reden=1-d1*cos1-d2*cos2
  imnum=-(c1*sin1+c2*sin2)
  imden=d1*sin1+d2*sin2

```

```

c Calculate real and imaginary parts of filter

```

```

  hre=(renum*reden+imnum*imden)/(reden*reden+imden*imden)
  him=(imnum*reden-renum*imden)/(reden*reden+imden*imden)

```

```

c Apply filter

```

```

  fftre=y(i)

```



```

    fftim=y(i+1)
    y(i)=(fftre*hre-fftim*him)
    y(i+1)=(fftre*him+fftim*hre)
10  continue
return
end

subroutine cosft(y,n,isign)
real*8 wr,wi,wpr,wpi,wtemp,theta
dimension y(n)
theta=3.14159265358979d0/dble(n)
wr=1.0d0
wi=0.0d0
wpr=-2.0d0*dsin(0.5d0*theta)**2
wpi=dsin(theta)
sum=y(1)
m=n/2
do 11 j=1,m-1
wtemp=wr
wr=wr*wpr-wi*wpi+wr
wi=wi*wpr+wtemp*wpi+wi
y1=0.5*(y(j+1)+y(n-j+1))
y2=(y(j+1)-y(n-j+1))
y(j+1)=y1-wi*y2
y(n-j+1)=y1+wi*y2
sum=sum+wr*y2
11  continue
call realft(y,m,+1)
y(2)=sum
do 12 j=4,n,2
sum=sum+y(j)
y(j)=sum
12  continue
if (isign.eq.-1) then
even=y(1)
odd=y(2)
do 13 i=3,n-1,2
even=even+y(i)
odd=odd+y(i+1)
13  continue
enf0=2.0*(even-odd)
sumo=y(1)-enf0
sume=(2.0*odd/float(n))-sumo
y(1)=0.5*enf0
y(2)=y(2)-sume

```

```

do 14 i=3,n-1,2
  y(i)=y(i)-sumo
  y(i+1)=y(i+1)-sume
14 continue
endif
return
end

```

```

subroutine realft(data,n,isign)

```

```

parameter (idim=10000)
real*8 wr,wi,wpr,wpi,wtemp,theta
real data(2*n)
theta=6.28318530717959d0/2.0d0/dble(n)
wr=1.0d0
wi=0.0d0
c1=0.5
if (isign.eq.1) then
  c2=-0.5
  call four1(data,n,+1)
  data(2*n+1)=data(1)
  data(2*n+2)=data(2)
else
  c2=0.5
  theta=-theta
  data(2*n+1)=data(2)
  data(2*n+2)=0.0
  data(2)=0.0
endif
wpr=-2.0d0*dsin(0.5d0*theta)**2
wpi=dsin(theta)
n2p3=2*n+3
do 11 i=2,n/2+1
  i1=2*i-1
  i2=i1+1
  i3=n2p3-i2
  i4=i3+1
  wrs=sngl(wr)
  wis=sngl(wi)
  h1r=c1*(data(i1)+data(i3))
  h1i=c1*(data(i2)-data(i4))
  h2r=-c2*(data(i2)+data(i4))
  h2i=c2*(data(i1)-data(i3))
  data(i1)=h1r+wrs*h2r-wis*h2i
  data(i2)=h1i+wrs*h2i+wis*h2r

```

```

    data(i3)=h1r-wrs*h2r+wis*h2i
    data(i4)=-h1i+wrs*h2i+wis*h2r
    wtemp=wr
    wr=wr*wpr-wi*wpi+wr
    wi=wi*wpr+wtemp*wpi+wi
11  continue
    if (isign.eq.1) then
    data(2)=data(2*n+1)
    else
    h1r=data(1)
    call four1(data,n,-1)
    endif
    return
    end

```

```

SUBROUTINE FOUR1(DATA,NN,ISIGN)
REAL*8 WR,WL,WPR,WPI,WTEMP,THETA

```

```

parameter (idim=10000)

```

```

DIMENSION DATA(2*NN)
N=2*NN
J=1
DO 11 I=1,N,2
    IF(J.GT.I)THEN
        TEMPR=DATA(J)
        TEMPI=DATA(J+1)
        DATA(J)=DATA(I)
        DATA(J+1)=DATA(I+1)
        DATA(I)=TEMPR
        DATA(I+1)=TEMPI
    ENDIF
    M=N/2
1  IF ((M.GE.2).AND.(J.GT.M)) THEN
        J=J-M
        M=M/2
        GO TO 1
    ENDIF
    J=J+M
11  CONTINUE
MMAX=2
2  IF (N.GT.MMAX) THEN
        ISTEP=2*MMAX
        THETA=6.28318530717959D0/(ISIGN*MMAX)

```

```

WPR=-2.D0*DSIN(0.5D0*THETA)**2
WPI=DSIN(THETA)
WR=1.D0
WI=0.D0
DO 13 M=1,MMAX,2
  DO 12 I=M,N,ISTEP
    J=I+MMAX
    TEMPR=SNGL(WR)*DATA(J)-SNGL(WI)*DATA(J+1)
    TEMPI=SNGL(WR)*DATA(J+1)+SNGL(WI)*DATA(J)
    DATA(J)=DATA(I)-TEMPR
    DATA(J+1)=DATA(I+1)-TEMPI
    DATA(I)=DATA(I)+TEMPR
    DATA(I+1)=DATA(I+1)+TEMPI
12  CONTINUE
    WTEMP=WR
    WR=WR*WPR-WI*WPI+WR
    WI=WI*WPR+WTEMP*WPI+WI
13  CONTINUE
    MMAX=ISTEP
GO TO 2
ENDIF
RETURN
END

```

C DFT code

c This program calculates Discrete Fourier Transform

c sf is the sampling frequency
c ndata is the number of used points
c j is the point in the frequency domain
c i is the point in the time domain
c e1 is the power spectral density

```
      real u(8200),y(8200),t(8200),dft(8200)
      integer ndata,i,j
      open(1,file='dsaraw')
      ndata=1
5     read(1,7,end=101) u(ndata+1),t(ndata+1)
7     format(1x,e17.6,2x,e17.6)
c     print*,u(ndata+1),t(ndata+1)
      ndata=ndata+1
      go to 5
101  continue
      write(*,*) ndata,'points read'
      write(*,*) t(ndata),'is the maximum time'
      sf=ndata/t(ndata)
      close(1)
      write(*,*)'Writing power spectrum in file DFT'
      open(2,file='DFT')

      do 10 j=1,ndata/2
      delta=t(j+1)-t(j)
      e1=0
      do 11 i=1,ndata/2
          yr=u(i)*cos(6.283185*i*j/ndata)*delta
          yi=u(i)*sin(6.283185*i*j/ndata)*delta
          y(i)=(yr*yr+yi*yi)
          e1=e1+y(i)
11     continue
      freq=j/float(ndata)*sf
      write(2,*) freq,e1/(ndata-1)
10     continue
      close(2)
      end
```

c FFT code

C Calculates the autocorrelation of a time series of data

c using FFT (fast Fourier transforms) from Numerical Recipes

c FOUR1 pg 394; REALFT pg 400

c The energy spectrum (power spectral density) can be obtained at midway

C General algorithm:

c DATA -> FFT -> FFT*complex conjugate -> inverse FFT -> autocorrelation

c -> E1 (power spectrum)

C -> filter in Fourier domain

c Filtering is done using a notch filter as described on pg 442

IMPLICIT NONE

REAL TSR(8192), FFT(8192),ANS(8192),MEAN,SUM,RMS,SF

INTEGER DATPTS,J,N,CHOICE,I,OLD

CHARACTER*7 FILE

c Set N=16384 to accomodate 10000 data points.

c This allows a 6384 lag autocorrelation.

N=2048

c Open data file

2 WRITE(*,*) 'Choose file type'

WRITE(*,*) '1) New time series input file'

WRITE(*,*) '2) Old FFT input file'

READ*,OLD

WRITE(*,*) 'Input data filename? (no .TSR)'

READ(*,'(A)') FILE

IF(OLD.EQ.1)THEN

OPEN(UNIT=10,FILE='dsaraw',STATUS='OLD')

WRITE(*,*) 'Sampling frequency? (kHz)'

READ*,SF

SF=SF*1000

C Read and mean center the data

SUM=0.

DO 30 J=1,N

READ(10,*,END=10) TSR(J)

SUM=SUM+TSR(J)

30 CONTINUE

10 DATPTS=J-1

MEAN=SUM/DATPTS

SUM=0

C Calculate RMS

```

DO 40 J=1,DATPTS
  TSR(J)=TSR(J)-MEAN
  SUM=SUM+TSR(J)*TSR(J)
40  CONTINUE
  RMS=SQRT(SUM/DATPTS)
c Zero padding to obtain an array of size = power of 2 (16384)
  IF(DATPTS.LT.N)THEN
    DO 20 J=DATPTS+1,N
      TSR(J)=0.0
20  CONTINUE
  ENDIF

```

C Data processing in the Fourier domain

```

c Create working array
  DO 5 I=1,1024
    FFT(I)=TSR(I)
5  CONTINUE
c Calculate FFT of data time series TSR and return the result in FFT.
c FFT contains the positive frequency half of the complex spectrum, with
c the first and last real results stored in array elements 1 and 2.
  CALL REALFT(FFT,N,1)
  ELSEIF(OLD.EQ.2)THEN
    OPEN(UNIT=10,FILE=FILE//'.FFT',STATUS='OLD')
    READ(10,*) SF,MEAN,RMS,DATPTS
    READ(10,*,END=7) (FFT(I),FFT(I+1),FFT(I+2),FFT(I+3),I=1,16384,4)
    CLOSE(10)
7  CONTINUE
  ELSE
    GOTO 2
  ENDIF

```

C Echo parameters

```

WRITE(*,*)'Sampling frequency',SF
WRITE(*,*)'data points',DATPTS
WRITE(*,*)'Mean is',MEAN
WRITE(*,*)'RMS',RMS

```

C Print menu for data treatment

```

1  WRITE(*,*)'Choose next step'
  WRITE(*,*)'1) Store spectrum as E1'
  WRITE(*,*)'2) Apply filter'
  WRITE(*,*)'3) Calculate autocorrelation'
  WRITE(*,*)'4) Store FFT for later use'
  WRITE(*,*)'5) Calculate inverse transform'

```

```

WRITE(*,*)'6) Stop'
READ*,CHOICE
IF(CHOICE.EQ.1)THEN
  CALL SPECPRN(FFT,N,DATPTS,SF)
  GOTO 1
ELSEIF(CHOICE.EQ.2)THEN
  CALL FILTER(FFT,N,SF)
  GOTO 1
ELSEIF(CHOICE.EQ.3)THEN
  CALL AUTCOR(FFT,N,DATPTS,RMS,SF,ANS)
  GOTO 1
ELSEIF(CHOICE.EQ.4)THEN
  OPEN(UNIT=15,FILE='FFT')
  WRITE(15,*) SF,MEAN,RMS,DATPTS
  WRITE(15,*) (FFT(I),FFT(I+1),FFT(I+2),FFT(I+3),I=1,8192,4)
  CLOSE(UNIT=15)
  GOTO 1
ELSEIF(CHOICE.EQ.5)THEN
  CALL FOUR1(FFT,N,-1)
  GOTO 1
  ELSEIF(CHOICE.EQ.6)THEN
    GOTO 999
ELSE
  GOTO 1
ENDIF
999 STOP
END

```

```

SUBROUTINE AUTCOR(FFT,N,DATPTS,RMS,SF,ANS)
c Calculate autocorrelation using real vectors only (store real and
c complex parts in adjacent elements)
C Modified from CORREL in Numerical Recipes (pg 416)
  REAL ANS(N),RMS,FFT(N),TIME
  CHARACTER*7 FILE
  INTEGER DATPTS
C Open file for printing of autocorrelation results
  PRINT*, 'Filename for autocorrelation storage? (7 char, no ext)'
  READ(*,'(A)') FILE
  OPEN(UNIT=11,FILE='COR')
c Normalize in advance for the inverse transform
  NO2=N/2
C Calculate the Fourier pair of the autocorrelation, which is F(f)F(f)*
c (the Fourier transform times its complex conjugate)
  ANS(1)=FFT(1)*FFT(1)/FLOAT(NO2)

```



```

ANS(2)=FFT(2)*FFT(2)/FLOAT(NO2)
DO 11 I=3,N-1,2
  TEMP=(FFT(I)*FFT(I)+FFT(I+1)*FFT(I+1))
  ANS(I)=TEMP/FLOAT(NO2)
  ANS(I+1)=0
11 CONTINUE
C ANS is a real array of length N/2 which contains the Fourier pair.
c REALFT calculates the inverse Fourier transform, returning it in ANS.
  CALL REALFT(ANS,NO2,-1)
c Step size for printing of result
C  JMAX=N-DATPTS
C Set for length of 1 second
C  J=SF+1
C  IF(J.GT.JMAX) J=JMAX
  J=N-DATPTS
  STEP=NINT(REAL(J)/500)
c Complete normalization of the autocorrelation coefficient, and write
DO 50 K=1,J,STEP
  TIME=(K-1)/SF
  WRITE(11,*) K,TIME,ANS(K)/(RMS**2*DAPPTS)
50 CONTINUE
CLOSE(UNIT=11)
RETURN
END

```

```

SUBROUTINE REALFT(DATA,N,ISIGN)
REAL*8 WR,WI,WPR,WPI,WTEMP,THETA
REAL DATA(2*N)
THETA=3.141592653589793D0/DBLE(N)
C1=0.5
IF (ISIGN.EQ.1) THEN
  C2=-0.5
  CALL FOUR1(DATA,N,+1)
ELSE
  C2=0.5
  THETA=-THETA
ENDIF
WPR=-2.0D0*DSIN(0.5D0*THETA)**2
WPI=DSIN(THETA)
WR=1.0D0+WPR
WI=WPI
N2P3=2*N+3
DO 11 I=2,N/2
  I1=2*I-1

```

```

I2=I1+1
I3=N2P3-I2
I4=I3+1
WRS=SNGL(WR)
WIS=SNGL(WI)
HIR=C1*(DATA(I1)+DATA(I3))
HII=C1*(DATA(I2)-DATA(I4))
H2R=-C2*(DATA(I2)+DATA(I4))
H2I=C2*(DATA(I1)-DATA(I3))
DATA(I1)=HIR+WRS*H2R-WIS*H2I
DATA(I2)=HII+WRS*H2I+WIS*H2R
DATA(I3)=HIR-WRS*H2R+WIS*H2I
DATA(I4)=-HII+WRS*H2I+WIS*H2R
WTEMP=WR
WR=WR*WPR-WI*WPI+WR
WI=WI*WPR+WTEMP*WPI+WI
11 CONTINUE
IF (ISIGN.EQ.1) THEN
  HIR=DATA(1)
  DATA(1)=HIR+DATA(2)
  DATA(2)=HIR-DATA(2)
ELSE
  HIR=DATA(1)
  DATA(1)=C1*(HIR+DATA(2))
  DATA(2)=C1*(HIR-DATA(2))
  CALL FOUR1(DATA,N,-1)
ENDIF
RETURN
END

SUBROUTINE FOUR1(DATA,NN,ISIGN)
REAL*8 WR,WI,WPR,WPI,WTEMP,THETA
REAL DATA(2*NN)
N=2*NN
J=1
DO 11 I=1,N,2
  IF(J.GT.I)THEN
    TEMPR=DATA(J)
    TEMPI=DATA(J+1)
    DATA(J)=DATA(I)
    DATA(J+1)=DATA(I+1)
    DATA(I)=TEMPR
    DATA(I+1)=TEMPI
  ENDIF

```

```

3   CONTINUE
    RMS=SQRT(E1/N**2)
    WRITE(*,*)'RMS from FFT routine',RMS
    OPEN(UNIT=12,FILE='SPC')
c Calculate printing step size
  STEP=2
  J=N
1   IF(J.GT.1024)THEN
    J=J/2
    STEP=STEP*2
    GOTO 1
  ENDIF
  WRITE(12,*) 'STEP,FREQUENCY,E(f)'
c Calculate the power spectrum, which is the FFT divided by the
c number of actual data points and the total number of points (after
c zero padding) to give E1.

```

```

    LAST=SPEC(2)*SPEC(2)
    SPEC(2)=0
    SUM=0+LAST
    DO 10 I=1,N,STEP
      E1=0
      DO 100 K=I,I+STEP-1
        AACONG=(SPEC(I)*SPEC(I)+SPEC(I+1)*SPEC(I+1))
        E1=E1+AACONG/FLOAT(N*DAPTPTS)
100  CONTINUE
      FREQ=FLOAT((I-1)/2)/FLOAT(N)*SF
      WRITE(12,*) FREQ,E1
c Calculate integral
    SUM=SUM+E1
10  CONTINUE
    CLOSE(12)
    RETURN
  END

```

c
c Filter subroutine for low-pass filtering

```

c
  SUBROUTINE FILTER(FFT,N,SF)
  REAL FFT(N),W0,C0,C1,C2,D1,D2,EPS,F0,PI,BOTTOM
  REAL FDELTA,SIN1,SIN2,COS1,COS2,RENUM,REDEN,IMNUM,IMDEN
  REAL HRE,HIM,FFTRE,FFTIM

```

c Enter filtering parameters
 PRINT*,'cut off frequency?'
 READ*, FA

```

M=N/2
1  IF ((M.GE.2).AND.(J.GT.M)) THEN
    J=J-M
    M=M/2
    GO TO 1
    ENDIF
    J=J+M
11 CONTINUE
MMAX=2
2  IF (N.GT.MMAX) THEN
    ISTEP=2*MMAX
    THETA=6.28318530717959D0/(ISIGN*MMAX)
    WPR=-2.D0*DSIN(0.5D0*THETA)**2
    WPI=DSIN(THETA)
    WR=1.D0
    WI=0.D0
    DO 13 M=1,MMAX,2
        DO 12 I=M,N,ISTEP
            J=I+MMAX
            TEMPR=SNGL(WR)*DATA(J)-SNGL(WI)*DATA(J+1)
            TEMPI=SNGL(WR)*DATA(J+1)+SNGL(WI)*DATA(J)
            DATA(J)=DATA(I)-TEMPR
            DATA(J+1)=DATA(I+1)-TEMPI
            DATA(I)=DATA(I)+TEMPR
            DATA(I+1)=DATA(I+1)+TEMPI
12     CONTINUE
        WTEMP=WR
        WR=WR*WPR-WI*WPI+WR
        WI=WI*WPR+WTEMP*WPI+WI
13     CONTINUE
        MMAX=ISTEP
    GO TO 2
    ENDIF
    RETURN
    END

SUBROUTINE SPECPRN(SPEC,N,DATPTS,SF)
REAL SPEC(N),SF,FREQ
INTEGER STEP,I,J,K,DATPTS
CHARACTER*7 FILE
C Open file for printing of energy spectrum results
WRITE(*,*)'Filename for energy spectrum storage? (7 char, no ext)'
READ(*,'(A)') FILE
DO 3 I=1,N,2
    E1=E1+(SPEC(I)*SPEC(I)+SPEC(I+1)*SPEC(I+1))

```

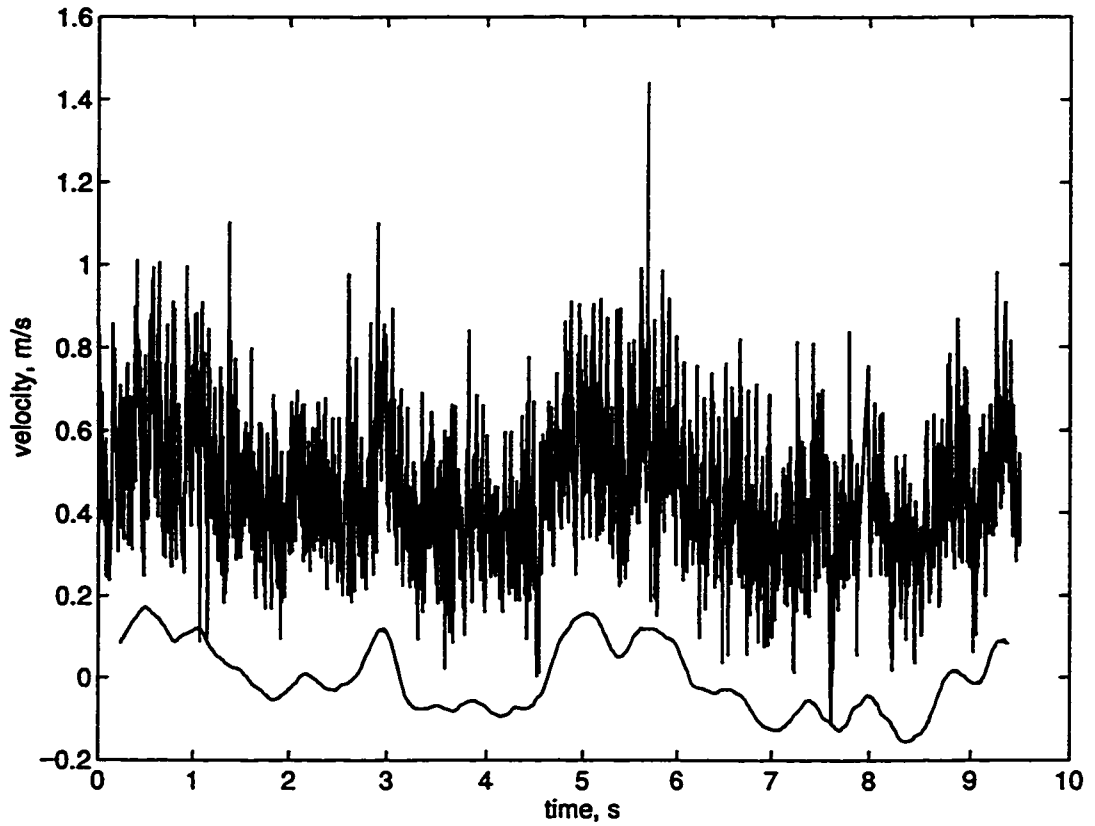
```

    PI=ACOS(-1.0)
    A=TAN(PI*FA/SF)
c Calculate filter constants
    BOTTOM=(1+A)
    C0=(-A)/BOTTOM
    C1=(-A)/BOTTOM
    C2=0
    D1=(1-A)/BOTTOM
    D2=0
C Loop to apply filter
    DO 10 I=1,N-1,2
c Calculate real and imaginary parts of numerator and denominator
    FDELTA=FLOAT((I-1)/2)/FLOAT(N)
    SIN1=SIN(2*PI*FDELTA)
    SIN2=SIN(4*PI*FDELTA)
    COS1=COS(2*PI*FDELTA)
    COS2=COS(4*PI*FDELTA)
    RENUM=C0+C1*COS1+C2*COS2
    REDEN=1-D1*COS1-D2*COS2
    IMNUM=-(C1*SIN1+C2*SIN2)
    IMDEN=D1*SIN1+D2*SIN2
c Calculate real and imaginary parts of filter

    HRE=(RENUM*REDEN+IMNUM*IMDEN)/(REDEN*REDEN+IMDEN*IMDEN)
    HIM=(IMNUM*REDEN-
    RENUM*IMDEN)/(REDEN*REDEN+IMDEN*IMDEN)
c Apply filter
    FFTRE=FFT(I)
    FFTIM=FFT(I+1)
    FFT(I)=FFTRE*HRE-FFTIM*HIM
    FFT(I+1)=FFTRE*HIM+FFTIM*HRE
10 CONTINUE
    RETURN
    END

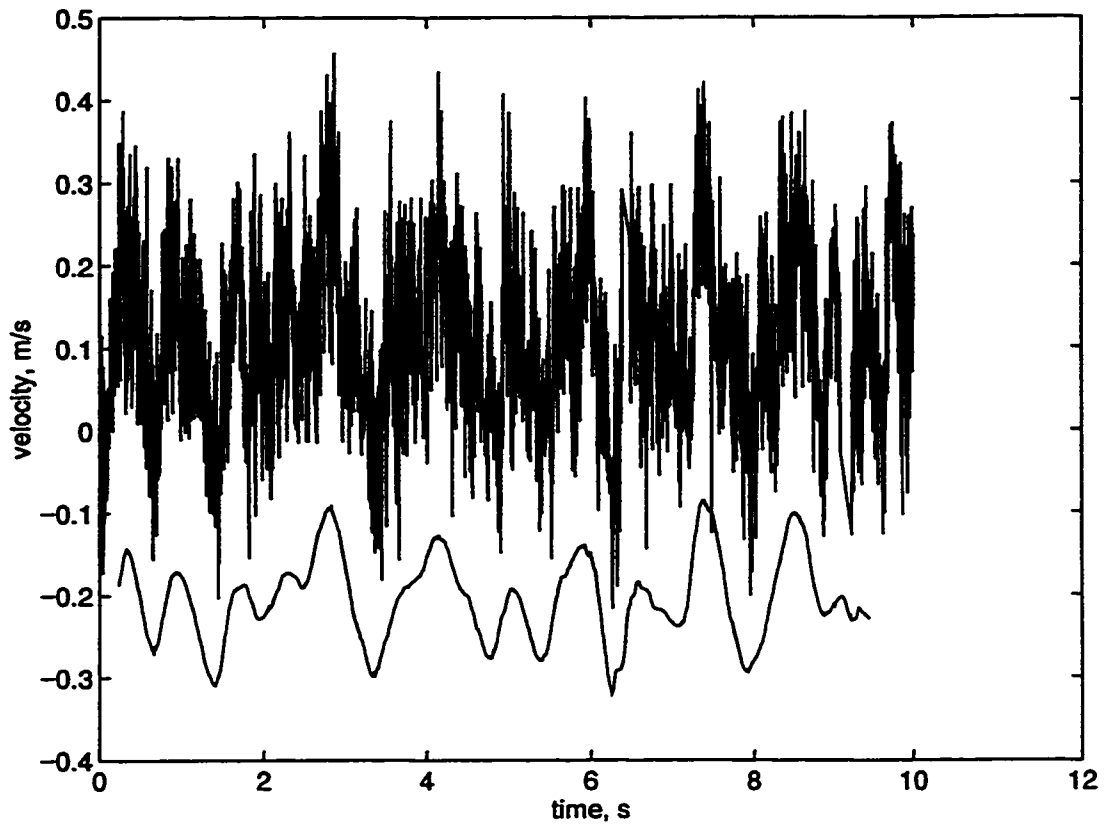
```

Appendix B

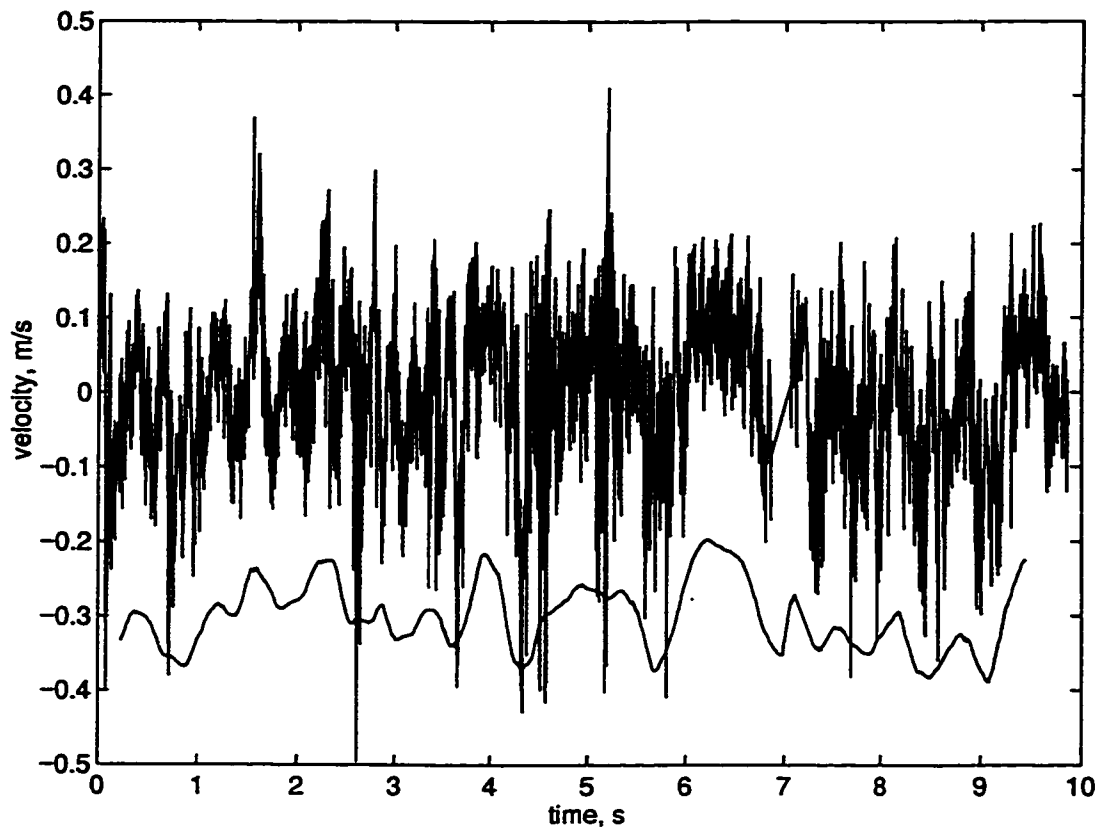


1a) impeller stream

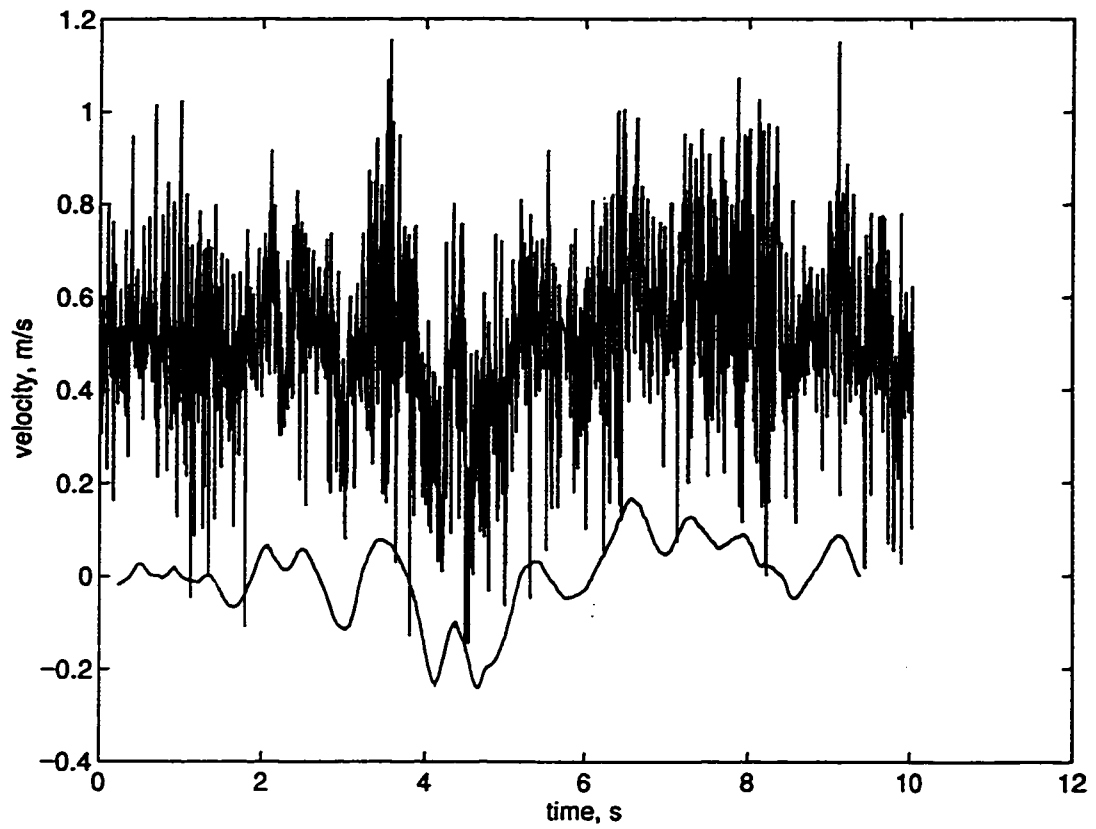
Figure 1: PBT time series: $D=T/2$, $C/D=1$, $N_f=4$, smoothed over 6 (2+4) blade passages.



1b) bottom corner

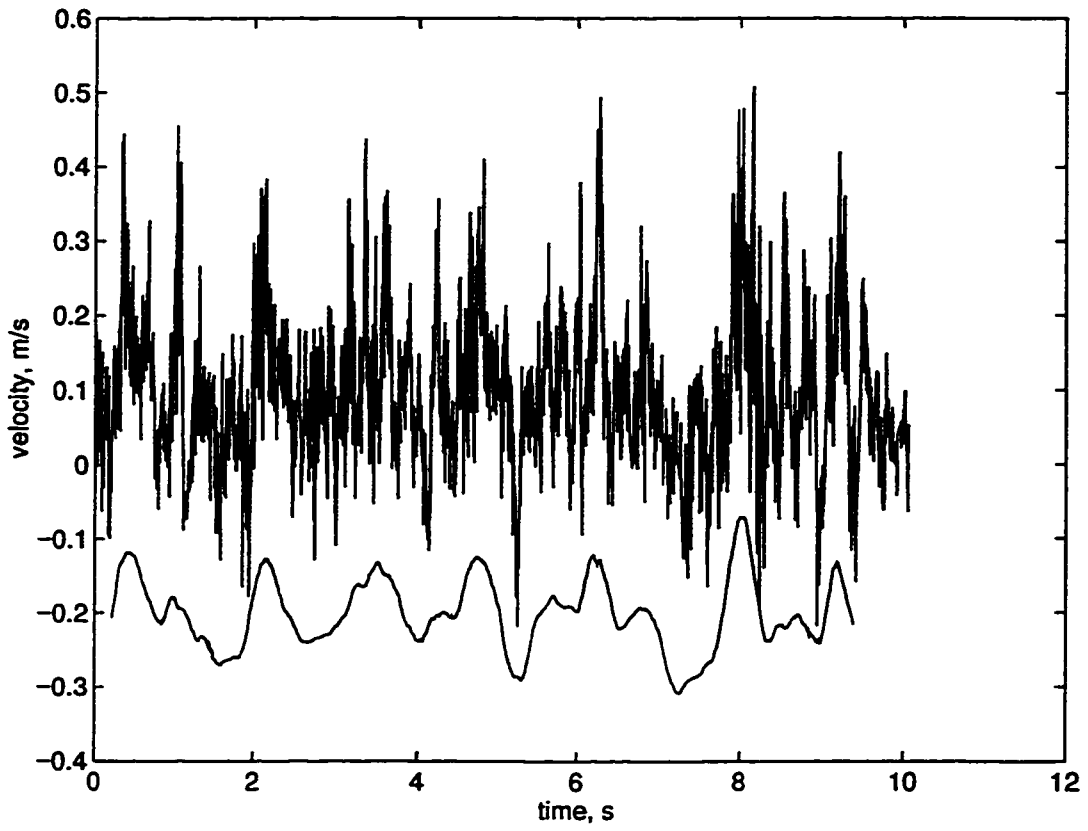


1c) top corner

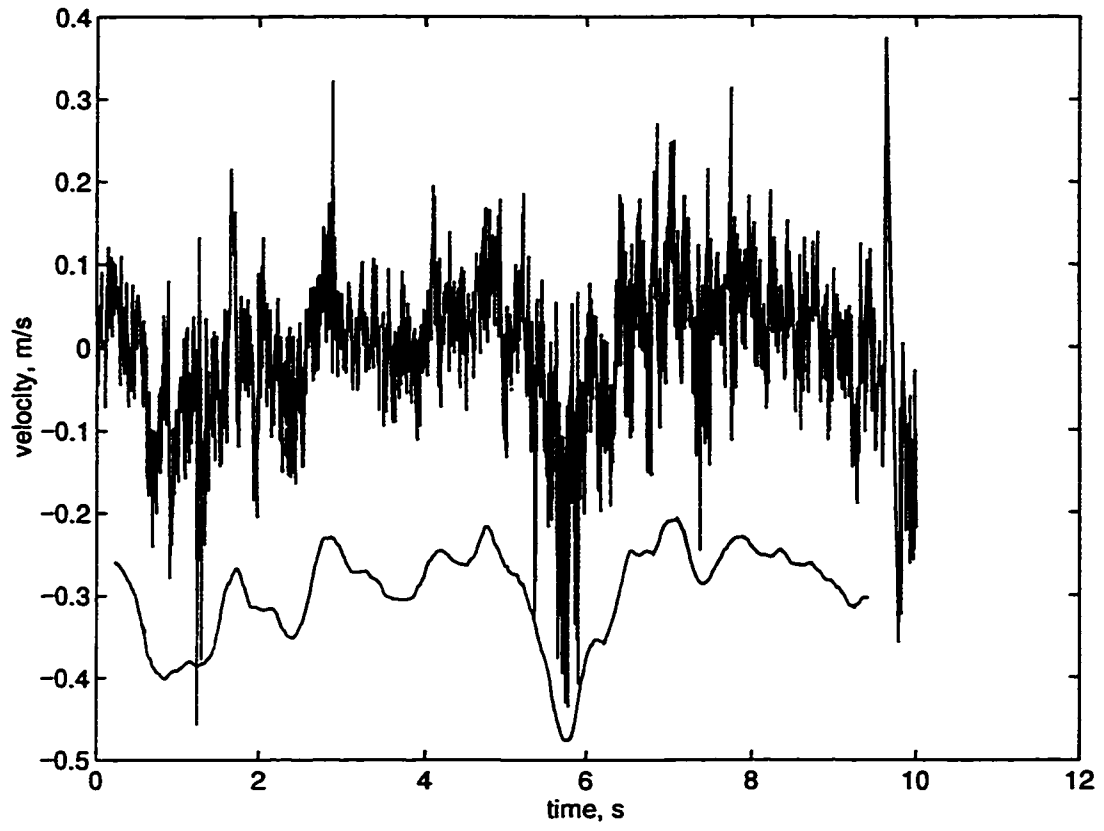


2a) impeller stream

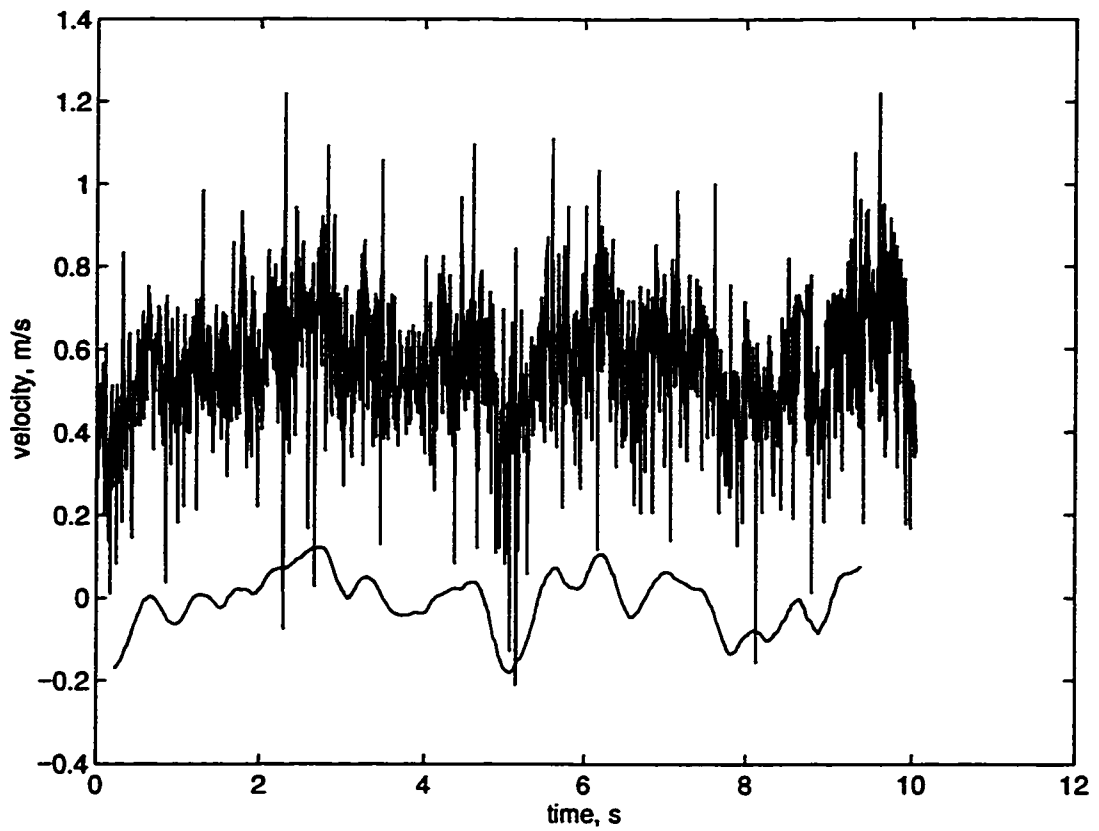
Figure 2: PBT time series: $D=T/2$, $C/D=1$, $N_f=2$, smoothed over 6 (2+4) blade passages.



2b) bottom corner

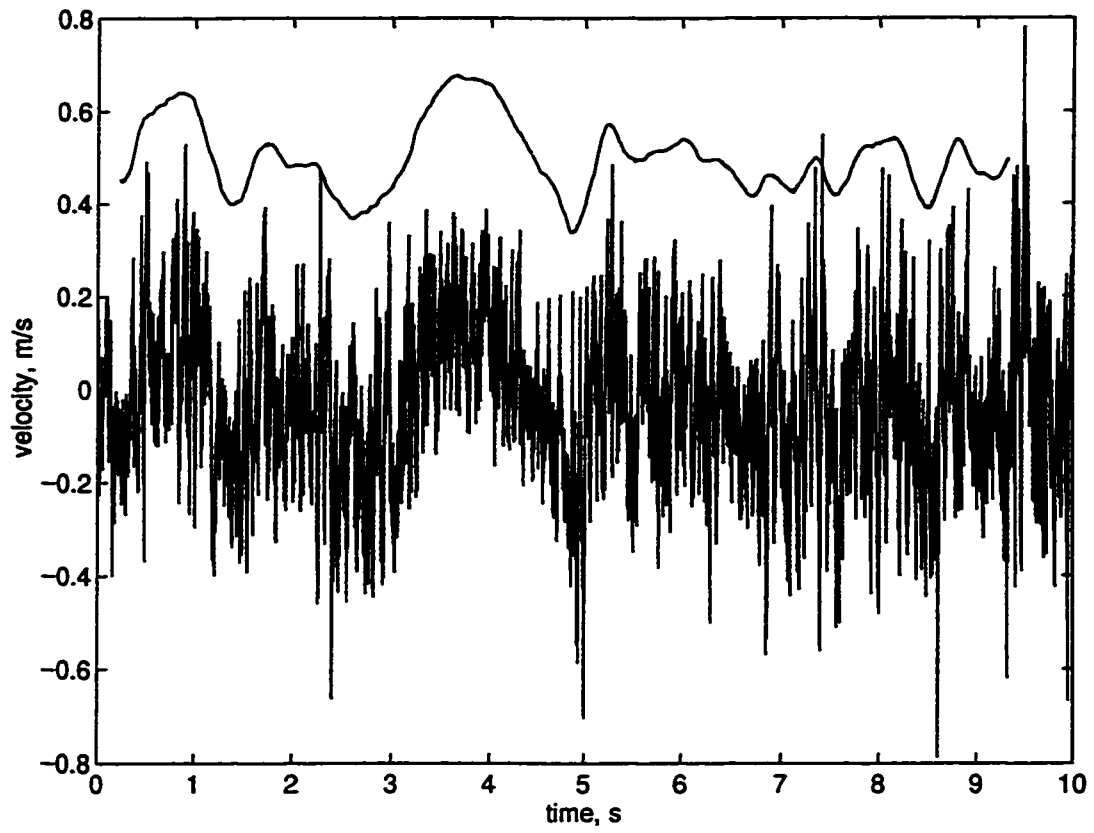


2c) top corner

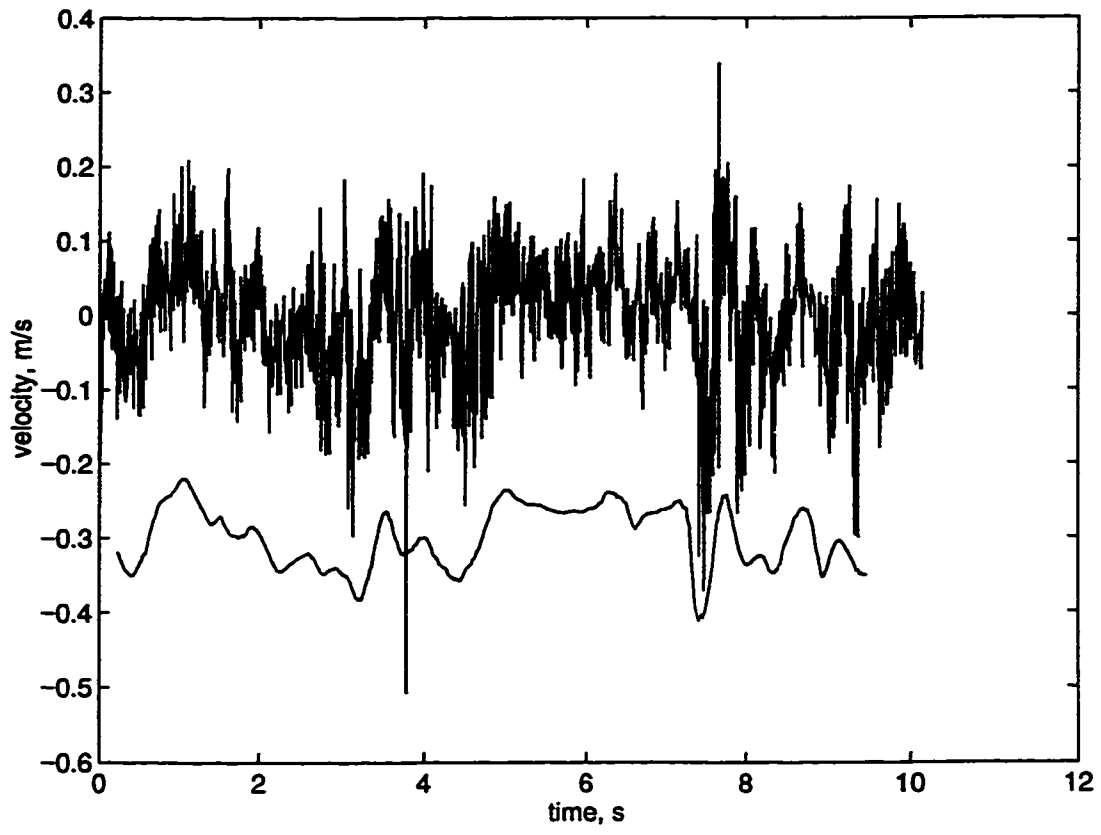


3a) impeller stream

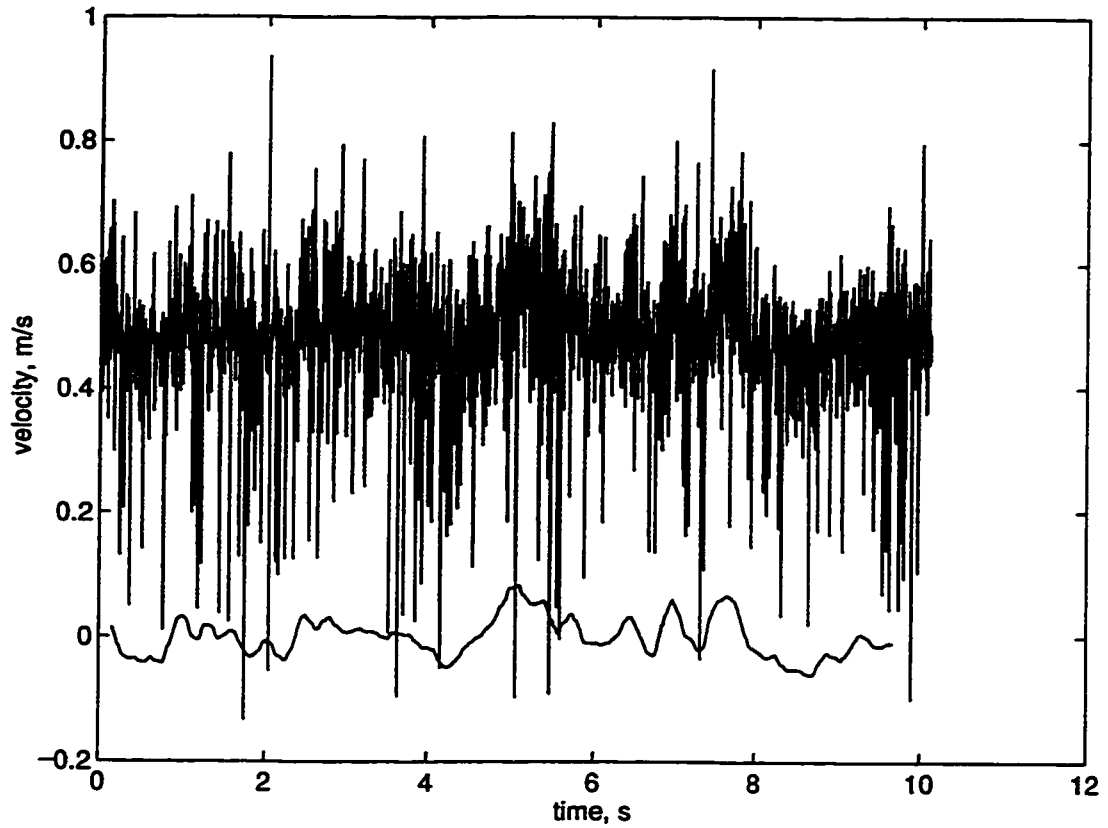
Figure 3: PBT time series: $D=T/2$, $C/D=0.5$, $N_f=4$, smoothed over 6 (2+4) blade passages.



3b) bottom corner

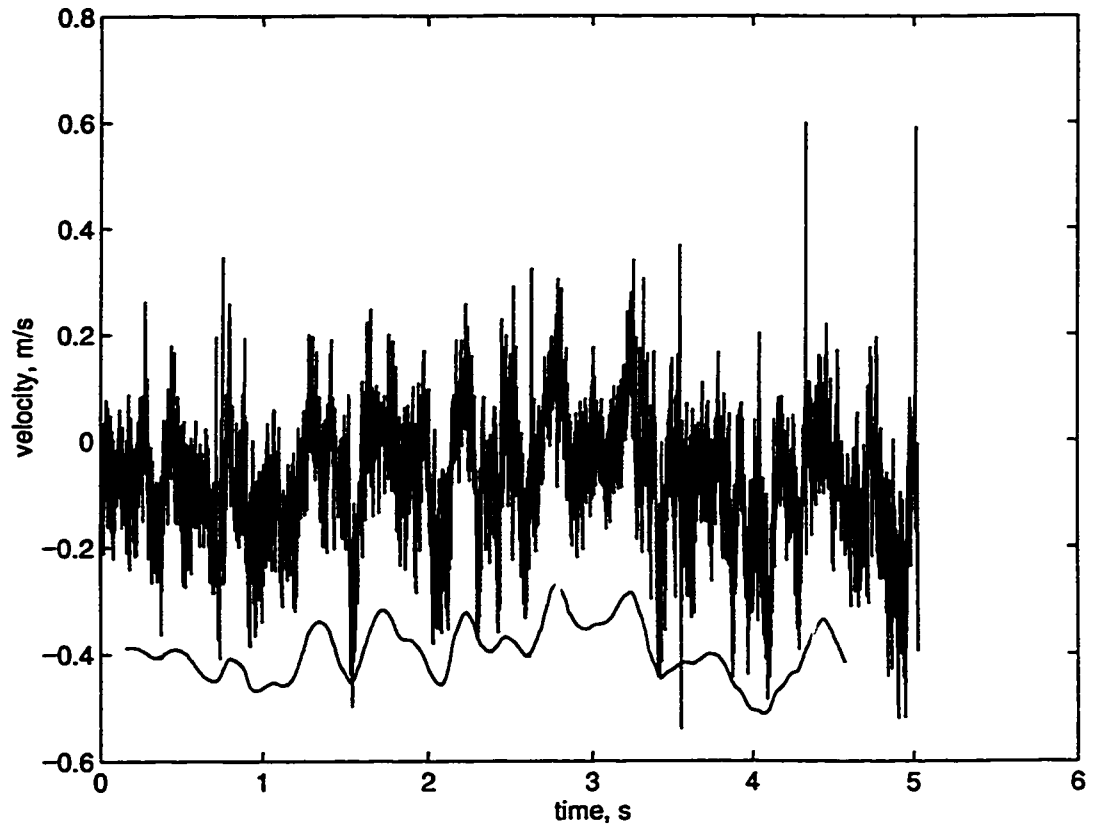


3c) top corner

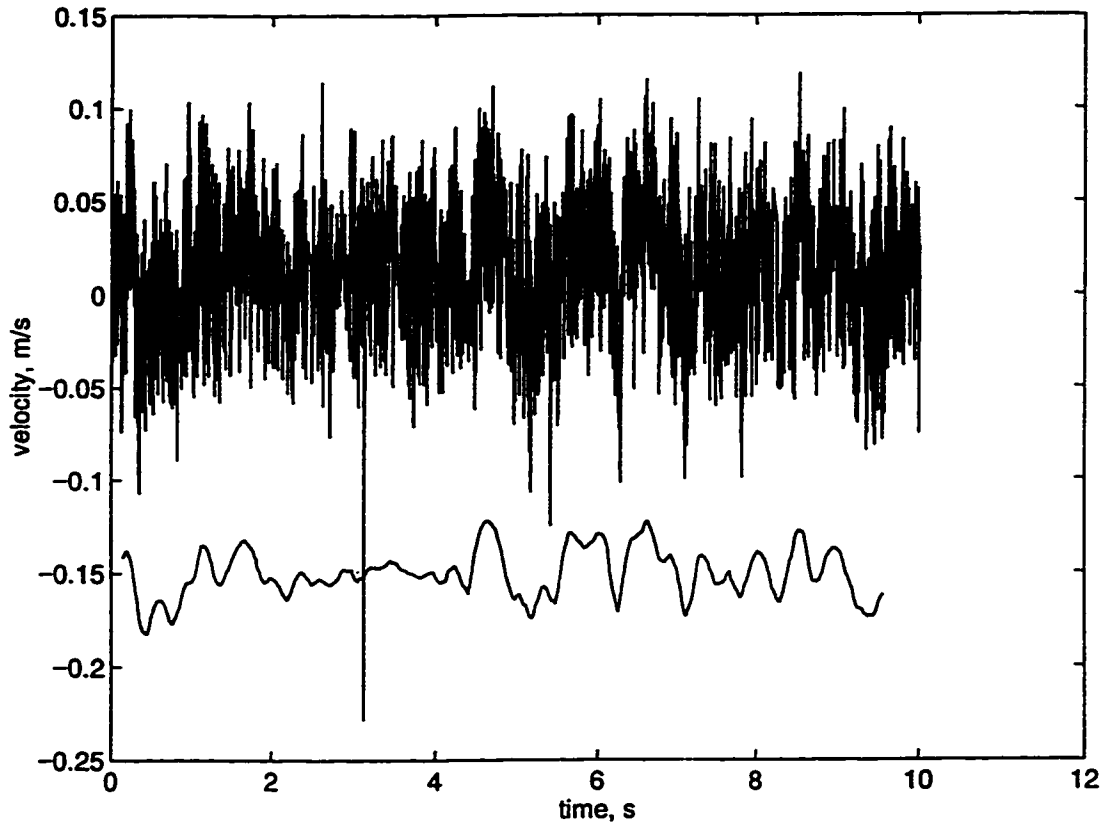


4a) impeller stream

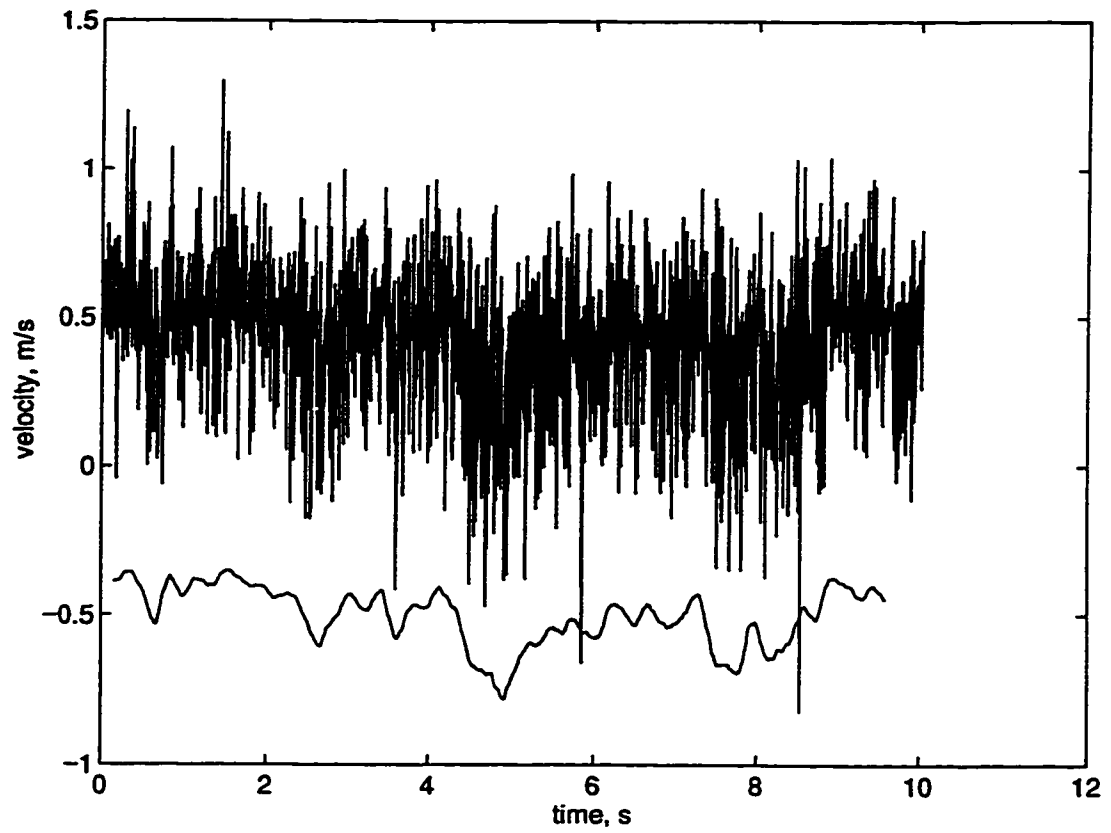
Figure 4: PBT time series: $D=T/4$, $C/D=1$, $N_f=4$, smoothed over 8 (4+4) blade passages.



4b) bottom corner

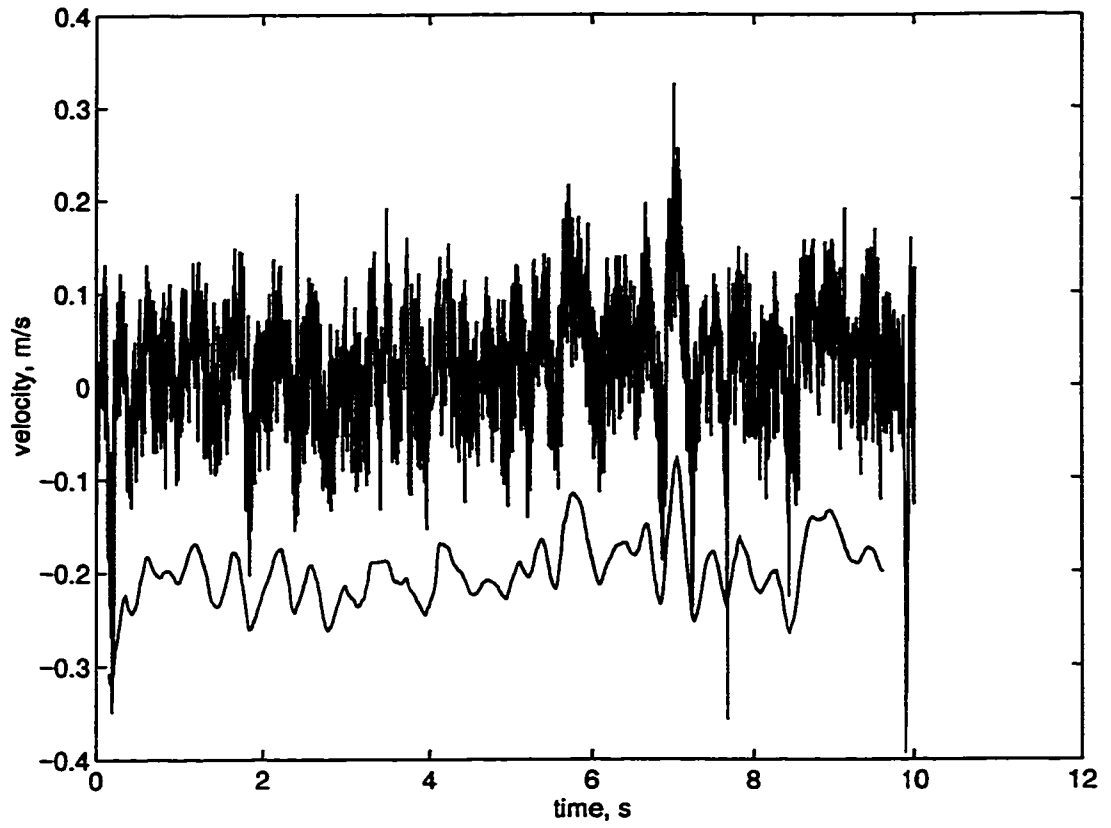


4c) top corner

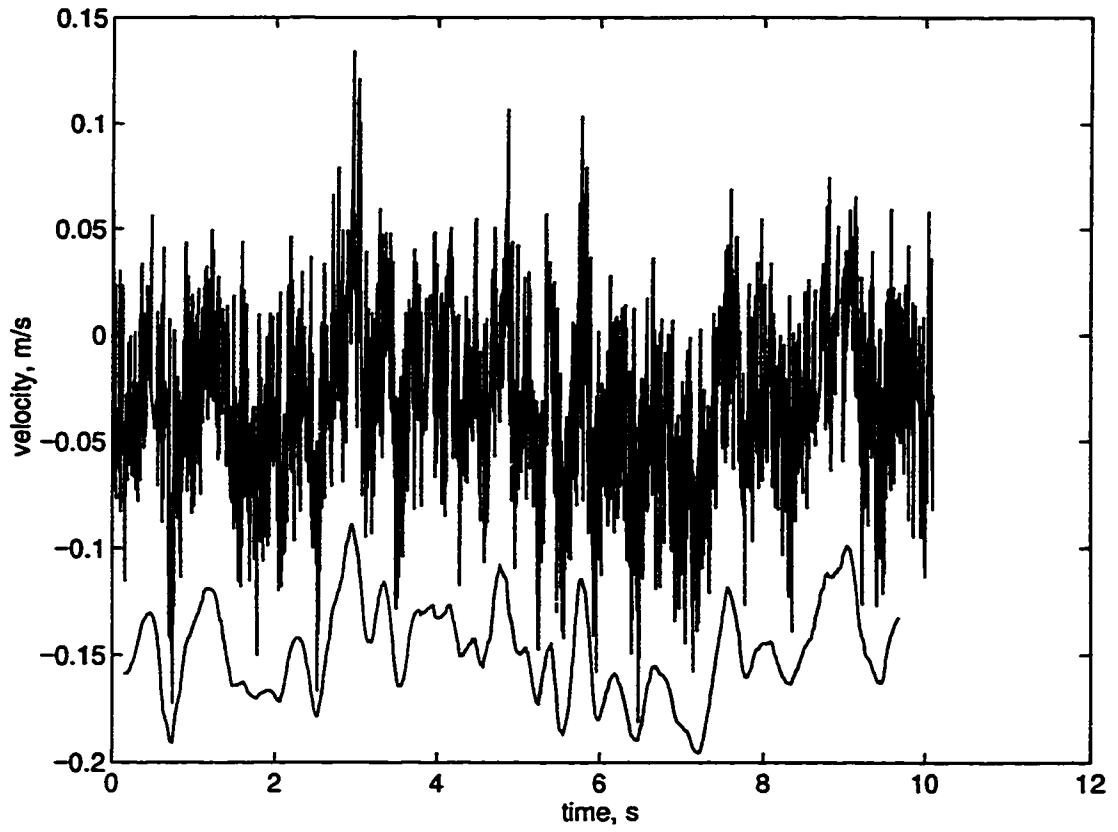


5a) impeller stream

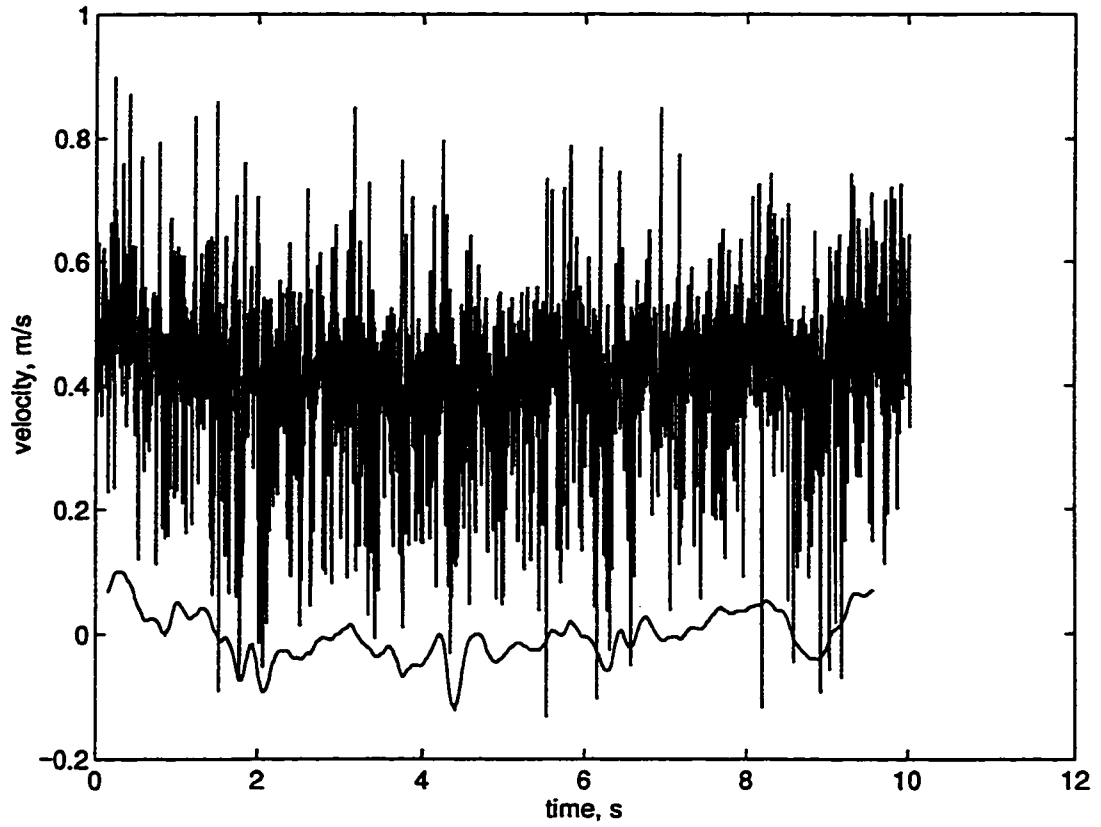
Figure 5: PBT time series: $D=T/4$, $C/D=0.5$, $N_f=2$, smoothed over 8 (4+4) blade passages.



5b) bottom corner

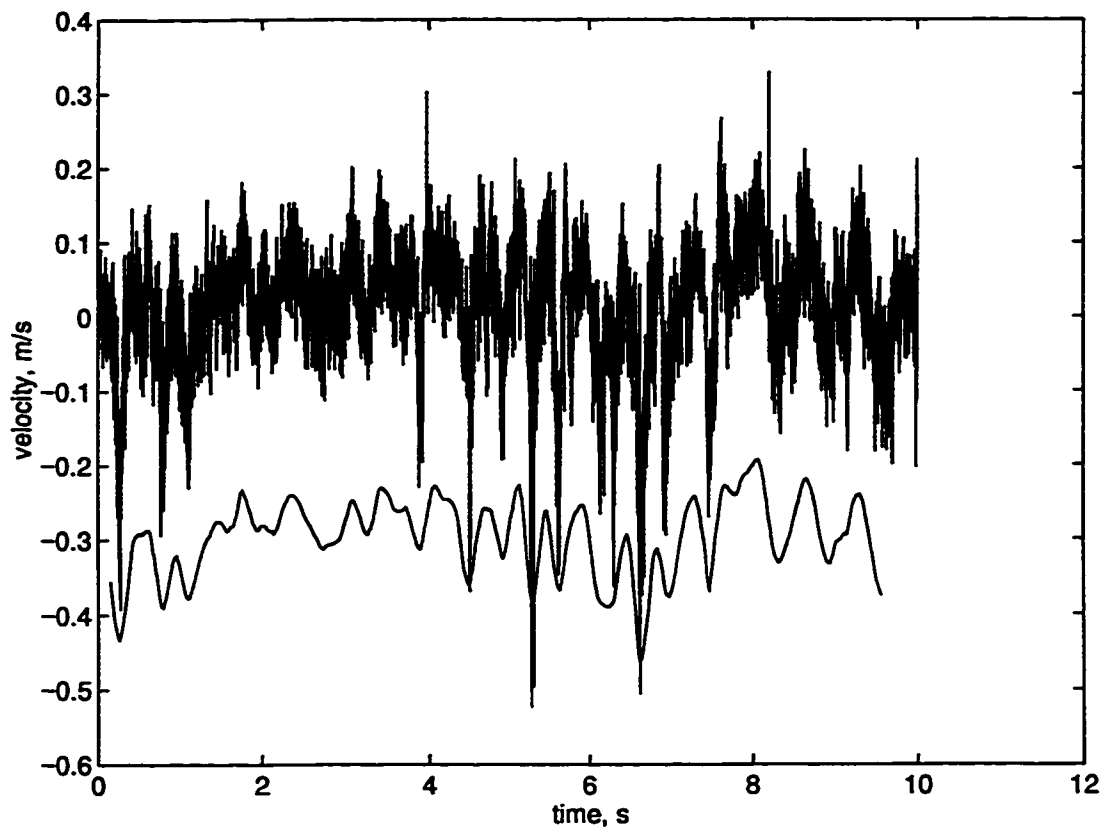


5c) top corner

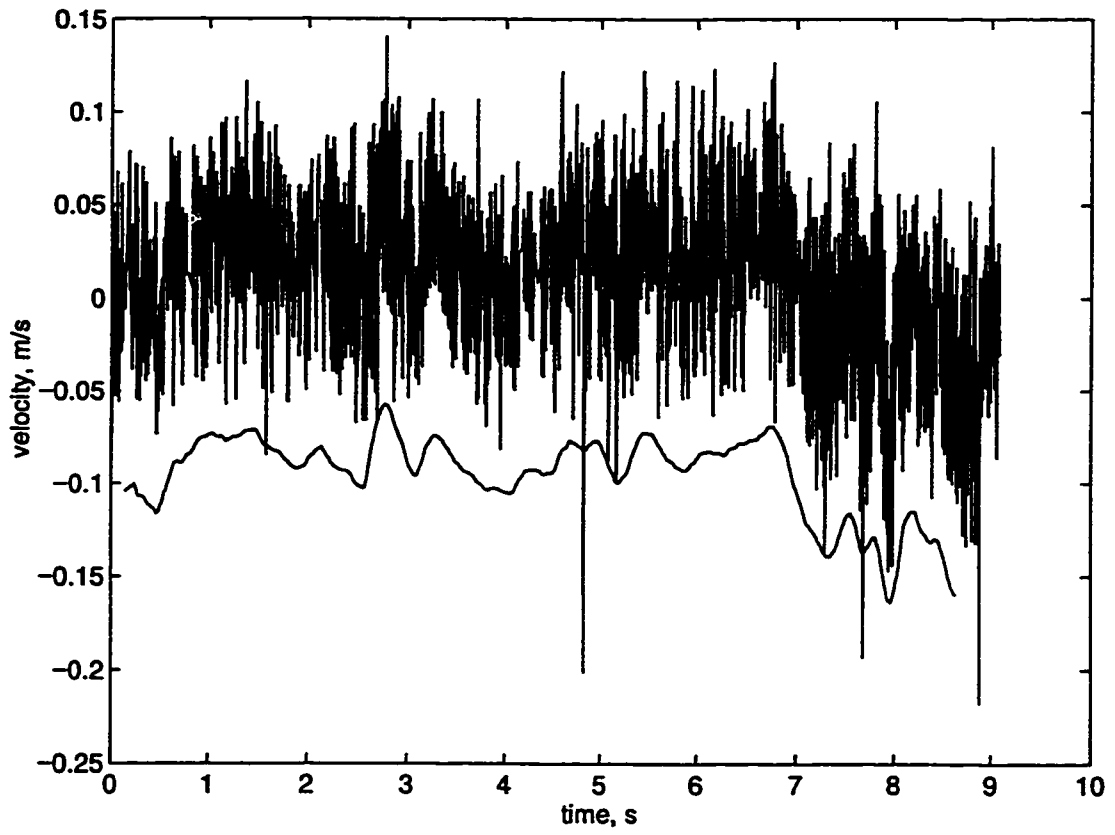


6a) impeller stream

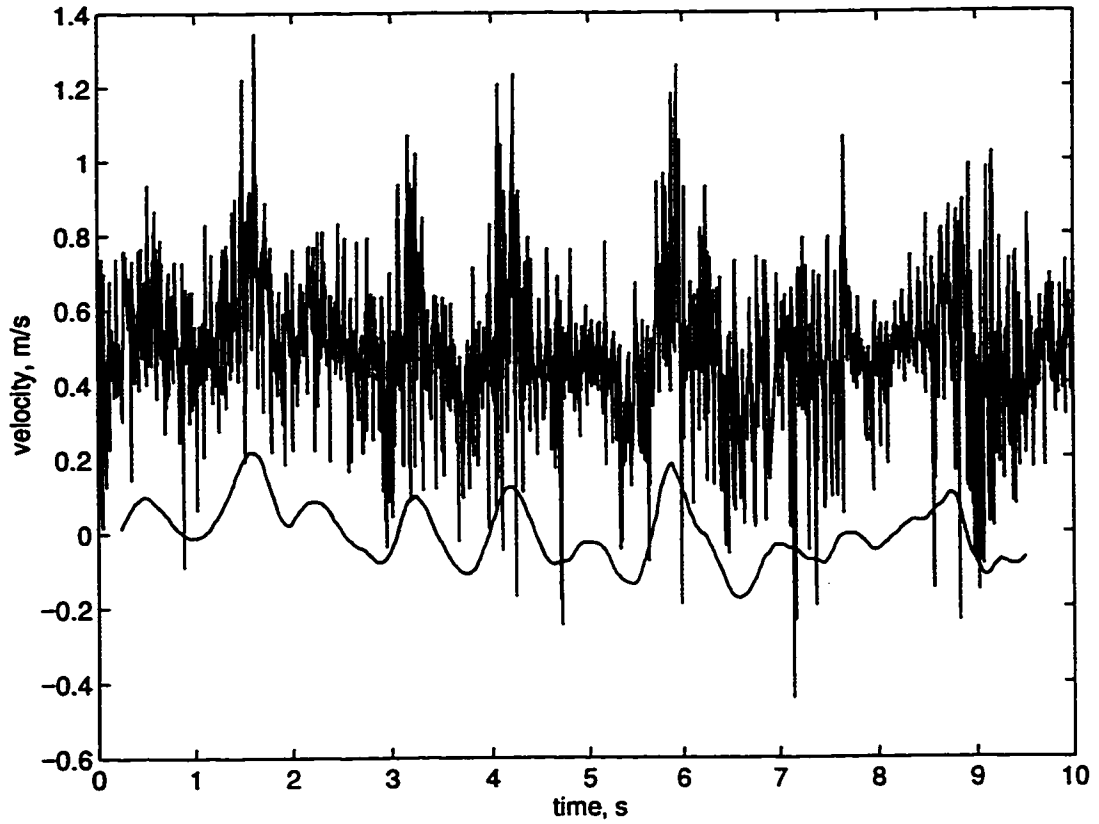
Figure 6: PBT time series: $D=T/4$, $C/D=0.5$, $N_f=4$, smoothed over 8 (4+4) blade passages.



6b) bottom corner

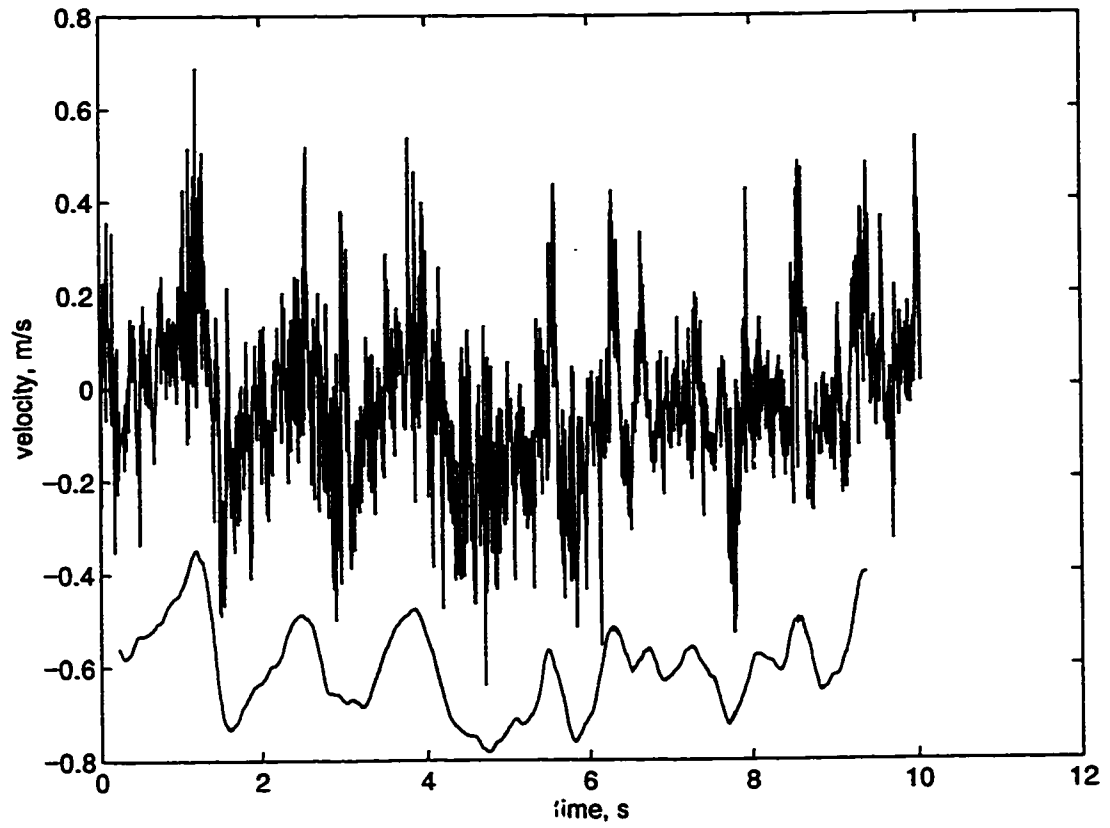


6c) top corner

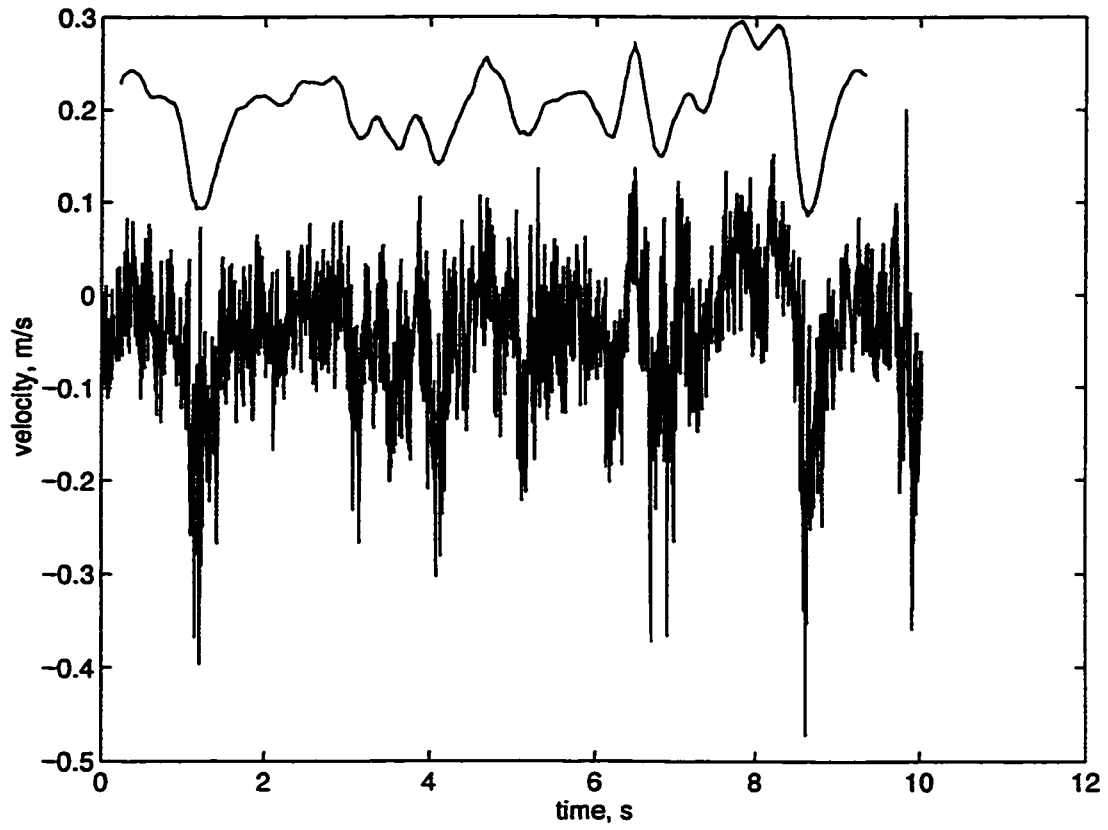


7a) impeller stream

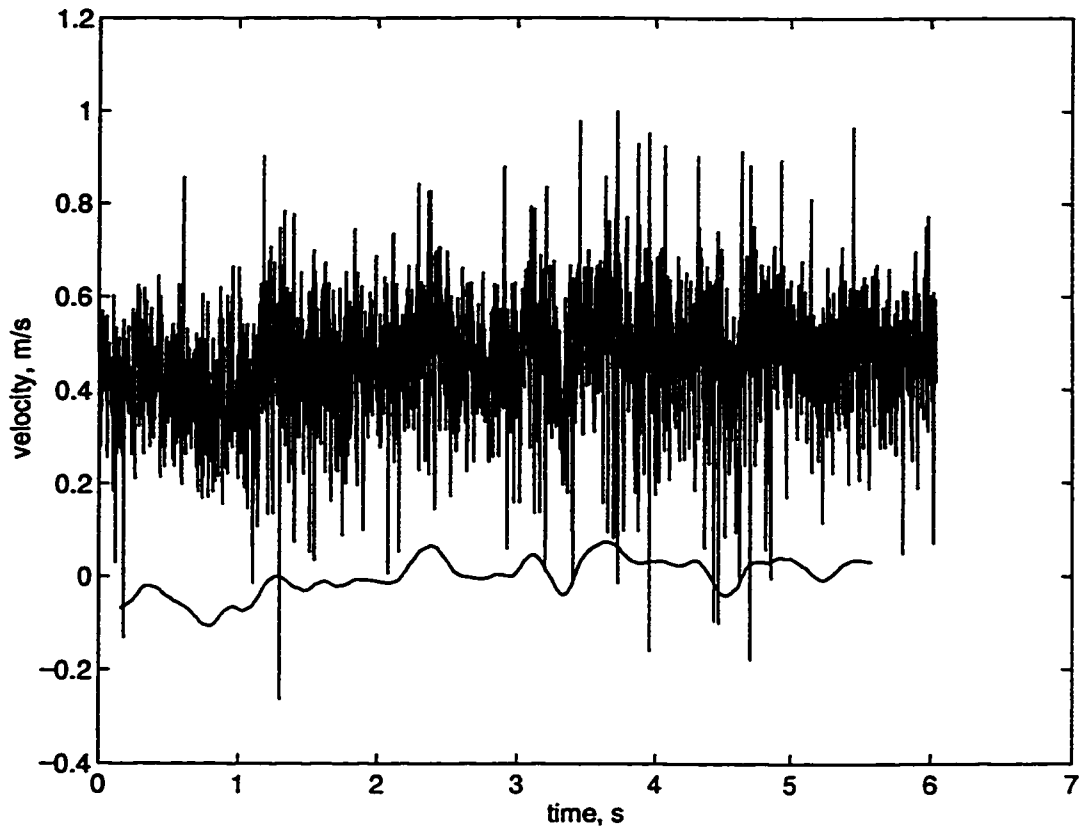
Figure 7: PBT time series: $D=T/2$, $C/D=0.5$, $N_f=2$, smoothed over 6 (2+4) blade passages.



7b) bottom corner

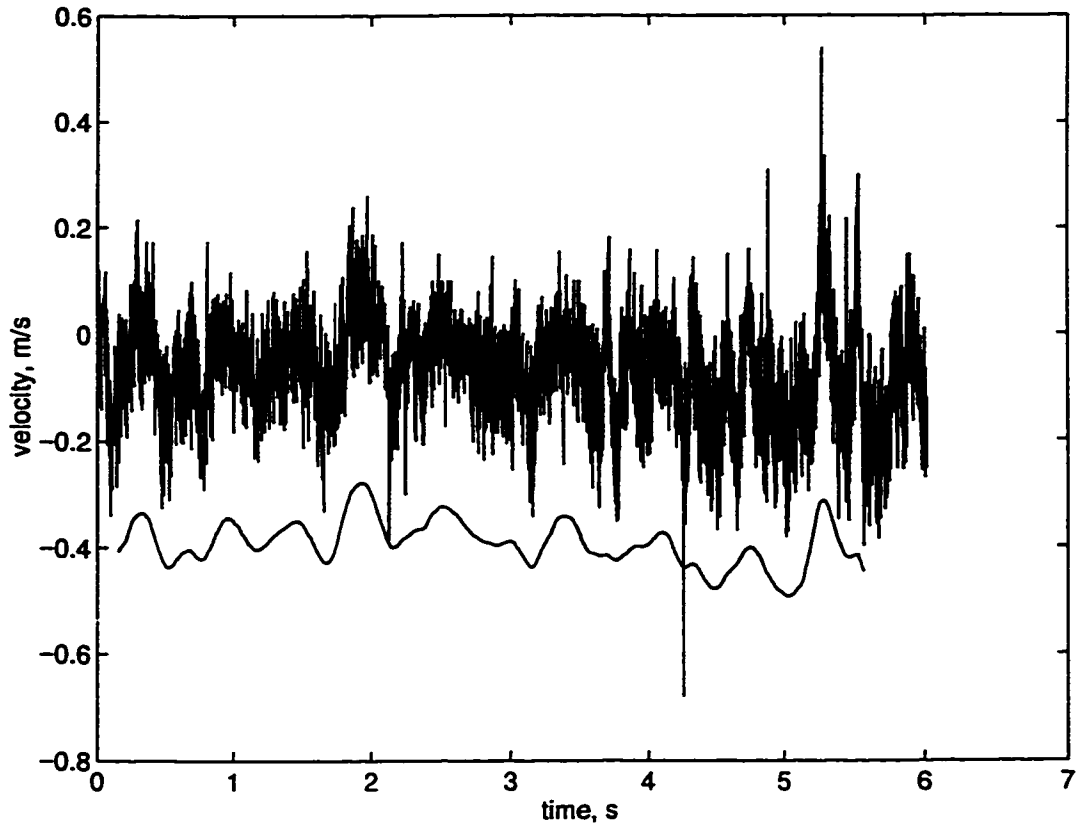


7c) top corner

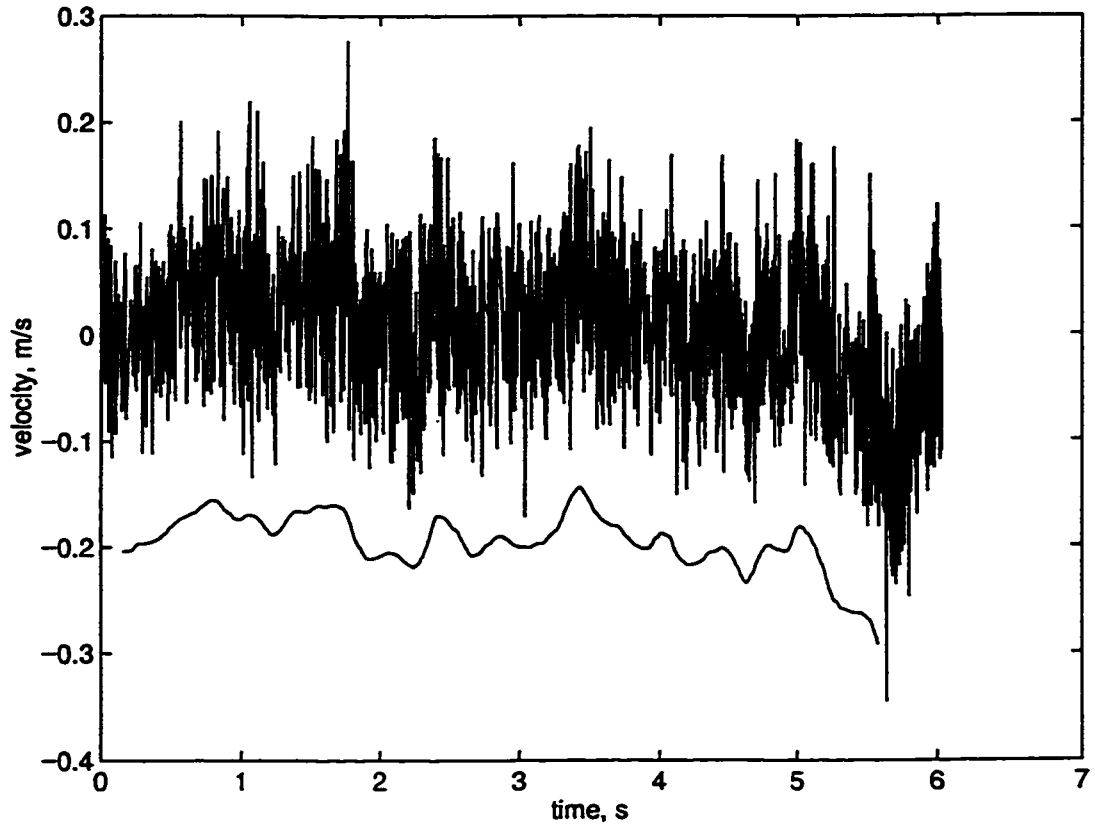


8a) impeller stream

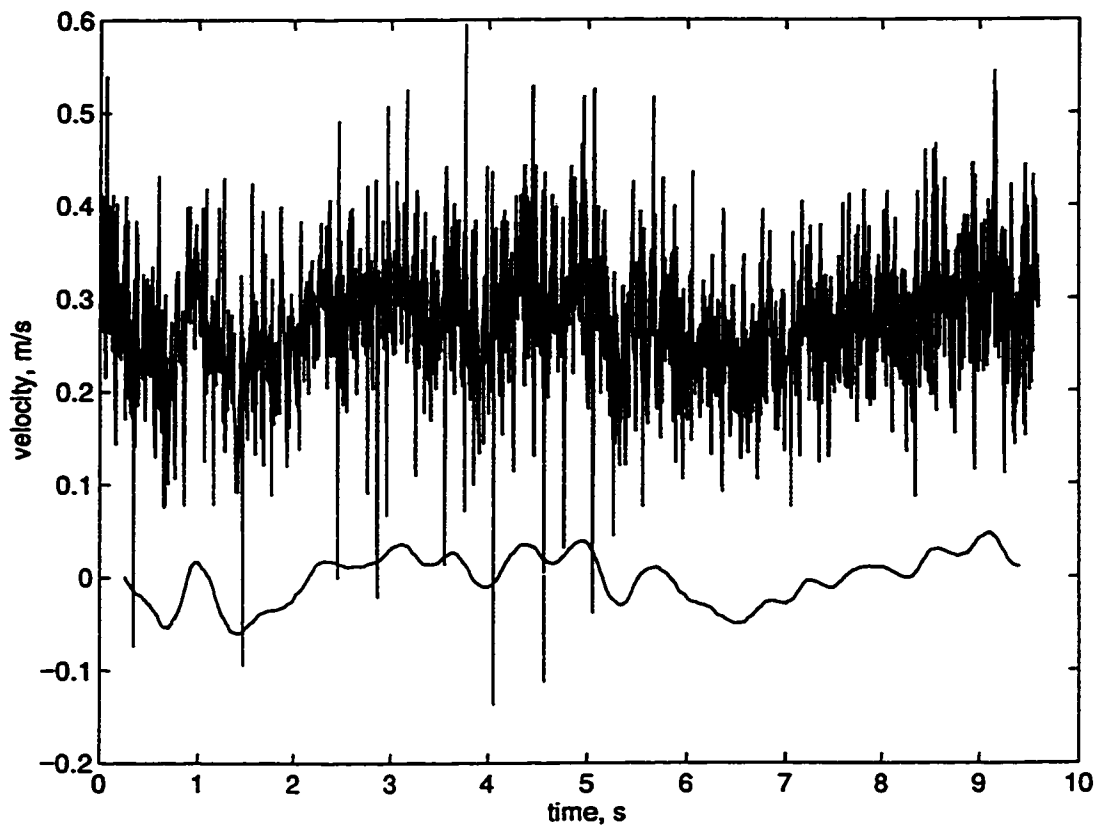
Figure 8: PBT time series: $D=T/4$, $C/D=1$, $N_f=2$, smoothed over 8 (4+4) blade passages.



8b) bottom corner

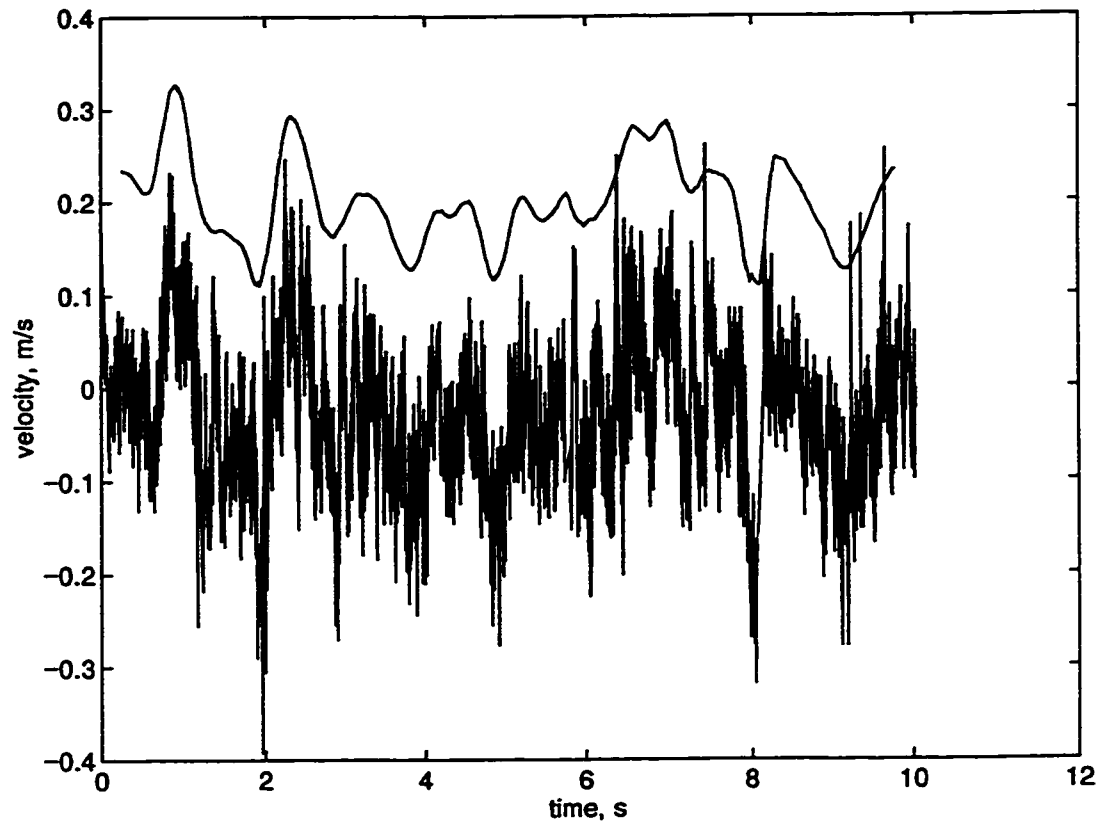


8c) top corner

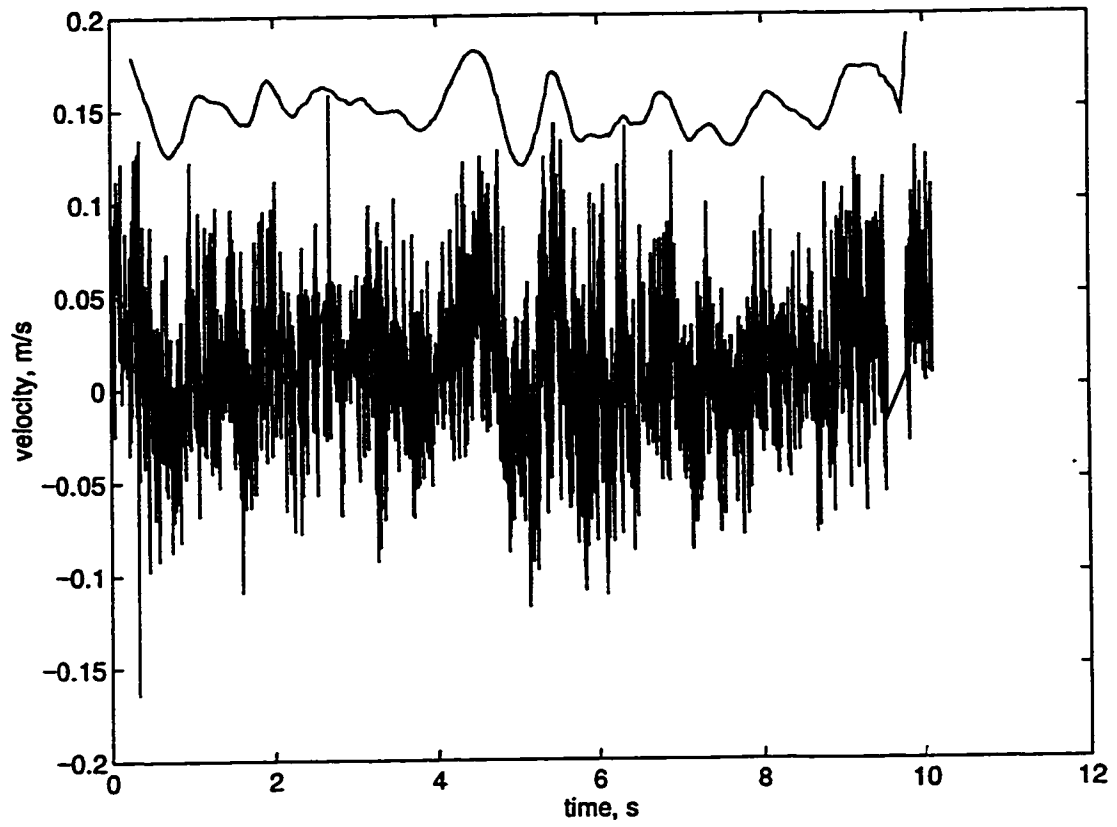


9a) impeller stream

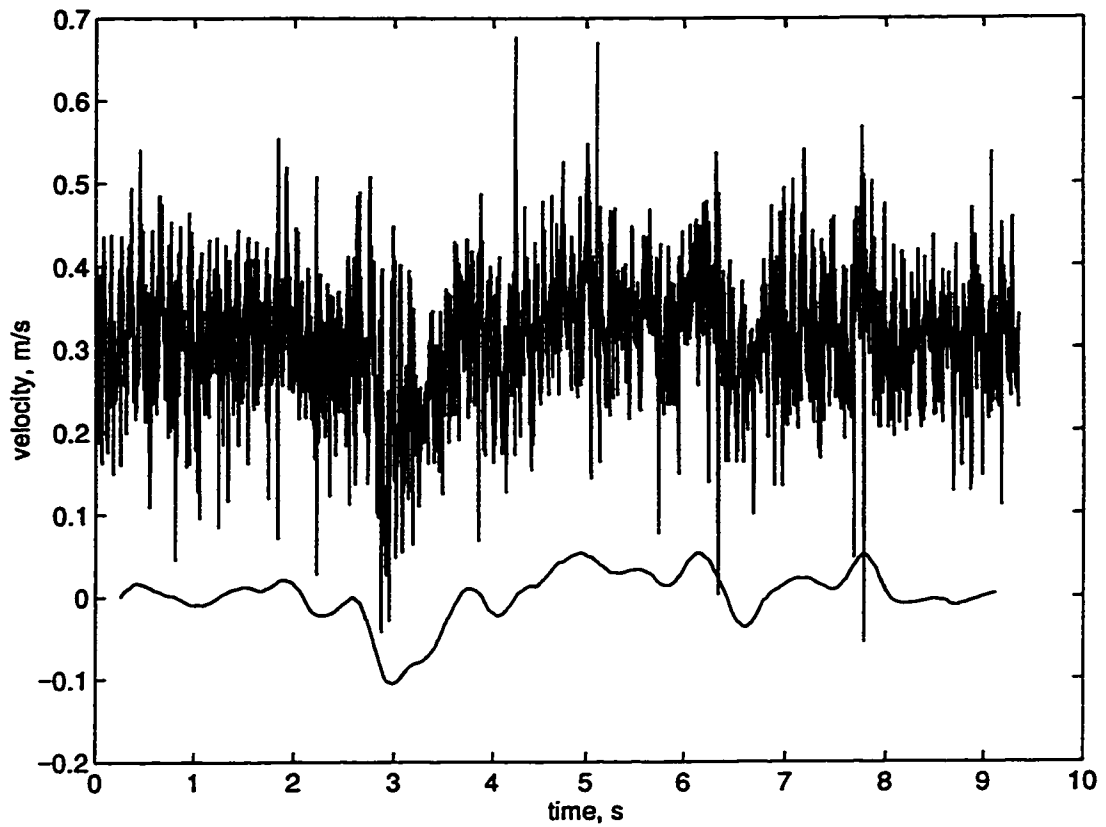
Figure 9: HE3 time series: $D=T/2$, $C/D=1$, $N_f=4$, smoothed over 10 (4+6) blade passages.



9b) bottom corner

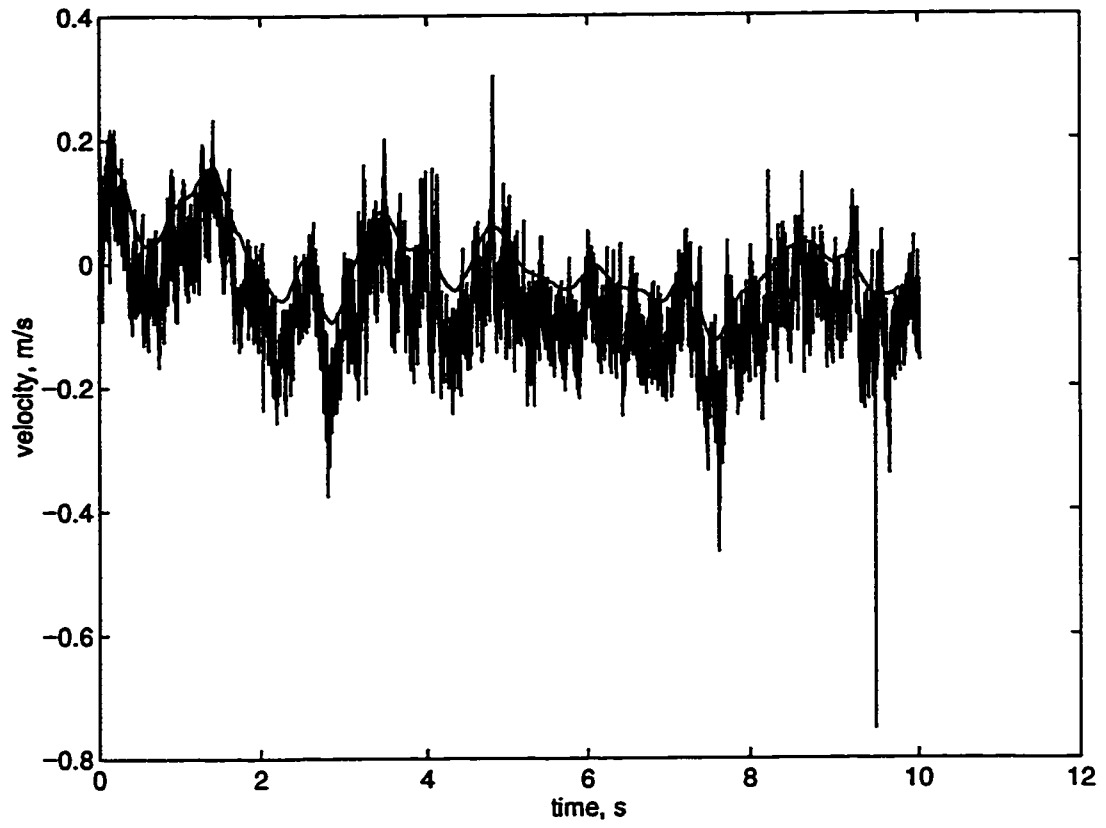


9c) top corner

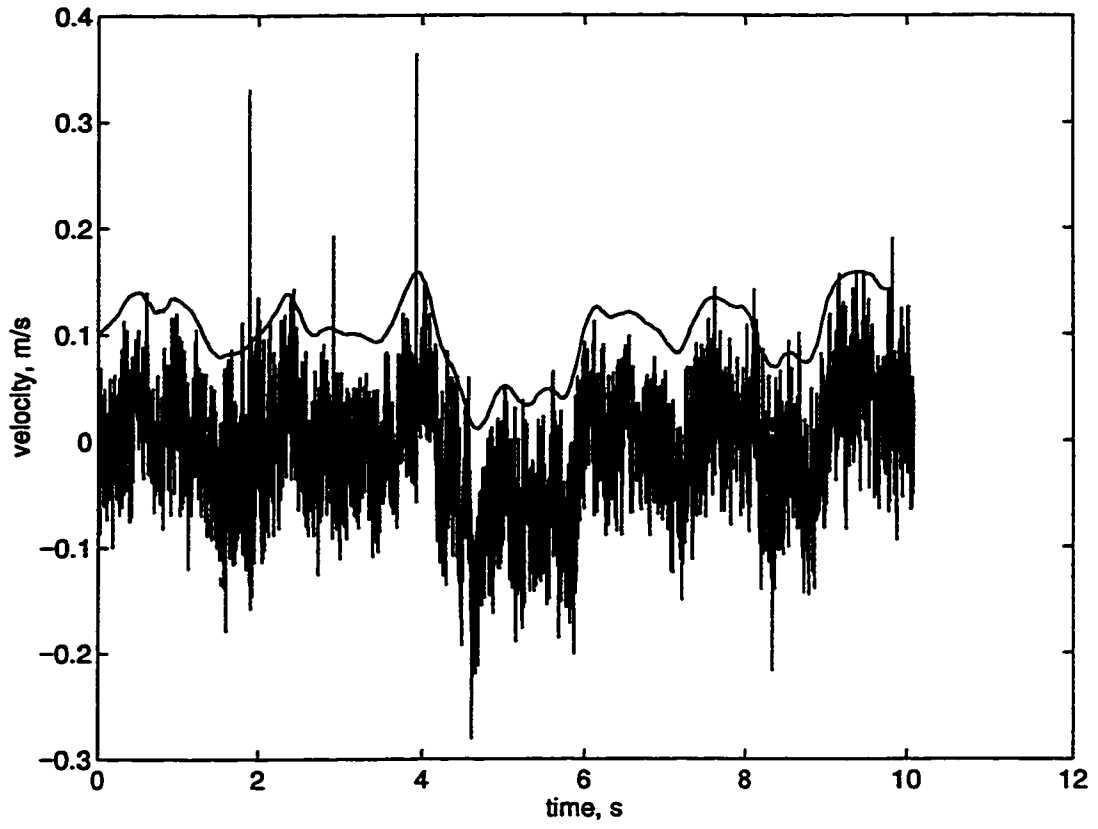


10a) impeller stream

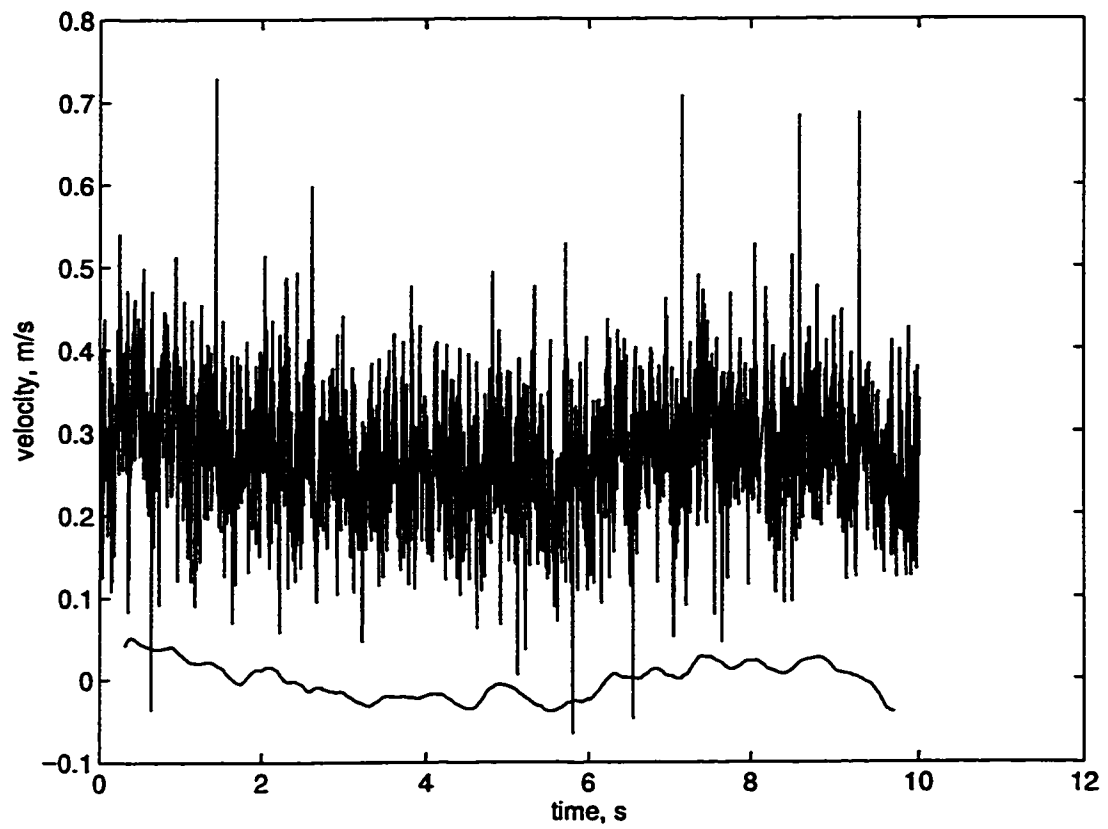
Figure 10: HE3 time series: $D=T/2$, $C/D=1$, $N_f=2$, smoothed over 10 (4+6) blade passages.



10b) bottom corner

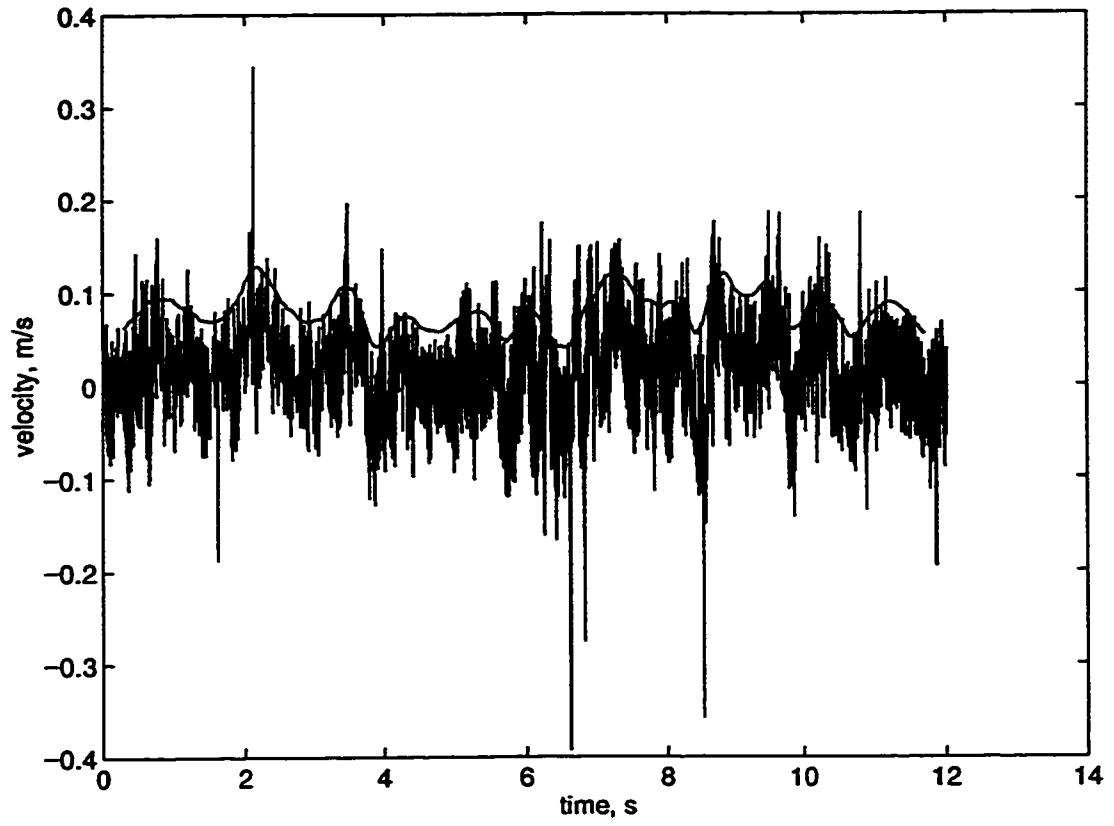


10c) top corner

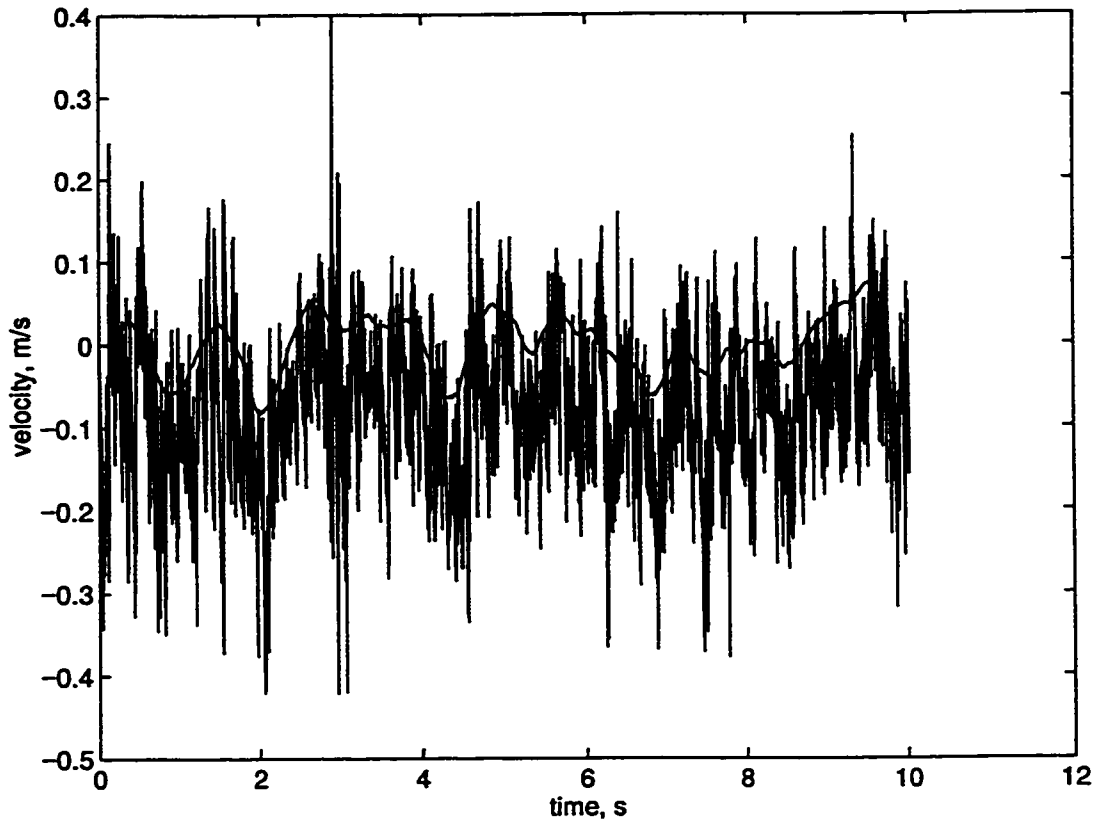


11a) impeller stream

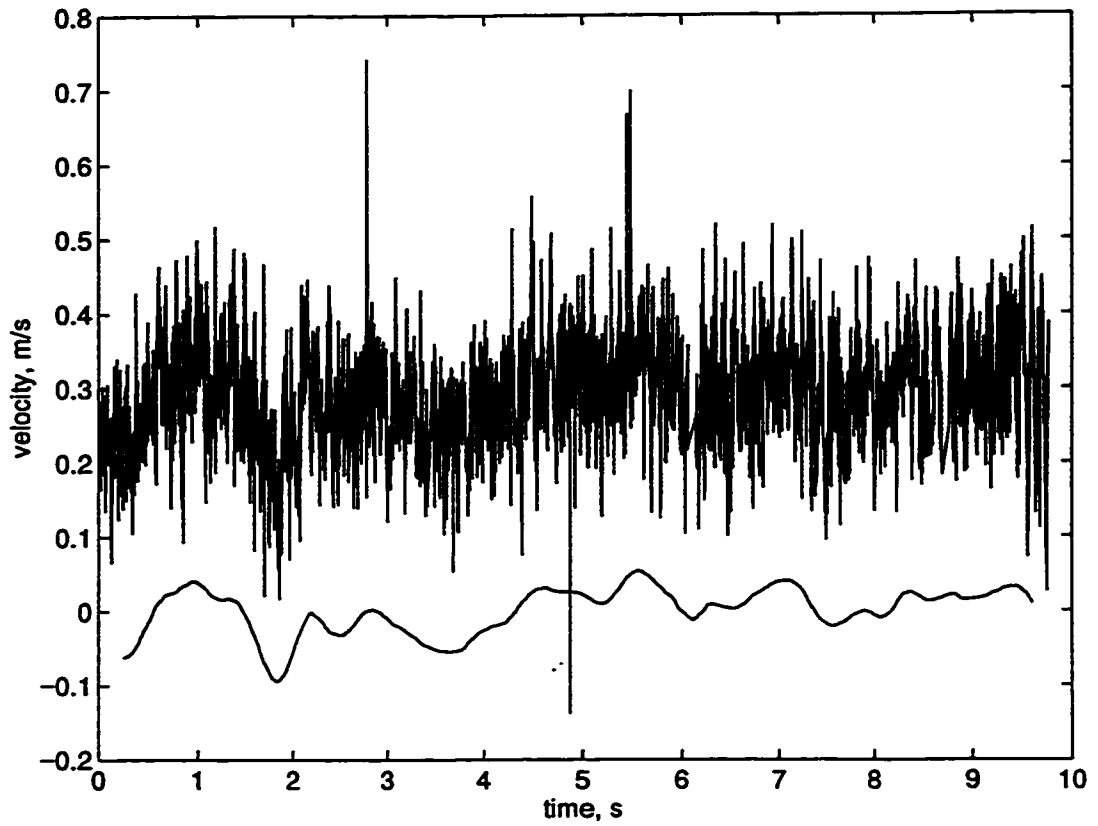
Figure 11: HE3 time series: $D=T/2$, $C/D=0.5$, $N_f=4$, smoothed over 12 (4+8) blade passages.



11b) bottom corner

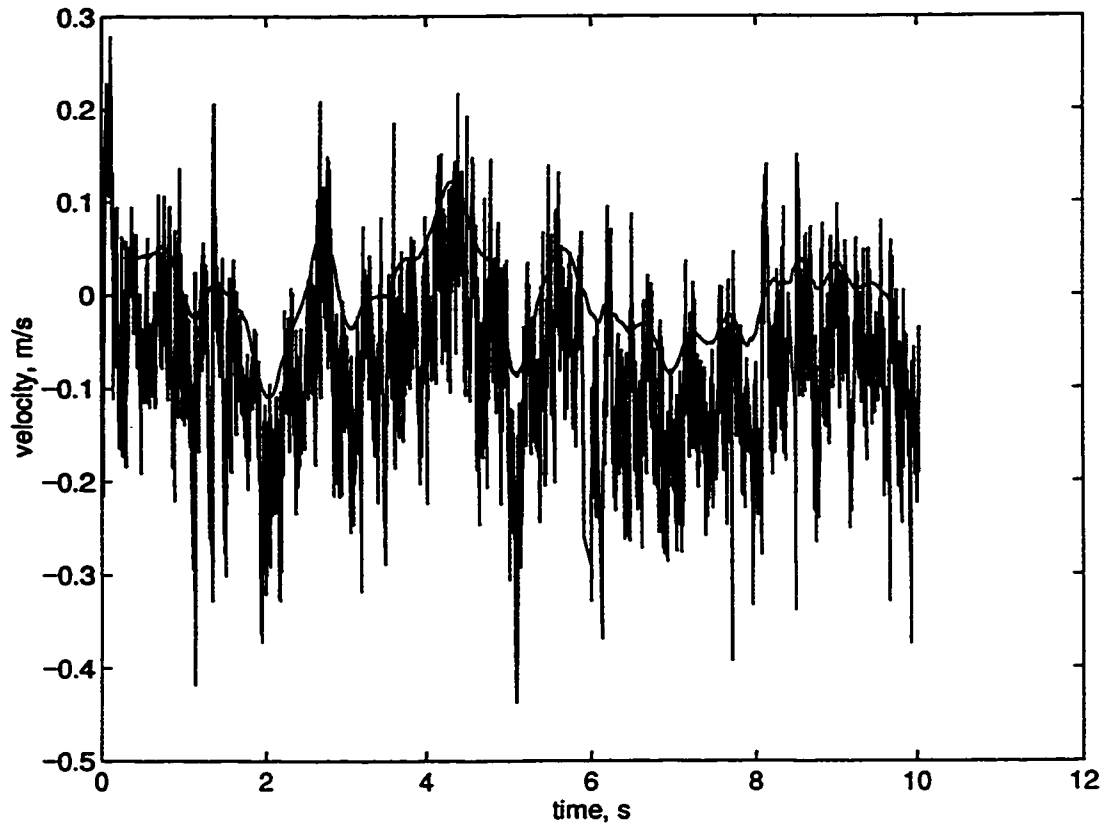


11c) top corner

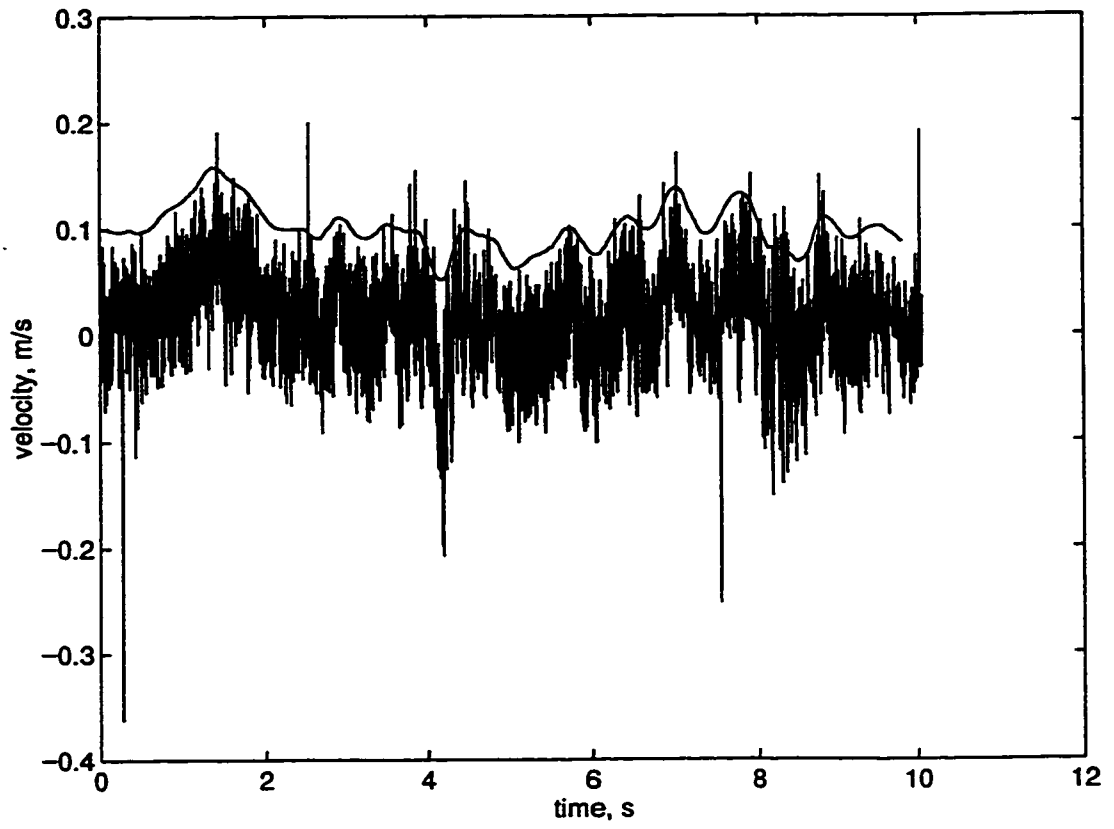


12a) impeller stream

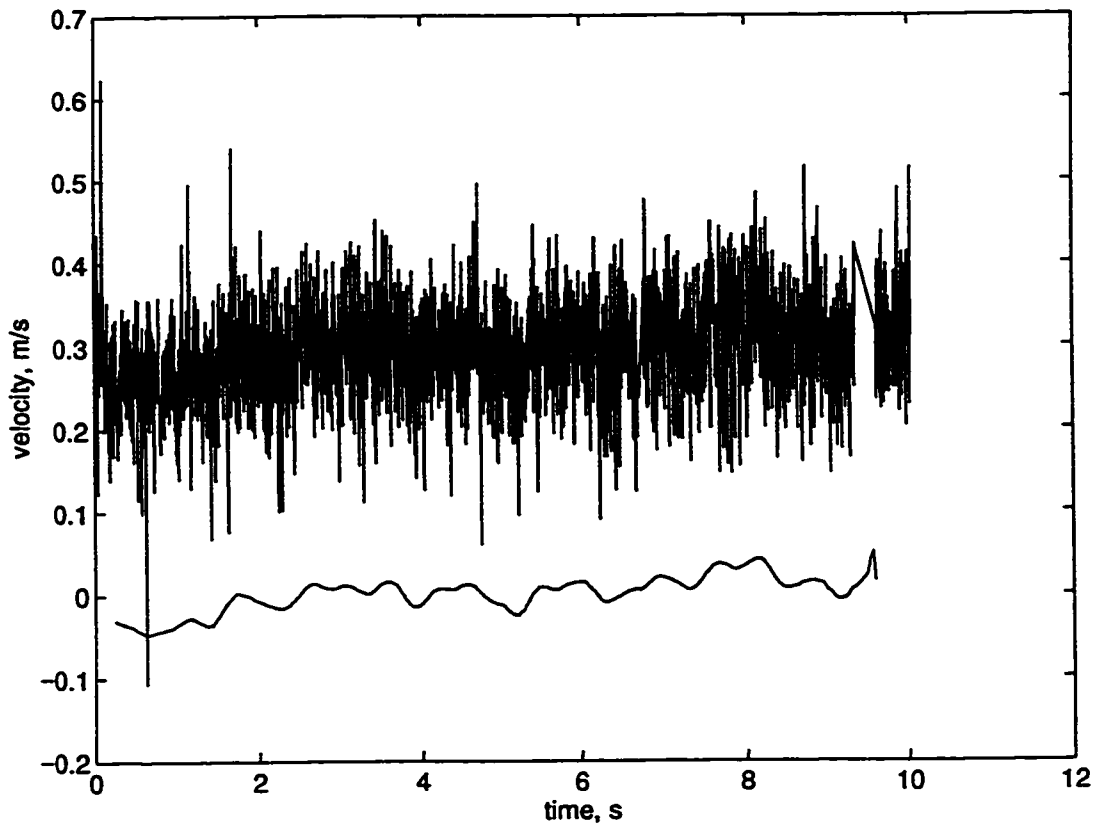
Figure 12: HE3 time series: $D=T/2$, $C/D=0.5$, $N_f=2$, smoothed over 10 (4+6) blade passages.



12b) bottom corner

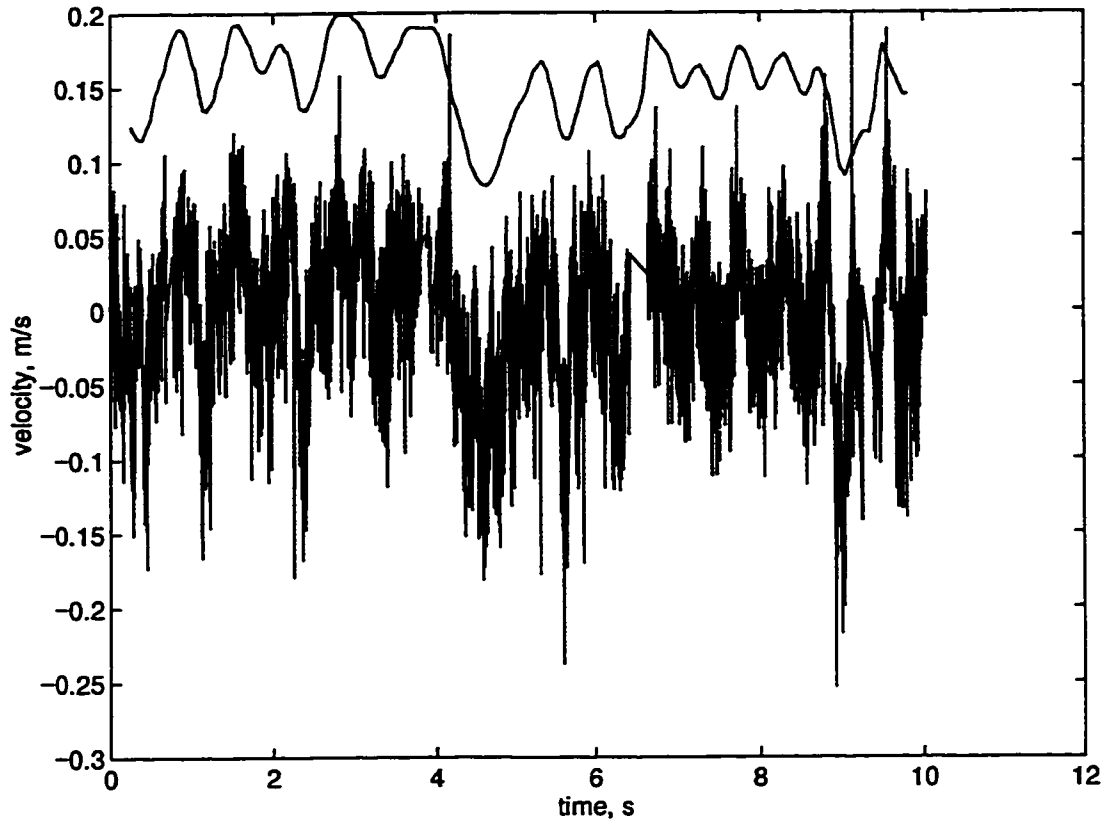


12c) top corner

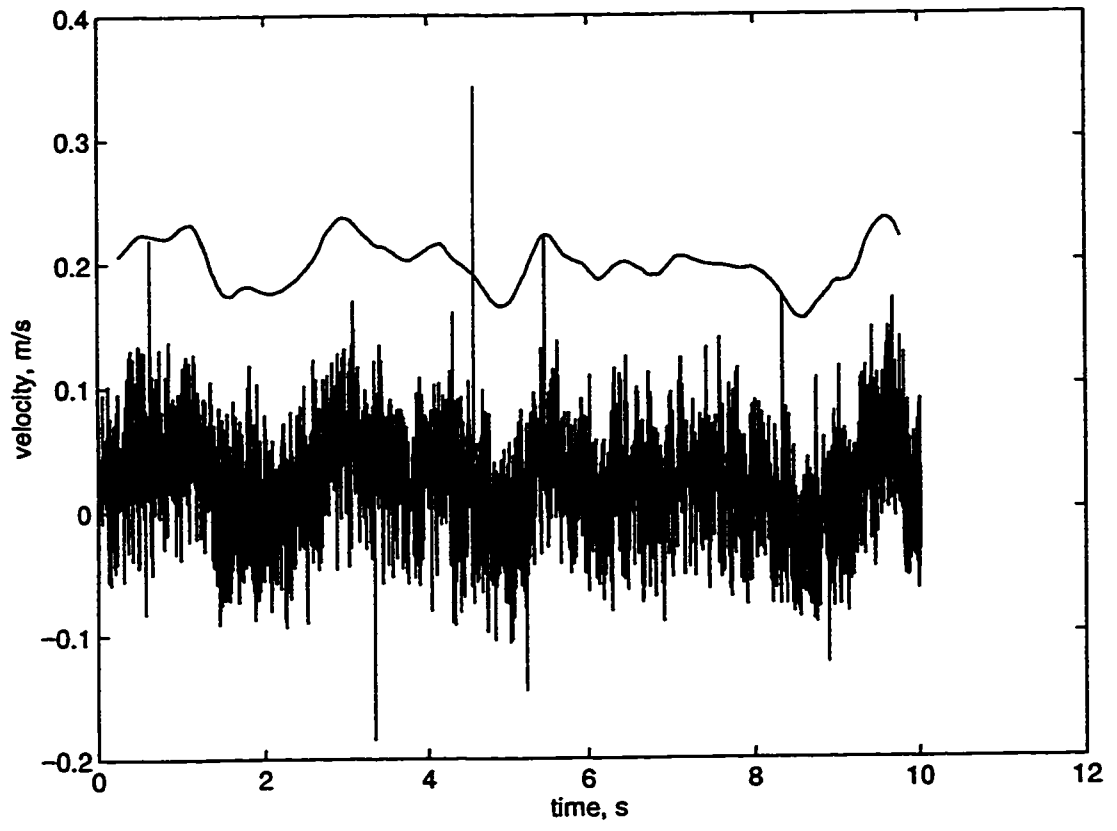


13a) impeller stream

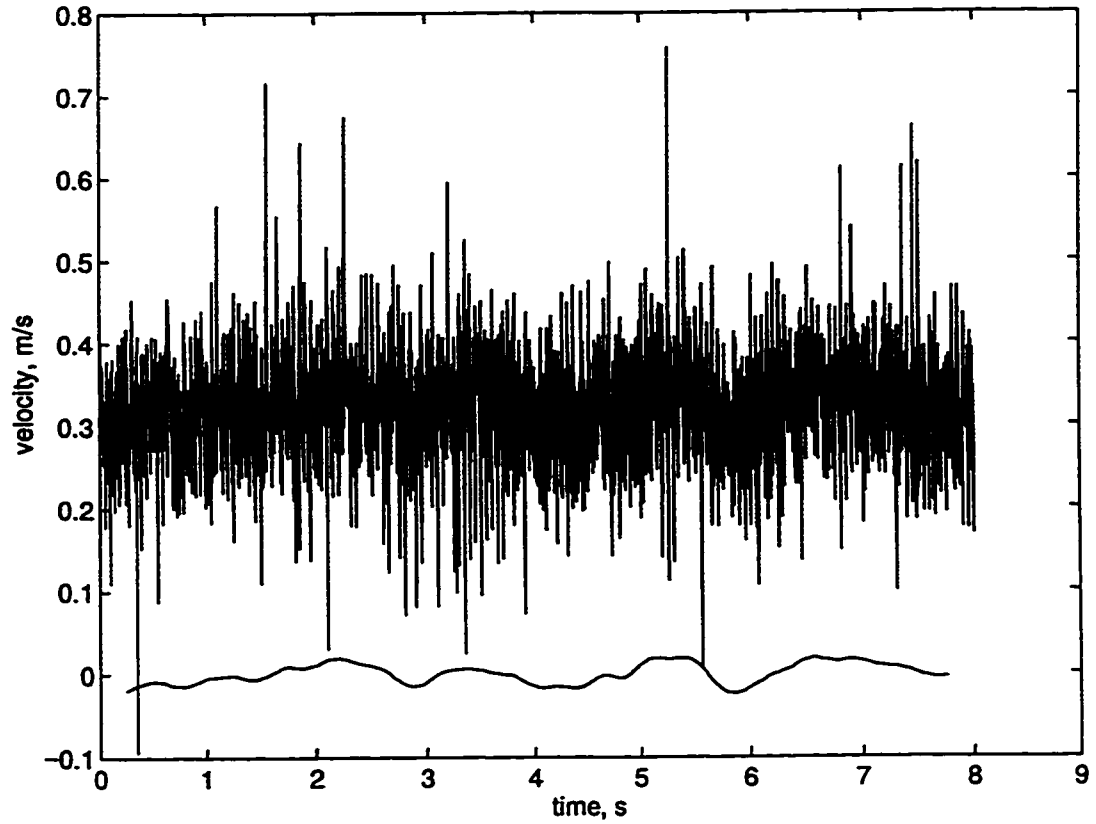
Figure 13: HE3 time series: $D=T/4$, $C/D=1$, $N_f=4$, smoothed over 10 (4+6) blade passages.



13b) bottom corner

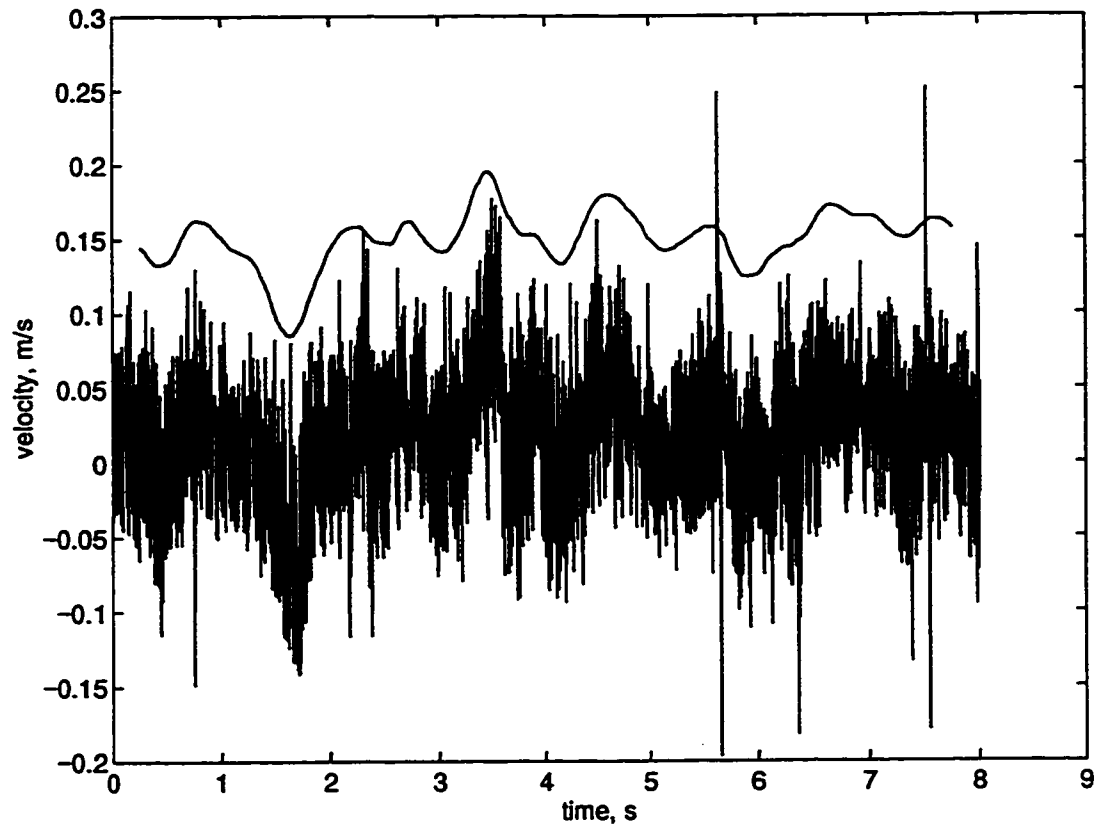


13c) top corner

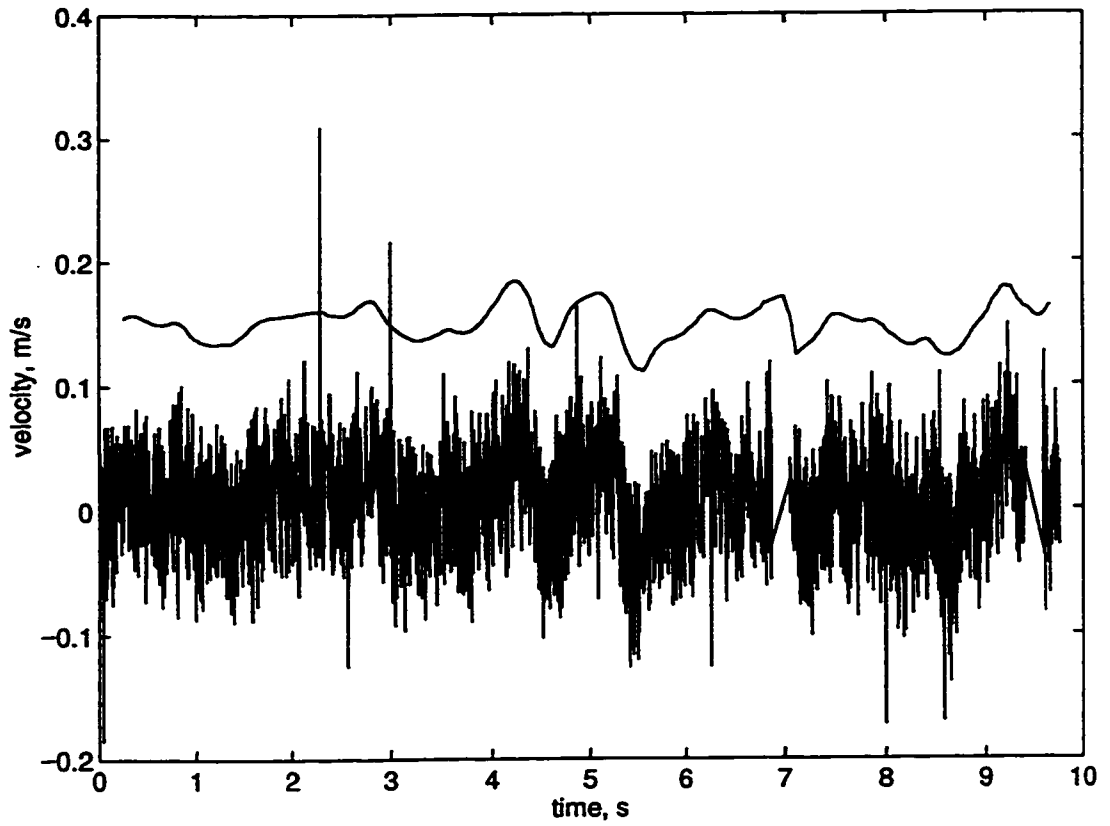


14a) impeller stream

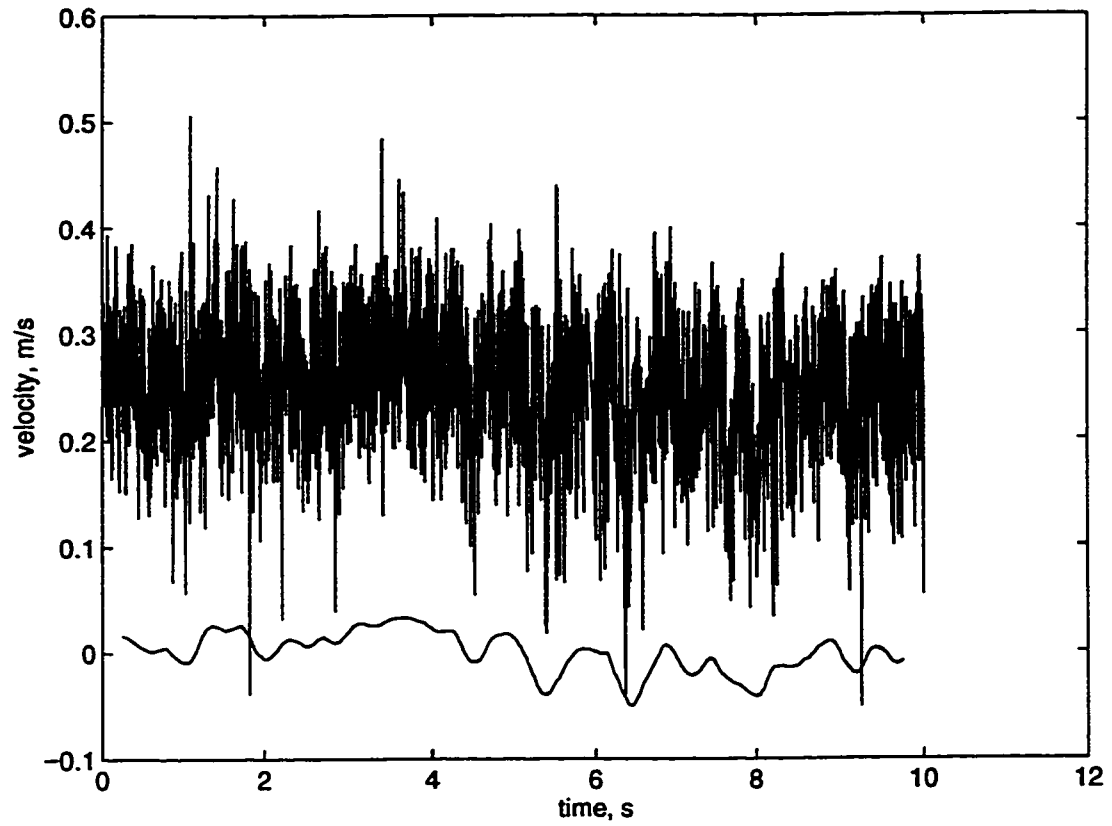
Figure 14: HE3 time series: $D=T/4$, $C/D=1$, $N_f=2$, smoothed over 10 (4+6) blade passages.



14b) bottom corner

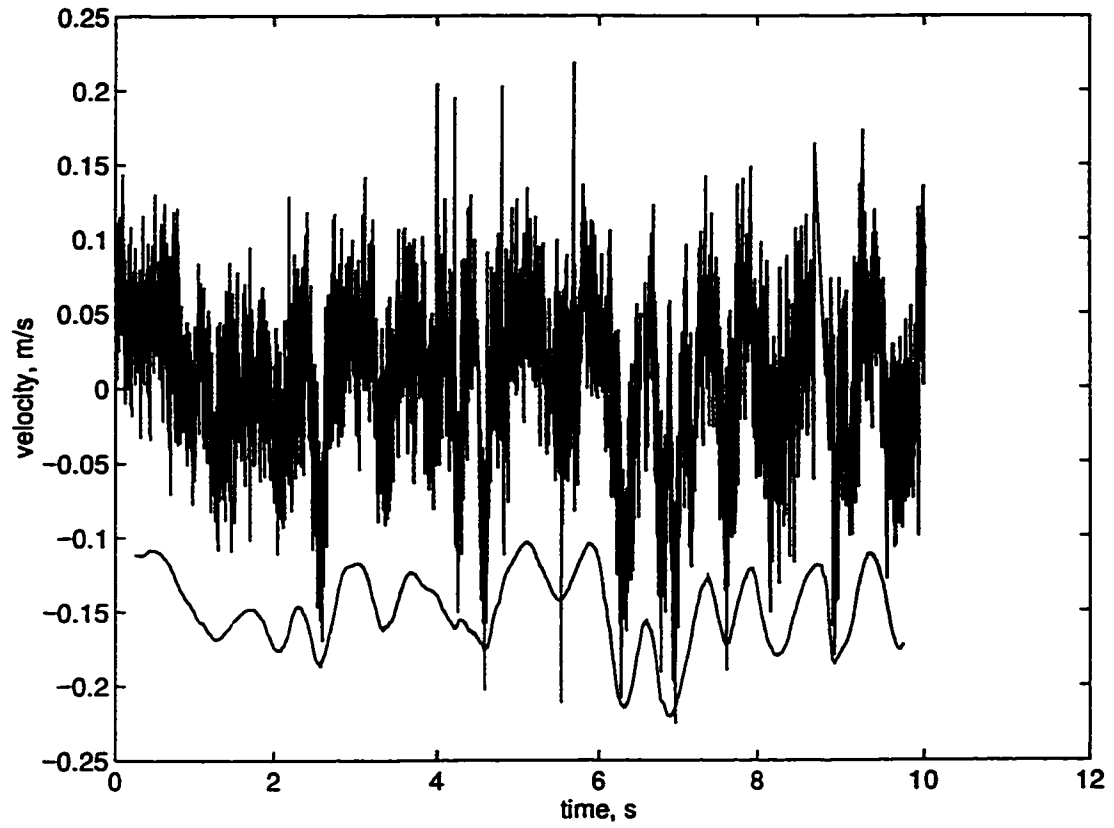


14c) top corner

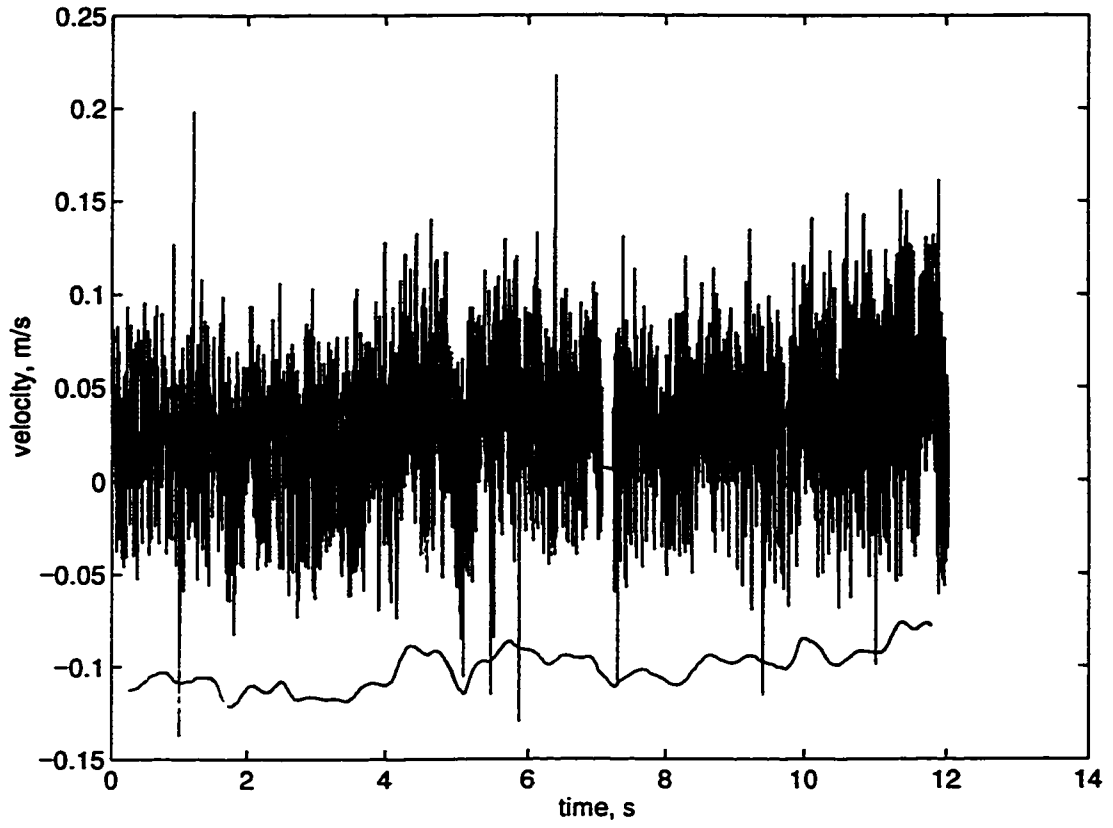


15a) impeller stream

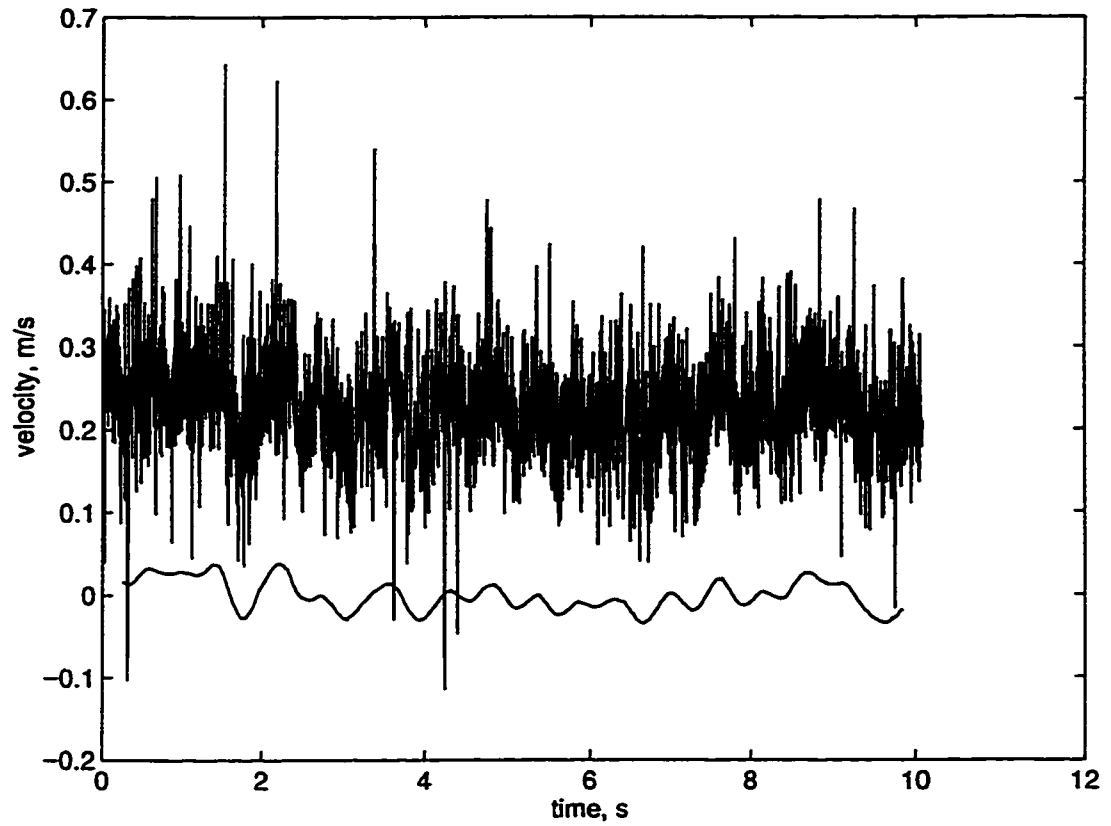
Figure 15: HE3 time series: $D=T/4$, $C/D=0.5$, $N_f=4$, smoothed over 10 (4+6) blade passages.



15b) bottom corner

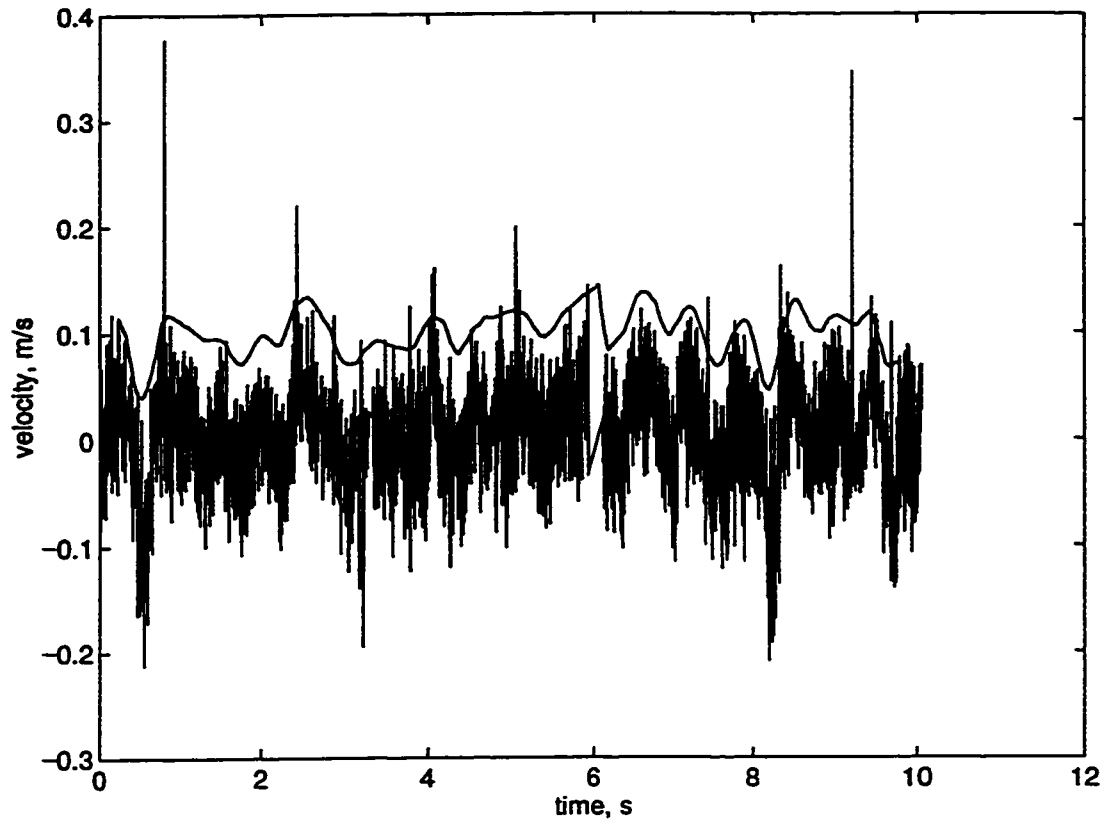


15c) top corner

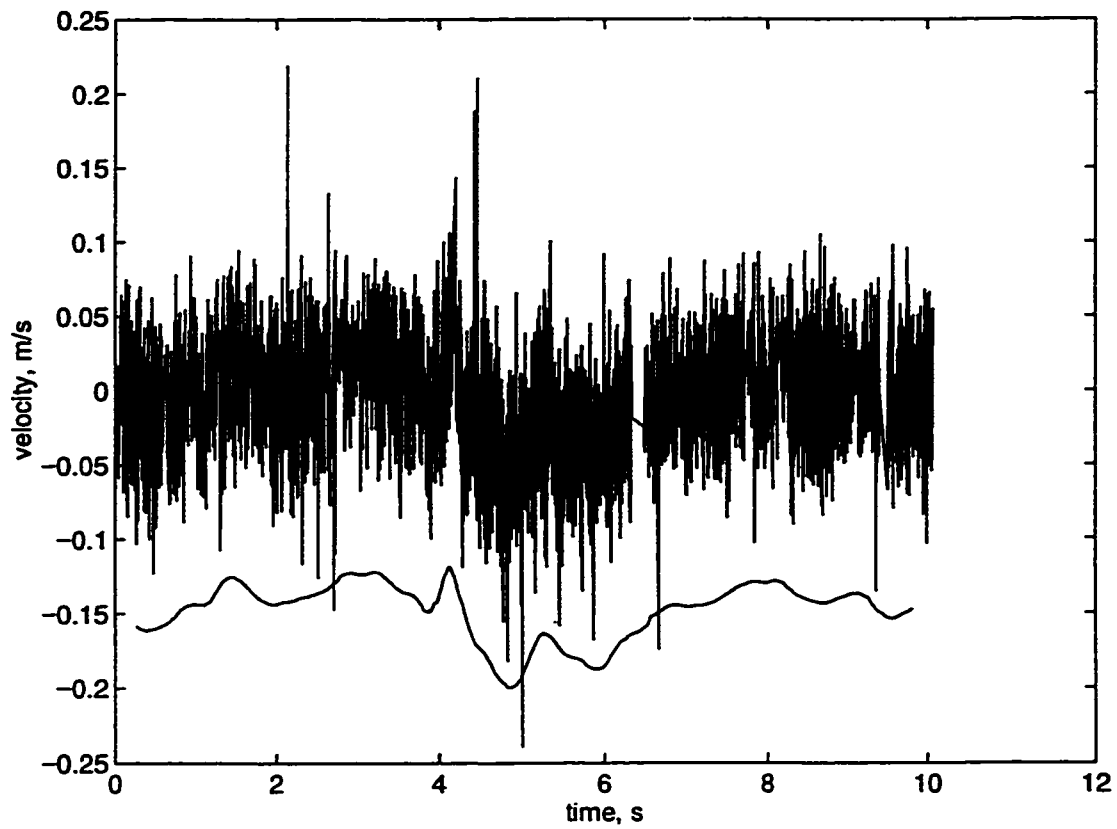


16a) impeller stream

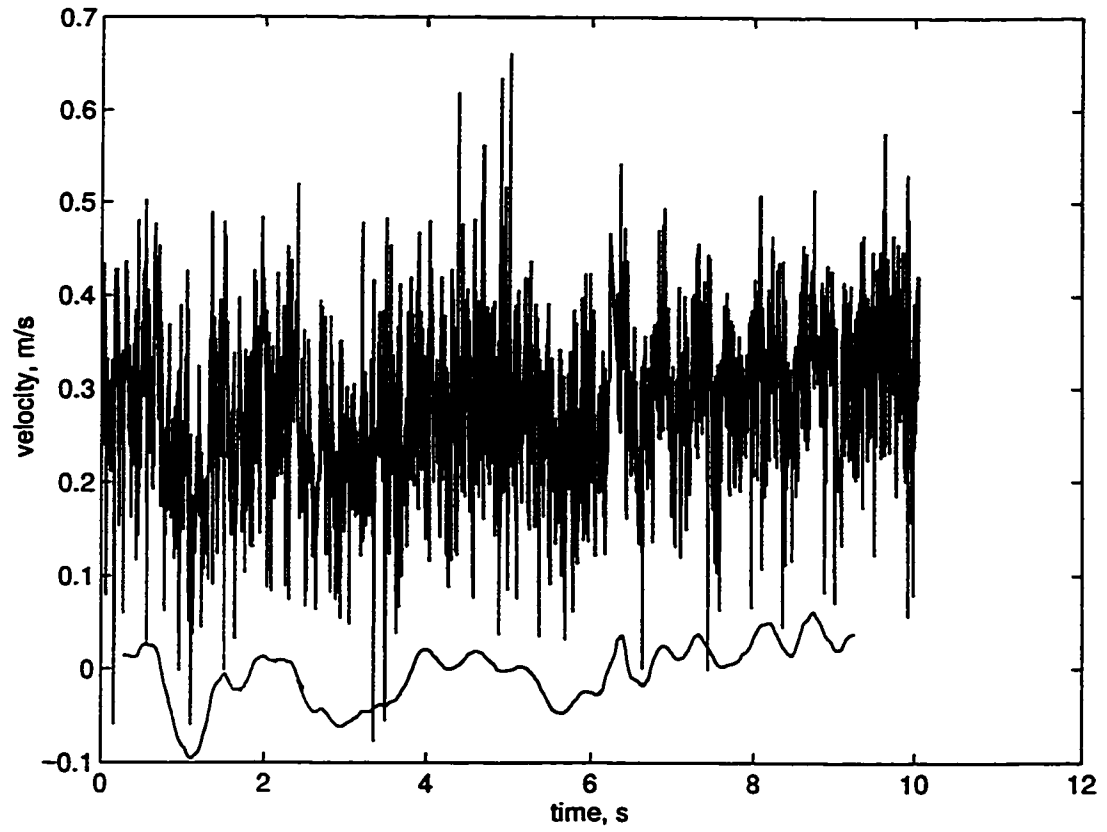
Figure 16: HE3 time series: $D=T/4$, $C/D=0.5$, $N_f=2$, smoothed over 10 (4+6) blade passages.



16b) bottom corner

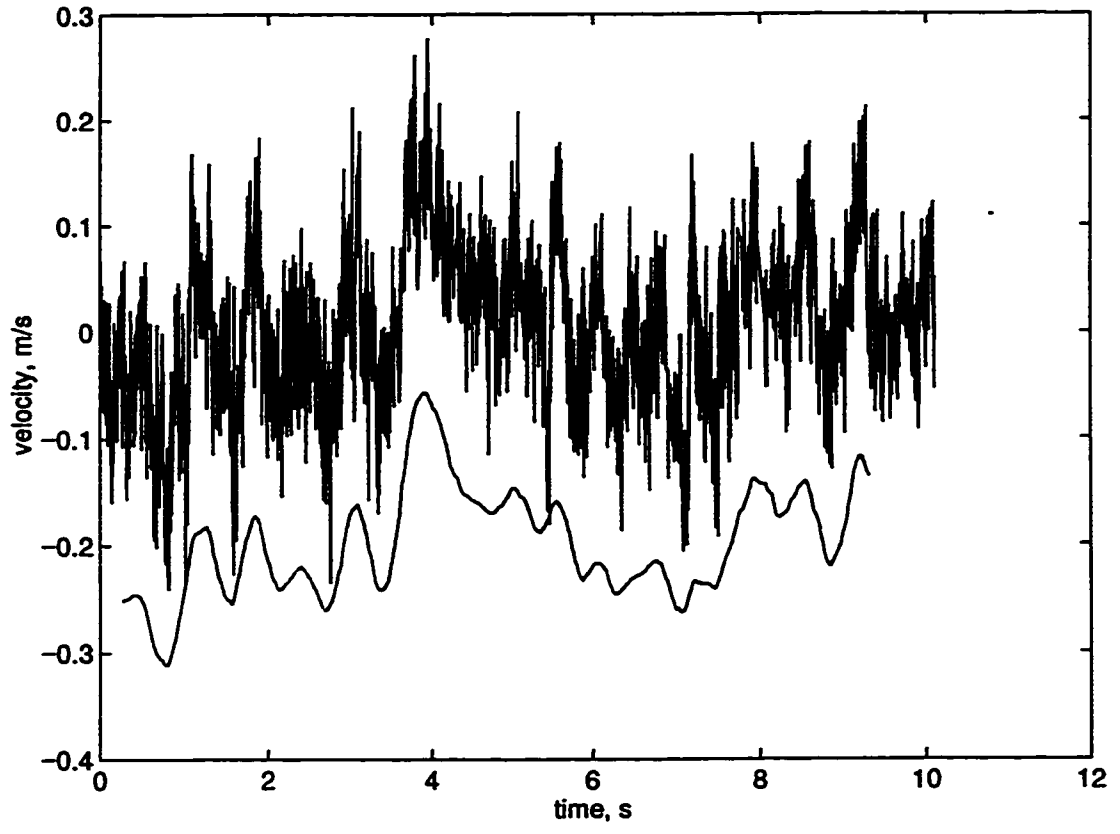


16c) top corner

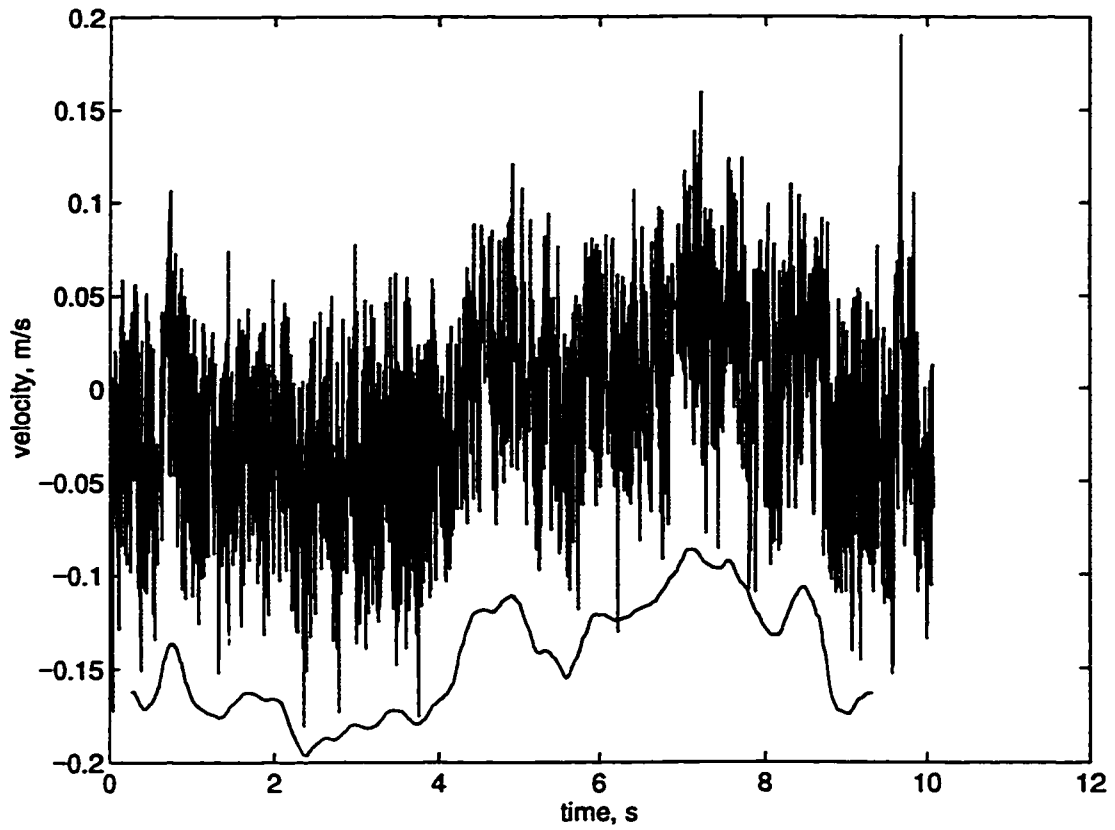


17a) impeller stream

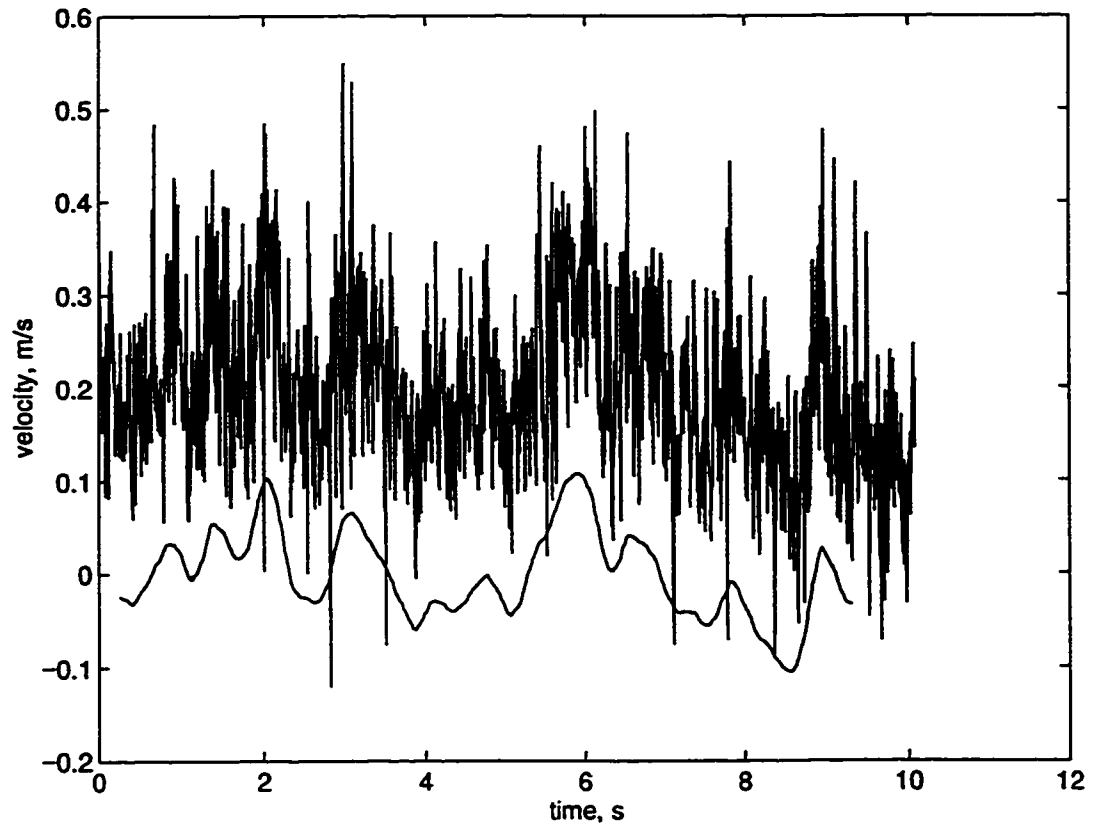
Figure 17: A310 time series: $D=T/2$, $C/D=1$, $N_f=4$, smoothed over 4 (2+2) blade passages.



17b) bottom corner

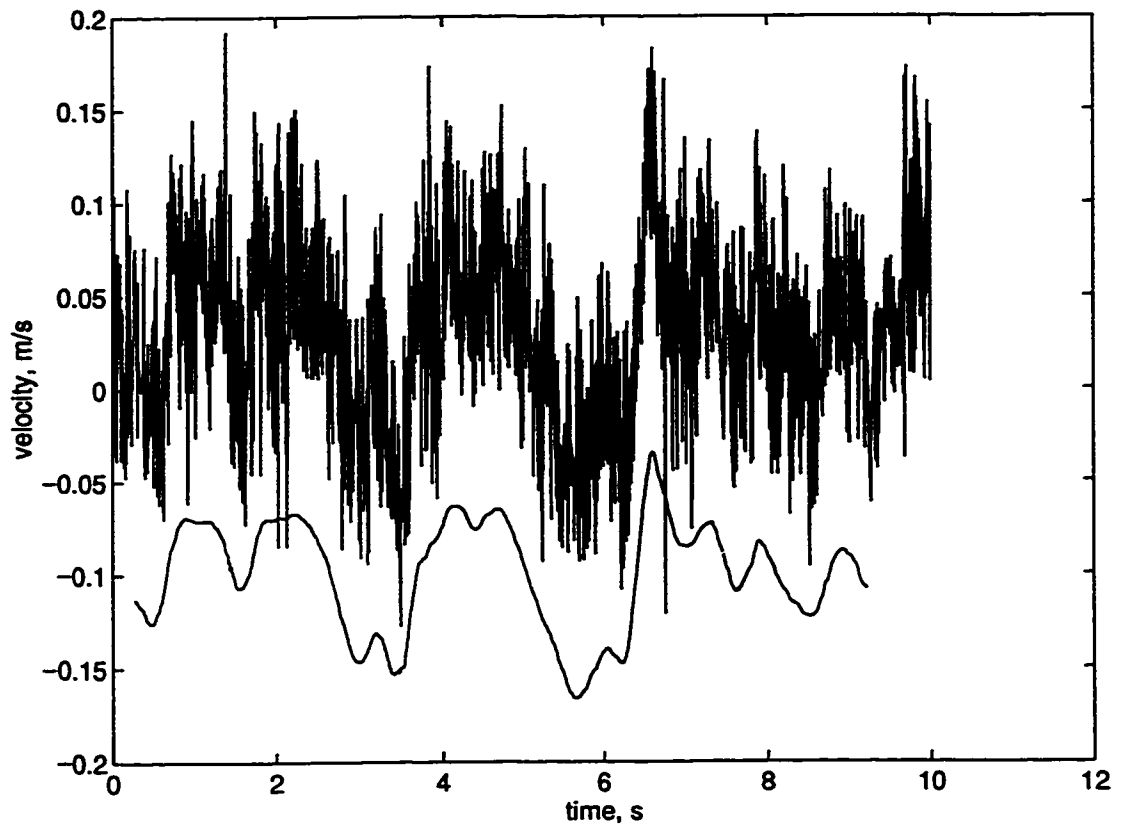


17c) top corner

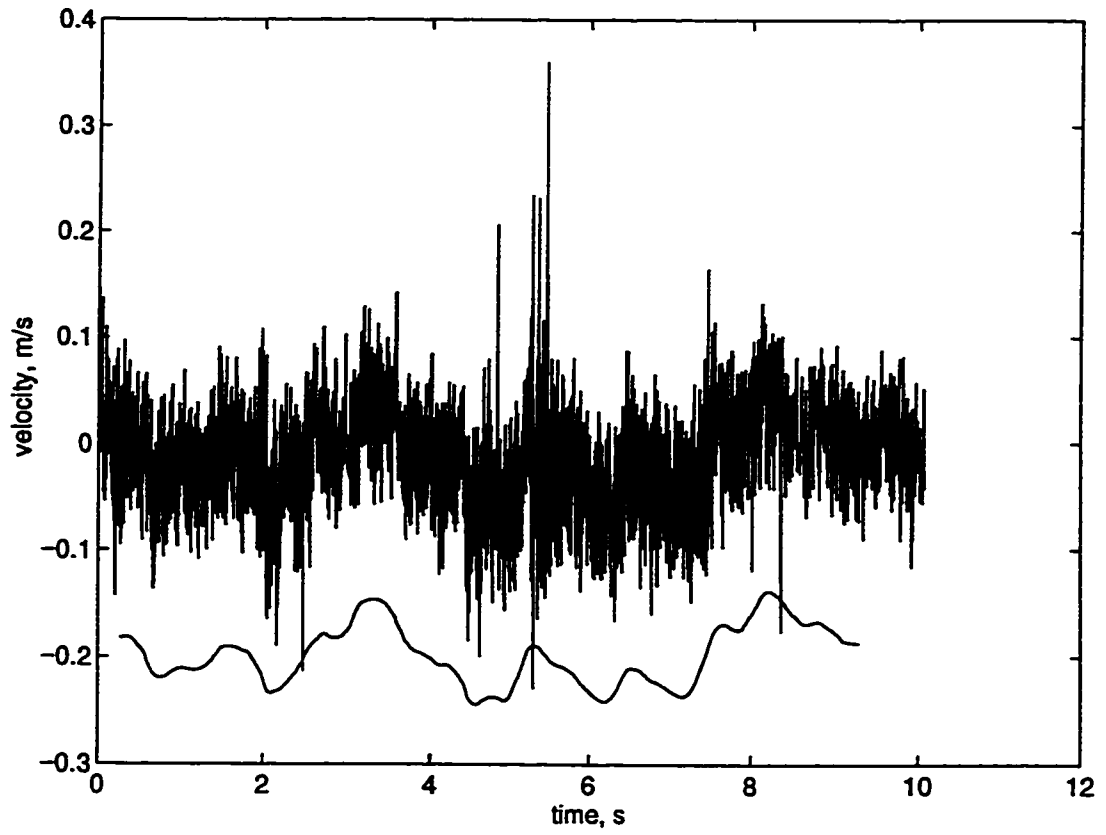


18a) impeller stream

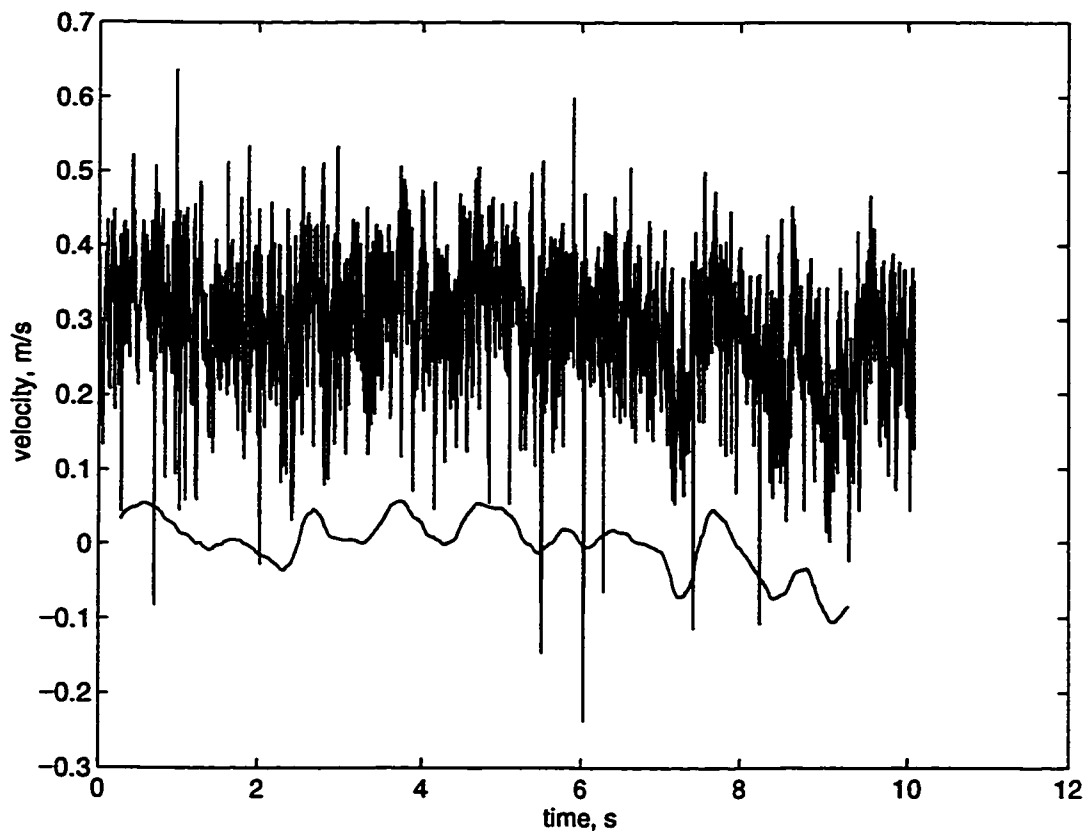
Figure 18: A310 time series: $D=T/2$, $C/D=1$, $N_f=2$, smoothed over 4 (2+2) blade passages.



18b) bottom corner

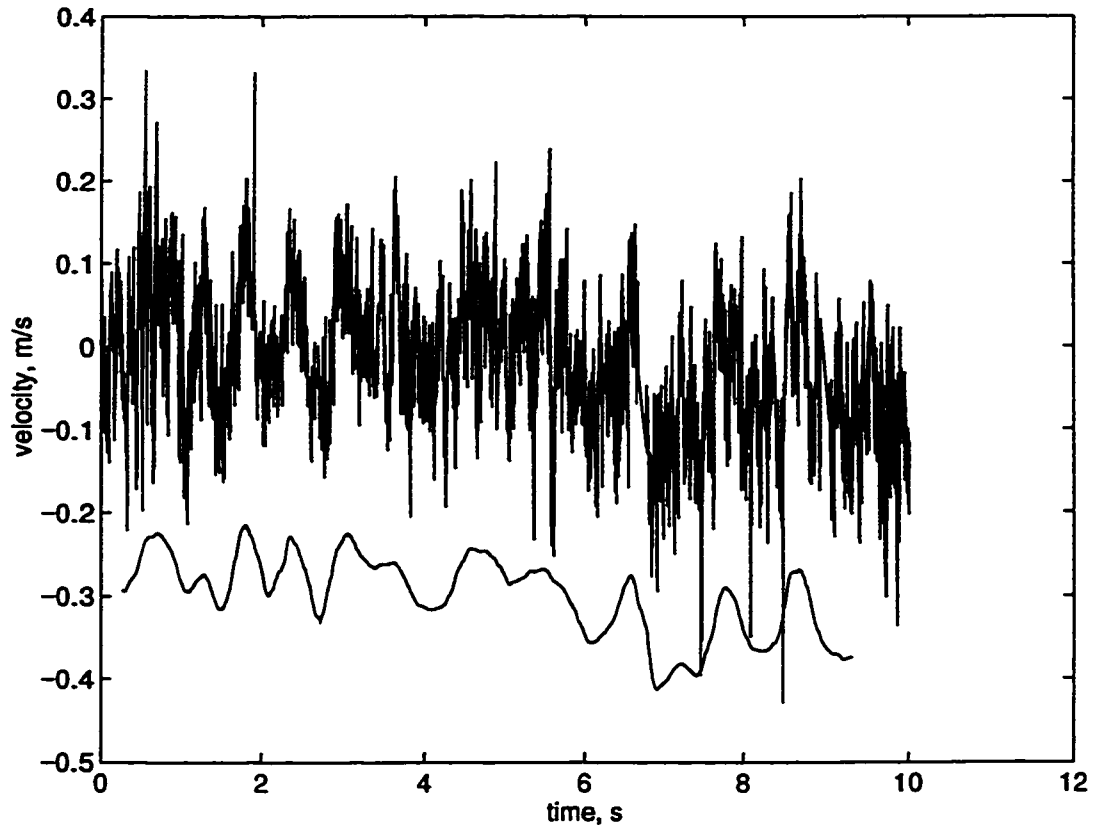


18c) top corner

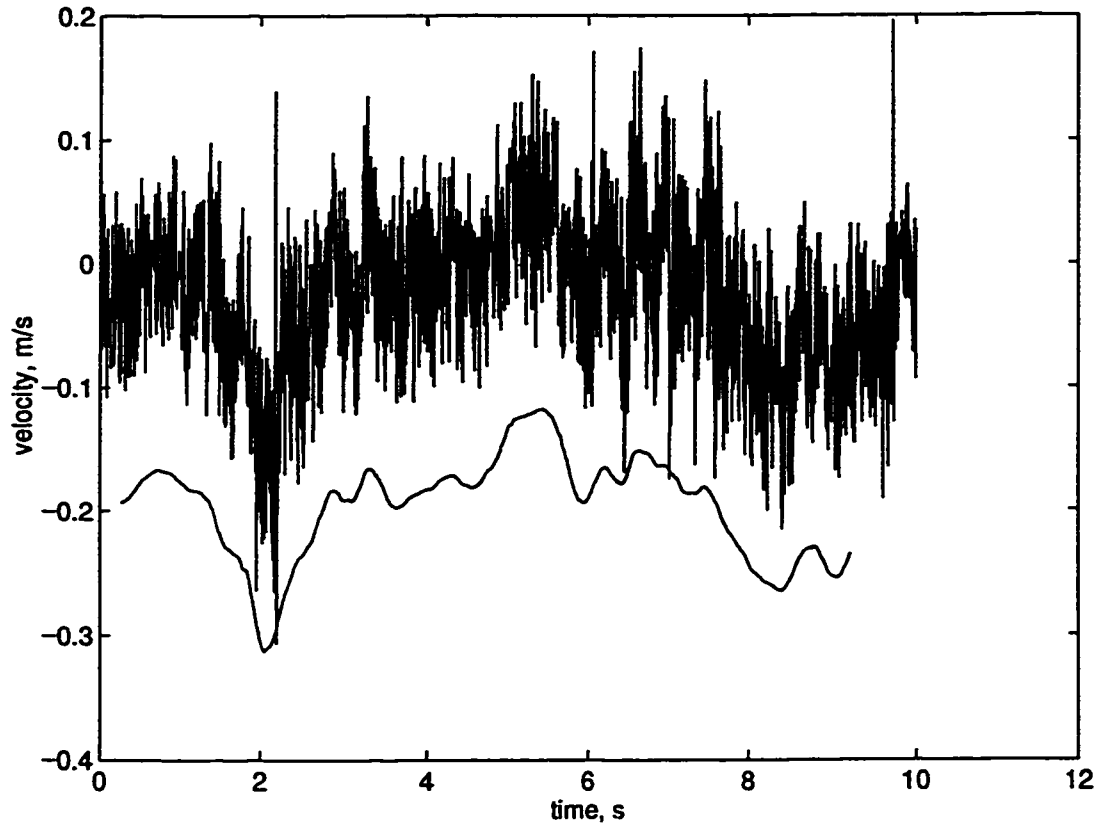


19a) impeller stream

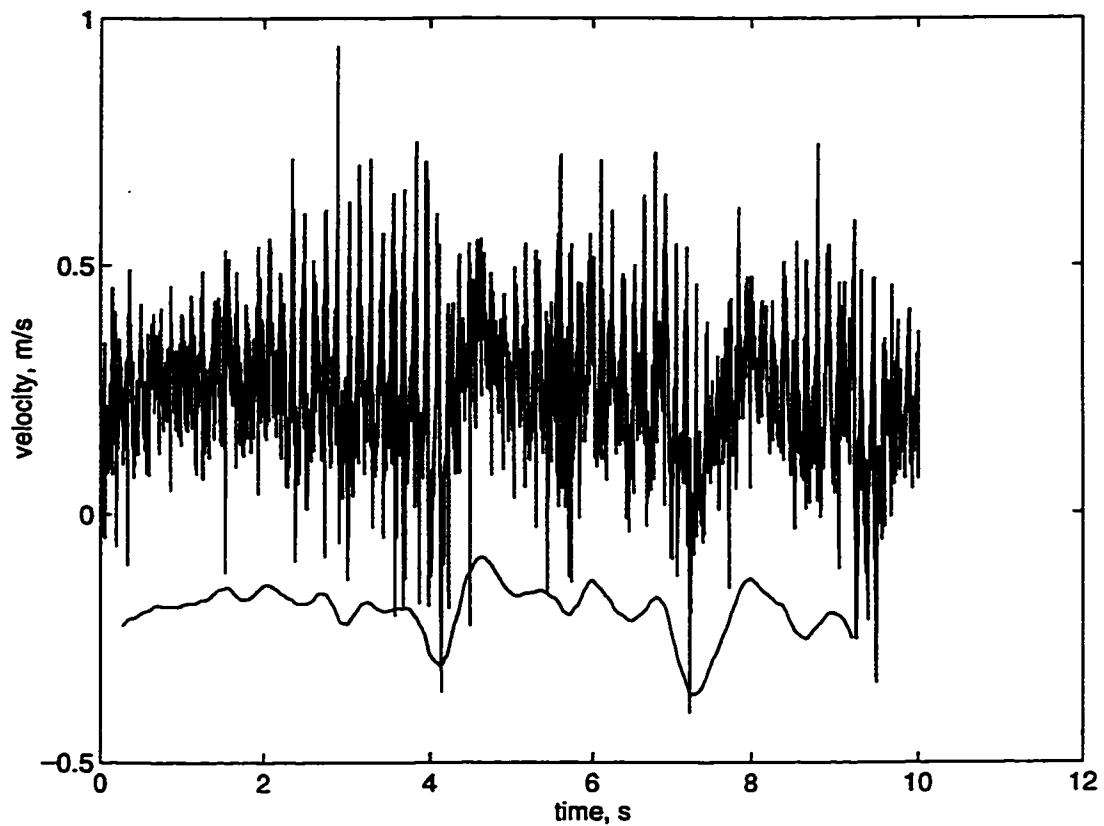
Figure 19: A310 time series: $D=T/2$, $C/D=0.5$, $N_f=4$, smoothed over 4 (2+2) blade passages.



19b) bottom corner

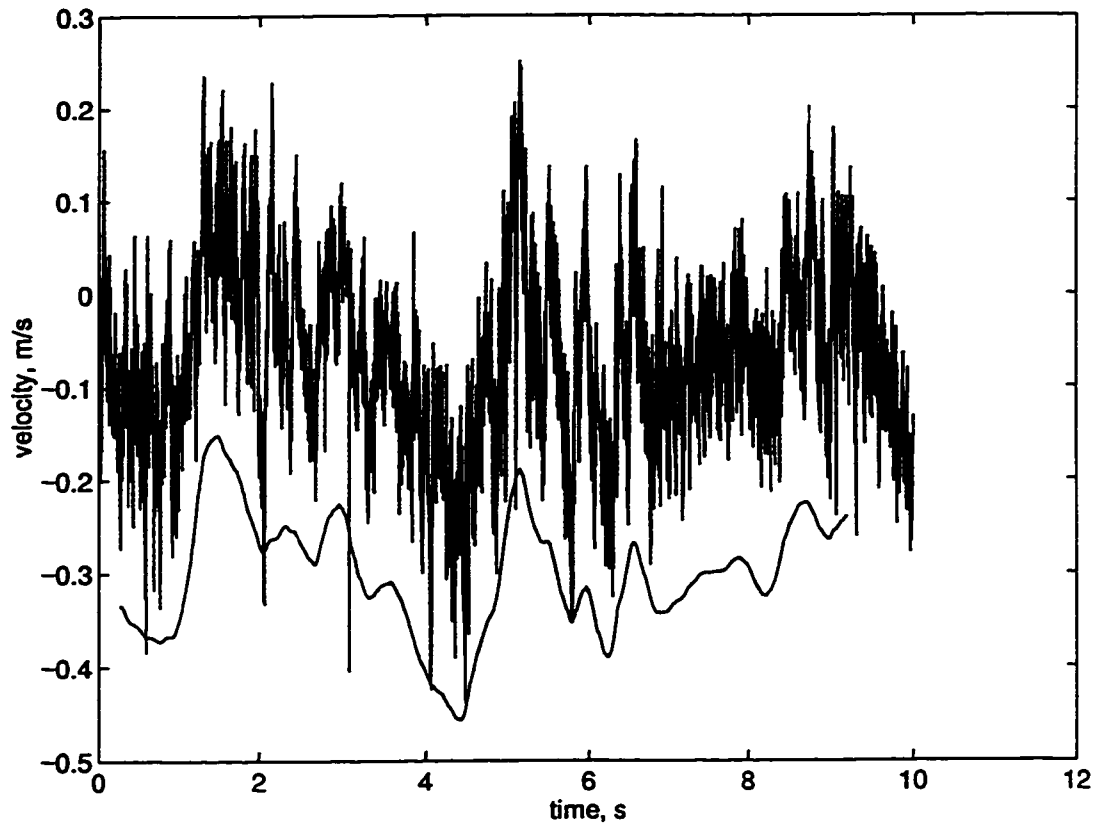


19c) top corner

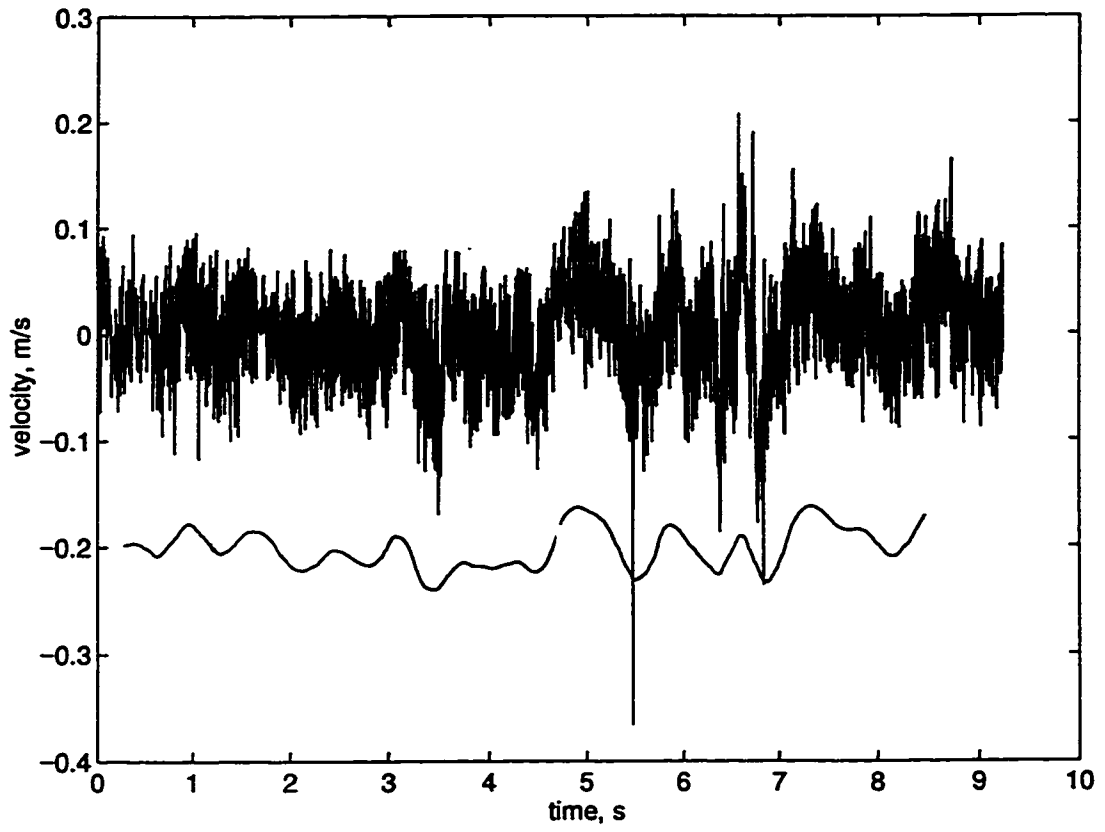


20a) impeller stream

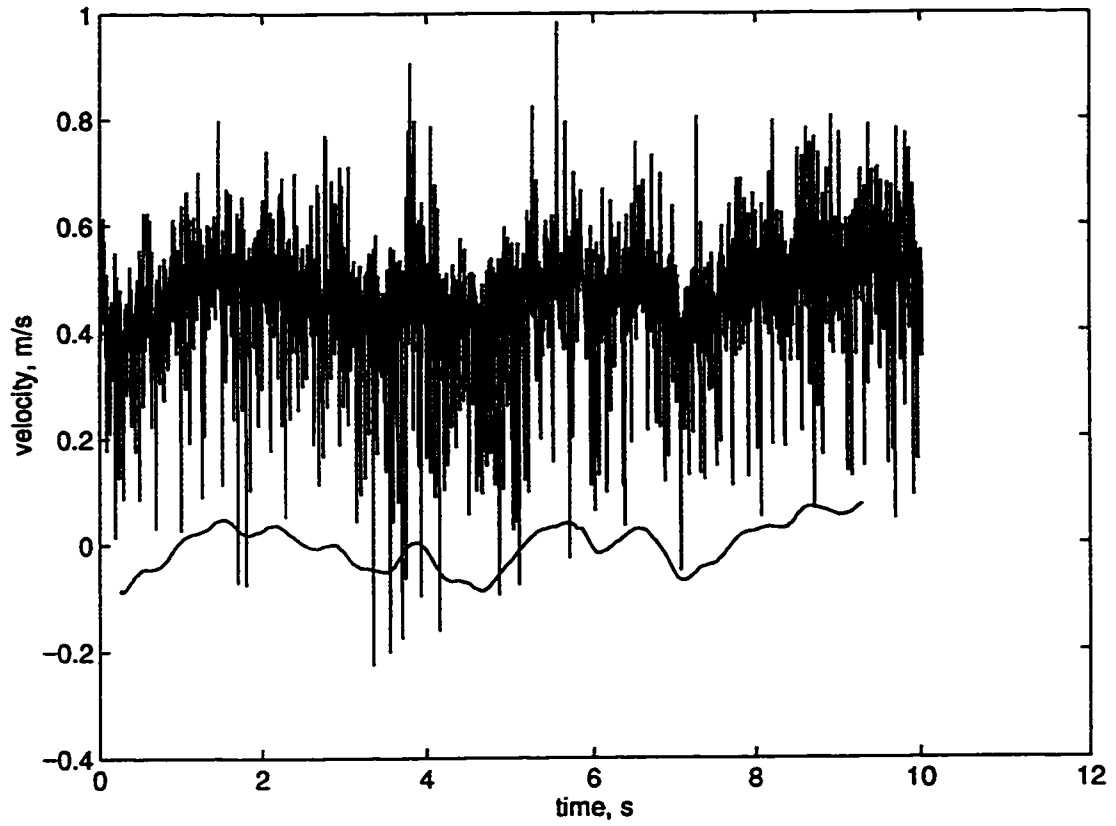
Figure 20: A310 time series: $D=T/2$, $C/D=0.5$, $N_f=2$, smoothed over 4 (2+2) blade passages.



20b) bottom corner

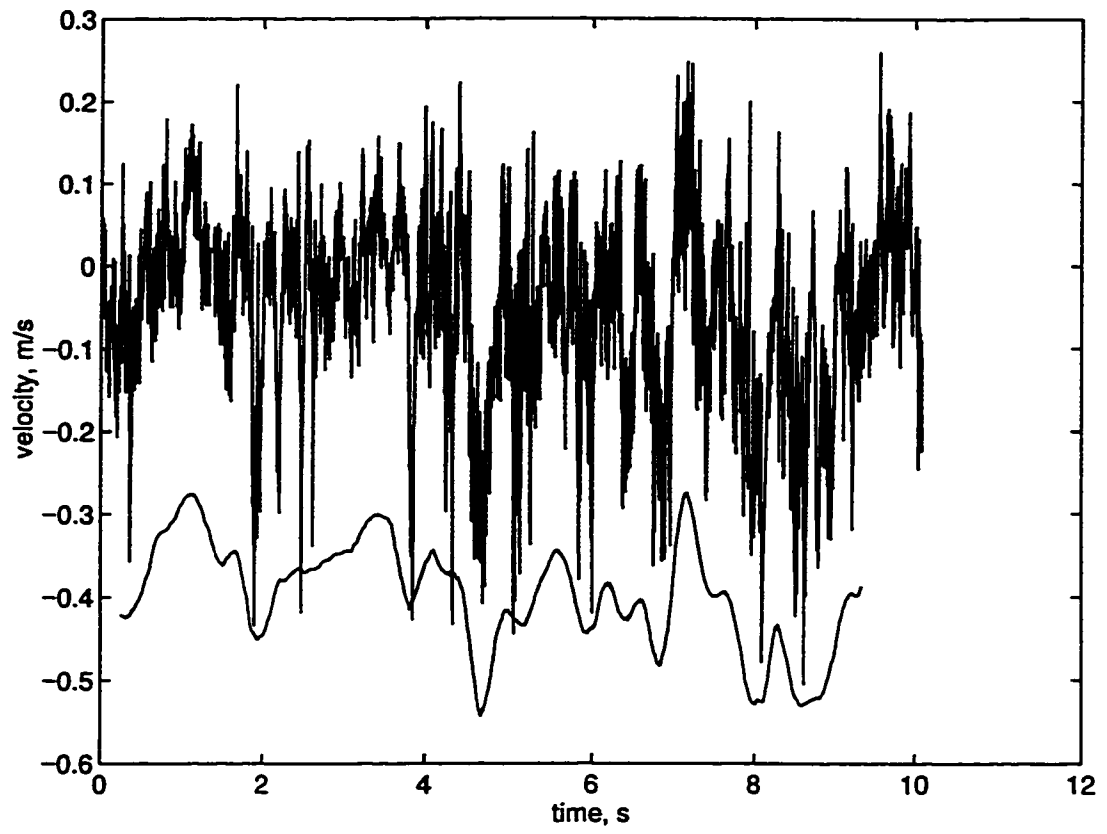


20c) top corner

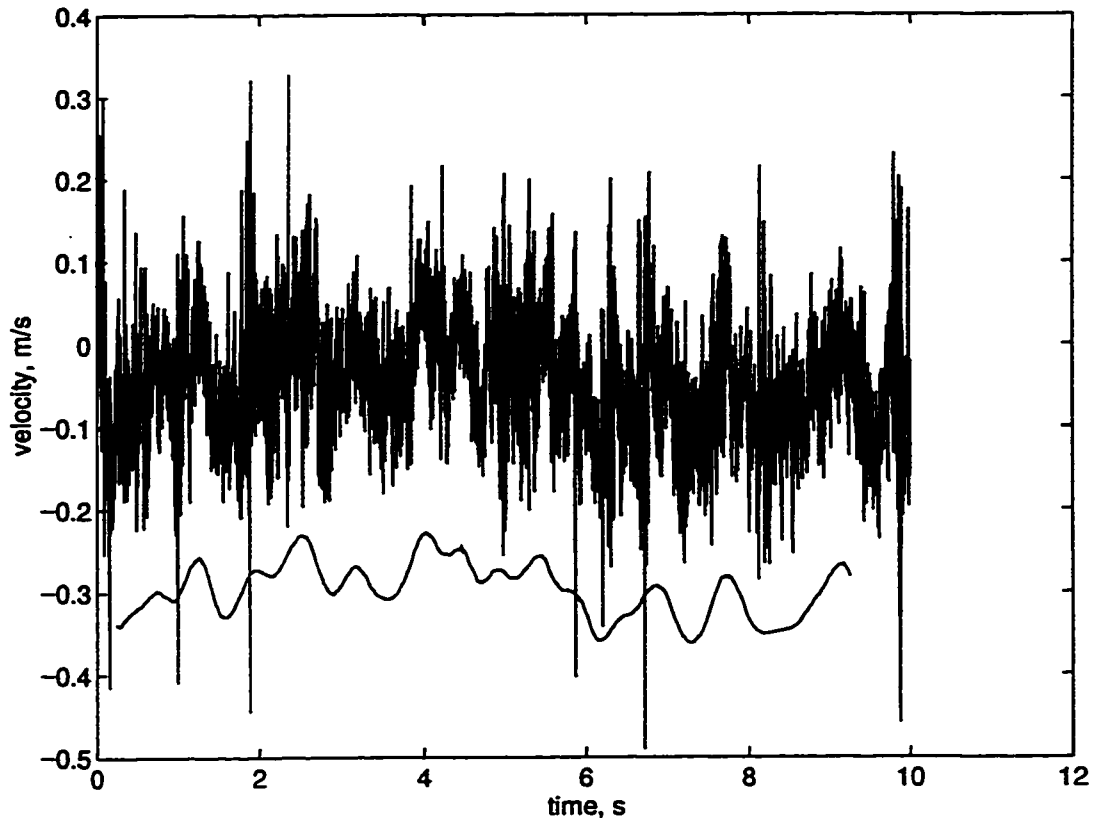


21a) impeller stream

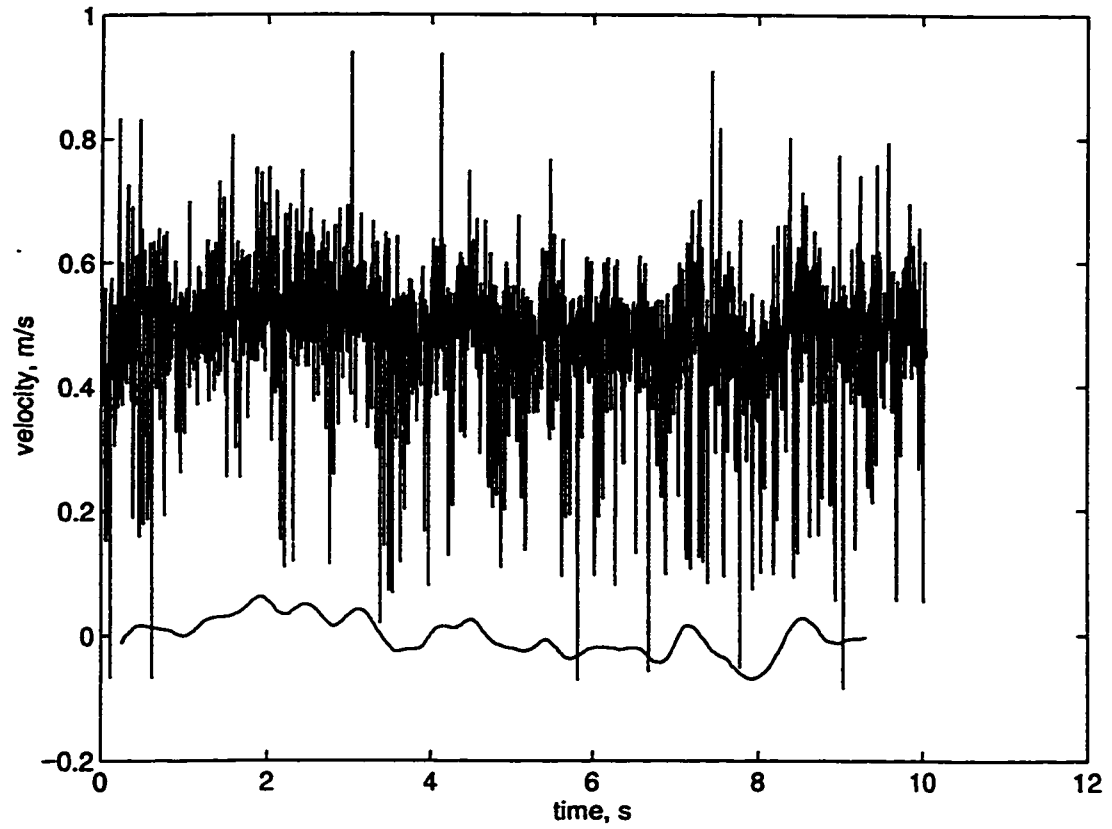
Figure 21: A310 time series: $D=T/4$, $C/D=1$, $N_f=2$, smoothed over 4 (2+2) blade passages.



21b) bottom corner

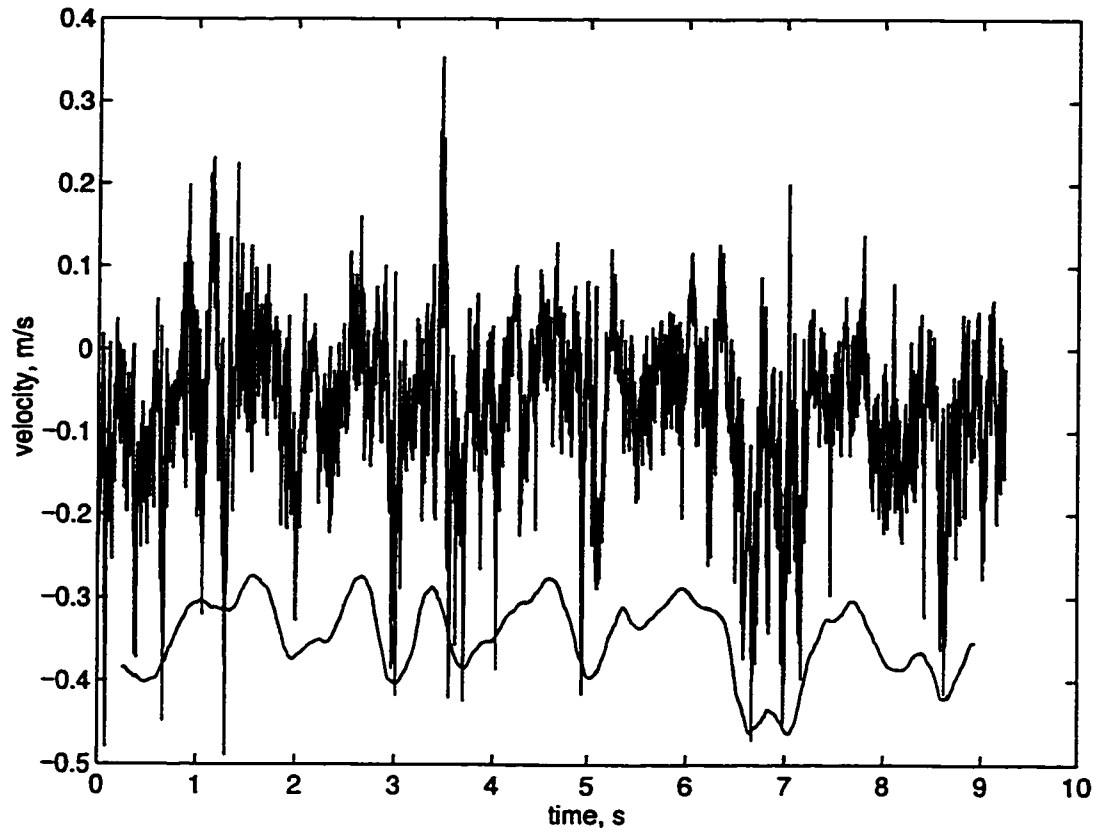


21c) top corner

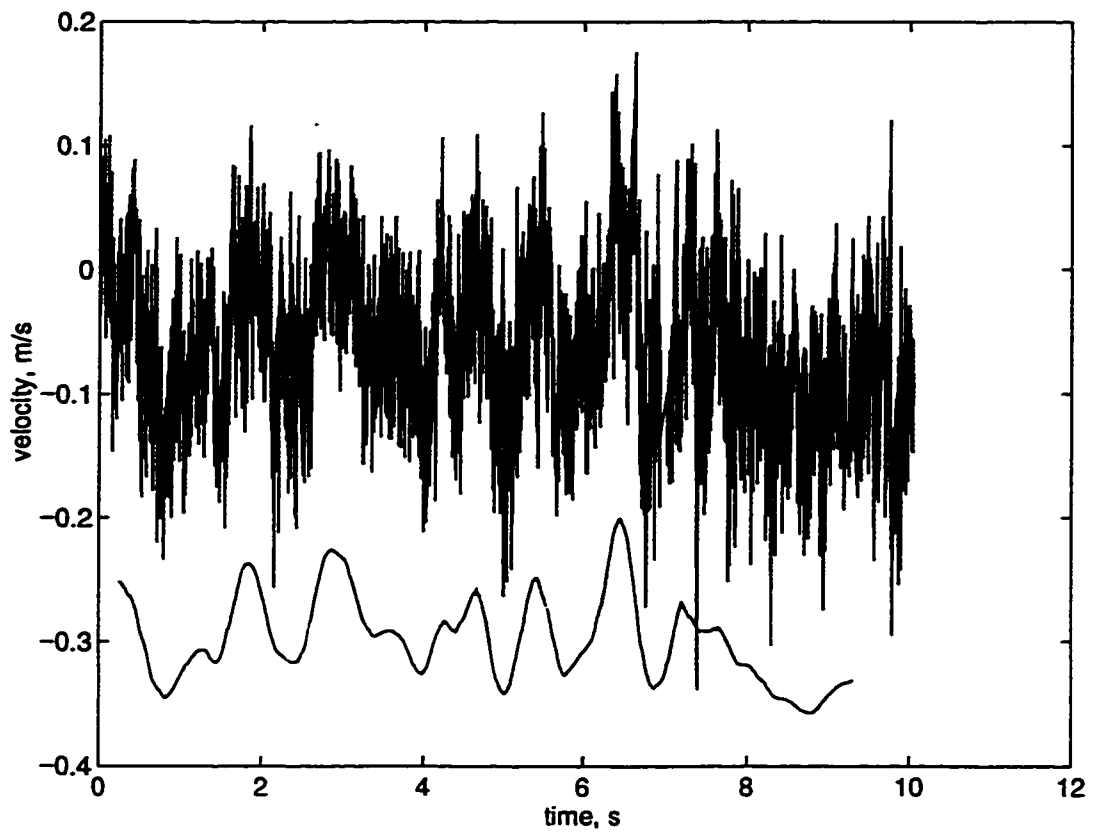


22a) impeller stream

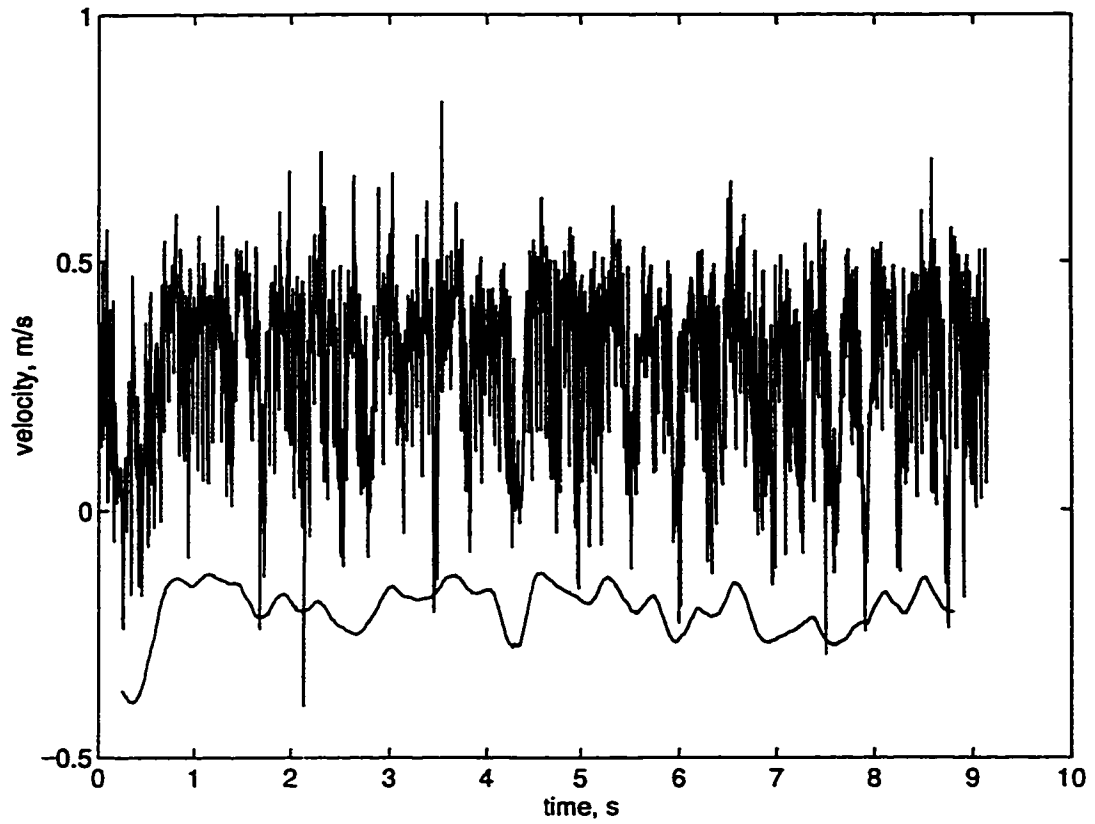
Figure 22: A310 time series: $D=T/4$, $C/D=1$, $N_f=4$, smoothed over 10 (4+6) blade passages.



22b) bottom corner

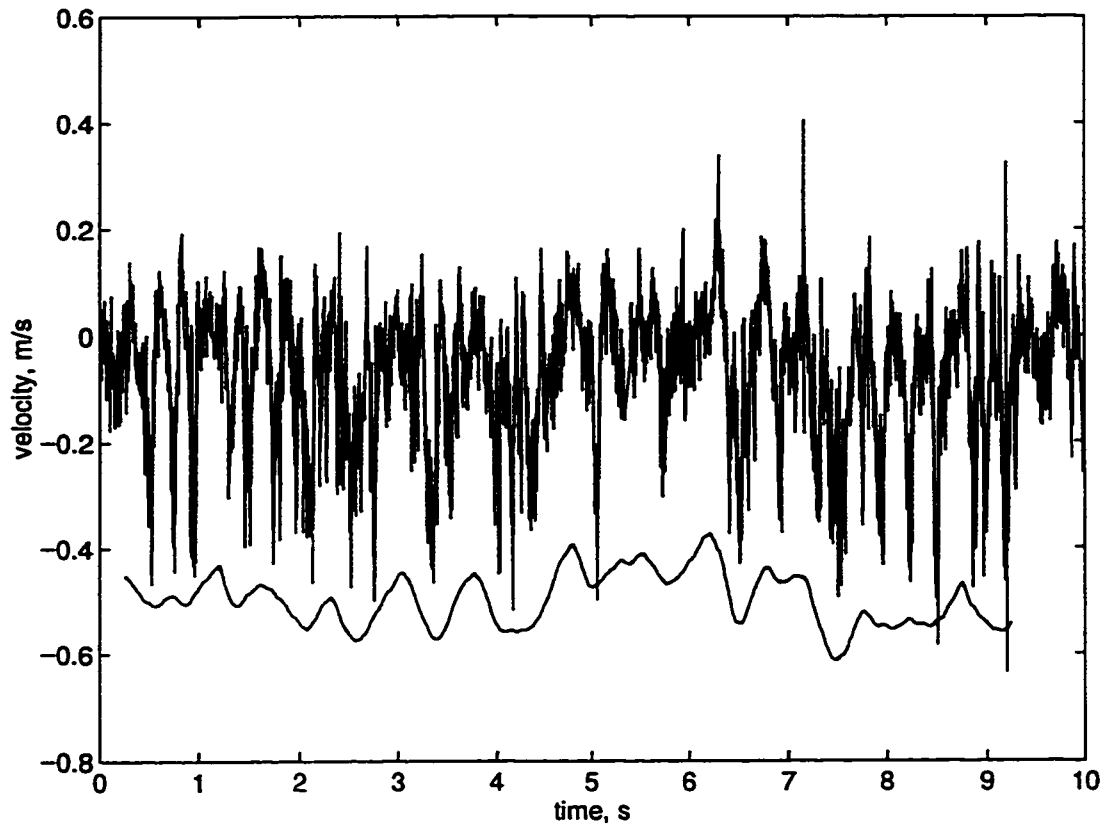


22c) top corner

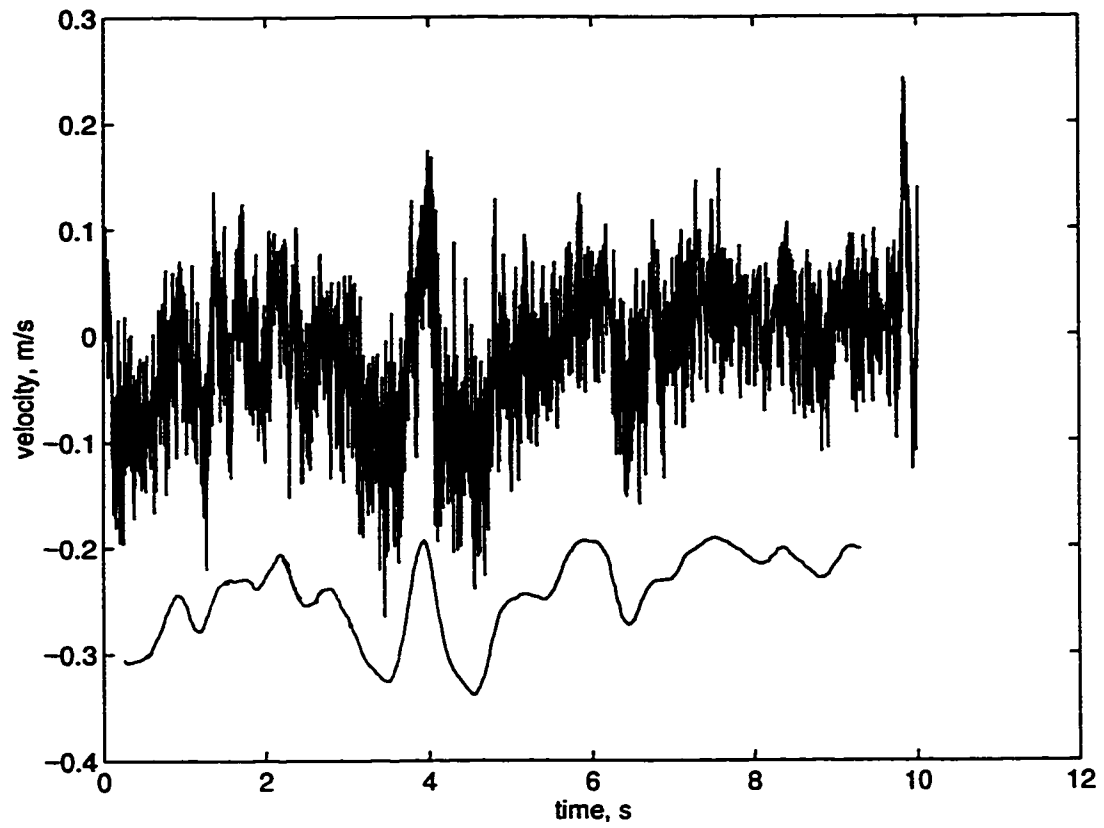


23a) impeller stream

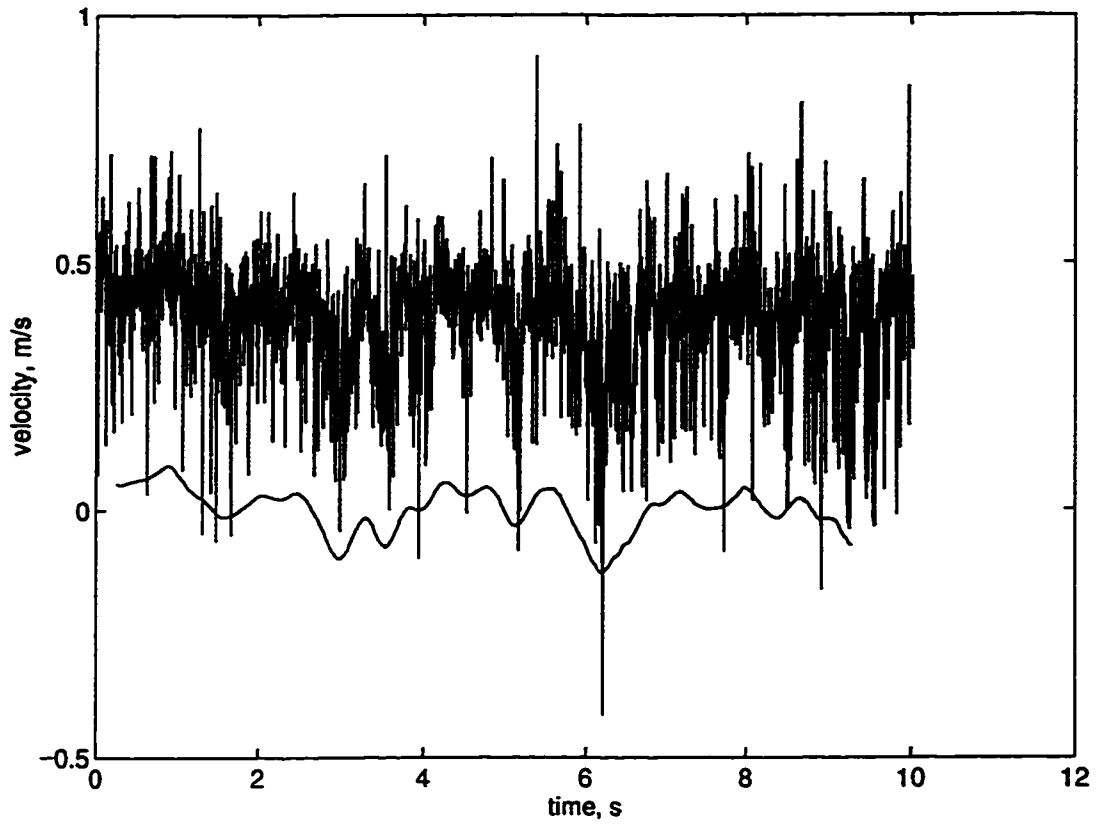
Figure 23: A310 time series: $D=T/4$, $C/D=0.5$, $N_f=4$, smoothed over 10 (4+6) blade passages.



23b) bottom corner

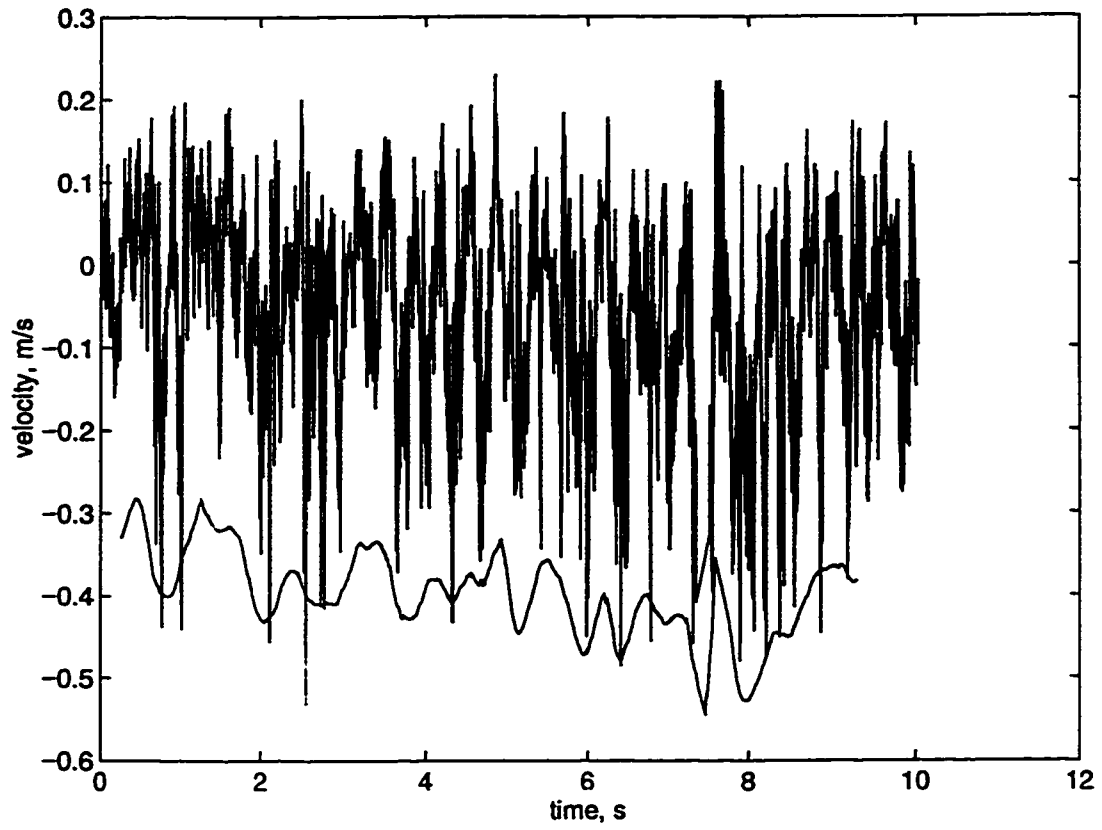


23c) top corner

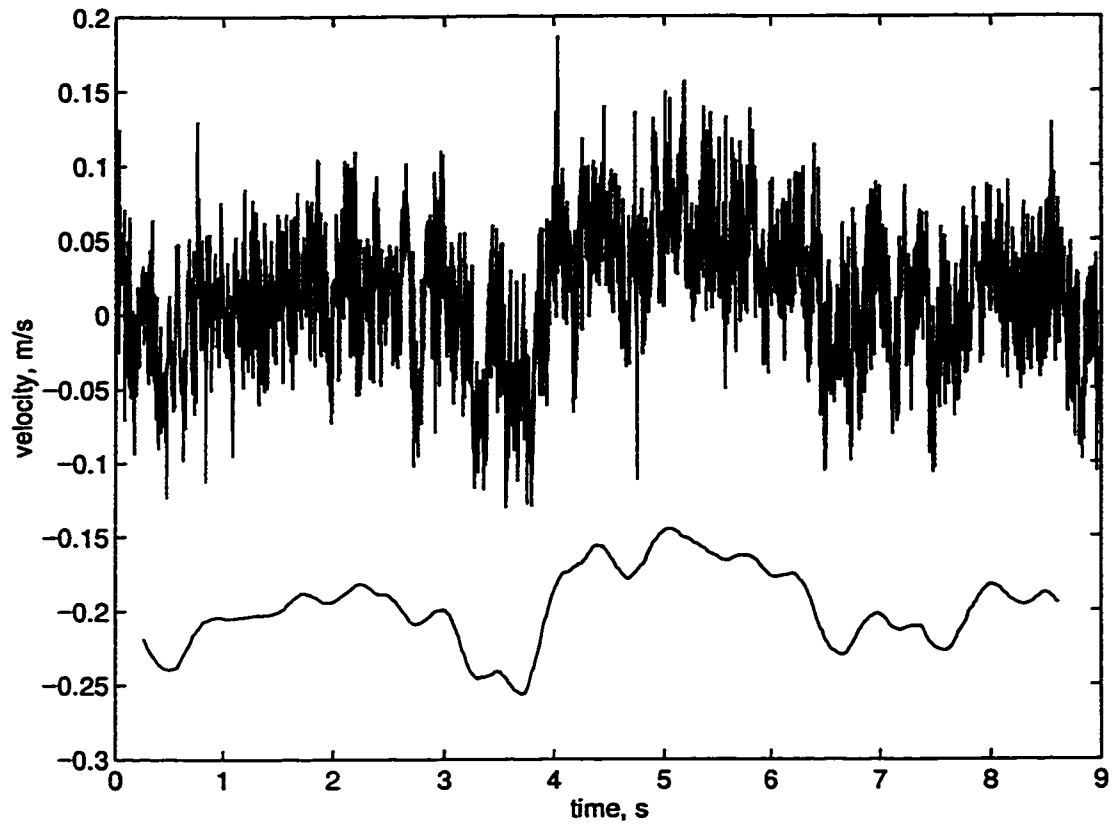


24a) impeller stream

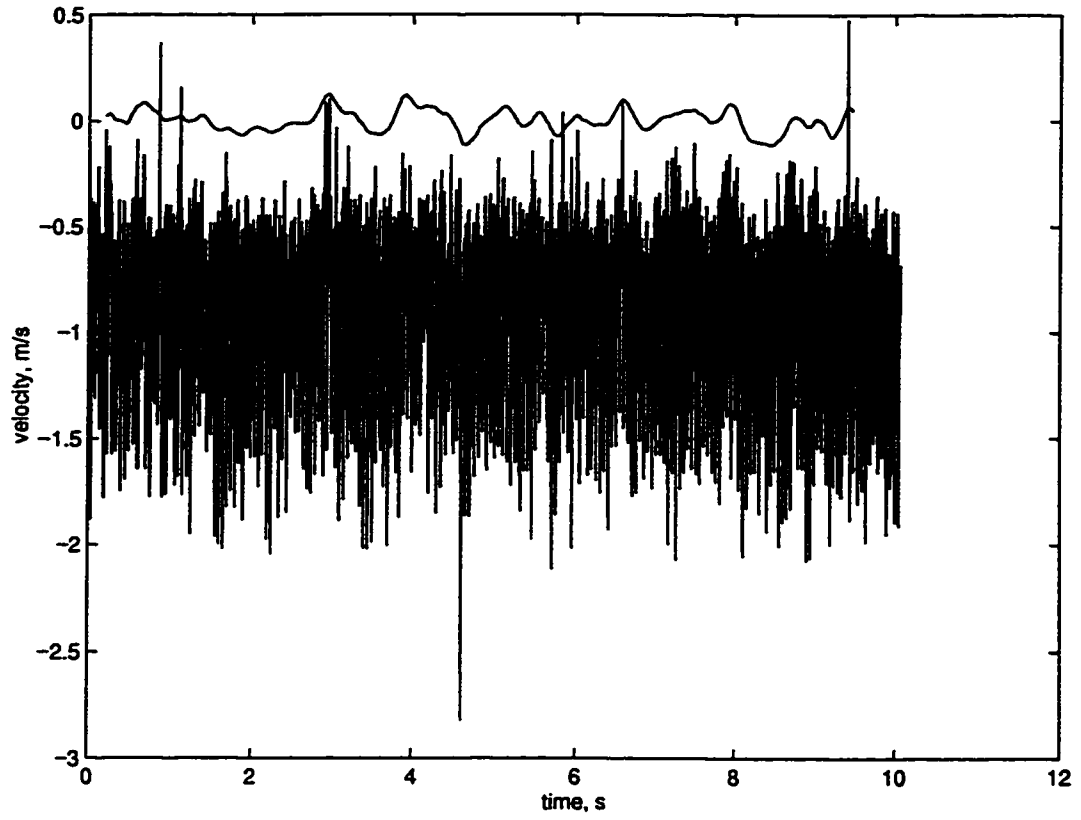
Figure 24: A310 time series: $D=T/4$, $C/D=0.5$, $N_f=2$, smoothed over 10 (4+6) blade passages.



24b) bottom corner

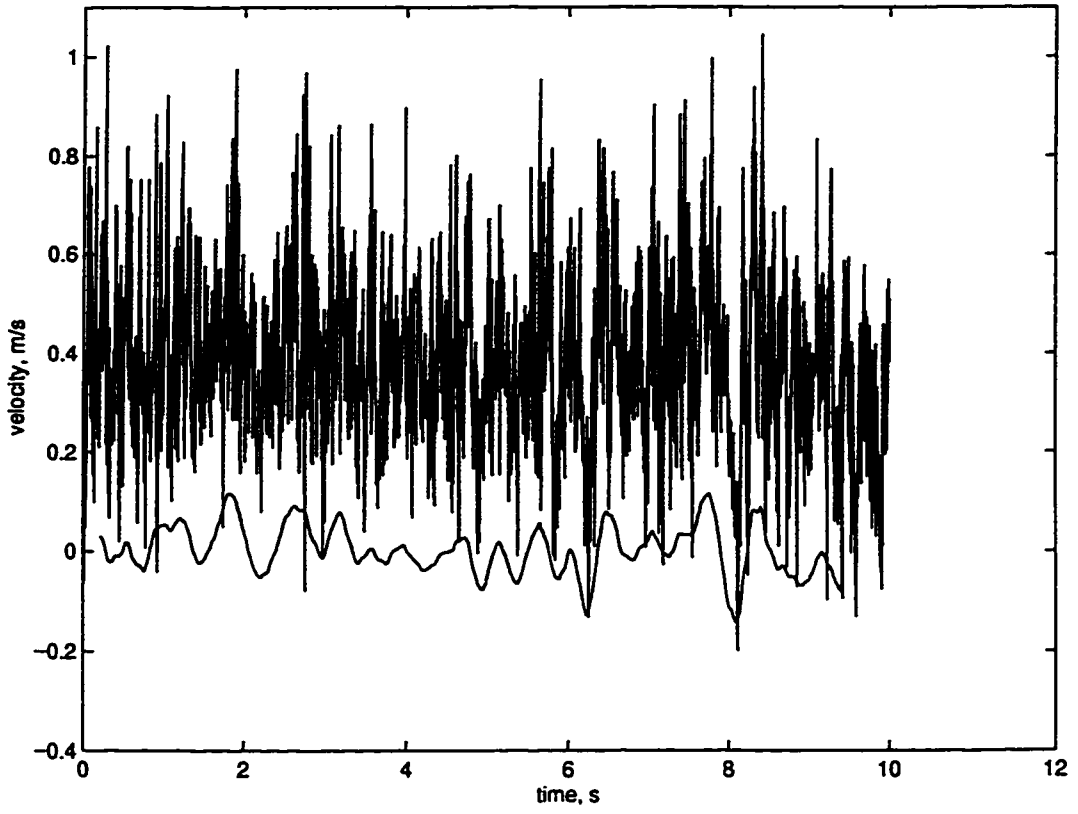


24c) top corner

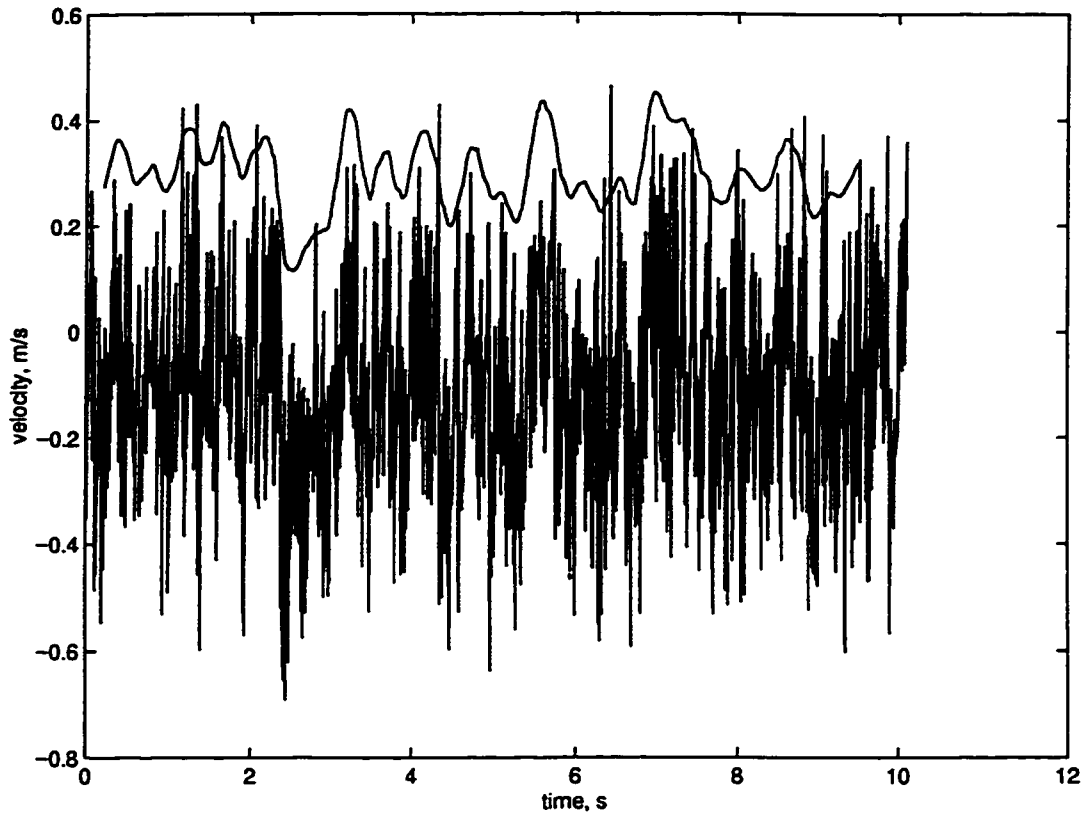


25a) impeller stream

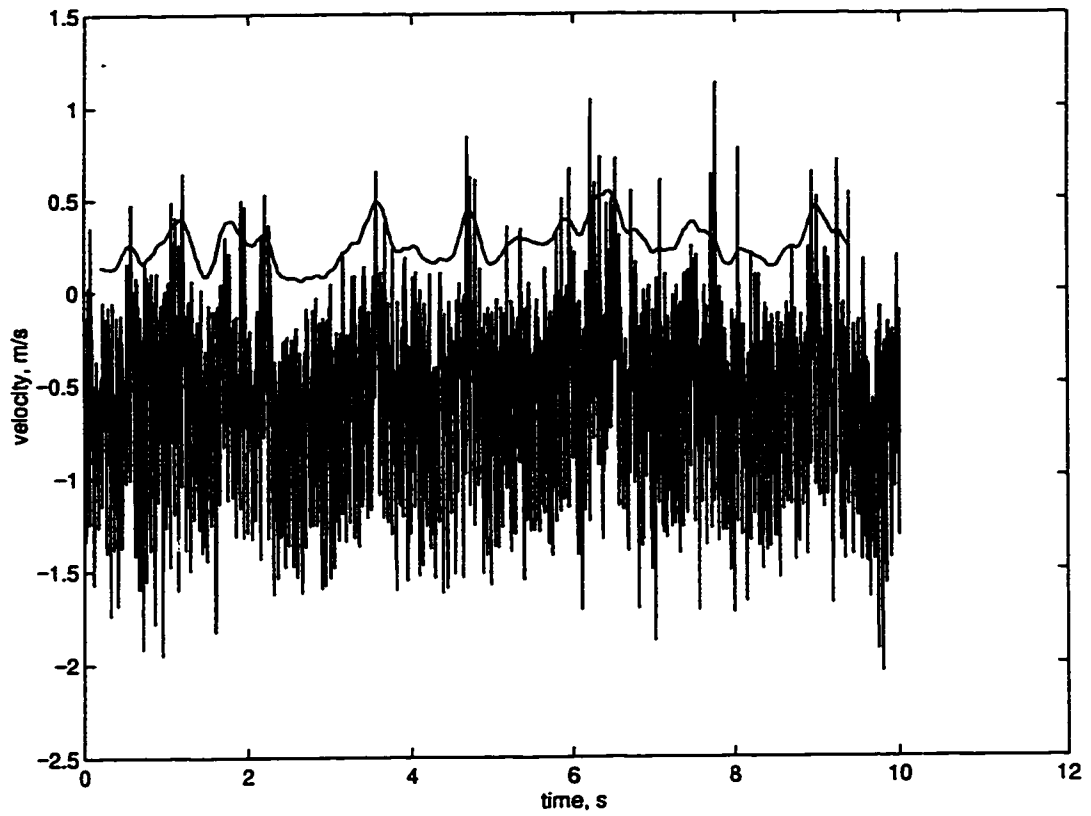
Figure 25: RT time series: $D=T/2$, $C=T/2$, $N_f=4$, smoothed over 8 (4+4) blade passages.



25b) bottom corner

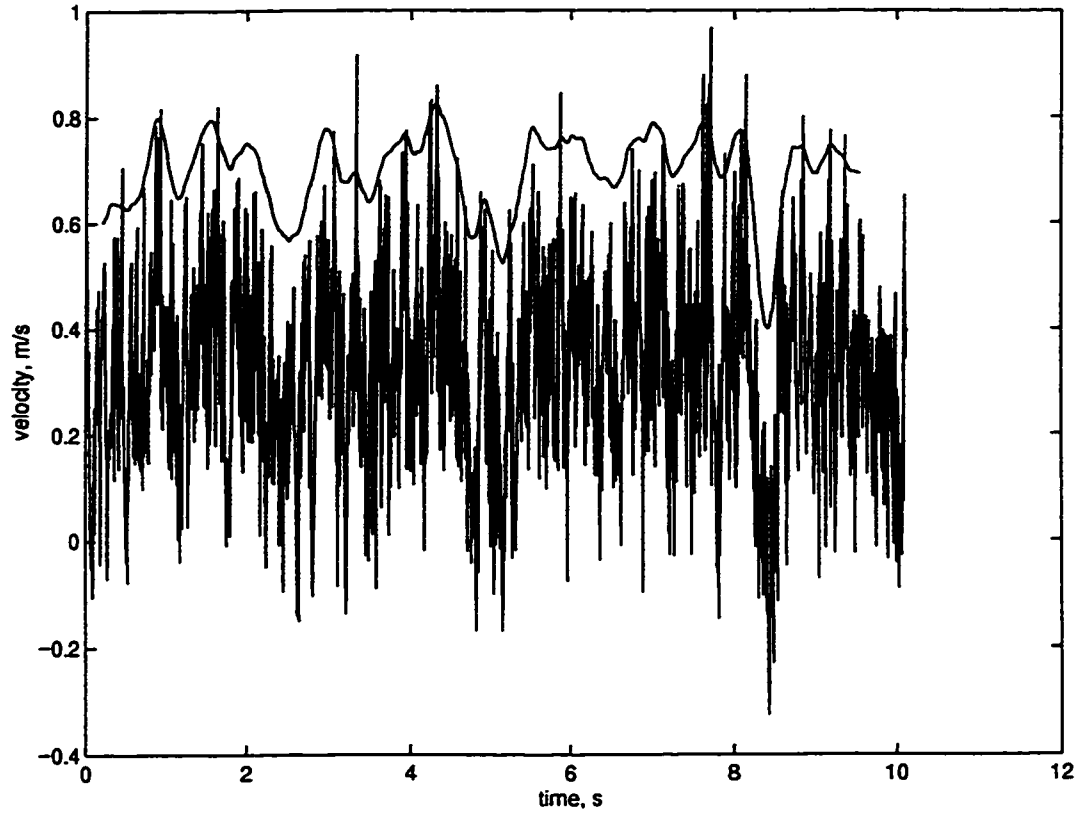


25c) top corner

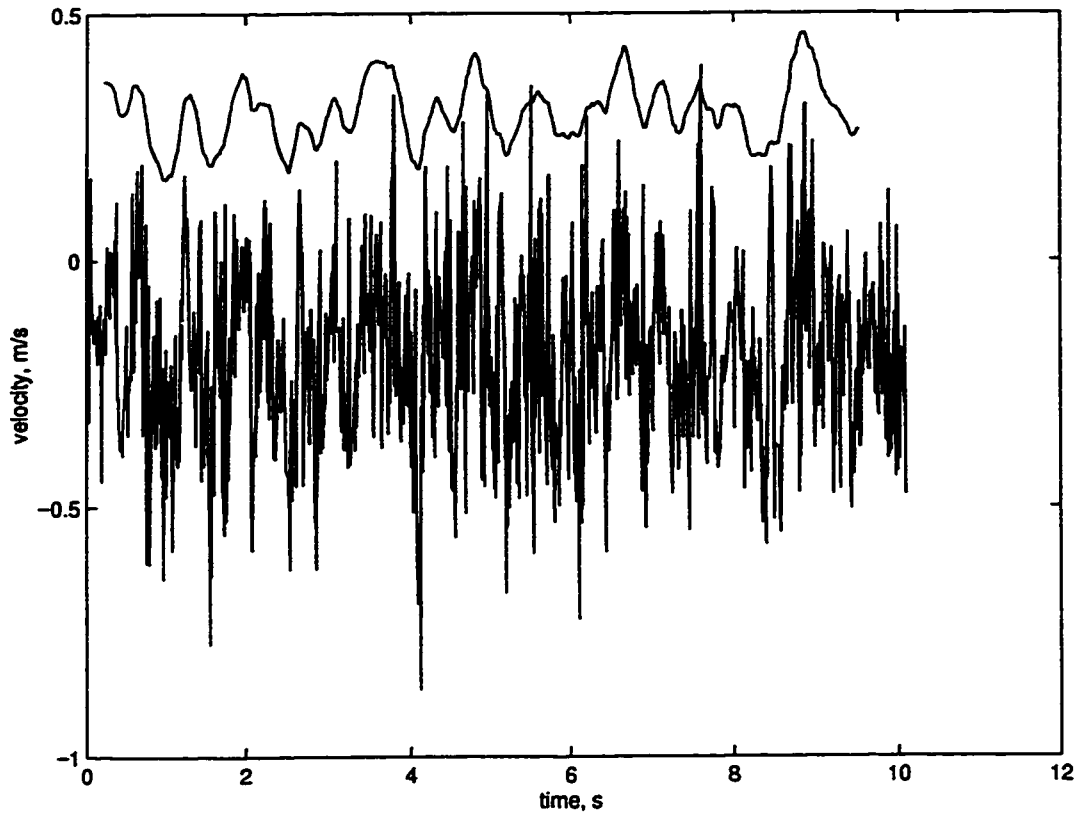


26a) impeller stream

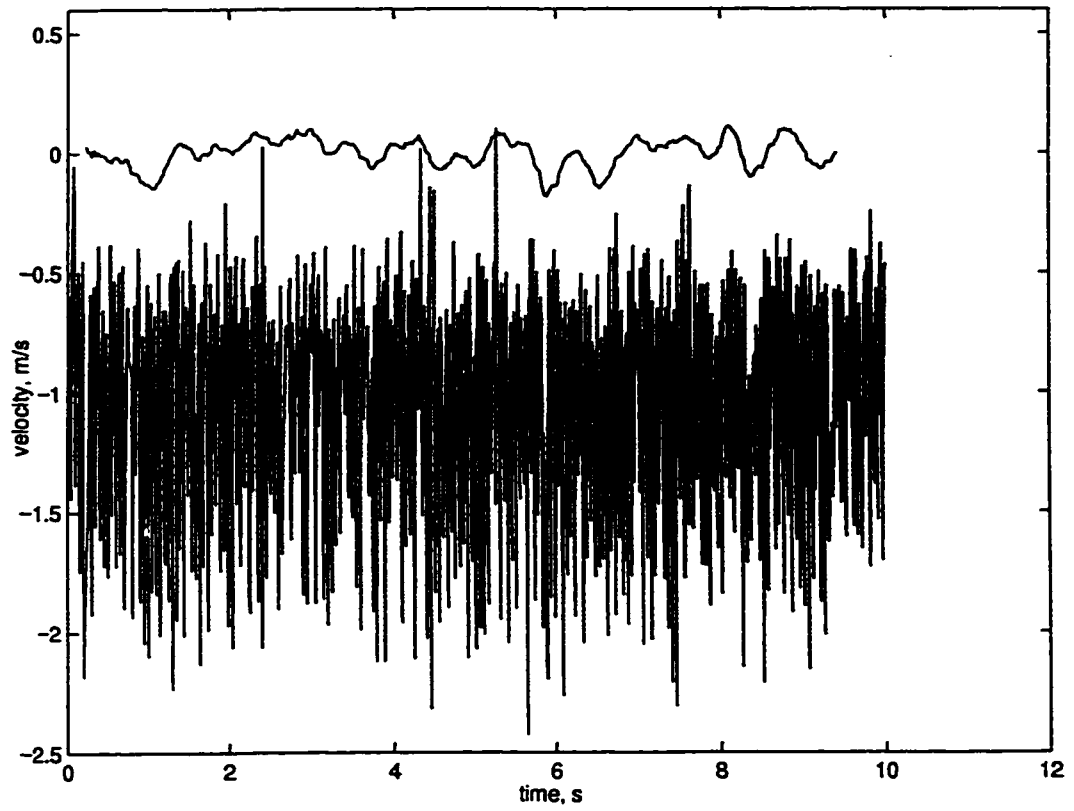
Figure 26: RT time series: $D=T/2$, $C=T/2$, $N_f=2$, smoothed over 8 (4+4) blade passages.



26b) bottom corner

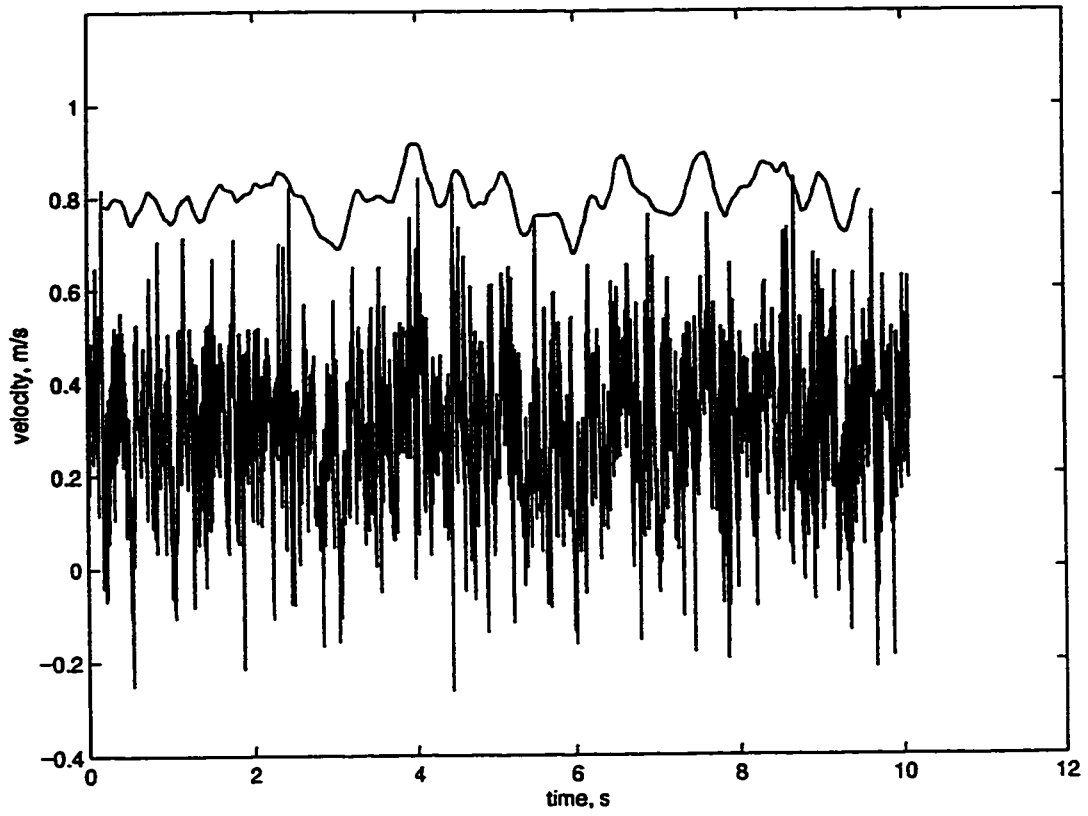


26c) top corner

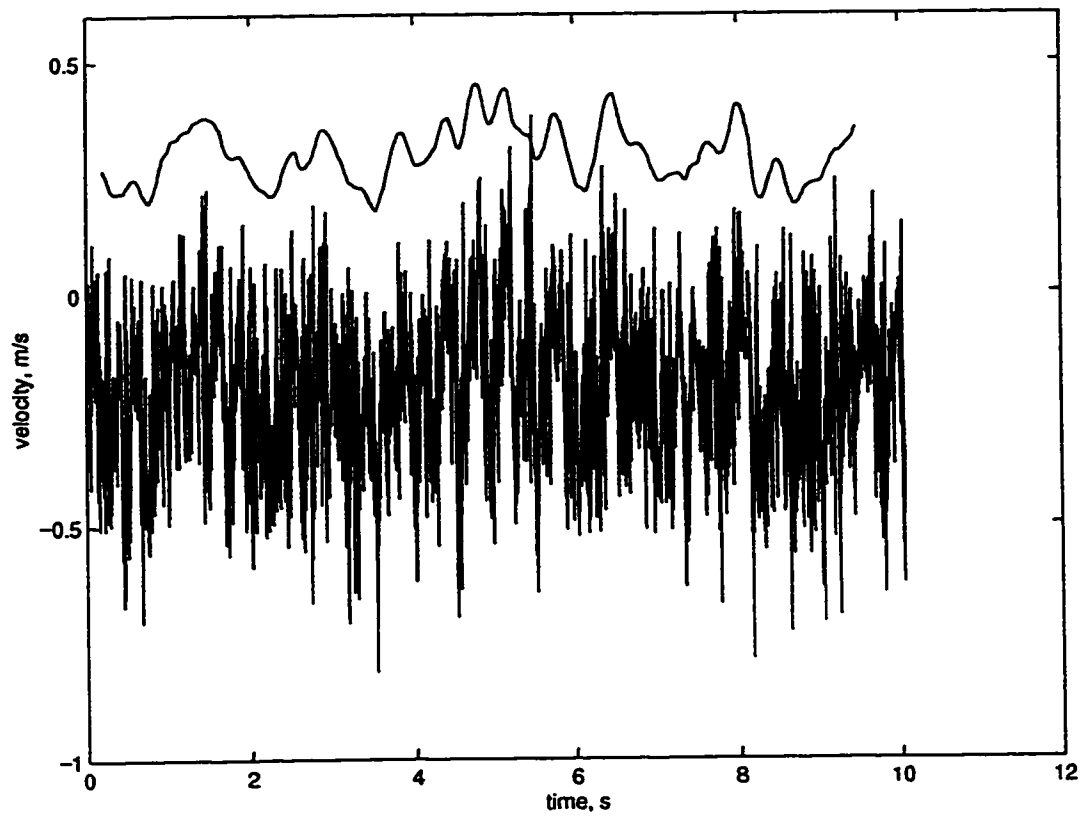


27a) impeller stream

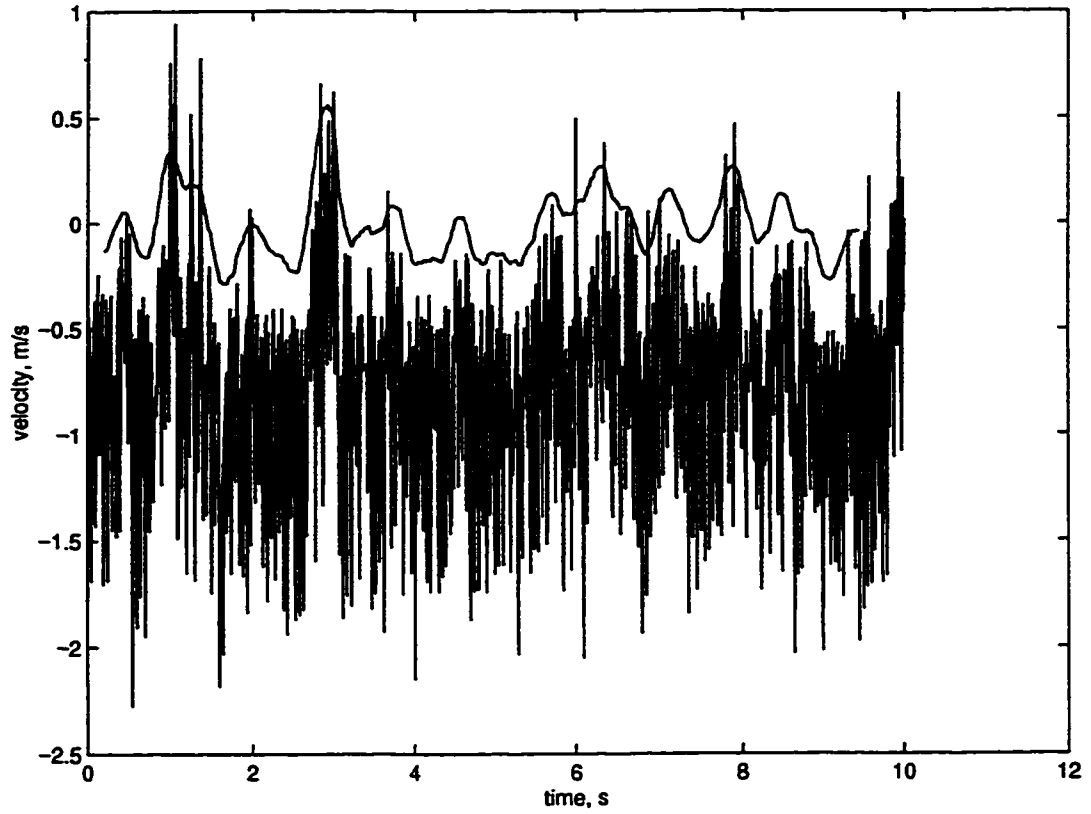
Figure 27: RT time series: $D=T/2$, $C=T/3$, $N_f=4$, smoothed over 8 (4+4) blade passages.



27b) bottom corner

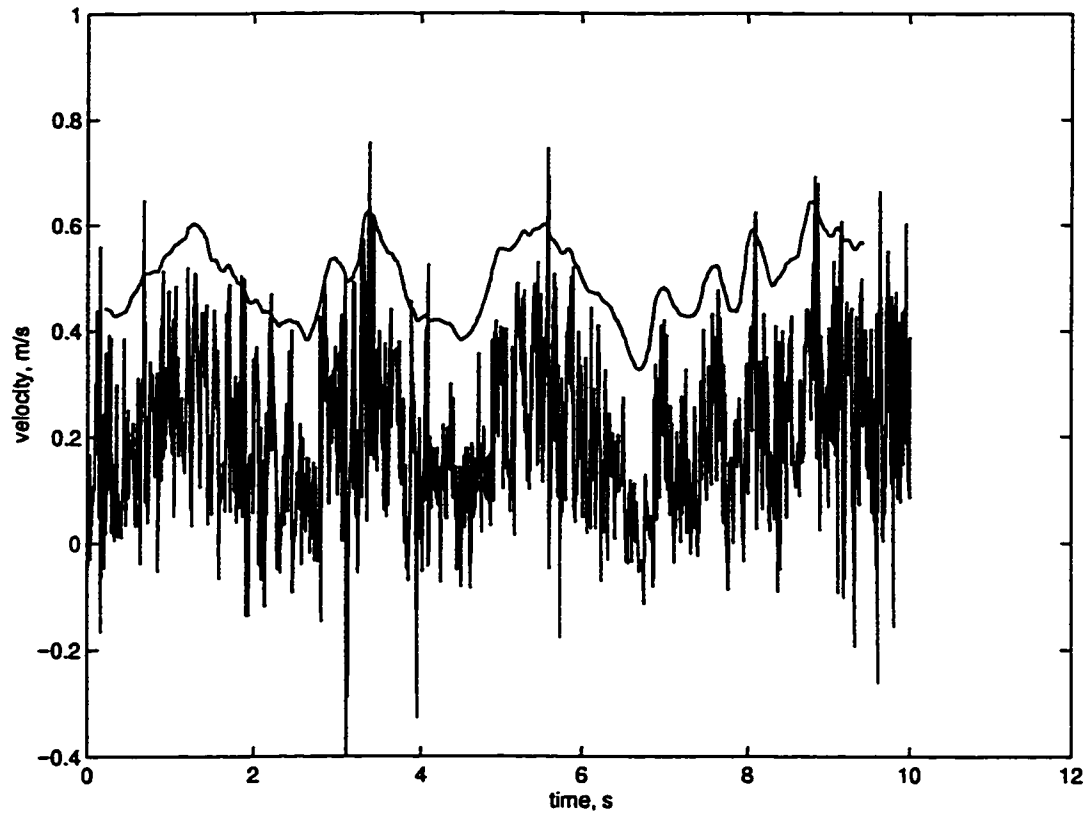


27c) top corner

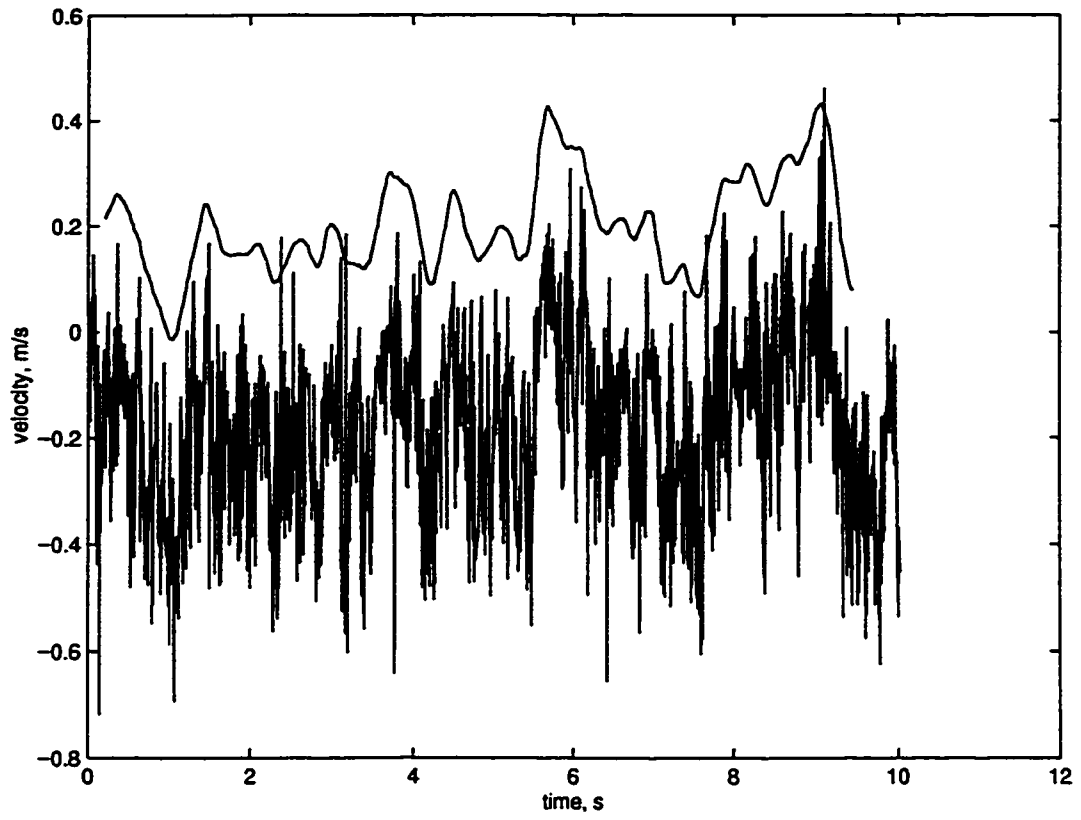


28a) impeller stream

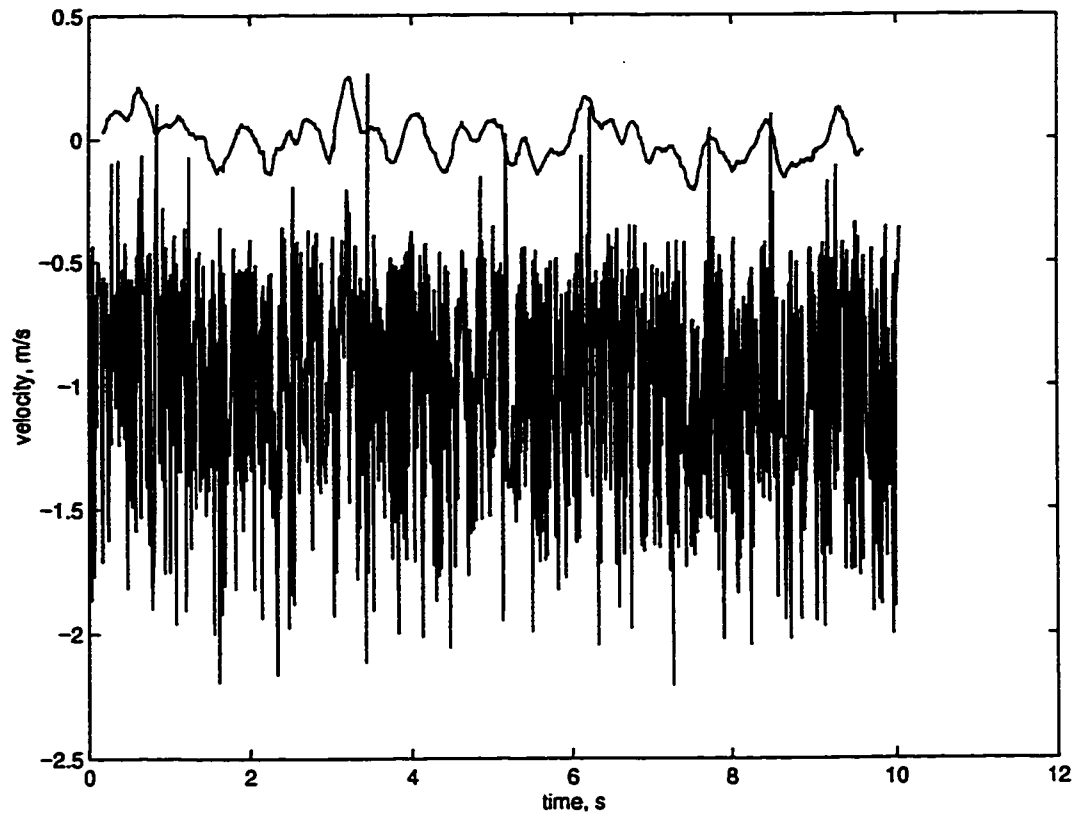
Figure 28: RT time series: $D=T/2$, $C=T/3$, $N_f=2$, smoothed over 8 (4+4) blade passages.



28b) bottom corner

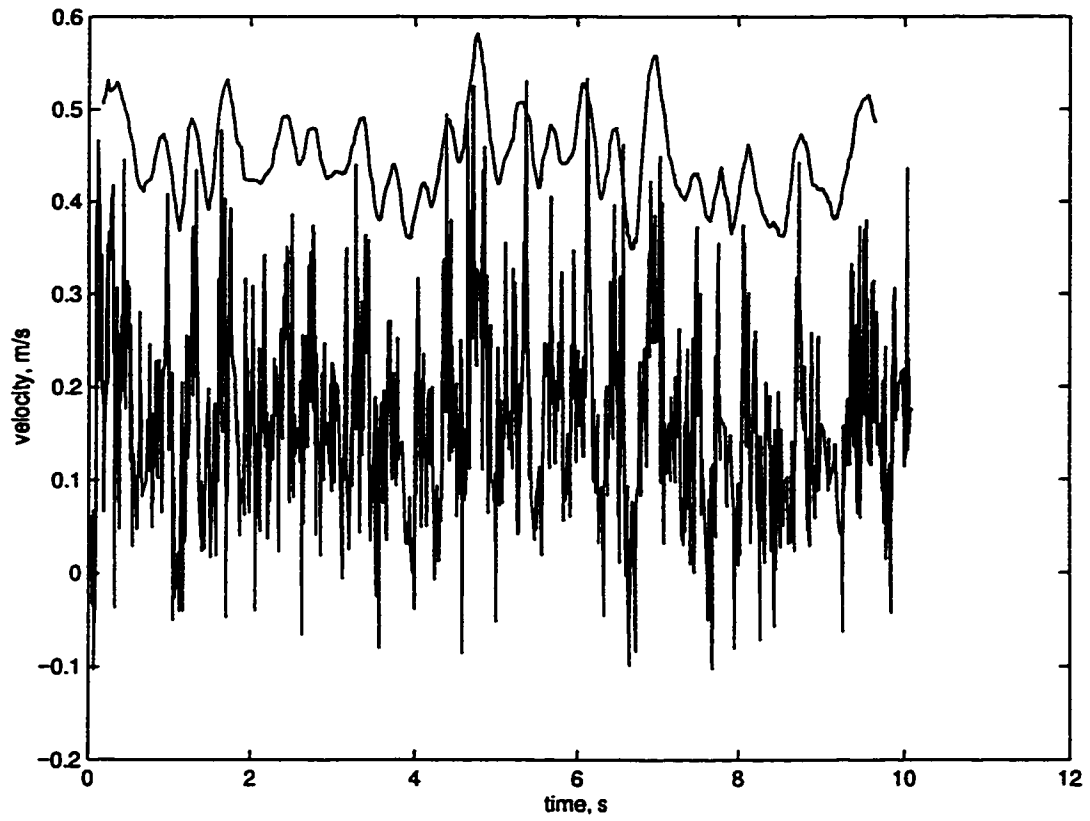


28c) top corner

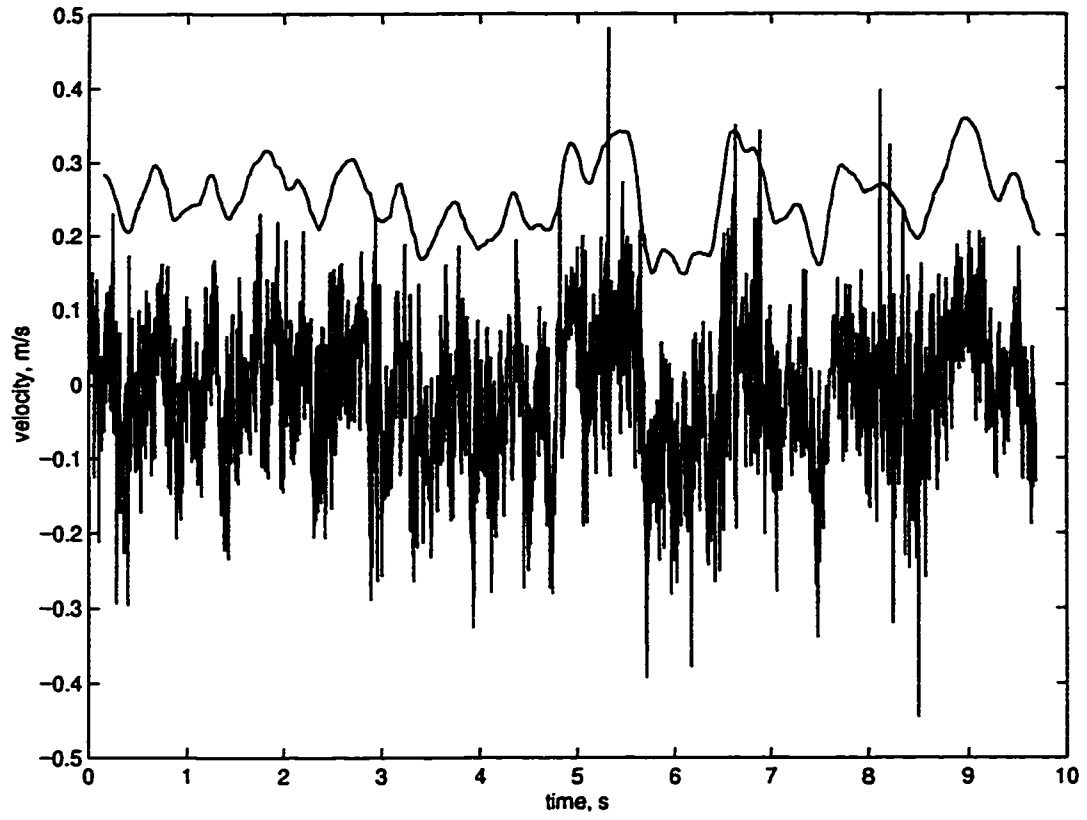


29a) impeller stream

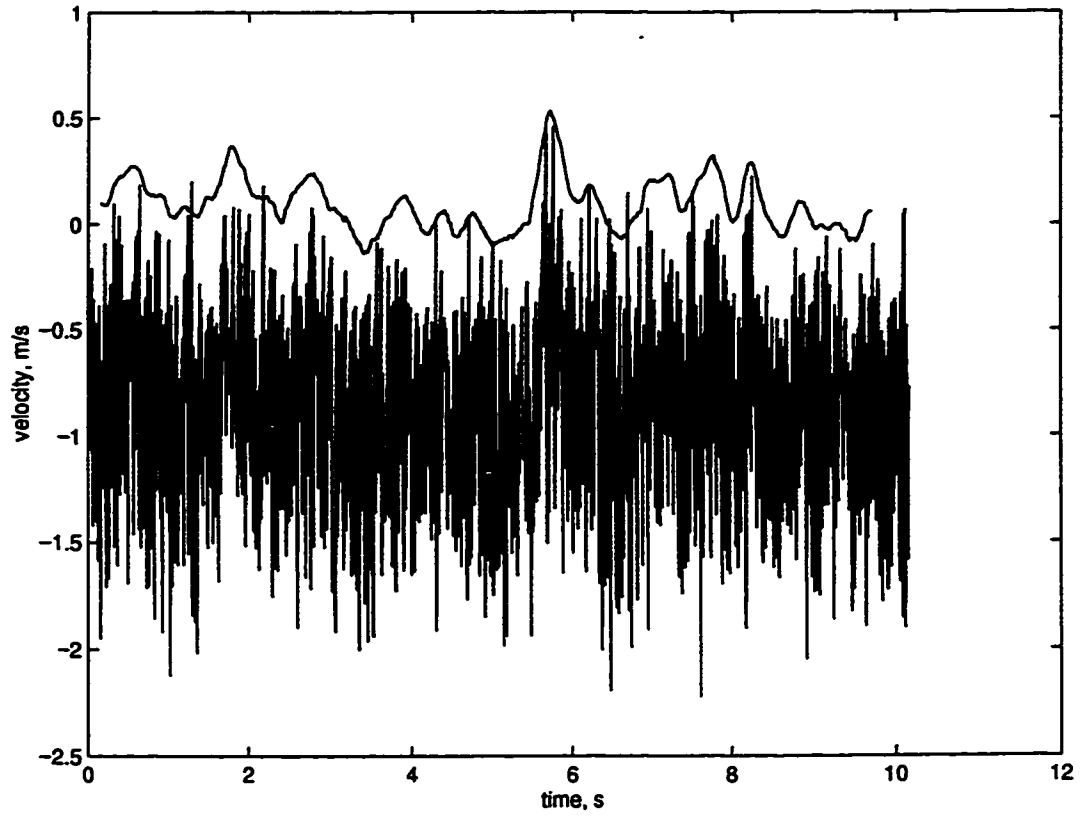
Figure 29: RT time series: $D=T/3$, $C=T/2$, $N_f=4$, smoothed over 9 (6+3) blade passages.



29b) bottom corner

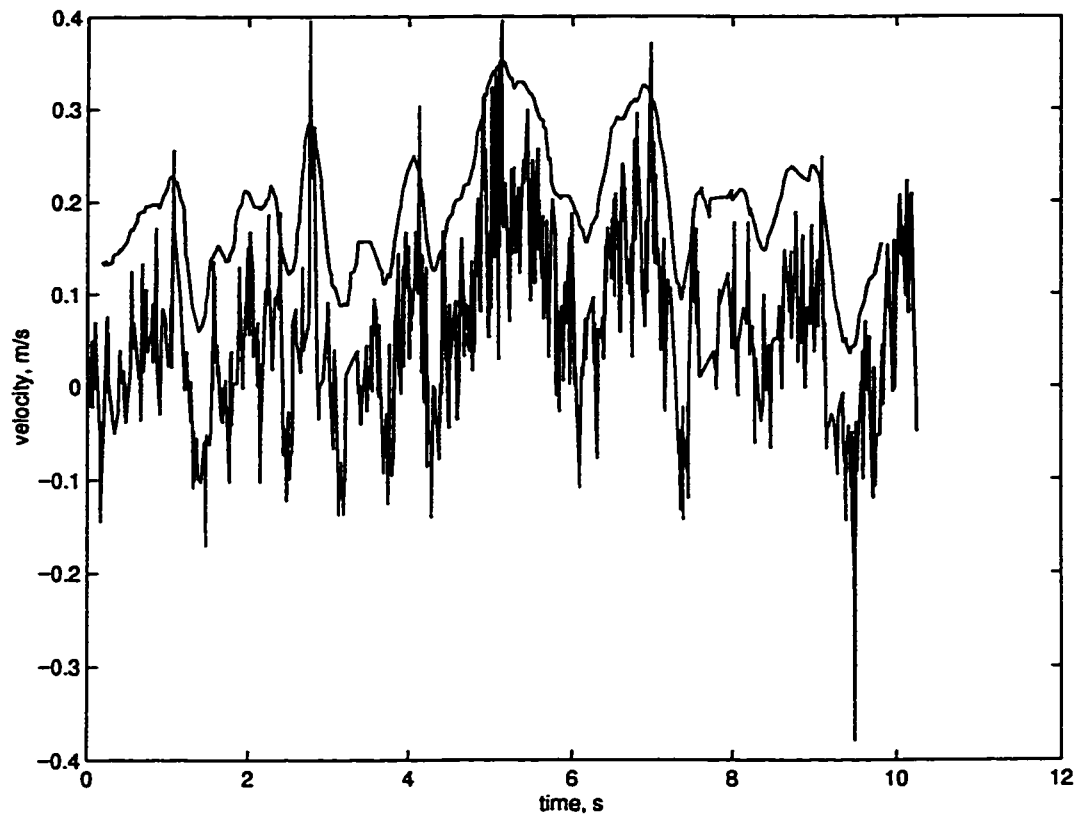


29c) top corner

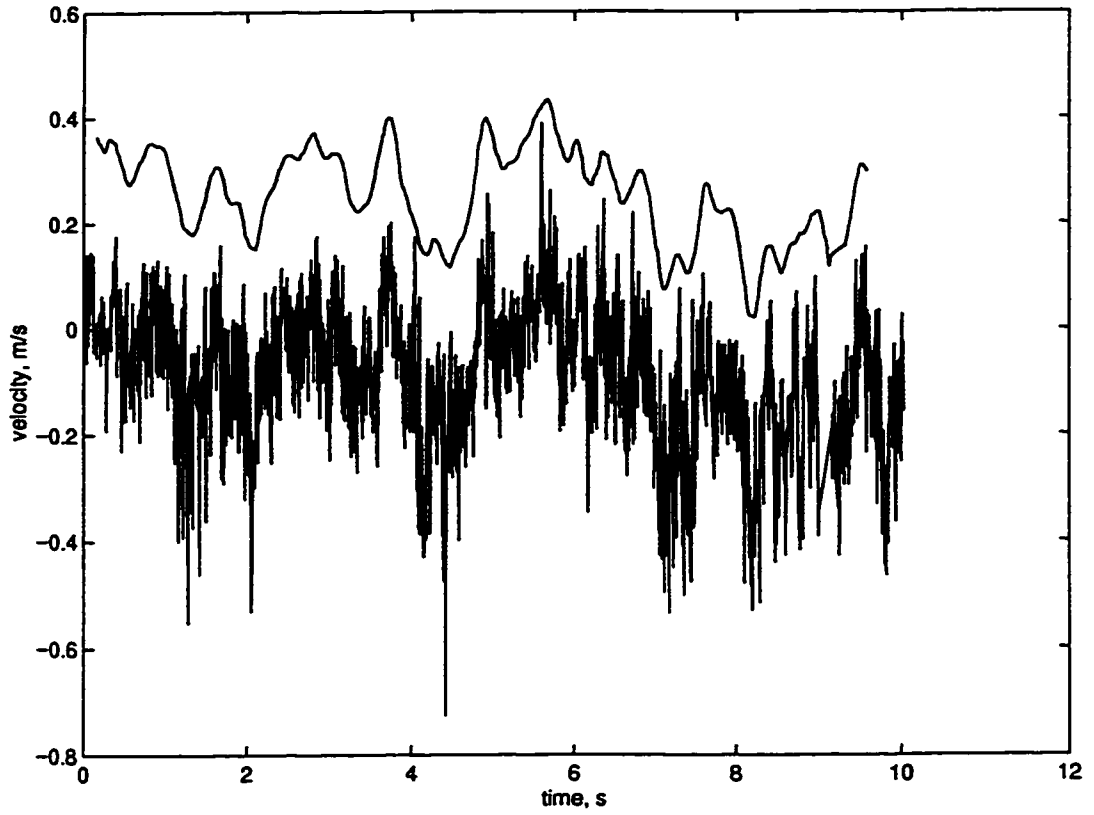


30a) impeller stream

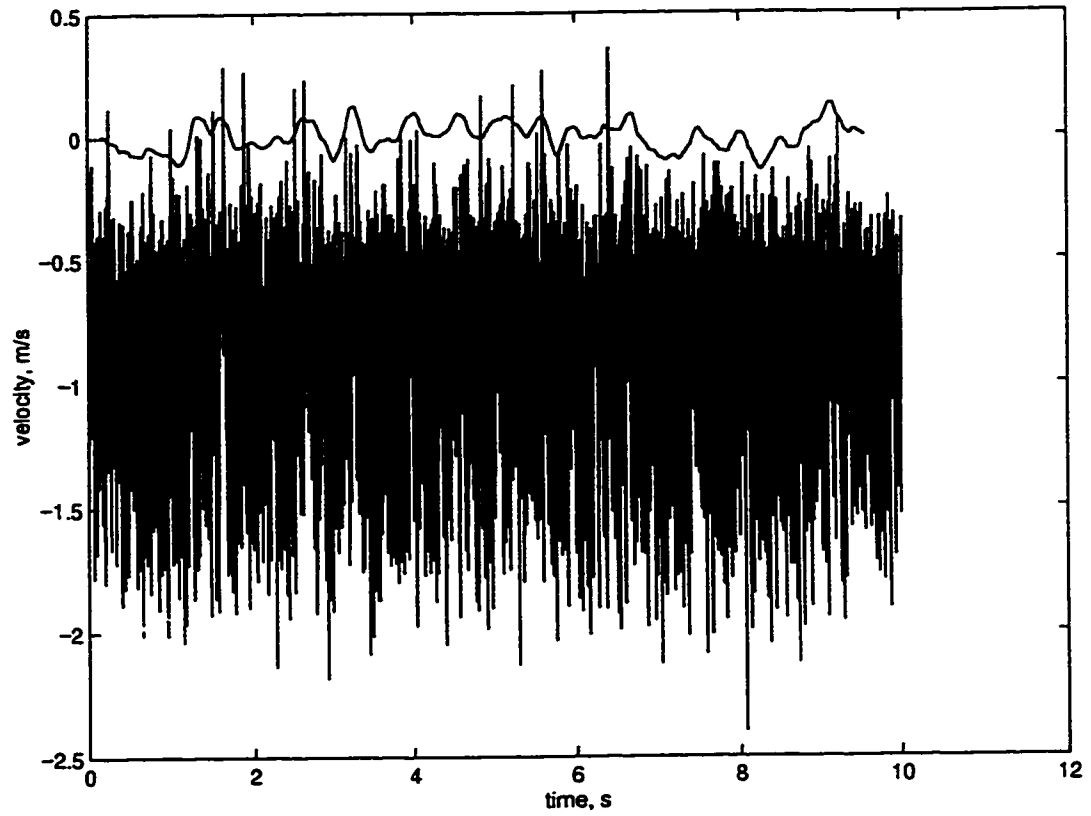
Figure 30: RT time series: $D=T/3$, $C=T/2$, $N_f=2$, smoothed over 9 (6+3) blade passages.



30b) bottom corner

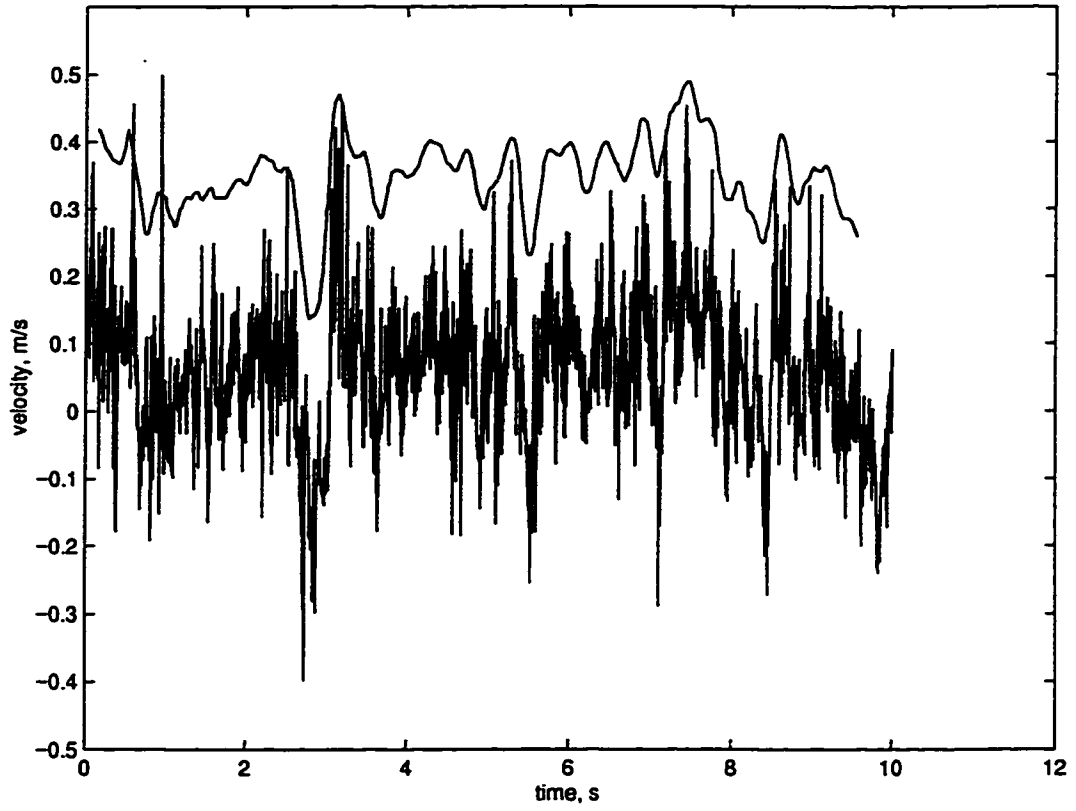


30c) top corner

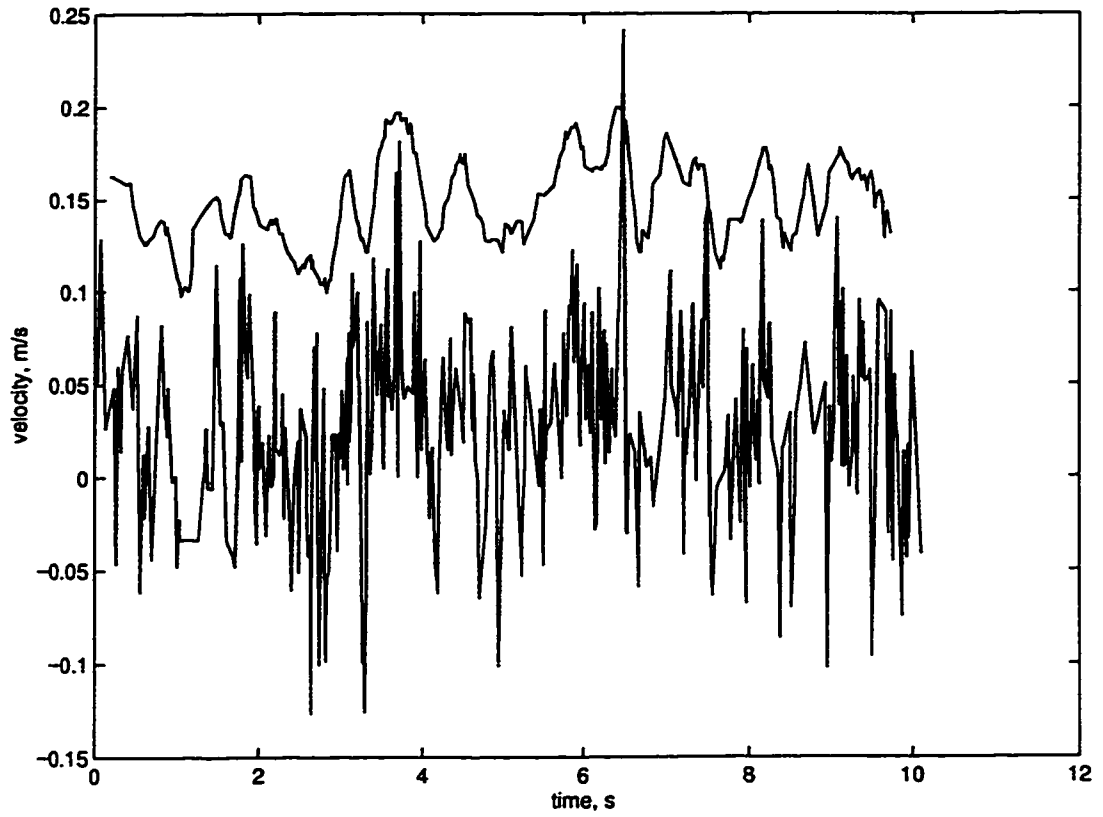


31a) impeller stream

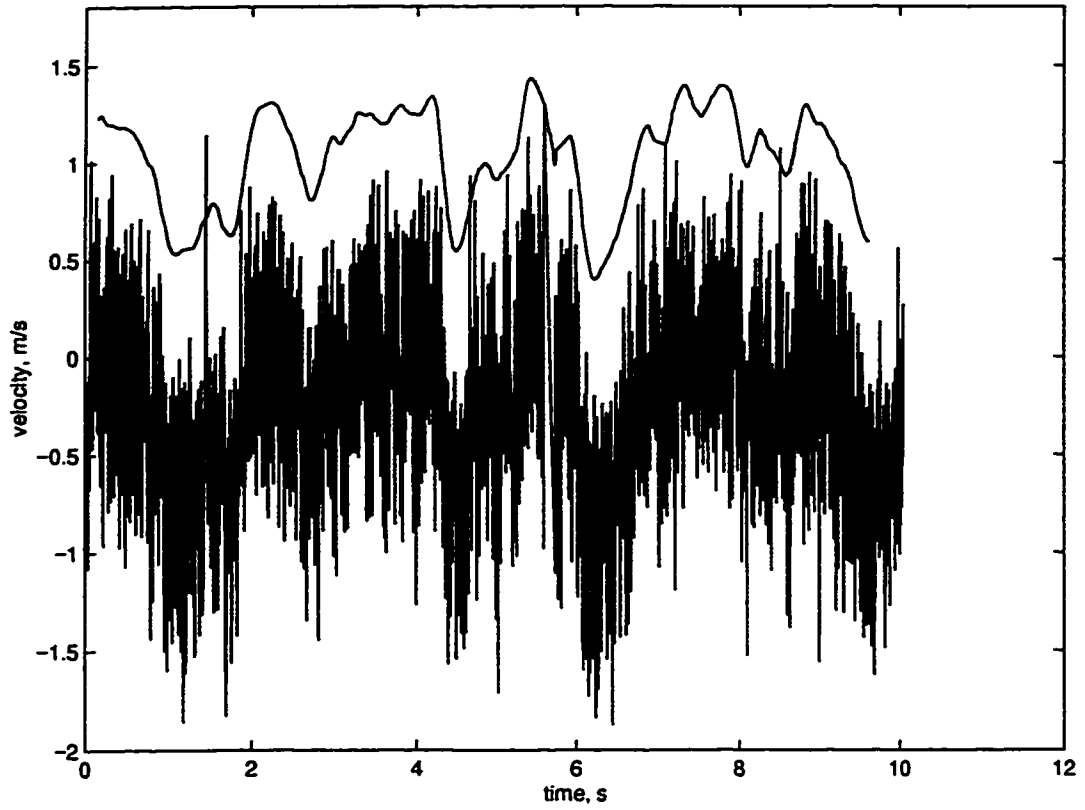
Figure 31: RT time series: $D=T/3$, $C=T/3$, $N_f=4$, smoothed over 9 (6+3) blade passages.



31b) bottom corner

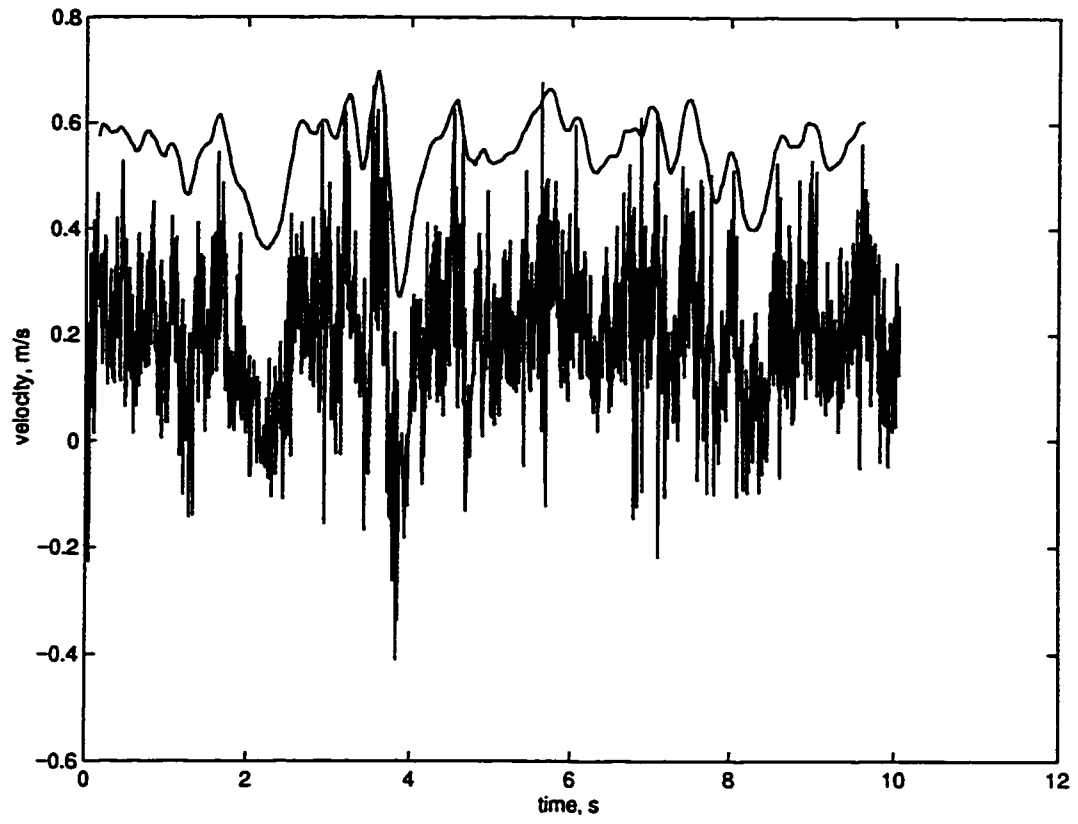


31c) top corner

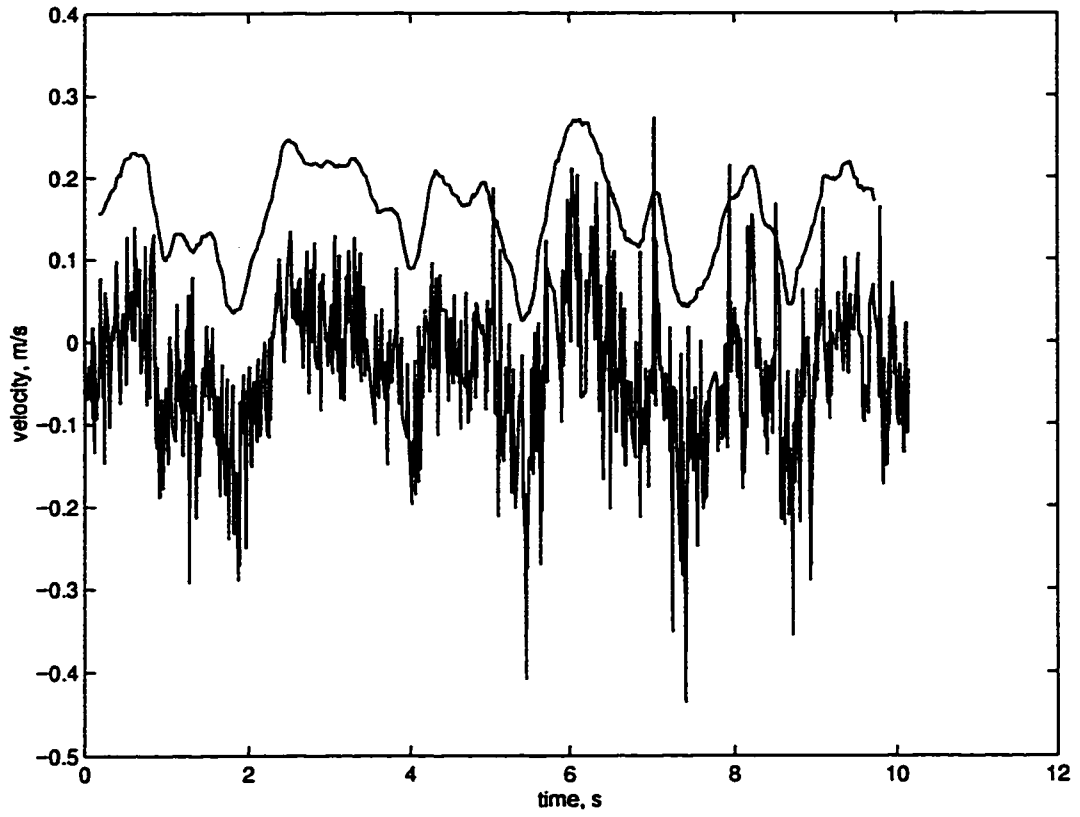


32a) impeller stream

Figure 32: RT time series: $D=T/3$, $C=T/3$, $N_f=2$, smoothed over 9 (6+3) blade passages.

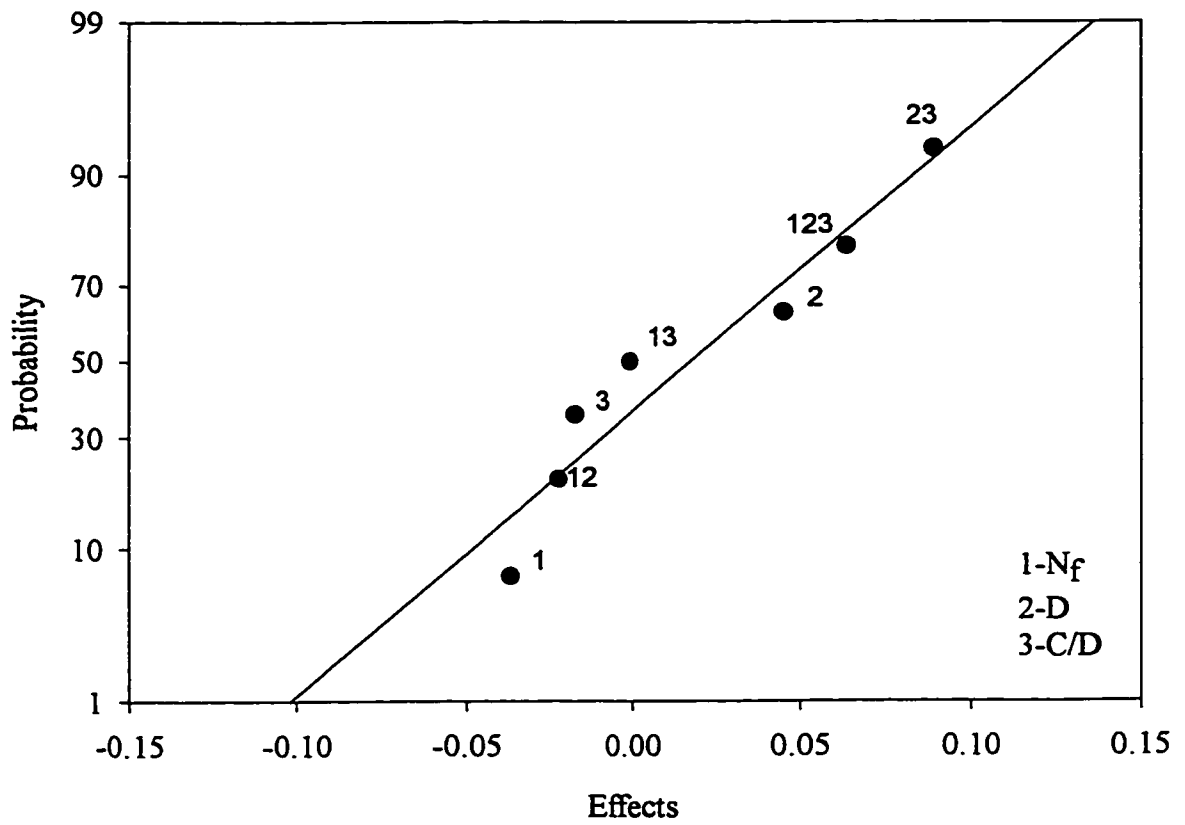


32b) bottom corner



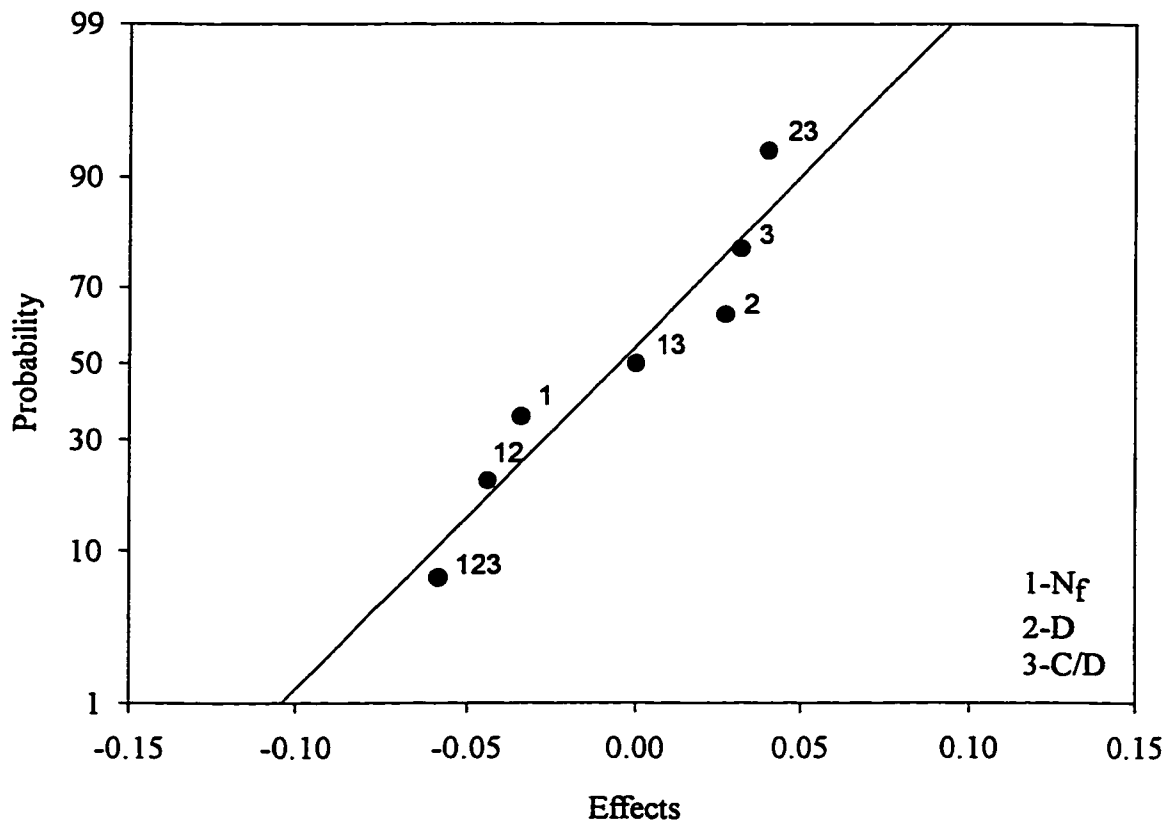
32c) top corner

Appendix C

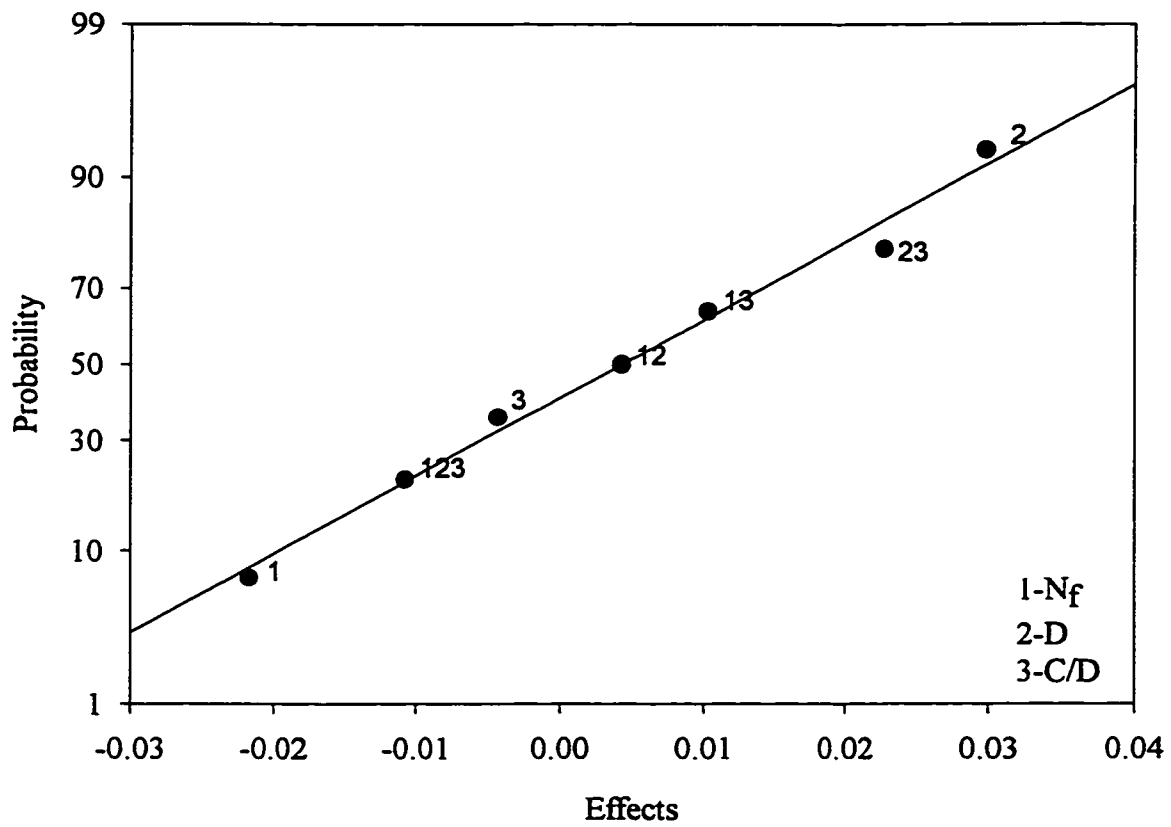


1a) bottom corner

Figure 1: PBT, effects of geometric variables on v_{LF}/v_{tot} .

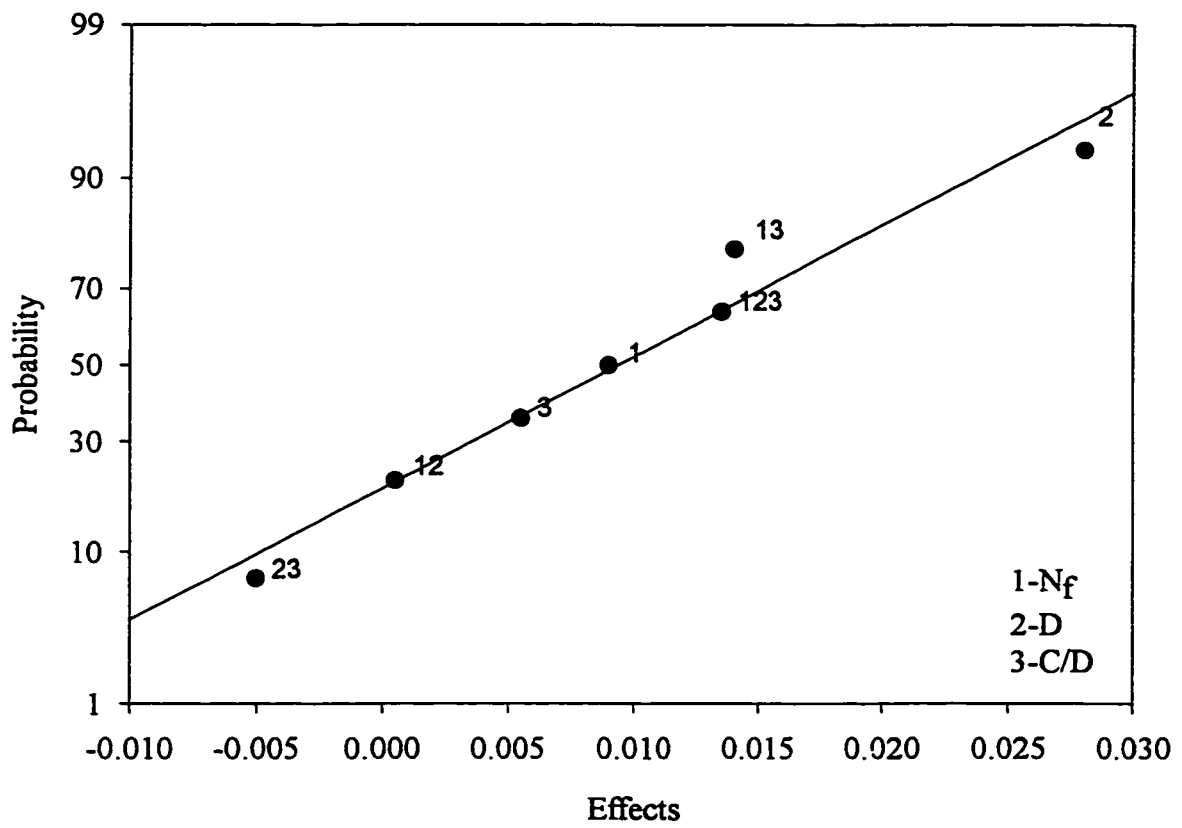


1b) top corner

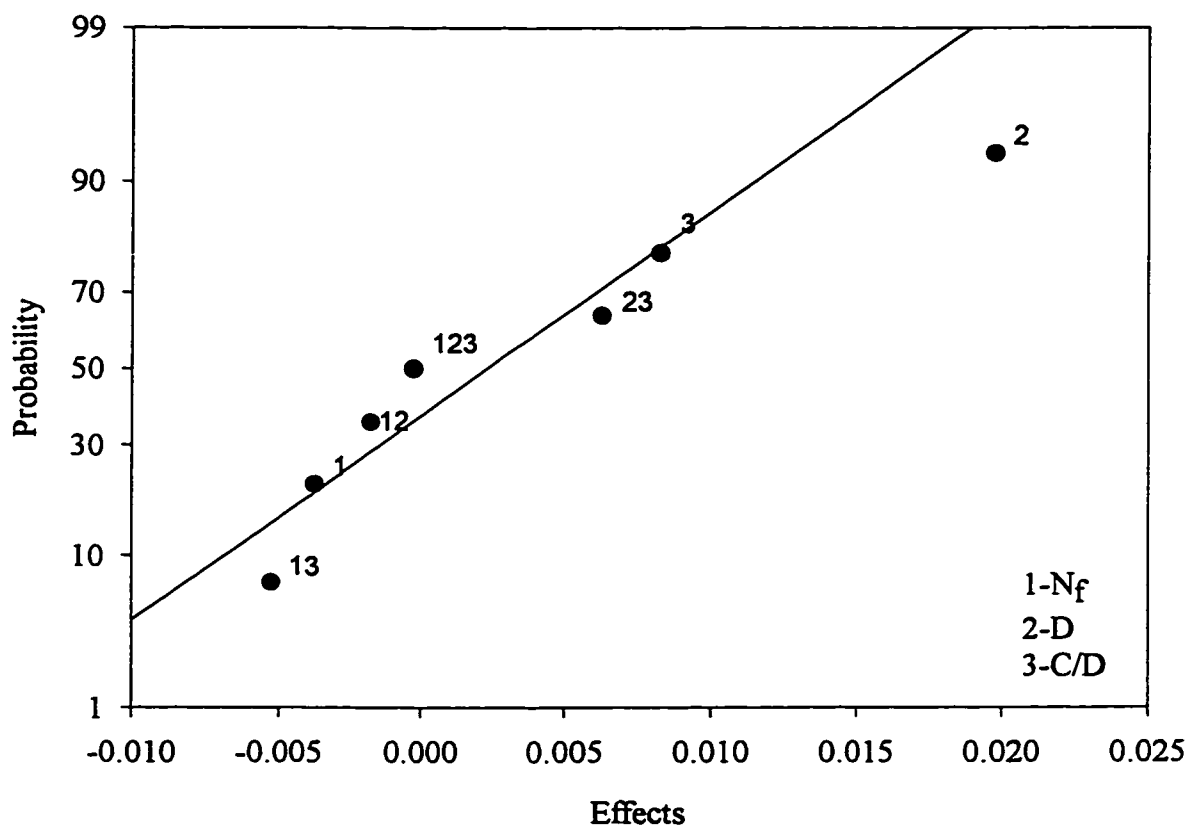


2a) impeller stream

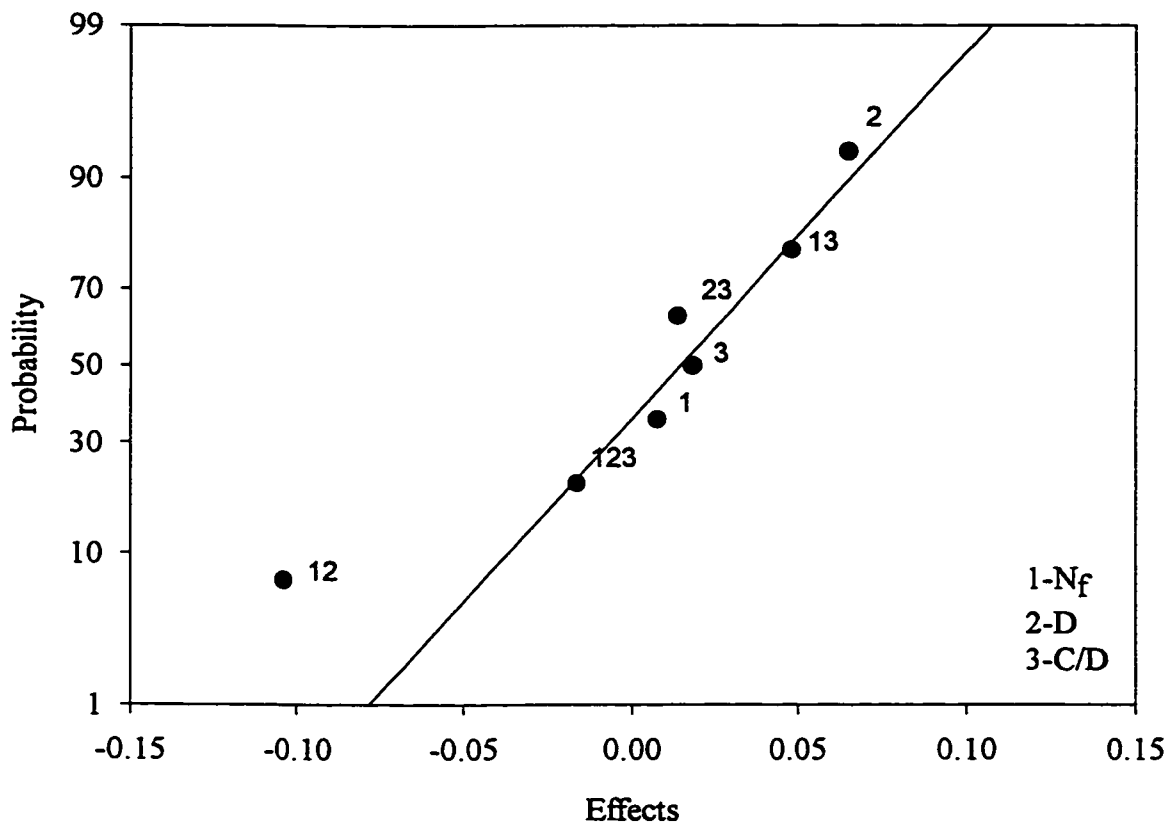
Figure 2: PBT, effects of geometric variables on v_{LF}/V_{tip} .



2b) bottom corner

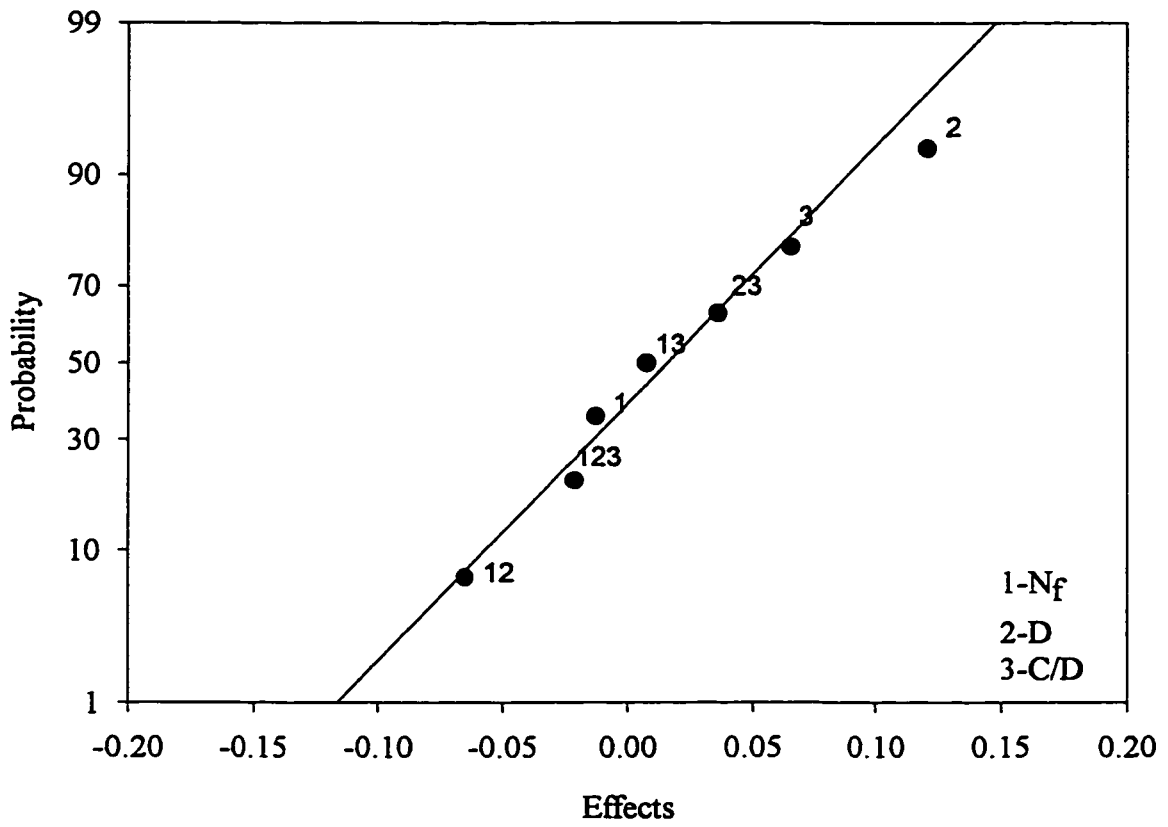


2c) top corner

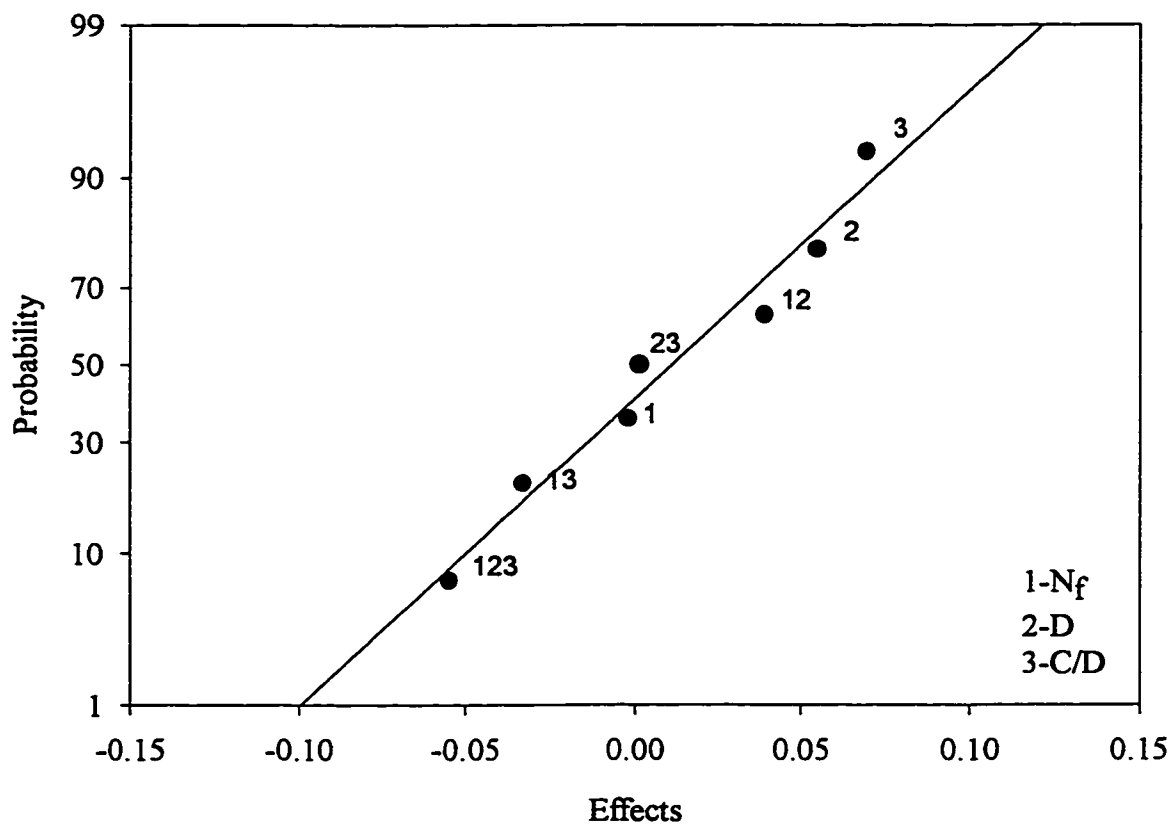


3a) impeller stream

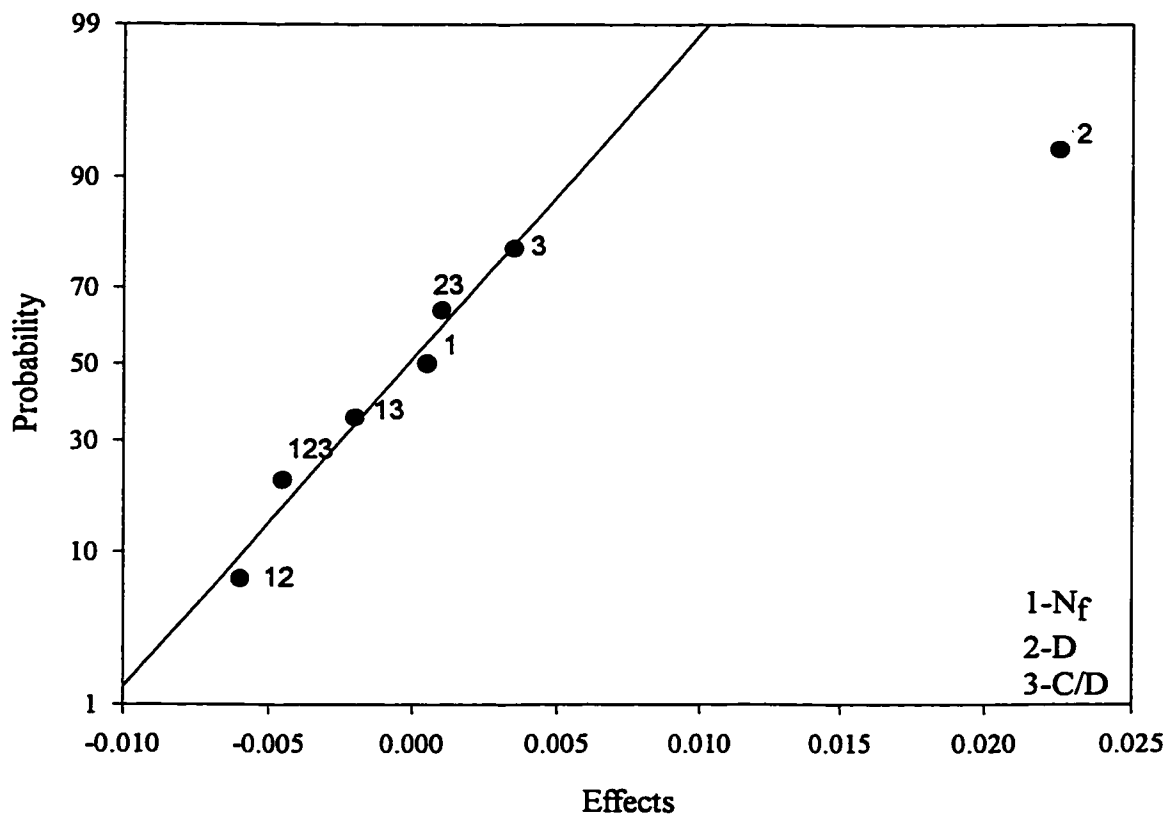
Figure 3: HE3, effects of geometric variables on v_{LF}/v_{tot} .



3b) bottom corner

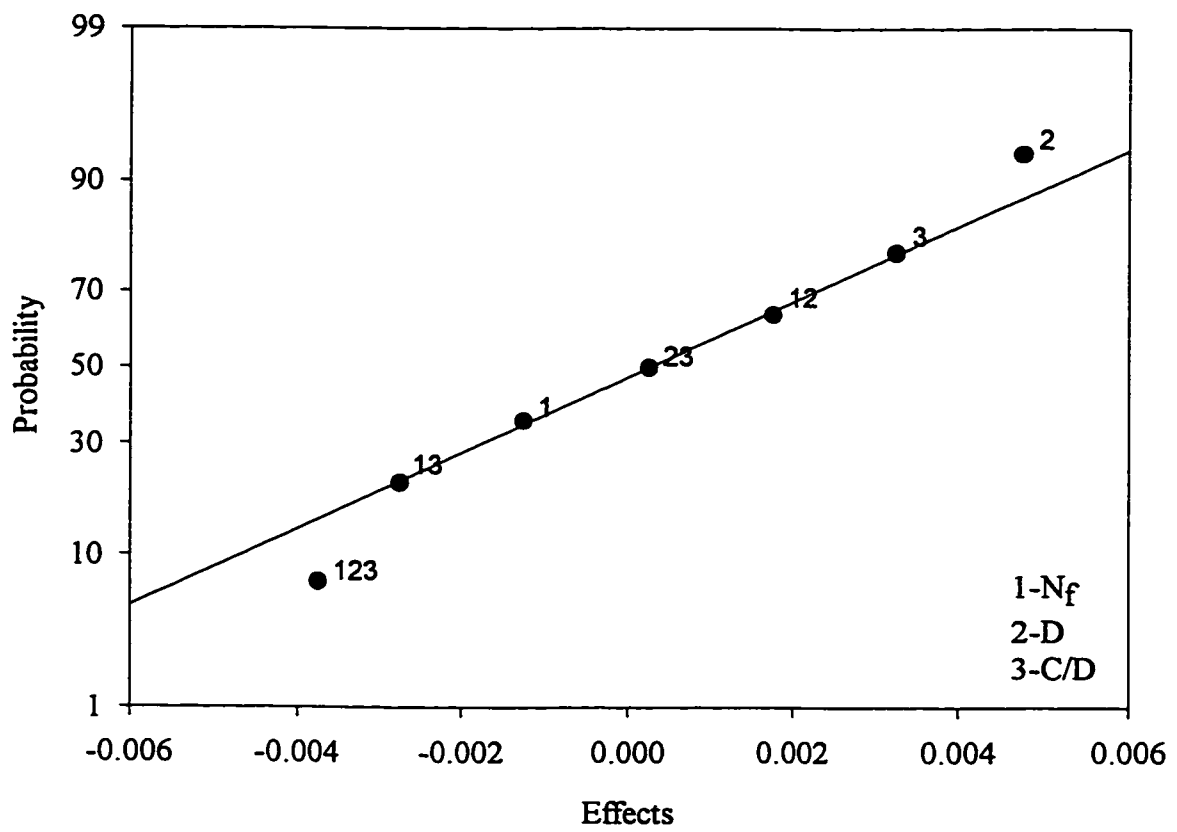


3c) top corner

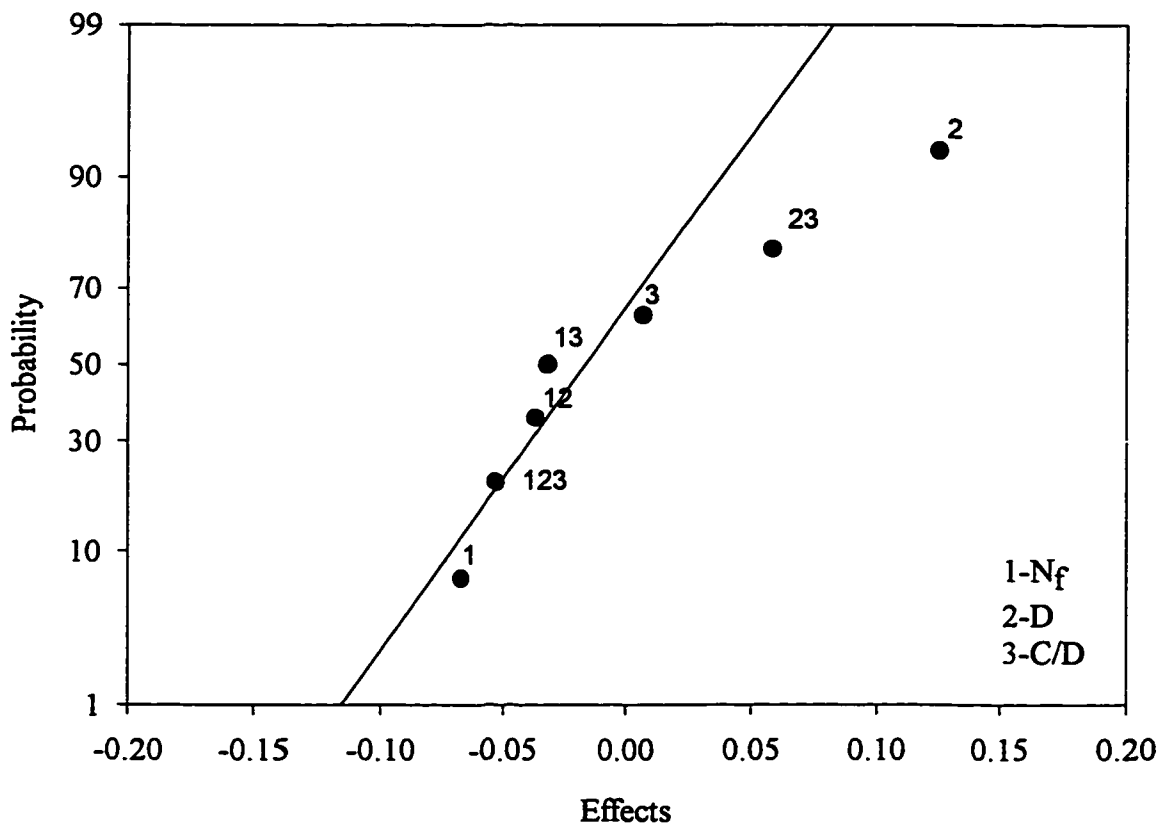


4a) bottom corner

Figure 4: HE3, effects of geometric variables on v_{LF}/V_{tip} .

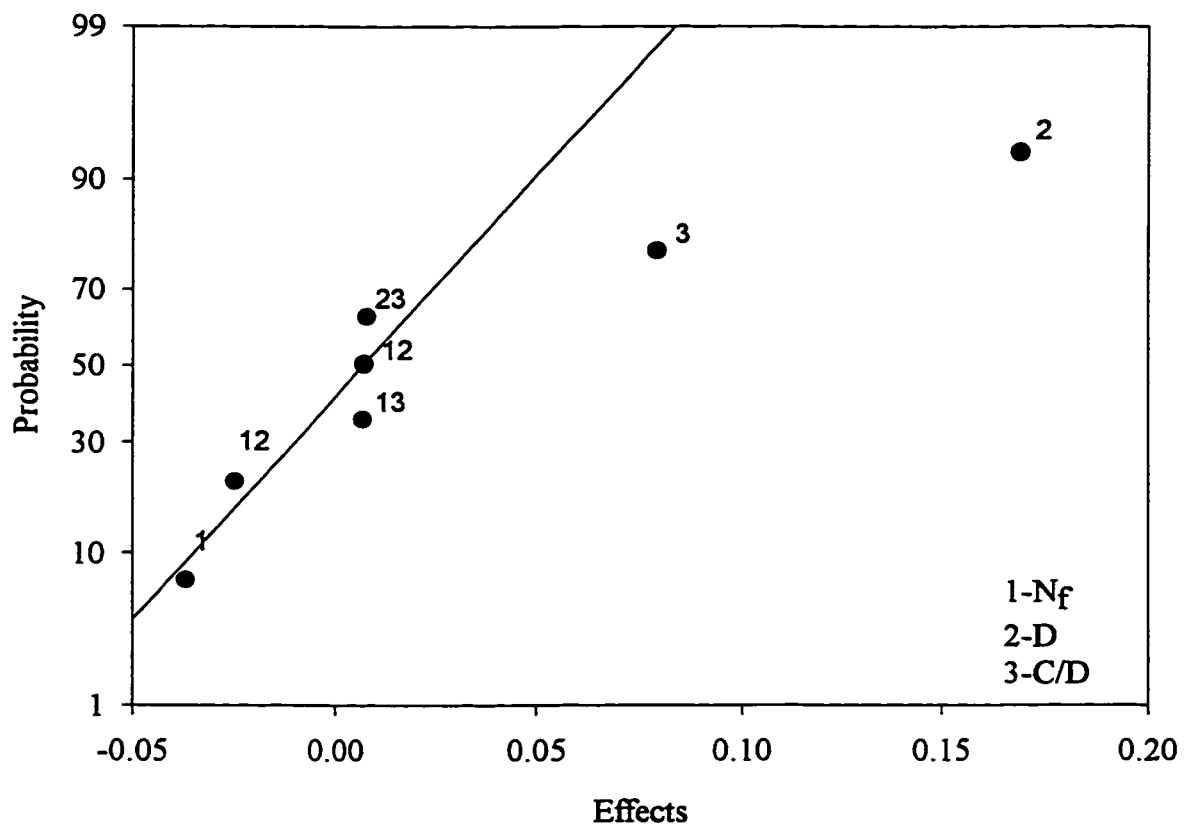


4b) top corner

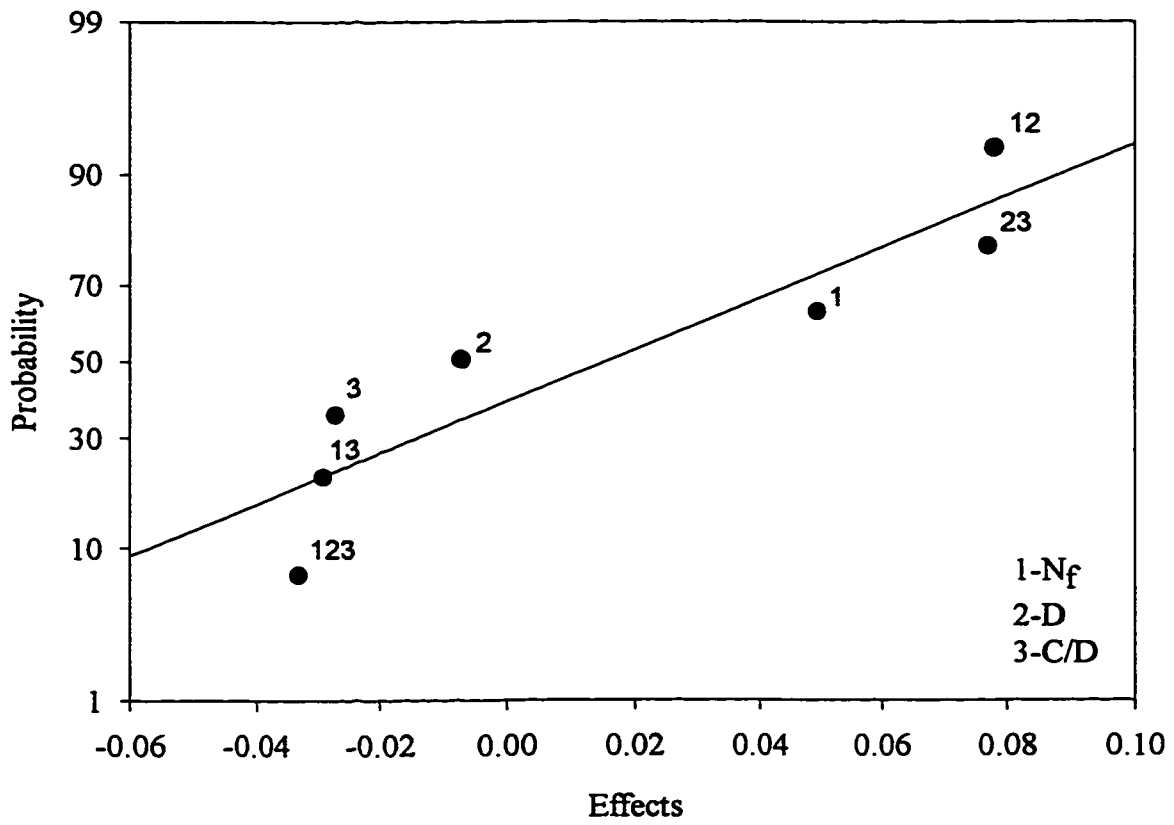


5a) impeller stream

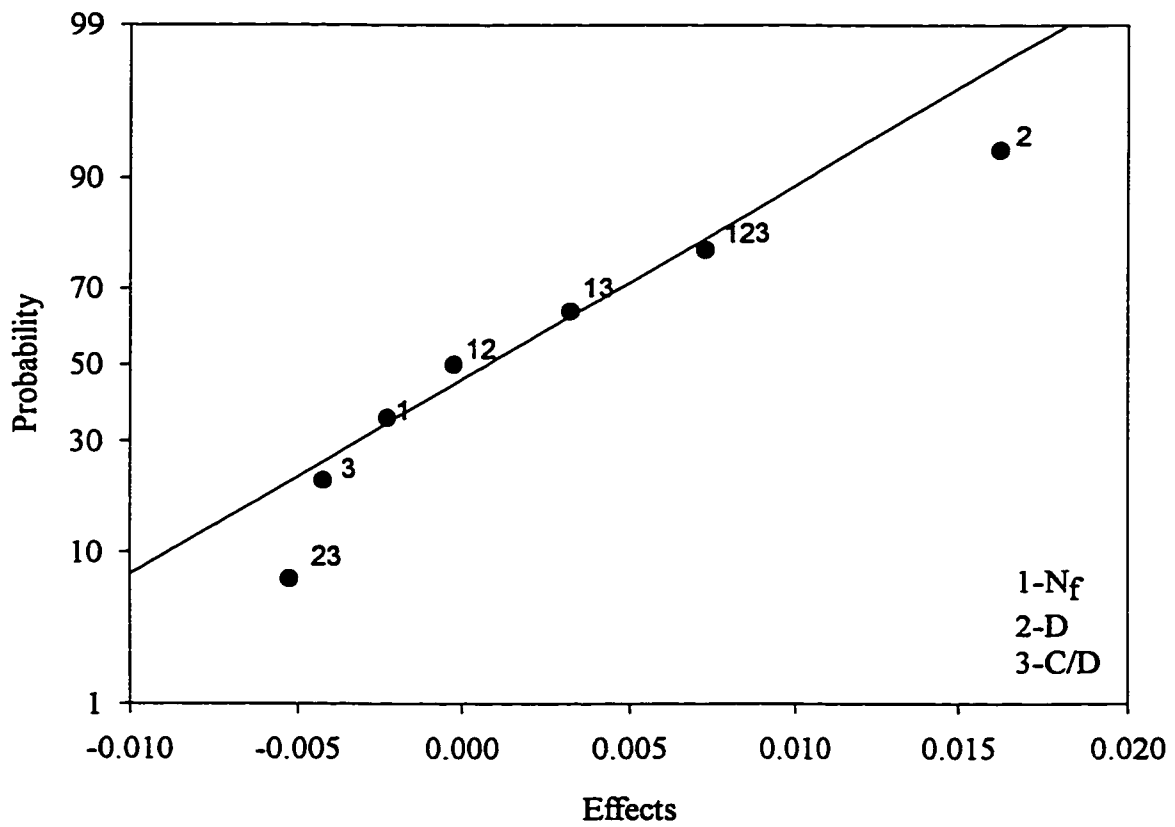
Figure 5: A310, effects of geometric variables on v_{LF}/v_{tot}



5b) bottom corner

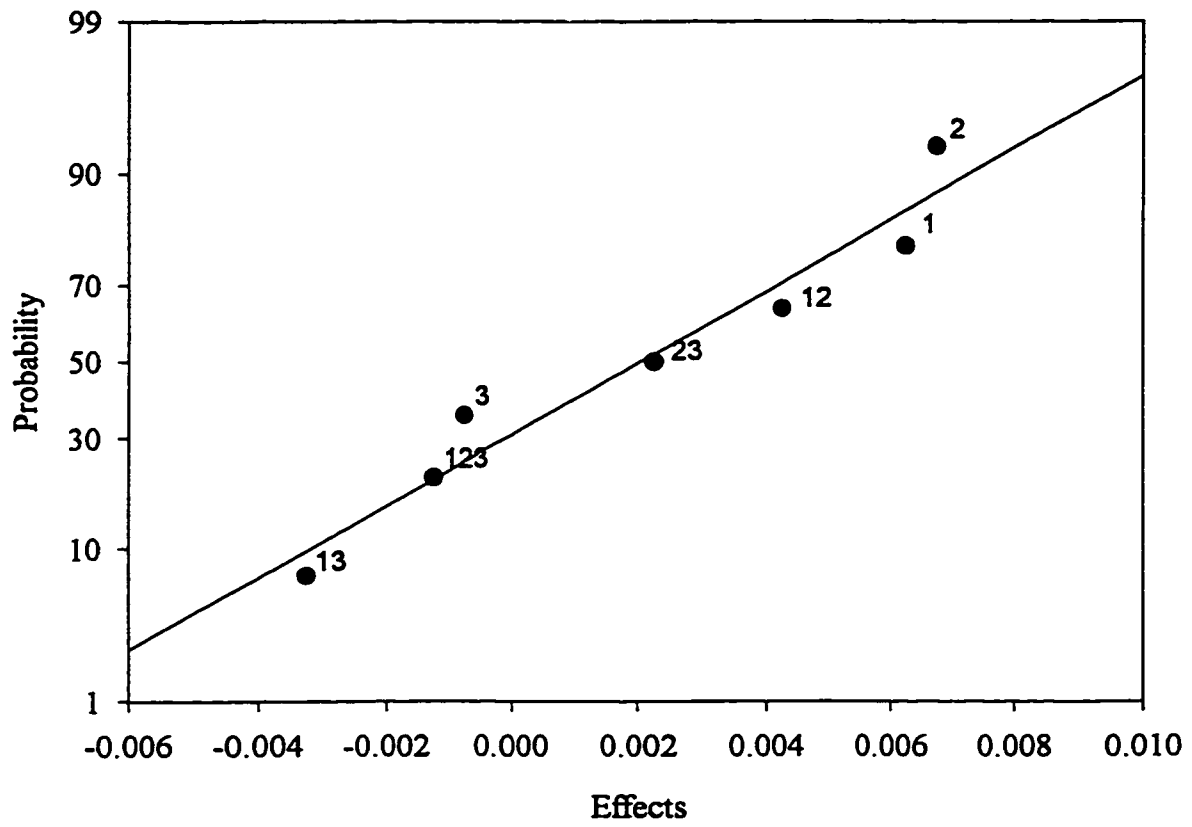


5c) top corner

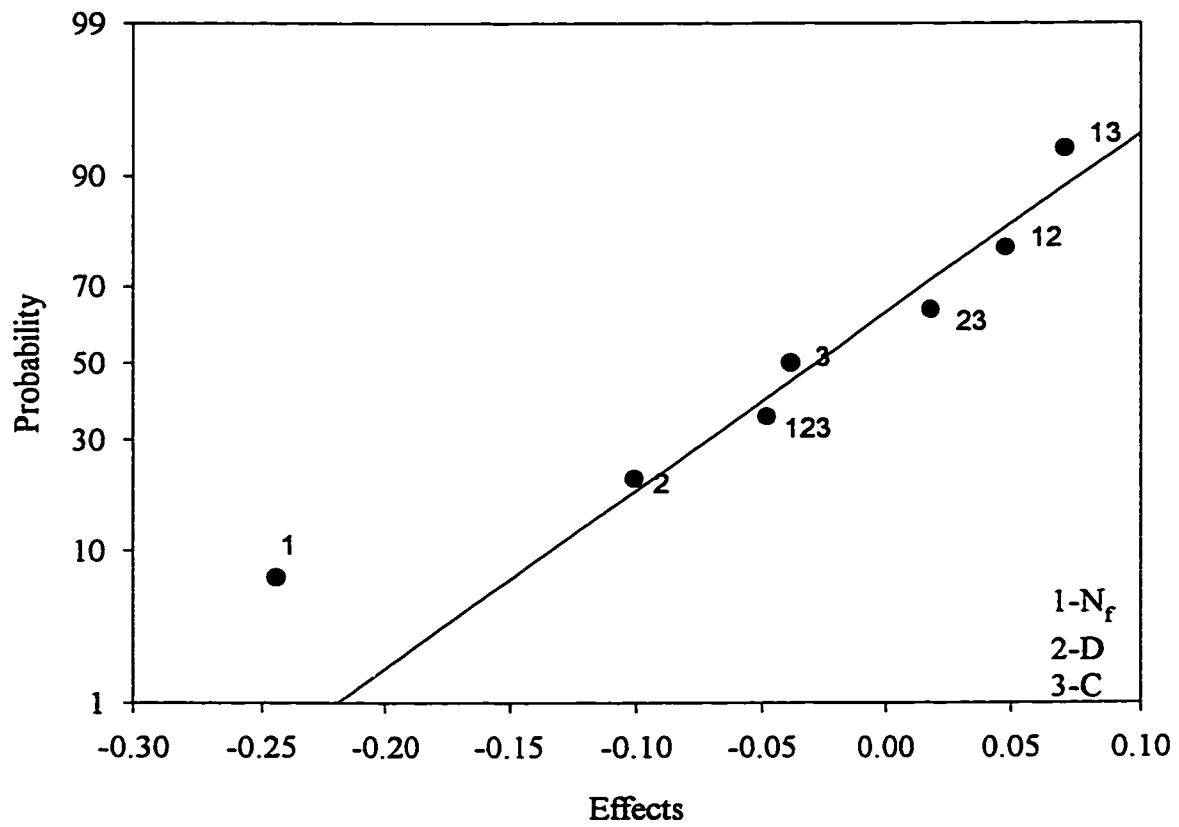


6a) bottom corner

Figure 6: A310, effects of geometric variables on v_{LF}/V_{tip} .

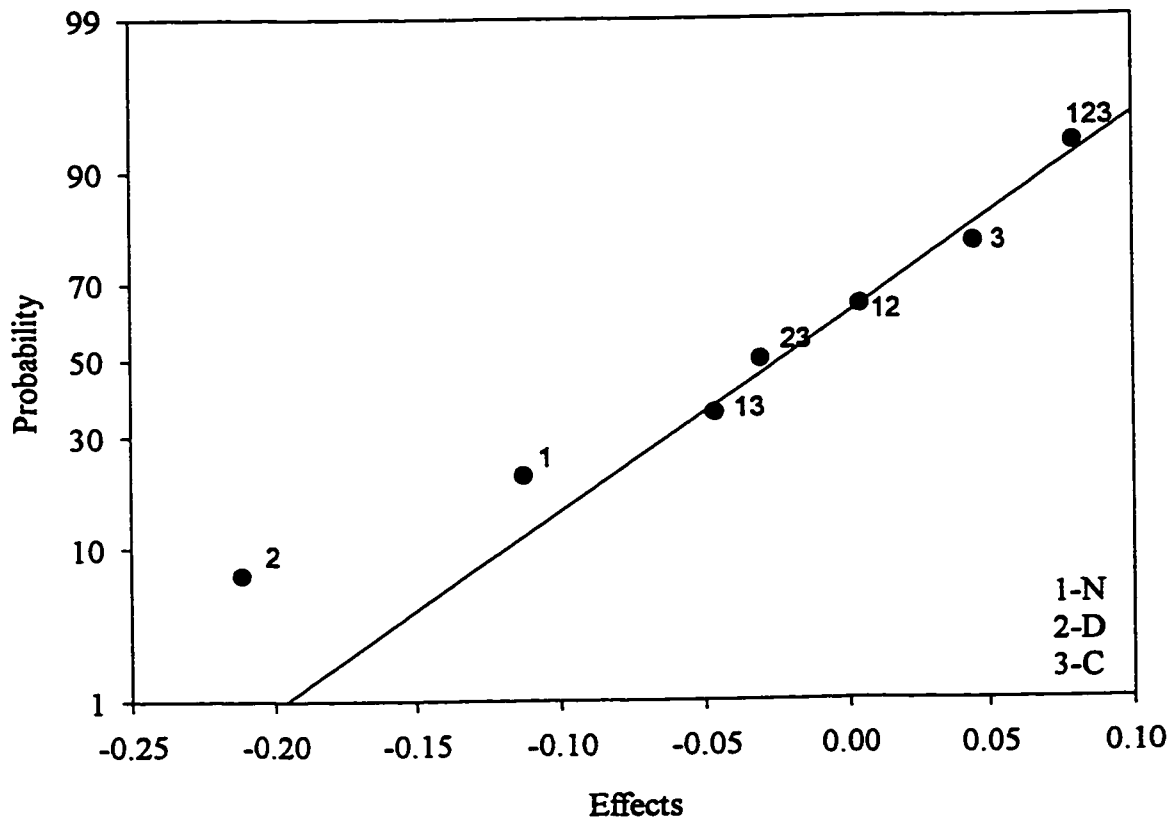


6b) top corner

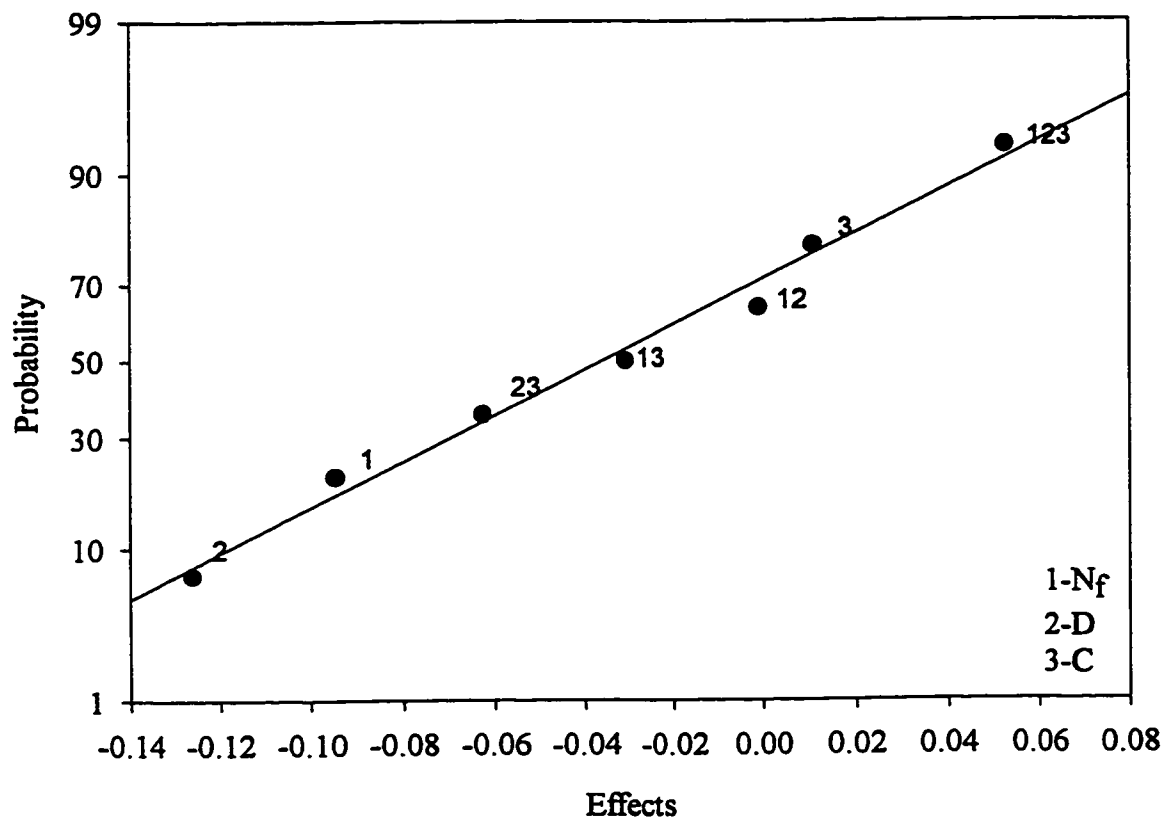


7a) impeller stream

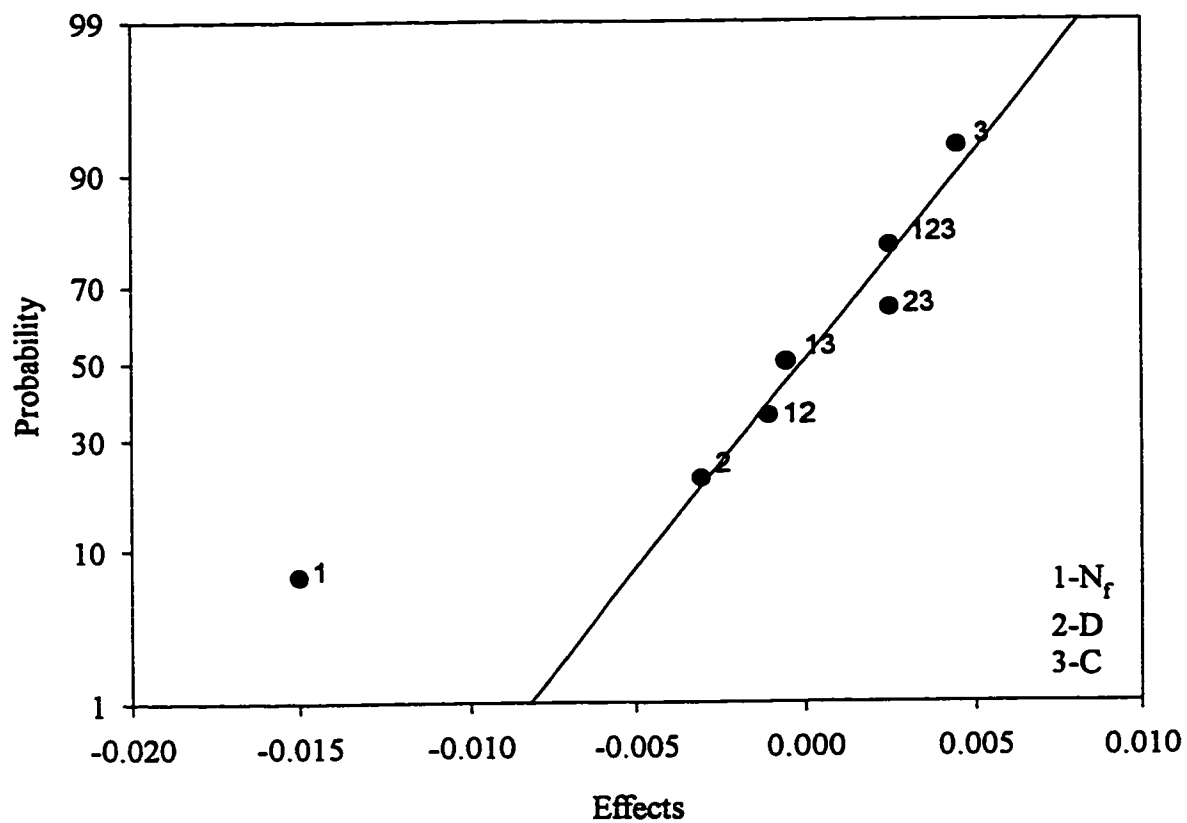
Figure 7: RT, effects of geometric variables on v_{LF}/v_{tot} .



7b) bottom corner

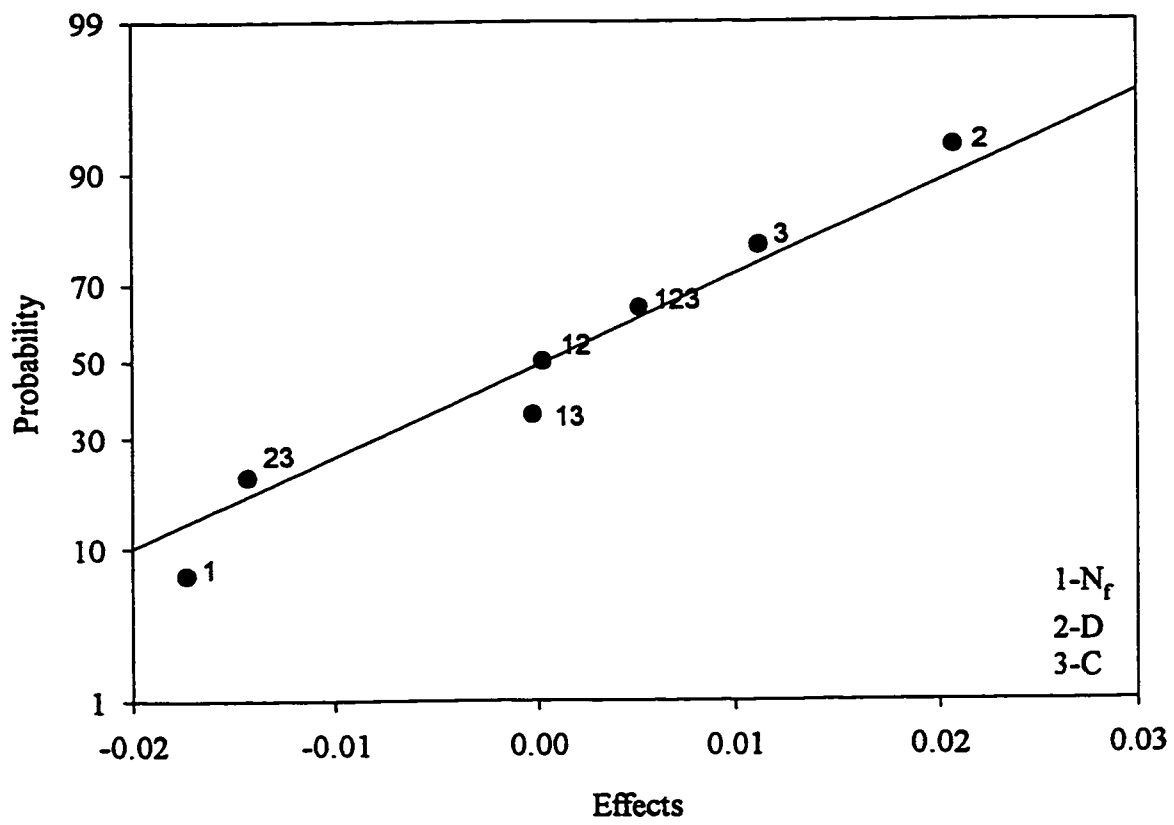


7c) top corner



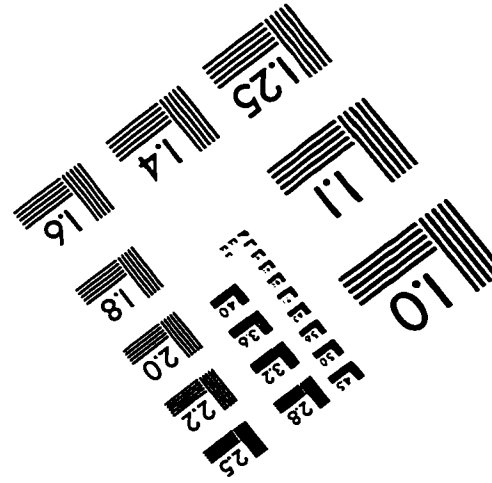
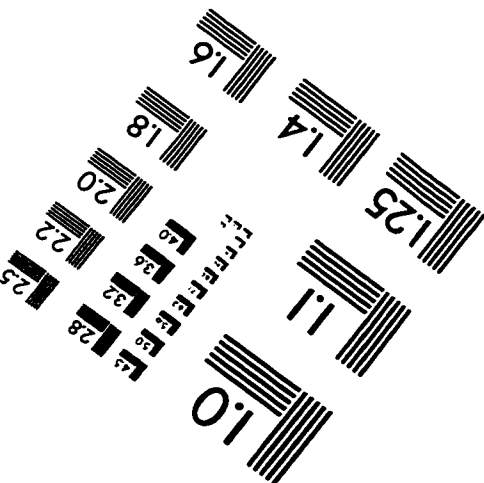
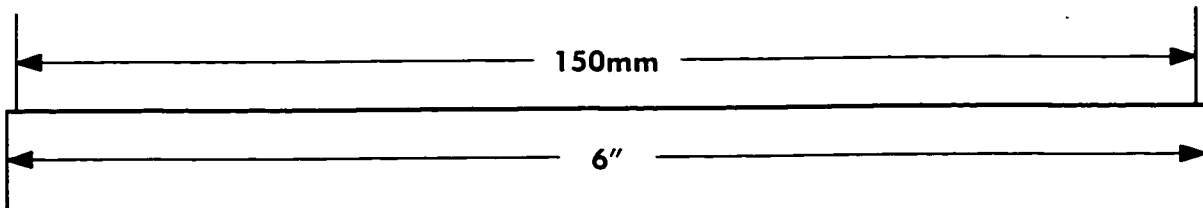
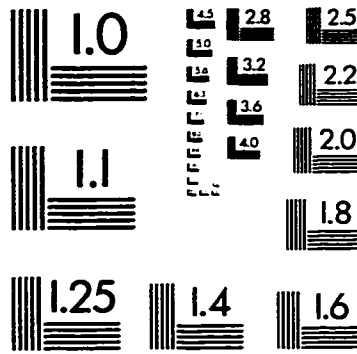
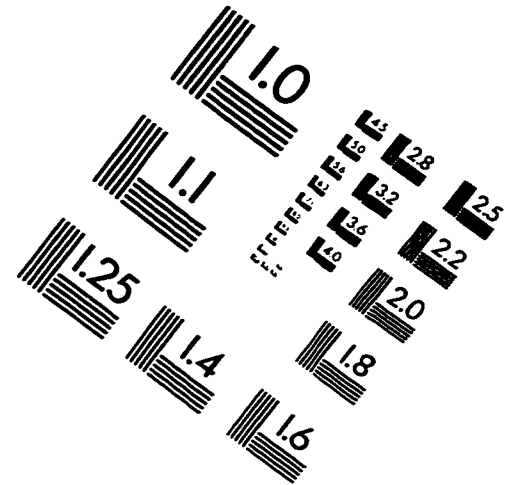
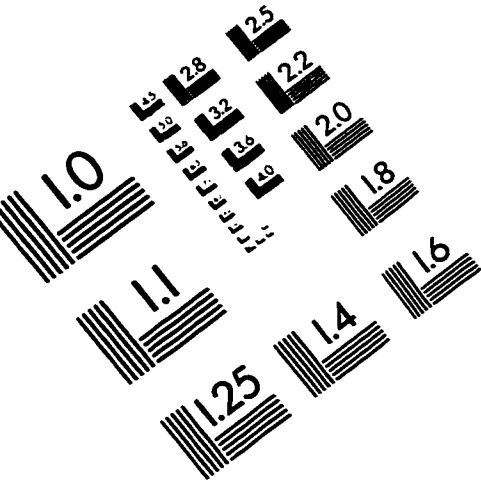
8a) bottom corner

Figure 8: RT, effects of geometric variables on v_{LF}/V_{tip} .



8b) top corner

IMAGE EVALUATION TEST TARGET (QA-3)



APPLIED IMAGE, Inc
 1653 East Main Street
 Rochester, NY 14609 USA
 Phone: 716/482-0300
 Fax: 716/288-5989

© 1993, Applied Image, Inc., All Rights Reserved